STEADY-STATE AND TRANSIENT PERFORMANCE OF EDDY-CURRENT COUPLINGS.

MICHAEL THOMAS WRIGHT. B.Sc.

A THESIS SUBMITTED FOR THE DEGREE OF DOCTOR OF PHILOSOPHY.

THE UNIVERSITY OF ASTON IN BIRMINGHAM.

NOVEMBER 1972.

Summary

This thesis presents a study of two outstanding problems in eddy-current coupling theory:

(a) the steady-state performance of copper-faced couplings.

(b) the transient performance of eddy-current couplings.

After a general introductory chapter which reviews the problems of coupling analysis and existing theories of the machine, the work falls, broadly, into two parts.

The first part (chapters 2-4) presents a three-dimensional theory of the copper-faced coupling and describes experiments designed to test the validity of the theory.

The second part (chapters 5-9) is devoted to the transient performance of eddy-current couplings; in particular, torque response at constant slip speed. After reviewing existing practice and possible theoretical approaches, a theory, based on the transient solution of the diffusion equation, is developed.

Experiments on a new test machine, which investigate the assumptions of the theory and the method of torque prediction, are discussed in detail.

Acknowledgements

The author wishes to acknowledge the following:

Professor E.J. Davies, Professor of Electrical Engineering in the University of Aston in B'ham, who supervised the majority of the work and who has been a source of continuous advice and encouragement.

Redman Heenan Froude Ltd, who have supported the author financially and supplied the experimental machine.

Dr. R.C. Johnson, who was advisor for the work on transient response.

Dr. H. Mc.Kibbin, who supervised the earlier work on the copper-faced coupling.

Mr. B. James, who contributed through many helpful discussions.

The technical staff of the Electrical Machines Centre, particularly Messrs. A.R. Stevenson, C. Partridge and L. Radford, for their unstinted assistance with practical work.

Honours students, P. Mason and N. Moore, who carried out much of the test work on the copper-faced coupling under the author's supervison.

His wife, who patiently typed the manuscript and corrected many minor errors.

Contents.

Page.

Page

List of principal symbols

b ..... transient amplitude of flux-density wave.

d ..... depth of copper-plating.

f ..... armature reaction multiplier.

g ..... airgap length.

h ..... harmonic order.

i ..... field current.

$\bar{i}$ ..... unit vector in x axis.

$\bar{j}$ ..... unit vector in y axis or $\sqrt{-1}$

$\bar{k}$ ..... unit vector in z axis.

m ..... drum saturation coefficient or axial harmonic order.

n ..... slip speed

n_m ..... slip speed for maximum torque.

p ..... rotor pole pairs.

r ..... fundamental flux/pole flux.

s ..... Laplace operator.

t ..... time.

v ..... field voltage.

x ..... cartesian co-ordinate.

y ..... cartesian co-ordinate.

z ..... cartesian co-ordinate.

A ..... transfer function.

B ..... flux-density.

C_1, C_2, C_3 ..... constants.

D ..... airgap diameter.

E ..... electric field strength.

F_g ..... excitation m.m.f.

F_ϕ ..... resultant m.m.f.

F_R ..... armature reaction m.m.f.

G ..... characteristic parameter of copper-faced coupling.

H ..... magnetic field strength.

I_f ..... field current.

J ..... current-density.

K ..... constant.

L ..... axial length of drum, or inductance.

L_a ..... axial length of pole.

M ..... constant.

N ..... winding turns factor.

P ..... dissipated power.

R ..... winding resistance, or amplitude of γ.

S ..... reluctance.

T ..... torque.

T_m ..... maximum torque.

W ..... weighting function.

X ..... function of x.

Y ..... function of y.

Z ..... function of z.

α ..... real part of γ, or reciprocal of skin depth.

β ..... imaginary part of γ.

γ ..... radial propogation coefficient.

δ ..... armature reaction angle.

ϵ ..... coefficient of axial variation.

ϕ ..... phase angle or flux.

ϕ_{ac} ..... fundamental flux per pole.

ψ ..... flux linkage.

ξ ..... drum parameter.

ζ ..... auxiliary drum parameter.

λ ..... pole wavelength.

μ ..... permeability.

ρ ..... resistivity.

τ_d ..... damper time constant.

τ_g ..... coupled time constant.

τ_l ..... leakage time constant.

ω ..... angular frequency.

Λ ..... permeance.

'$\wedge$' above a symbol implies a maximum.

'—' above a symbol denotes either the Laplace transform of the symbol or a vector quantity.

'—' below a symbol denotes a vector quantity.

All quantities are in M.K.S. units.

Variations on the principal symbols, as indicated by different subscripts, are defined in the text.

CHAPTER 1.

EDDY-CURRENT COUPLINGS.

1. Eddy-current couplings.

1.1 Introduction.

The eddy-current coupling has been applied in a wide variety of industrial applications for many years. In the last decade, however, there has been an upsurge in the use of couplings, and machines ranging from less than 1 kW. to almost 2 MW. are now being manufactured in the U.K.

The technological and economic reasons for the increasing use of eddy-current couplings, in preference to other types of drive, have been discussed by the author in two recent publications.[49,50]

The object of this chapter is to review the problems that arise in the analysis of eddy-current couplings and to critically apraise the relevant published work.

1.2 Evolution of the machine.

The eddy-current coupling was the earliest, and is basically the simplest, of all electrical machines. Arago's disc, the famous apparatus designed to illustrate Oersted's discovery of electromagnetism (1820) and first demonstrated by Arago in 1824, was a rudimentary form of eddy-current coupling. The device was in use by Faraday and others, even before the invention of the electromagnet by Sturgeon in 1825.

The elementary form of a practical eddy-current coupling is shown in fig 1.1. It comprises a ferromagnetic loss drum (replacing the disc in Arago's apparatus) mounted concentrically around a field system of alternate poles. The drum is mechanically independent of the pole member, from which it is separated by a small radial airgap. Both members are free to rotate, but

the term 'rotor' is usually applied only to the pole member. To assist with cooling, the drum is usually the input member, since this rotates at the higher speed.

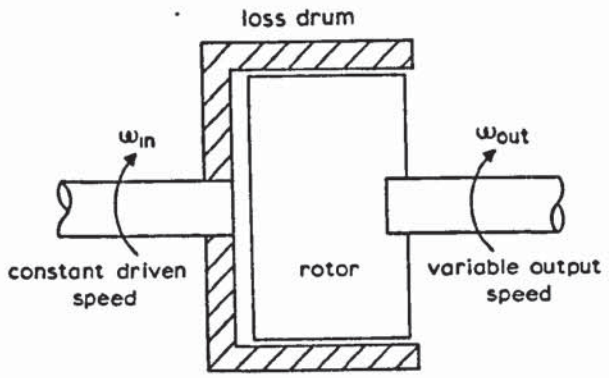

Fig. 1.1

When both members are stationary and the field system is excited, a magnetic-field pattern of alternating polarity is established. If the field pattern is now rotated, eddy-currents will be induced in the drum. The eddy-current field interacts with the airgap flux to produce a torque which is a function of the field current and slip speed.

Fuller details of the operation of the coupling, are given elsewhere.[e.g. 8,49.]

The coupling evolved, parallel with other electrical machines,in terms of magnetic circuit design, insulation and electric loading etc, but the machine had limited use, because of its inherent inefficiency, until the early 1940's. At this time an American company introduced the idea of a brushless eddy-current coupling which, in drives of less than 75 kW, could be incorporated in the same frame as the induction drive machine. The attraction of a brushless, packaged drive was sufficient to promote the coupling to a position of prominence in the variable speed drive market.

However, the elimination of brushes was achieved to the detriment of performance. Figure 1.2 shows how a basic Lundell coupling is modified to eliminate the brushgear.

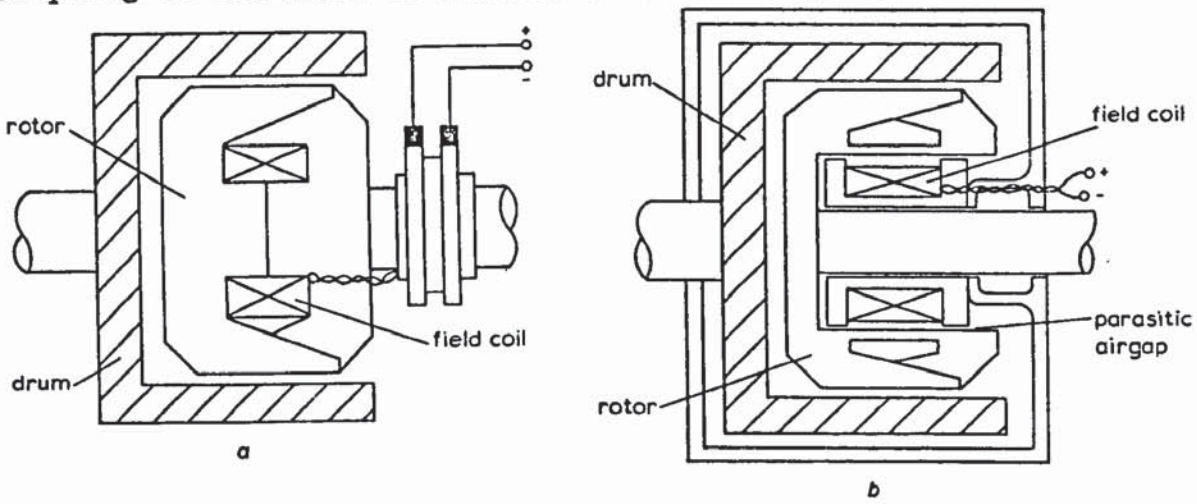

Slip-ring coupling. Brushless coupling.

Fig 1.2

The stationary field in the brushless coupling prevents the shaft from being in its natural place as part of the field structure; instead, the shaft has to pass through the centre of the stationary part of the field system. In small eddy-current couplings, where electromagnetic design is more difficult, this restriction of flux-carrying sections reduces output. The diagram clearly shows that the mechanical construction is complicated, and needs additional bearings. The mechanical design of the cantilevered pole structure demands stiffness in all parts, at the expense of active volume.

Two additional, parasitic airgaps have to be introduced into the magnetic circuit to keep the coil stationary; the m.m.f. for these airgaps is subtracted from the field m.m.f.

Because of space restrictions, the natural slope of the partially-interdigitated poles has to be modified into the flattened form shown. This results in poles that are less effective magnetically, making torque production more difficult.

The magnetic circuit is completely unlaminated. Whilst it is feasible to laminate a part of the stationary iron, this is not done in practice, as it would be difficult and expensive. Part of the stationary iron must be unlaminated and so must the poles. As a result, these machines normally have a slow torque response.[16]

A 75 kW. commercial brushless air-cooled drive, incorporating an integral eddy-current brake and flange-mounted drive motor, is shown in fig 1.3. This form of eddy-current coupling drive is by far the most popular: about 80% of all couplings produced in the U.K. are now made to this type of design.

1.3 Background to the theory of eddy-current couplings.

All of the published literature on the subject deals with the steady state performance of eddy-current couplings with homogeneous solid drums. Usually the object of the analysis is to predict the relationships between torque, slip speed and exciting current. This involves determining the drum loss by an investigation of the field distribution within the drum and in the airgap.

The problems associated with a theoretical treatment of the eddy-current coupling are common to those encountered in any analysis of the electromagnetic field in or near a conducting region where eddy-currents are present. These problems can be conveniently separated into two categories:

(a) problems arising during the solution of the linear partial differential equations which are assumed to govern the field distributions,

(b) problems associated with the non-linear magnetic characteristics of the drum iron.

Consider in detail the first category of problems. On the assumption of constant permeability and resistivity and for frequencies up to and well beyond the maximum operating range of eddy-current couplings, the distribution of eddy-currents in the drum is governed by the diffusion equation, the solution of which is a classical problem in electromagnetic theory.

i.e. $$\nabla^2 \bar{J} = \frac{\mu}{\rho} \frac{\partial \bar{J}}{\partial t} \qquad (1.1)$$

If curvature effects are important then it is necessary to solve (1.1) in cylindrical co-ordinates and express the

solution in a series of Bessel functions. However the intrinsic skin depth of any ferromagnetic material is small, except at extremely low frequencies, and little error is introduced if curvature effects are neglected. A Cartesian reference frame may then be specified with a subsequent simplification in the analysis.

The expanded form of (1.1) in Cartesian co-ordinates is

$$\frac{\partial^2 \bar{J}}{\partial x^2} + \frac{\partial^2 \bar{J}}{\partial y^2} + \frac{\partial^2 \bar{J}}{\partial z^2} = \frac{\mu}{\rho} \frac{\partial \bar{J}}{\partial t} \qquad (1.2)$$

The solution of (1.2) introduces up to eight arbitrary constants which must be evaluated from boundary conditions.

In view of the complexity of the complete three-dimensional solution, the problem is usually simplified by assuming the drum to be infinite in the radial and axial directions. These assumptions reduce the diffusion equation to two dimensions and considerably simplify the analysis.

The assumption of effectively infinite radial depth is reasonable since, at normal frequencies, the depth of penetration is very much less than the physical depth of the drum. However the assumption of infinite axial length is less satisfactory since, in a radial airgap machine where the axial component of magnetic field strength is usually negligible, this constrains the eddy-currents to flow axially along the drum and does not admit the possibility of peripheral or radial closing paths which must exist in a real machine.

It is normally considered that end effects are the largest source of error in the two-dimensional theory.

Under load conditions the m.m.f. produced by eddy-currents flowing in the drum interacts with the standstill m.m.f generated by the field current. This changes both the distribution of flux-density across the pole and the nett value of flux per pole. The calculation of this armature reaction effect is a major analytical problem in the theory of eddy-current couplings. The non-uniformity of the airgap in a practical coupling means that the field and armature reaction m.m.f.s, which are displaced in space, act on different permeances. It is consequently necessary to weigh the effectiveness of field and armature reaction m.m.f. in producing airgap flux.

The second group of problems is associated with variable ρ and μ in the drum iron. The value of ρ has a definite effect on performance, but all coupling theory published to date has been based on the assumption that a thermal steady state has been achieved, and that one effective value of resistivity sufficies for the whole volume of the drum.

The problem of variable permeability is much more complicated since μ varies in three ways:

(i) μ is a function of the amplitude of the airgap flux,

(ii) μ varies with the position in the drum as the magnetic field strength varies with position,

(iii) μ changes due to hysteresis.

The amplitude variation of μ can be taken into account by an approximate analytic relationship for the magnetisation curve of the drum iron. The use of such an approximation theoretically precludes the use of the diffusion equation, which is derived on the basis of constant μ , to describe the field

distribution in the drum. The attempts of individual authors to deal with amplitude dependant μ is dealt with in this literature survey.

The spatial variation of μ is usually neglected and an overall effective value of permeability is taken. This effective value is normally the permeability corresponding to the amplitude of the surface H wave.

No published treatment of eddy-current couplings considers hysteresis to be a major factor affecting performance. The effects of hysteresis on the drum permeability are therefore neglected and hysteresis loss is assumed negligible, or accounted for by a small correction factor.

The two categories of problems resolve themselves into three specific analytical difficulties:

(i) end effects

(ii) armature reaction

(iii) amplitude dependent μ.

Most writers on eddy-current couplings consider armature reaction and one of the other two topics, the remaining problem being treated as a subsidiary effect. There is still conjecture whether end effect or variable μ is more important in governing coupling performance.

No author has yet offered an analysis of the eddy-current coupling which adequately covers all three points. The most sucessful treatments to date have been those that consider armature reaction and variable μ as fundamental problems and introduce suitable corrections for end effects after a solution has been obtained.

In the following section the efforts of individual writers

on the eddy-current coupling are critically reviewed.

1.4 Survey of literature.

The earliest publication dealing with eddy-current couplings (or brakes) is Rudenburg's classic work of 1906 [1]. The field distribution in the loss drum was analysed for a two-dimensional model assuming constant permeability. Rudenburg included armature reaction effects in his initial formation of the diffusion equation by defining the resultant magnetic field in the drum as

$$\bar{H} = \bar{H}_o + \bar{H}_R \tag{1.3}$$

where $\bar{H}_o$ = field due to excitation winding,

$\bar{H}_R$ = field due to eddy-currents,

and $\bar{H}$ = resultant field.

Substitution of (1.3) into the diffusion equation for $\bar{H}$ yields

$$\nabla^2(H_o + H_R) = \frac{\mu}{\rho}\frac{\partial}{\partial t}(H_o + H_R)$$

Since both the divergence and curl of $\bar{H}_o$ are zero,

$$\nabla^2 \bar{H}_o = 0 \tag{1.4}$$

and

$$\nabla^2 \bar{H}_R = \frac{\mu}{\rho}\frac{\partial \bar{H}_o}{\partial t} + \frac{\mu}{\rho}\frac{\partial \bar{H}_R}{\partial t} \tag{1.5}$$

After solving (1.4) for $\bar{H}_o$, Rudenburg postulated a solution for (1.5) and reduced the analysis to a boundary value problem. He showed how the field distribution within the drum was modified under load conditions and went on to derive equations for the dissipated power.

Rudenburg did not present any experimental corroboration

of his theoretical results and it has been found in practice that his equations do not adequately describe coupling performance over a wide speed range. This is almost certainly due to his neglect of variable permeability.

However Rudenburg's paper is a major contribution to the general field of eddy-current phenomena, since he formulated an elegant theoretical approach which has since been refined and successfully used by many other writers.

Rudenburg's work later provided the basis for two other studies of eddy-current couplings: those of Glazenko[5] and Bahler and van der Hoek.[13]

Glazenko[5] used Rudenburg's theory to calculate maximum torque and the slip at which this occurs. He assumes that the distribution of flux-density in the airgap is unchanged by armature reaction and consequently that the no-load and load flux-densities have the same harmonic content. Allowing for the torque contribution of these harmonics, Glazenko calculates torque-slip curves which agree well with his published experimental results. The success of Glazenko's approach is surprising since he neglects end-effects and variable permeability.

Bahler et al[13] show that Rudenburg's theory works very well for a coupling with a non-ferrous drum. The authors derive the normalized torque equation for such a machine. This equation is identical to the normalized torque equation of an induction motor with negligible stator resistance.

Some 17 years after Rudenburg, Rosenburg[2] made the first attempt to deal with the problem of variable permeability. Rosenburg assumed the fields to vary with radial depth in the manner shown in fig. 1.4. He assumes the flux-density to be

constant up to the skin depth where it falls to zero. The current-density is assumed to fall linearly from the surface value to zero at the skin depth.

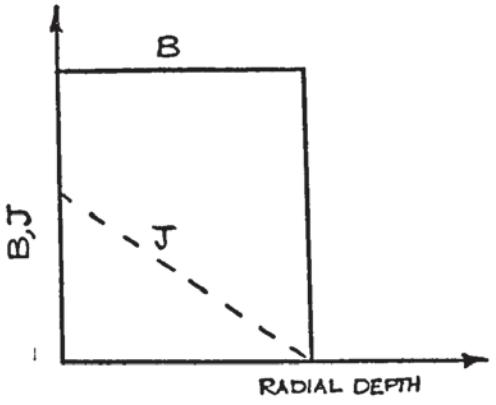

Fig 1.4

Rosenburg ignores the logical inconsistency of a constant flux-density associated with a reducing current-density. The assumption of constant flux-density implies that the drum iron is fully saturated throughout the skin depth. A rectangular magnetisation curve as fig.1.5 is thus assumed.

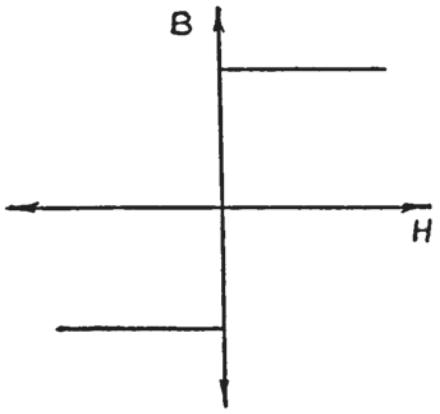

Fig 1.5

Making these bold assumptions and applying Faraday's and Kirchoff's laws to the resulting analytical model, Rosenburg derived his equation for the loss per unit area of the drum:

$$W = \tfrac{2}{3} \rho H_o^2 \alpha$$

where H_o is the externally applied field and α is the reciprocal of the skin depth. This is 4/3 times the loss predicted

by Rudenburg for high slip operation.

Despite the fact that Rosenburg's theory neglects armature reaction and end effects and contains several disturbing inconsistencies, his predicted loss agrees well with observed loss at high slip. Rosenburg's analysis, however, gives incorrect answers over a wide speed range.

The failure of both the linear theory of Rudenburg and Rosenburg's fully saturated theory indicated the need for a more refined and less extreme representation of the magnetisation curve.

The first successful treatment of the eddy-current coupling was given by Gibbs[3] in 1946. For the purpose of deriving the fundamental equations Gibbs made the usual simplifying assumptions that the drum was infinitely long, carried only axially directed eddy-currents and possessed constant permeability. Gibbs also neglected the peripheral distribution of current-density and began with the one-dimensional form of the diffusion equation:

$$\frac{\partial^2 J_z}{\partial y^2} = \frac{\mu}{\rho}\frac{\partial J_z}{\partial t} \qquad (1.6)$$

The notation for the Cartesian co-ordinates is

x = peripheral dimension,

y = radial dimension,

z = axial dimension.

Gibbs specified J_z as

$$J_z = J_m e^{j\omega t}$$

This means that (1.6) may be written,

$$\frac{\partial^2 J_z}{\partial y^2} = \alpha^2 (1+j)^2 J_z \qquad (1.7)$$

where α is the reciprocal of the skin depth and is given by

$$\alpha = \left(\frac{\omega \mu}{2\rho}\right)^{1/2} \qquad (1.8)$$

The solution of (1.7) is

$$J_z = J_m e^{-\alpha y} e^{j(\omega t - \alpha y)} \qquad (1.9)$$

The loss per unit area of drum surface was calculated by integrating the loss density through the drum depth (which is considered infinite).

ie. $$W = \frac{1}{2} \int_0^\infty \rho J_z^2 . dy$$

The loss is thus given by

$$W = \frac{\rho J_m^2}{4\alpha} \qquad (1.10)$$

Gibbs then proceeded to develope the relationships between flux, current-density and speed. By integrating J through the drum depth and over a pole pitch he derived the armature reaction m.m.f., which he added to the resultant gap m.m.f. to obtain the required field excitation. He assumed that the standstill distribution of flux-density was unchanged under load conditions.

Having derived the basic equations of the coupling using a simplified linear analysis, Gibbs then treated end effects and variable permeability.

Gibbs' conception of end effects is best summarised in his own words[3]:

"The introduction of the finite length 'l' along the

z axis necessitates the inclusion of 'end effects' i.e. the effects of the end paths of the eddy-currents where they close. These effects are considered to occur wholly outside the influence of the inducing flux-density wave, which can be termed the 'active' part extending to a length 'l'. Therefore the sole consequence is to put additional resistance to the current flow. They are best accounted for by the use of a multiplier with ρ , so that $(r.\rho)$ becomes the effective resistivity replacing ρ , and 'r' is the multiplier now to be found".

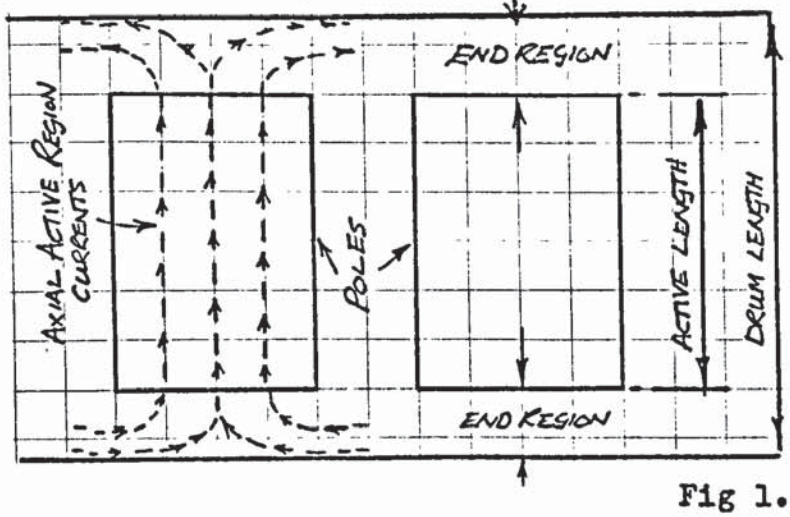

Fig 1.6

Fig.1.6 illustrates this analytical model proposed by Gibbs.

Gibbs calculated the equivalent resistance of the end region over a pole pitch and then, by comparing this with the resistance of the active region, he derived the resistivity multiplier 'r' which is a function of pole pitch and active length, but is independent of slip. To determine this equivalent resistance Gibbs simplified the end region field configuration using the Schwartz-Christoffel transformation. The use of the transformation assumes that Laplace's equation is valid in the end region i.e. the end region currents are resistance-limited.

To include variable permeability Gibbs neatly rearranged his equations to give

$$\mu^{1/4} H_m = \left(\frac{8W^2}{\rho\omega}\right)^{1/4} \qquad (1.11)$$

Using an experimental curve relating $\mu^{1/4} H_m$ and H_m, Gibbs was then able to relate the loss W to the surface field strength H_m. In this manner the fundamental flux, ϕ_{ac}, required to generate the loss W at frequency ω was determined.

Gibbs gave a sample design of an inductor coupling and showed that the theoretical and experimental torque-slip curves correlated closely. Gibbs' paper was an important step towards a realistic theory of the eddy-current coupling and the first publication of practical significance in coupling design. His work illustrated two important points in the treatment of end effects and variable permeability.

(a) The end effect multiplier 'r' is independent of slip. This suggests that the influence of end effects is to reduce the torque at all slips in equal proportion i.e the shape of the torque-slip curve is unaffected. In practice this is not quite correct, but the constant multiplier adequately corrects for end effects over the operating speed range of the coupling.

(b) Although it is mathematically invalid to apply the results of an analysis based on the diffusion equation to a situation with variable permeability, satisfactory results can be obtained by such a procedure.

Gibbs' analysis is, however, unsatisfactory in certain aspects. His neglect of the spatial field distributions leads

to the conclusion that the loss equation (1.10) applies at all frequencies, where in reality it is only valid for a limiting frequency condition.[8] Gibbs adds the armature and resultant m.m.f.s arithmetically, even though they are displaced in space. He further assumes that the standstill flux-density pattern applies under load conditions, which is incorrect, even at very low slips.[14]

Gibbs' model of the eddy-current distribution in the drum (flowing axially over the active length, where the current-density is governed by the diffusion equation, and then crossing from pole to pole in the end region, where Laplace's equation is assumed to be valid) is unlikely to be a true physical picture, since there is no logical reason to suppose that the currents flow in such a constrained manner. A more reasonable supposition is that the eddy-currents form closed loops within the 'active' region and that the whole of the drum is governed by the diffusion equation. Application of the diffusion equation to the end-regions of a coupling implies finite end-region inductance, the presence of which has been suggested by Davies[6] and experimentally detected by James.[14]

The fact remains however that, apart from machines with very short drum overhangs, the discretionary use of Gibbs' multiplier 'r' yields good results in practice.

Gibbs' approach provided the stimulus for Davies' theory of the eddy-current coupling published in 1963.[8] Davies extended Gibbs' analysis to include the peripheral field distributions and gave a more rigorous treatment of armature reaction effects. His work runs parallel to that of Gibbs up to the point where the earlier author resorted to an empirical curve

to account for variable permeability. At this point Davies introduces an analytic relationship for μ . The remainder of his work is involved with the derivation of the couplings performance equations in the light of his equation for μ . Davies derives the torque-slip equation of the coupling in both absolute and normalised form and shows how the variable drum permeability intimately governs the performance of the machine.

Davies begins with the normal two-dimensional model, subject to the assumptions discussed earlier. Following the same co-ordinate notation as (1.6), Davies writes the diffusion equation as

$$\frac{\partial^2 J_z}{\partial x^2} + \frac{\partial^2 J_z}{\partial y^2} = \frac{\mu}{\rho}\frac{\partial J_z}{\partial t} \qquad (1.12)$$

The surface current density wave is defined as

$$J_z = J_m \cos(\omega t - \frac{2\pi x}{\lambda}) \qquad (1.13)$$

where J_m is the amplitude of surface density, and λ is the wavelength of peripheral variation.

The solution for (1.12) is

$$J_z = J_m e^{-\beta y} \cos(\omega t - \frac{2\pi x}{\lambda} - \gamma y) \qquad (1.14)$$

where β and γ are complex functions of the skin depth (1.8) and λ.

Davies shows that, when the skin depth is small (α is large), both β and γ tend to α . The quantitative criteria for this condition is

$$\sqrt{2}\,\alpha \gg \frac{2\pi}{\lambda} \qquad (1.15)$$

Under these circumstances the current-density equation simplifies to

$$J_z = J_M e^{-\alpha y} \cos(\omega t - \frac{2\pi x}{\lambda} - \alpha y) \qquad (1.16)$$

For the conditions where (1.15) is valid it is shown that

$$H_x \simeq \frac{J_z}{\sqrt{2}\alpha} \angle 45^\circ ,$$

$$H_y \simeq -\frac{\lambda J_z}{\alpha^2 \pi} ,$$

and, therefore,

$$H_x \gg H_y$$

This means that the resultant magnetic field strength $\bar{H}$ can be taken as H_x.

i.e. $$H = \frac{J_z}{\sqrt{2}\alpha} \angle 45^\circ . \qquad (1.17)$$

The surface current-density amplitude J_m is then related to the fundamental flux per pole Φ_{ac} to give

$$\Phi_{ac} = \frac{2\rho L J_M}{\omega}$$

where L is the active length of the machine.

Davies then goes on to calculate the drum loss and shows that Gibbs' loss equation,

$$W = \frac{\rho J_M^2}{4\alpha} \qquad (1.10)$$

is only valid provided (1.15) holds.

He then rearranges his expressions to yield Gibbs' substitution equation, where the earlier author considered variable permeability:

$$\mu^{1/4} H_m = \left(\frac{8W}{\omega\rho}\right)^{1/4} \qquad (1.11)$$

At this juncture Davies introduced an analytic relationship for μ . He discovered that the magnetisation curves of many ferromagnetic materials could be accurately represented around and above the knee by the expression

$$B = a.H^{b} \tag{1.18}$$

For substitution in (1.11) this is more conveniently written in the form,

$$\mu^{1/4}.H = k.H^{m} \tag{1.19}$$

The material almost universally used for eddy-current coupling drums is wrought iron, which Davies showed to obey the equation,

$$\mu^{1/4}.H = 0{\cdot}97.H^{0{\cdot}77} \tag{1.20}$$

Using (1.20) Davies was able to proceed from (1.11) and present a non-linear theory of the eddy-current coupling which was completely analytic. In common with Gibbs, Davies neglected the spatial and hysteretic variations of permeability.

The relationship between flux, torque and slip speed was shown to be

$$\Phi_{ac} = 1{\cdot}02.M.T.^{0{\cdot}35}\, n^{0{\cdot}325} \tag{1.21}$$

where M is a parametric constant of the machine.

Davies calculated the armature reaction m.m.f. F_R by integrating J_z over the depth of the drum and with respect to the peripheral co-ordinate 'x'. This produced an equation which showed that, if $\sqrt{2}\alpha \gg 2\pi/\lambda$, F_R was 45° out of phase with the surface J and hence 135° out of phase with the inducing flux. The relationship between F_R , torque and slip speed is

$$F_R \propto \frac{T^{0.625} \cdot n^{0.325}}{M.P^2} \qquad (1.22)$$

Davies calculated the excitation m.m.f. F_g from the vector sum of F_R and the flux component of m.m.f. F_ϕ .

i.e. $$F_g^2 = F_\phi^2 + F_R^2 - 2 F_\phi F_R \cos\delta \qquad (1.23)$$

where δ tends to 135^0 if $\sqrt{2}\alpha \gg 2\pi/\lambda$.

Equation (1.23) was expressed in terms of torque and slip speed and differentiated to determine the maximum torque T_m corresponding to a given value of F_g . The slip n_m at which this torque occurs was also derived. Using these relationships, Davies then developed the normalised torque equation of the eddy-current coupling.

Davies was the first author to present a detailed experimental study of the coupling.[8] His experimental work, carried out on a specially designed Lundell machine, was extensive and corroborated his theoretical work.

Davies later extended the results of his earlier work[6,8] to include the general relationship (1.19).[12] This broadened the scope of his theory to cover any drum material that obeys (1.18). Davies extends the process of normalisation to give generalised flux and armature reaction curves. The effects of different rotor pole configerations (Lundell, inductor etc) are examined in detail. Davies undertakes a theoretical comparison of Lundell and inductor couplings during which the influence of the non-uniform airgap is analysed. The factor 'f', by which F_R is multiplied to yield the effective value of armature reaction m.m.f., is calculated for a range of pole designs.

This paper also represents the first attempt to deal with the difficult problem of optimum coupling design.

Davies' analysis does not include end effects, although he shows how his equations may be modified to take account of them.[6] His major contribution is in enhancing a basic understanding of the phenomena that govern coupling performance. The exclusion of end effects does not seriously detract from this, since, as Gibbs has shown, they appear to be accountable by a constant multiplier. It is probably for this reason that Davies' normalised curves[12] work equally well for machines with substantial end effects (Davies' experimental machine) and machines where end effect is reduced to a minimum (James' endring coupling).

Davies' performance equations are limited to the conditions where (1.15) is valid. Since the skin depth (α^{-1}) increases as frequency reduces, it can be seen that there will be some lower frequency limit at which (1.15) will cease to apply. However, in practice, the lower frequency limit does not appear to be a serious limitation.

James'[14] work indicates that the normalised curves are completely reliable down to a slip of 20% of the slip for maximum torque. (In James' case this corresponds to a lower frequency limit of 5 Hz or 50 r.p.m. slip).

The linear theory implies that superposition is valid and Davies assumes this to be so, even after the μ substitution is made. On this basis he estimates that the torque contribution of the harmonic flux is negligible over the practical speed range of the machine. He consequently limits his considerations to fundamental quantities.

Davies' theory of the coupling is open to the same criticism as that of Gibbs[3], in that it uses the results of the linear analysis in combination with a non-linear substitution for μ. However, judging by the close correlation of theory and experiment, in common with Gibbs' work, it seems valid in practice.

This point of view is also held by James.[14] He concludes that,

> "The generalised curves (of torque, flux and armature reaction m.m.f.) have been shown to be within the limits of accuracy required for design studies of couplings over the range $0.2 \leqslant \frac{\Omega}{\Omega_m} \leqslant 0.4$. This demonstrates that, even when faced with the analytic intractability of solid iron, a judicious blend of theory and practice, as used by Gibbs and Davies, can yield results of practical usefulness".

James' work[14] was essentially an experimental comparison of couplings with and without end effects. Copper endrings were brazed onto the edges of the drum to reduce end effects. James' experimental work showed that, although endrings eliminated the end region loss, they did not prevent the variation of flux-density over the axial length.

The flux-density in the endring machine was shown to have a significantly higher harmonic content than the flux-density in the same machine with a homogeneous iron drum (Davies' coupling). Using these harmonic flux-densities and assuming superposition to be valid, James estimates up to 40% harmonic torque at high slips. The presence of this substantial harmonic torque would appear to mean that Davies' theory, which was derived for fundamental quantities only, is not applicable to the

endring coupling. However, James found that the experimental results for this machine correlated very well with the theory. Thus it would appear that harmonic flux is less effective in producing torque than the linear theory would indicate. The discrepancy almost certainly lies in the doubtful procedure of applying the superposition theorem to a non-linear situation.

James offered an alternative end effect treatment to that of Gibbs. He assumed discrete active and end regions in the same manner as the earlier author, then, treating the end regions as Laplacean, he derived an equation for the end region scalar electric potential. From this potential equation, James determined both the loss and nett current of the end region and hence the equivalent resistance. Comparing this with the active region resistance given by Gibbs, he then derived a loss multiplier to account for the extra end region loss. James' experimental work shows that this alternative end effect treatment correlates significantly better with test results than does Gibbs' theory.

James' theory of end effects, although yielding useful practical results, is unsatisfactory in that it is based on the same physically unreasonable model as Gibbs'. The assumption that Laplaces' equation governs the end regions is equivalent to neglecting the interaction of the end region and excitation fields, the effect of which is evident in James' measured axial flux-density distribution.

In order to overcome this vexing problem of end effects, Malti and Ramakumar[9] carried out a three-dimensional analysis of the eddy-current coupling. End effects are implicit in their theory but they assumed constant permeability.

The authors follow Rudenburg's approach in dividing the flux-density into excitation and reaction components and give (1.5) as their basic equation. To determine the effect of the reaction flux-density they multiply the physical airgap by the ratio of pole pitch to pole arc. The logic involved in such a step is not clearly explained.

Malti and Ramakumar give experimental torque-slip curves, taken at very low excitations to avoid saturation, which they claim agree well with theory. However this theory is of little practical significance, since commercial couplings operate with the drum iron well into the saturation region. Industrial experience has shown that Malti and Ramakumar's analysis gives satisfactory results for machines with non-ferrous drums where armature reaction does not predominate.

Sharov[4] based his treatment of armature reaction in the coupling on the d.q. axis theory of synchronous machines. From a one-dimensional field solution he derives an equation for armature reaction m.m.f., which is similar to that later given by Davies.[8] He quotes experimental drum "power factor angles" of 18-31° at 5% slip. Sharov did not consider end effects.

Gonen and Stricker[11] give the only theory of the coupling that includes the spatial variation of permeability. The variation of drum permeability with depth is represented by Ollendorf's equation[17]:

$$\mu = \mu_s e^{\lambda y}$$

where μ_s is the surface permeability and λ is approximately equal to α (see (1.8)).

The introduction of this relationship for μ produces a solution of Maxwell's equations in terms of first order Hankel functions. The authors neglect armature reaction effects and take account of end effects using a resistivity multiplier derived by Fillmore[18] for drag cup induction motors. Applying the superposition theorem to the assumed rectangular distribution of airgap m.m.f., they estimate a harmonic torque contribution of approximately 40%. They found that good correlation with test results was achieved if, "The values (of torque) obtained from (the fundamental torque equation) were increased by 35% to allow for hysteresis and higher harmonics". This procedure implies that the harmonic torque content is independent of slip speed and, whilst this may be approximately true at low slips in inductor couplings, in general it will not be valid.

The problems involved in analysing the coupling led Erdelyi and Kolatorowicz[7] to conclude that, " .....attempts to find a purely analytical solution of this problem encounter great difficulties, and these at present seem insurmountable". Their approach was to apply the rules of model theory to the experimentally determined torque-slip curves of a prototype coupling. The discrepency between predicted and measured torques for larger scaled machines was an average of 11%, which they consider adequate for design studies.

Hansen and Timmler[10] also rejected the conventional field theory approach to coupling analysis. Their treatment is based on sketching the airgap flux patterns. From these patterns they derived equations for the currents flowing in the drum and an equivalent circuit to represent the different drum regions. Then by applying F = B.l.I, they estimated the torque per pole.

Kundu's paper[15] is essentially a reworking of the initial part of Davies' 1963 paper[8] and Gibbs' end effect treatment[3], which he erroneously claims to be original. The author uses a five term power series, determined by a numerical curve fit to the magnetisation curve, to take account of variable permeability, but does not explain how this is used in the calculation of performance. In fact the paper is vague in most aspects and contributes little to the field, but is included here for completeness.

As far as the author is aware, the only publication dealing with the transient performance of the coupling is that by Davies, James and Wright,[16] based on the experimental work described in chapters 8 and 9 of this thesis.

There is no published work on copper-faced couplings.

1.5 Purpose of this thesis.

This thesis presents a study of the two outstanding problems in the theory and design of eddy-current couplings:

(a) eddy-current couplings with copper-plated (copper-faced) drums

(b) the transient performance of eddy-current couplings.

Chapters 2, 3 and 4 deal with the copper-faced coupling, whilst the remainder of the thesis is devoted to the transient performance of eddy-current couplings.

CHAPTER 2.

COPPER-FACED EDDY-CURRENT COUPLINGS.

2. Copper-faced eddy-current couplings.

2.1 Introduction.

In the same way that induction motor torque-slip curves are modified to suit different applications (e.g. N.E.M.A. classifications A to D), it is often desirable to tailor the torque-slip curve of the coupling to suit individual drive requirements. Normally it is required to reduce the slip speed, n_m, at which peak torque occurs and, in so doing, increase the torque at low slip. The difficulty of obtaining torque at low slip (where the machine will usually be rated) is often a serious problem, particularly in inductor couplings which are typically rated at a slip corresponding to $\frac{n}{n_m} = 0.02 - 0.05$.

The most effective ways of altering the torque-slip curve are by brazing copper endrings onto the extremities of the drum or by coating the internal drum surface with a thin sleeve of copper. The endring method, although effective, gives little control over the shape of torque-slip curve and does not allow the selection of a particular value of n_m, since it simply eliminates the end region loss.[14] On the other hand the method of copper-facing allows close control of n_m and, with experience, it is possible to select the depth of copper required to produce a given n_m with reasonable accuracy.

As the requirement for special purpose eddy-current couplings grows, the copper-faced coupling may be expected to become an increasingly important adjunct to the conventional machine.

2.2 The effect of copper-facing on the performance of the coupling.

The effect of copper-facing on the torque-slip curve of a coupling is shown in fig 2.1. The machine involved was a large inductor coupling, but the general effects illustrated are typical of all copper-faced machines.

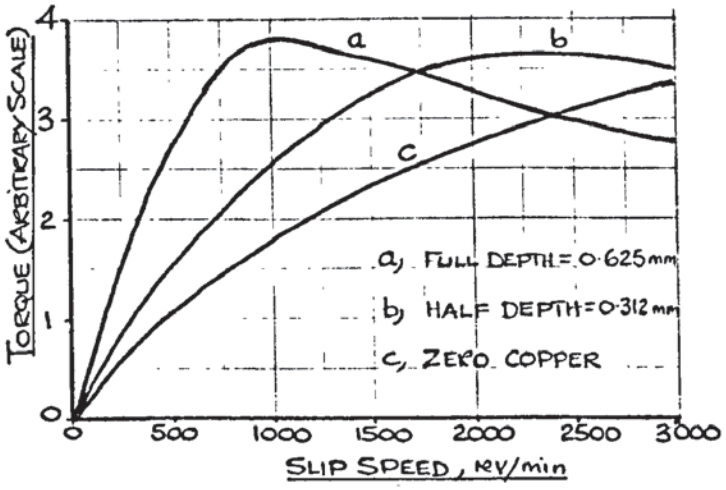

Fig 2.1

Torque-slip curves were measured with two depths of copper on the drum (curves (a) and (b)). The copper was then fully machined-off, leaving a conventional solid iron drum, and a third torque-slip curve, (c), taken. The magnetic airgap (g+d) was the same in all three cases. The curves illustrate two important points:

(a) The peak torque does not depend on the depth of copper, or even if any copper is present, only on the magnetic airgap.

(b) The value of n_m is approximately inversely proportional to the depth of copper ($\frac{d_a}{d_b} = 2$; $\frac{n_{mb}}{n_{ma}} = 2{\cdot}2$)

The first of these "rules" is valid for all couplings, whether the depth of copper is substantial or very small.* The

---

*This is logical since Davies[12] shows that T_m is independent of 'm' and hence does not depend on the composition of the drum.

second, however, regarding n_m, tends to fall down when the depth of copper is small (say less than 0.1 mm). This means that, as the depth of copper reduces, and the influence of the backing-iron fields is felt, the situation is much more complex than the simple relationship suggests.

Provided the magnetic airgap is kept constant, copper-facing the drum has negligible effect on the transient response of the machine, except at very low slips where the copper-facing reduces the torque response time by 5-15% depending on the rotor design. This fact is discussed in the second part of the thesis which deals with the transient performance of eddy-current couplings.

2.3 Background to the theory of copper-faced couplings.

2.3.1 Nature of the problem.

As discussed in chapter 1, the major problem in the analysis of conventional couplings is variable μ. However, because of the dramatic effect of copper-facing on the torque-slip curves of a coupling, it is logical to suppose that a major proportion of the torque is produced by the currents flowing in the copper and, hence, that the problem of variable μ, which applies only to the backing-iron, is less important.* It is, therefore, reasonable to expect adequate results from a linear theory.

However, even when reduced to a problem of linear analysis, the copper-faced coupling is much more complex than the

---

*The influence of variable μ is discussed in detail in section 3.4.4 of chapter 3.

conventional machine. A complete theory must account for the eddy-current distribution in both regions of the drum (i.e. copper and iron), the loss due to these currents and their combined effect on the excitation m.m.f. The theory should, ideally, be three-dimensional, because end effects cannot be satisfactorily eliminated by endrings, due to the relatively low impedance of the copper-face, and also because the present end effect theories[3,14] are physically unreasonable.

The essence of the problem is thus to analyse the field-distribution in a three-dimensional double-region structure carrying eddy-currents and to interpret the results in terms of machine parameters.

2.3.2 Parallel theories of cylindrical-rotor induction machines.

There is no published literature on the copper-faced coupling, but there are a number of papers on copper-cylinder (i.e. sleeve rotor or "drag cup") induction machines[e.g. 18-23] which deal with similar electromagnetic configurations. Since the induction machine is a.c. voltage-forced, it can be considered to be flux-forced over a limited speed range and hence none of the theories deal with armature reaction effects. Also, because of the rotor construction, backing-iron loss usually has only a minor influence on performance and is neglected. For these reasons the theory of copper-cylinder induction machines does not apply directly to copper-faced couplings. However the various methods of calculating the loss in the copper cylinder are relevant to the copper-faced coupling.

The total power dissipated in the copper is determined by

evaluating the integral of $\rho.J^2$ throughout the volume of the cylinder. However, with the normal open-ended type of rotor construction, which is analogous to the copper-faced drum, the current-density divides into two components, axial and circumferential, which vary in three dimensions. It is the difficulty of determining the $\bar{J}$ paths explicitly which leads to uncertainty in the loss calculation.

The standard paper on the subject, which is referenced by most other writers, is that of Russell and Norsworthy,[19] in which the authors analyse the eddy-current distribution in a copper-cylinder with and without endrings. They neglect skin effect and calculate the $\bar{J}$ contours assuming radial flux penetration of the copper in the active region and Laplacean end regions. From these results they extract end effect multipliers for both endring and open-ended rotors. (End effects are present in the endring rotor because of the low active region impedance: see section 2.3.1). The paper can be considered as a compromise between the approach of Gibbs[3], which assumes axial $\bar{J}$ paths in the active region, and a more rigorous diffusion analysis of the whole eddy-current member which is offered by this work.

To allow for circumferential leakage current in axially laminated rotors, Russell and Norsworthy introduced anistrotropic conductances for the cylinder, but did not deal with the effects of the backing-iron fields. Their paper largely superceded an earlier work with the same objectives by Fillmore.[18]

Russell and Norsworthy's end-effect theory has been used by subsequent authors on induction machines, notably in an

excellent paper on "thick cylinder" motors by West and Hesmondalgh.[21] The authors analyse a servo-motor of the double stator type, (as do Jayawant and Parr[23]) where the annular copper rotor is made thick for mechanical strength and is thus subject to significant skin effect and relatively high leakage flux. The analysis is not suitable for normal copper-faced couplings, where the depth of plating is always much less than the intrinsic skin depth of copper, but should correspond closely to couplings with solid copper drums, as described by Bahler and van der Hoek[13] (see chapter 1). Indeed, if the torque-slip curves shown in fig 11 of reference 21 are normalised, they conform closely to the normalised torque equation given by Bahler and van der Hoek.

It is demonstrated, in chapter 3, that the theories of Russell and Norsworthy and Bahler and van der Hoek (and hence West and Hesmondalgh) agree, for limiting conditions, with the more general theory of eddy-current loss given in this thesis.

2.3.3 The wave impedance theory.

In multi-region machines, the wave impedance analysis has been used to obtain simple and rapid solutions to complex problems [e.g 23] and is often advocated as an alternative to traditional field theory methods.[e.g 20] In view of the efficient way in which Jayawant and Parr[23] applied the concept of wave impedance to thick cylinder induction motors, handling airgap, copper and iron in one impedance term, it seemed logical to investigate whether the method could advantageously be applied to the copper-faced coupling.

A wave impedance theory of the copper-faced coupling was developed along the lines of Cullen and Barton's classical paper,[25] using transmission line notation. The transmission line analogue of the machine is shown in fig 2.2,

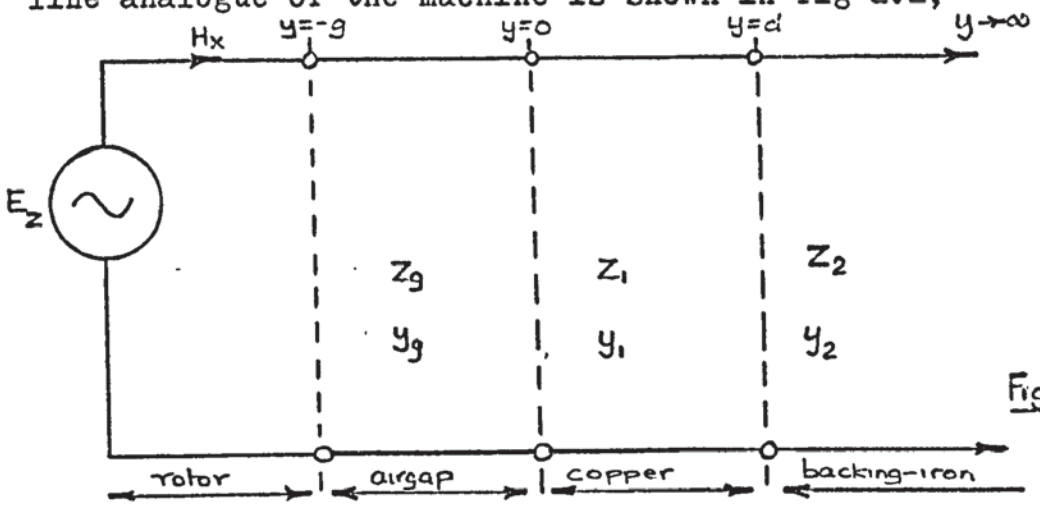

Fig 2.2

where $z_{g1,2} = j\omega\mu_{g1,2}$ Ωm^{-1}

$y_g = j\omega\epsilon_0 + j(\frac{2\pi}{\lambda})^2/\omega\mu_0$ υm^{-1}

and $y_{1,2} = \frac{1}{\rho_{1,2}} + j(\frac{2\pi}{\lambda})^2/\omega\mu_{1,2}$ υm^{-1}

The theory was very useful because it introduced, through calculation of the region impedances, the scheme of successive approximations in the theory of chapter 3, which are necessary to obtain performance relationships from the general three-dimensional field equations.

The wave impedance theory, however, suffers from two overwhelming defects: it does not include armature reaction or end effects. Although, in his original paper, Schelkunoff[24] showed that the impedance method could be applied to three-dimensional problems requiring solution in cartesian, cylindrical [e.g. 22] or spherical co-ordinates, when more than two dimensions are involved, the method loses its essential advantage of simplicity.

It was for these reasons that the wave impedance theory

was rejected in favour of a "traditional" field theory approach.

2.4 General theoretical method.

The theory of chapter 3 is a general analysis of the eddy-current distribution in a three-dimensional double region structure. Initially no constraints are imposed on the materials or dimensions of the structure, except the assumption that the backing region is semi-infinite. This is not an essential assumption, but one which is reasonable and considerably reduces labour.

After the general current-density equations have been derived, attention is paid to the particular materials and relative dimensions of the copper-faced drum and simplified equations are obtained.

This procedure leads finally to very simple performance equations which are verified experimentally in chapter 4. The overall result is a practical method of analysing and designing copper-faced couplings which is based on a sound mathematical foundation.

CHAPTER 3.

THEORY OF THE COPPER-FACED EDDY-CURRENT COUPLING.

3. Theory of the copper-faced eddy-current coupling.

3.1 Introduction.

To simulate the eddy-current distribution in a practical copper-faced loss drum, a two-region drum model of finite axial length, with axial and peripheral eddy-current components present is analysed using linear theory. Expressions for the power dissipated in each region of the model are shown to reduce to approximate forms which are valid for slip speeds well beyond the normal operating range of couplings. These losses are compared to show that a linear analysis is justified, except at very low slip speeds. Torque-speed relationships are then derived from the power equations. The effects of armature reaction are examined in detail and the resulting relationships between armature reaction m.m.f., torque, speed and flux used to develop generalised performance relationships which are valid for all copper-faced couplings.

3.2 Analytical model.

Since the depth of copper used in normal industrial copper-faced couplings seldom exceeds a few millimetres, and the intrinsic depth of penetration for iron is very small, except at extremely low frequencies, little error is involved in using a cartesian reference frame in the theoretical analysis[3]. Figure 3.1 shows the developed analytical model and the co-ordinate system used. The reference frame is fixed in the drum. Figures 3.2(a) and 3.2(b) show the drum model viewed in the y.z and x.y planes respectively. The drum extends to infinity in both directions along the x-axis. The y-axis is measured from the airgap into the drum; the copper-iron interface is at y = d and the

iron is considered to extend to infinity in the y-direction. The z-axis is measured from the axial centre of the drum and the drum thus extends from $z = \frac{-L}{2}$ to $z = \frac{L}{2}$. Figures 3.2(a) and 3.2(b) also define the region subscripts which will be used throughout the analysis. The bounds on the two regions are summarised as follows:

regions 1 and 2: $-\infty \leq x \leq \infty$, $-\frac{L}{2} \leq z \leq \frac{L}{2}$

region 1: $0 \leq y \leq d$

region 2: $d \leq y < \infty$

Throughout the analysis the region permeabilities, μ_1 and μ_2, and the resistivities, ρ_1 and ρ_2, are treated as constants.

It will be assumed that the rotor poles are positioned symmetrically about the axial centre line (z = 0) of the drum. In a practical eddy-current coupling this may not be true, but James[14] has shown that there is negligible difference between the torque-speed curves of a coupling with a symmetrically positioned rotor and an identical machine with grossly assymmetrical end regions.

3.3 Current-density distributions.

3.3.1 Boundary conditions.

The current distributions are assumed to be sinusoidally distributed in time and space at the drum surface (y = 0). At first only the fundamental components of current-density will be considered. Harmonics will be introduced later.

To satisfy the continuity conditions at the drum extremities ($z = \pm \frac{L}{2}$), the axial component of $\bar{J}$ must be zero at these points.

Therefore $$J_z(x, y, \pm\tfrac{L}{2}) = 0 \qquad (3.1)$$

At the drum surface (y = 0), the radial component of $\bar{J}$ must also be zero to satisfy continuity conditions.

Hence,

$$J_y(x,0,z) = 0 \tag{3.2}$$

Due to symmetry, the x-component of $\bar{J}$ must be zero at the axial centre of the drum (z = 0). Since the current-densities are sinusoidally distributed at y = 0, and $J_y = 0$ at y = 0,

$$\text{at } z = 0,\ y = 0,\ \bar{J} = R_e \bar{k} \hat{J} e^{j(\frac{2\pi}{\lambda}x - \omega t)} \tag{3.3}$$

It is also assumed that

$$\bar{J} \text{ remains finite as y tends to infinity} \tag{3.4}$$

3.3.2 General forms of the components of current-density.

For ease of solution the 'R_e' in (3.3) may be omitted and the eddy-current density may be written in the general cartesian form

$$\bar{J} = (\bar{i} F_x + \bar{j} F_y + \bar{k} F_z) . e^{j(\frac{2\pi}{\lambda}x - \omega t)} \tag{3.5}$$

where F_x, F_y and F_z are functions of y and z only. The real part is reintroduced later when the loss is deduced. The distribution of $\bar{J}$ is governed by the diffusion equation,

$$\nabla^2 \bar{J} = \frac{\mu}{\rho} \frac{\partial \bar{J}}{\partial t}$$

which from (3.5) yields three equations of the form

$$\frac{\partial^2 F}{\partial y^2} + \frac{\partial^2 F}{\partial z^2} - \delta^2 = 0 \tag{3.6}$$

where $\delta^2 = (\frac{2\pi}{\lambda})^2 + j\omega\frac{\mu}{\rho}$ and F is any one of F_x, F_y or F_z.

Writing F = Y(y)Z(z) and substituting in (3.6) yields, after separation of variables,

$$\frac{1}{Y}\frac{\partial^2 Y}{\partial y^2} + \frac{1}{Z}\frac{\partial^2 Z}{\partial z^2} - \delta^2 = 0$$

which implies that

$$\frac{1}{Y}\frac{\partial^2 Y}{\partial y^2} - \delta^2 = -\frac{1}{Z}\frac{\partial^2 Z}{\partial z^2} = -\epsilon^2 \qquad (3.7)$$

The solutions of (3.7) have the general forms

$$Y = Ae^{\gamma y} + A'e^{-\gamma y}$$

$$Z = Ce^{\epsilon z} + C'e^{-\epsilon z}$$

where $\gamma = (\delta^2 - \epsilon^2)^{1/2}$

Therefore each component of $\bar{J}$ has the general form

$$J_{x,y,z} = (Ae^{\gamma y} + A'e^{-\gamma y}).(Ce^{\epsilon z} + C'e^{-\epsilon z}) \qquad (3.8)$$

The various arbitrary constants in (3.8) must now be evaluated for each of the current-density vectors in accordance with the boundary conditions laid out in section 3.3.1.

3.3.3 Current-density vectors

Consider first the J_y vector. In region 1,

$$J_{y1} = (A_{y1}e^{\gamma_1 y} + A'_{y1}e^{-\gamma_1 y}).(C_{y1}e^{\epsilon_1 z} + C'_{y1}e^{-\epsilon_1 z})$$

Setting y = 0 and applying boundary condition (3.2) yields that $J_{y1} = 0$. In region 2,

$$J_{y2} = (A_{y2}e^{\gamma_2 y} + A'_{y2}e^{-\gamma_2 y}).(C_{y2}e^{\epsilon_2 z} + C'_{y2}e^{-\epsilon_2 z})$$

At the copper-iron interface $J_{y2} = J_{y1} = 0$.

Therefore $C_{y_2}e^{\epsilon_2 z} + C'_{y_2}e^{-\epsilon_2 z} = 0$.

Hence, everywhere in the drum,

$$J_y(x,y,z) = 0 \tag{3.9}$$

Consider now the J_x and J_z vectors. In region 1,

$$J_{x1} = \left(A_{x1}e^{\gamma_1 y} + A'_{x1}e^{-\gamma_1 y}\right).\left(C_{x1}e^{\epsilon_1 z} + C'_{x1}e^{-\epsilon_1 z}\right).e^{j\left(\frac{2\pi}{\lambda}x - \omega t\right)} \tag{3.10}$$

$$J_{z1} = \left(A_{z1}e^{\gamma_1 y} + A'_{z1}e^{-\gamma_1 y}\right).\left(C_{z1}e^{\epsilon_1 z} + C'_{z1}e^{-\epsilon_1 z}\right).e^{j\left(\frac{2\pi}{\lambda}x - \omega t\right)} \tag{3.11}$$

In region 2, due to boundary condition (3.4) the coefficient of $e^{\gamma_2 y}$ is zero and hence

$$J_{x2} = A'_{x2}e^{-\gamma_2 y}.\left(C_{x2}e^{\epsilon_2 z} + C'_{x2}e^{-\epsilon_2 z}\right).e^{j\left(\frac{2\pi}{\lambda}x - \omega t\right)} \tag{3.12}$$

$$J_{z2} = A'_{z2}e^{-\gamma_2 y}.\left(C_{z2}e^{\epsilon_2 z} + C'_{z2}e^{-\epsilon_2 z}\right).e^{j\left(\frac{2\pi}{\lambda}x - \omega t\right)} \tag{3.13}$$

From symmetry

$$J_{x1}(z) = -J_{x1}(-z)\ ,\quad J_{x2}(z) = -J_{x2}(-z),$$

therefore

$$C_{x1} = -C'_{x1}\ ,\quad C_{x2} = -C'_{x2}\ .$$

Applying boundary condition (3.1) in equation (3.11) yields

$$C_{z1}e^{\epsilon_1\frac{L}{2}} + C'_{z1}e^{-\epsilon_1\frac{L}{2}} = C_{z1}e^{-\epsilon_1\frac{L}{2}} + C'_{z1}e^{\epsilon_1\frac{L}{2}},$$

from which we obtain $C_{z1} = C'_{z1}$ and

$$C_{z1}\left(e^{\frac{\epsilon_1 L}{2}} + e^{-\frac{\epsilon_1 L}{2}}\right) = 0\ .$$

Hence, either $C_{z1} = 0$, or

$$e^{\frac{\epsilon_1 L}{2}} + e^{-\frac{\epsilon_1 L}{2}} = 2\cosh\frac{\epsilon_1 L}{2} = 0$$

The condition $C_{z1}=0$ is trivial and, consequently, it is necessary to consider only the second condition which requires that

$$\epsilon_1 = j\frac{m.\pi}{L} \quad , \quad m= 1,3,5,7,9\ldots\ldots \tag{3.14}$$

Similarly, $C_{z2}= C'_{z2}$ and $\epsilon_2=j\frac{m.\pi}{L}$.

Incorporating these results into equations (3.10) to (3.13) and making the following substitutions,

$$K_{x1} = 2A_{x1}\, C_{x1}$$
$$K'_{x1} = 2A'_{x1}\, C_{x1}$$
$$K_{z1} = 2A_{z1}\, C_{z1}$$
$$K'_{z1} = 2A'_{z1}\, C_{z1}$$
$$K_{x2} = 2A_{x2}\, C_{x2}$$
$$K_{z:2} = 2A_{z2}\, C_{z2} \quad , \text{ gives,}$$

$$J_{x1} = \left(K_{x1}e^{\gamma_1 y} + K'_{x1}e^{-\gamma_1 y}\right).\sin\frac{m\pi z}{L}\,.\,e^{j\left(\frac{2\pi x}{\lambda}-\omega t+\frac{\pi}{2}\right)} \tag{3.15}$$

$$J_{z1} = \left(K_{z1}e^{\gamma_1 y} + K'^{-\gamma_1 y}_{z1}\right).\cos\frac{m\pi z}{L}.e^{j\left(\frac{2\pi x}{\lambda}-\omega t\right)} \tag{3.16}$$

$$J_{x2} = K_{x2}e^{-\gamma_2 y}.\sin\frac{m\pi z}{L}.\,e^{j\left(\frac{2\pi x}{\lambda}-\omega t+\frac{\pi}{2}\right)} \tag{3.17}$$

$$J_{z2} = K_{z2}e^{-\gamma_2 y}.\cos\frac{m\pi z}{L}.\,e^{j\left(\frac{2\pi x}{\lambda}-\omega t\right)} \tag{3.18}$$

Applying boundary condition (3.3) in equation (3.16) yields

$$K_{z1} + K'_{z1} = \hat{J} \tag{3.19}$$

From Maxwell's equations, div $\bar{J}$ = 0; hence,

$$\frac{\partial J_x}{\partial x} = -\frac{\partial J_z}{\partial z}$$

Substituting for J_{x1} from (3.15) and for J_{z1} from (3.16), we obtain

$$-\frac{2\pi}{\lambda}\left(K_{x1}e^{\gamma_{1}y}+K_{x1}e^{-\gamma y}\right)=\frac{m\pi}{L}\left(K_{z1}e^{\gamma_{1}y}+K'_{z1}e^{-\gamma_{1}y}\right) \qquad (3.20)$$

Setting y = 0

$$K_{x1}+K'_{x1}=\frac{\lambda m}{2L}\left(K_{z1}+K'_{z1}\right)$$

$$=-\frac{\lambda m}{2L}\hat{J} \qquad \text{, from (3.19).}$$

Therefore $$K'_{x1}=-\left(\frac{\lambda m}{2L}\hat{J}+K_{x1}\right) \qquad (3.21)$$

Substituting (3.19) and (3.21) in (3.20) gives

$$-\frac{2\pi}{\lambda}\left[-\lambda m\hat{J}e^{-\gamma y}+K_{x1}\left(e^{\gamma_{1}y}-e^{-\gamma_{1}y}\right)\right]$$
$$=\frac{m\pi}{L}\left[\hat{J}e^{-\gamma_{1}y}+K_{z1}\left(e^{\gamma_{1}y}-e^{-\gamma_{1}y}\right)\right]$$

Hence,

$$K_{x1}=-\frac{\lambda m}{2L}K_{z1} \qquad (3.22)$$

From (3.21), therefore,

$$K'_{x1}=\frac{\lambda m}{2L}\left(K_{z1}-\hat{J}\right) \qquad (3.23)$$

Two continuity conditions have to be satisfied at the copper-iron interface (y = d):

$$\bar{J}\wedge\left(\bar{E}_{2}-\bar{E}_{1}\right) \qquad (3.24)$$

and $$\bar{J}\wedge\left(\bar{H}_{2}-\bar{H}_{1}\right) \qquad (3.25)$$

Consider first the continuity requirements on the $\bar{E}$ vector. From (3.24), at y = d,

$$\bar{\imath}\left(E_{z2}-E_{z1}\right)-\bar{k}\left(E_{x2}-E_{x1}\right)=0$$

therefore

$$E_{x2} = \rho_2 J_{x2} = E_{x1} = \rho_1 J_{x1} \;, \quad E_{z2} = \rho_2 J_{z2} = E_{z1} = \rho_1 J_{z1}$$

Hence, from (3.15) and (3.17)

$$\rho_1 \left(K_{x1} e^{\gamma_1 d} + K'_{x1} e^{-\gamma_1 d} \right) = \rho_2 K_{x2} e^{-\gamma_2 d}$$

Substituting for K_{x1} , K'_{x1} and K_{x2} in accordance with (3.21), (3.22) and (3.23) yields

$$K_{x2} = -\frac{\lambda m}{2L} \frac{\rho_1}{\rho_2} e^{\gamma_2 d} \left[\hat{J} e^{-\gamma_1 d} + K_{z1} \left(e^{\gamma_1 d} - e^{-\gamma_1 d} \right) \right] \tag{3.26}$$

Similarly it can be shown that

$$K_{z2} = \frac{\rho_1}{\rho_2} e^{\gamma_2 d} \left[\hat{J} e^{-\gamma_1 d} + K_{z1} \left(e^{\gamma_1 d} - e^{-\gamma_1 d} \right) \right] \tag{3.27}$$

Equations (3.19) to (3.27) give the relationships between the various arbitrary constants appearing in the current-density equations (3.15) to (3.18). Using these relationships, the current-density equations can now be expressed in terms of one arbitrary constant, K_{z1} , and the surface current-density amplitude $\hat{J}$, which was defined as a boundary condition in (3.3), i.e.

$$J_{x1} = \frac{\lambda m}{2L} \left[\hat{J} e^{-\gamma_1 y} + K_{z1} \left(e^{\gamma_1 y} - e^{-\gamma_1 y} \right) \right] \sin \frac{m\pi z}{L} \, e^{j\left(\frac{2\pi x}{\lambda} - \omega t - \frac{\pi}{2}\right)} \tag{3.28}$$

$$J_{z1} = \left[\hat{J} e^{-\gamma_1 y} + K_{z1} \left(e^{\gamma_1 y} - e^{-\gamma_1 y} \right) \right] \cos \frac{m\pi z}{L} \, e^{j\left(\frac{2\pi x}{\lambda} - \omega t\right)} \tag{3.29}$$

$$J_{x2} = \frac{\lambda m}{2L} \frac{\rho_1}{\rho_2} \left[\hat{J} e^{-\gamma_1 d} + K_{z1} \left(e^{\gamma_1 d} - e^{-\gamma_1 d} \right) \right] e^{\gamma_2 (d-y)} \sin \frac{m\pi z}{L} \, e^{j\left(\frac{2\pi x}{\lambda} - \omega t - \frac{\pi}{2}\right)} \tag{3.30}$$

$$J_{z2} = \frac{\rho_1}{\rho_2} \left[\hat{J} e^{-\gamma_1 d} + K_{z1} \left(e^{\gamma_1 d} - e^{-\gamma_1 d} \right) \right] e^{\gamma_2 (d-y)} \cos \frac{m\pi z}{L} \, e^{j\left(\frac{2\pi x}{\lambda} - \omega t\right)} \tag{3.31}$$

From Maxwell's equations

$$\nabla \wedge \bar{E} = -\frac{\partial \bar{B}}{\partial t} \;, \quad \nabla \wedge \bar{J} = \frac{\mu}{\rho} j\omega \bar{H} \;.$$

Since it is assumed that the fields are sinusoidal in time,

$$\nabla \wedge \bar{J} = j\omega\mu_\rho \bar{H} \tag{3.32}$$

From the continuity requirement on the $\bar{H}$ vector,

$$\bar{\imath}\left(H_{z2} - H_{z1}\right) - \bar{k}\left(H_{x2} - H_{x1}\right) = 0$$

Therefore $H_{z1} = H_{z2}$

Thus, from (3.32)

$$\frac{\rho}{\mu_1}\cdot\frac{\partial J_{x1}}{\partial y} = \frac{\rho}{\mu_2}\cdot\frac{\partial J_{x2}}{\partial y}$$

Substituting for J_{x1} and J_{x2} from (3.28) and (3.30) yields, after manipulation,

$$K_{z1} = \hat{J}\cdot\xi \tag{3.33}$$

where $$\xi = \frac{(\mu_2\gamma_1 - \mu_1\gamma_2)\,e^{-\gamma_1 d}}{(\mu_2\gamma_1 + \mu_1\gamma_2)\,e^{\gamma_1 d} + (\mu_2\gamma_1 - \mu_1\gamma_2)\,e^{-\gamma_1 d}} \tag{3.34}$$

Substituting for K_{z1} in (3.28) to (3.31), we obtain the final form of the equations of current-density distribution. However, in (3.14), it was shown that 'm' could take up any odd integer value and, for every value of 'm', there will be a different peak current-density '$\hat{J}$', a different value of radial propagation coefficient, γ and a different ξ. Consequently, there will be an infinite number of solutions for each of the $\bar{J}$ vectors, each corresponding to one value of 'm'. The general solution for each of the $\bar{J}$ distributions will therefore be an infinite series summed over 'm'. Hence,

$$J_{x1} = \frac{\lambda}{2L}\cdot e^{j\left(\frac{2\pi x}{\lambda} - \omega t - \frac{\pi}{2}\right)} \sum_{m=1}^{\infty}\left[\left(1-\xi_m\right)e^{-\gamma_{1m}y} + \xi_m e^{\gamma_{1m}y}\right] m\cdot\hat{J}_m \sin\frac{m\pi z}{L} \tag{3.35}$$

$$J_{z1} = e^{j(\frac{2\pi x}{\lambda} - \omega t)} \sum_{m=1}^{\infty} \left[(1-\xi_m) e^{-\gamma_{1m} y} + \xi_m e^{\gamma_{1m} y} \right] \hat{J}_M \cos \frac{m\pi z}{L} \qquad (3.36)$$

$$J_{x2} = \frac{\rho_1}{\rho_2} \frac{\lambda}{2L} e^{j(\frac{2\pi x}{\lambda} - \omega t - \frac{\pi}{2})} \sum_{m=1}^{\infty} \left[(1-\xi_m) e^{-\gamma_{1m} d} + \xi_m e^{\gamma_{1m} d} \right] e^{\gamma_{2m}(d-y)} \, m. \hat{J}_M \sin \frac{m\pi z}{L} \qquad (3.37)$$

$$J_{z2} = \frac{\rho_1}{\rho_2} e^{j(\frac{2\pi x}{\lambda} - \omega t)} \sum \left[(1-\xi_m) e^{-\gamma_{1m} d} + \xi_m e^{\gamma_{1m} d} \right] e^{\gamma_{2m}(d-y)} \hat{J}_m \cos \frac{m\pi z}{L} \qquad (3.38)$$

Equations (3.35) to (3.38) completely describe the fundamental current-density distribution in both regions of the drum.

The current-densities are sinusoidal in 'x' and 't', J_x lagging J_z by $\frac{\pi}{2}$ radians. The axial (z) variation is expressed as a Fourier series which can take account of any actual distribution (this is discussed further in section 3.3.8). The variation of current-density with depth (y) is more complicated since both γ and ξ are complex quantities which impart both amplitude and phase changes to the $\bar{J}$ distributions.

In the following section, an approximation for ξ is introduced which, when substituted in the current-density equations, renders them considerably more explicit and enables the way in which current density varies with depth to be examined in detail.

3.3.4 Simplified current-density equations

Equations (3.35) to (3.38) are valid for any combination of metals in the drum. Considerable simplification can be achieved if the particular combination of a thin non-ferrous sheet and a ferrous backing material is considered. The resulting simplified equations are then valid for any such drum construction including, of course, the copper-faced drum. From (3.34)

$$\xi_m = \frac{(\mu_2 \gamma_{1m} - \mu_1 \gamma_{2m}) \cdot e^{-\gamma_{1m} d}}{(\mu_2 \gamma_{1m} + \mu_1 \gamma_{2m}) e^{\gamma_{1m} d} + (\mu_2 \gamma_{1m} - \mu_1 \gamma_{2m}) e^{-\gamma_{1m} d}}$$

Writing $\zeta_m = \frac{\mu_1 \gamma_{2m}}{\mu_2 \gamma_{1m}}$ we obtain

$$\xi_m = \frac{1}{1 + \frac{(1+\zeta_m)}{(1-\zeta_m)} \cdot e^{2\gamma_{1m} d}} \qquad (3.39)$$

Now, for both regions

$$\gamma_m^2 = \left(\frac{2\pi}{\lambda}\right)^2 + \left(\frac{m\pi}{L}\right)^2 + j\omega\frac{\mu}{\rho} = R_m^2 e^{2j\phi_m} \qquad (3.40)$$

Therefore

$$\frac{\gamma_{2m}^2}{\gamma_{1m}^2} = \frac{R_{2m}^2 e^{2j\phi_{2m}}}{R_{1m}^2 e^{2j\phi_{1m}}} = \frac{1 + j\tan 2\phi_{2m}}{1 + j\tan 2\phi_{1m}}$$

Now

$$\frac{\tan 2\phi_{2m}}{\tan 2\phi_{1m}} = \frac{\mu_2 \rho_1}{\mu_1 \rho_2} = \frac{\mu_r \rho_1}{\rho_2}$$

hence,

$$\frac{\gamma_{2m}^2}{\gamma_{1m}^2} = \frac{1 + j\mu_r \rho_1/\rho_2 \tan 2\phi_{1m}}{1 + j\tan 2\phi_{1m}}$$

Thus

$$\zeta_m = \frac{1}{\mu_r} \cdot \left(\frac{1 + j\mu_r \rho_1/\rho_2 \tan 2\phi_{1m}}{1 + j\tan 2\phi_{1m}}\right)^{1/2}$$

and

$$|\zeta_m| = \frac{1}{\mu_r}\left[\frac{\cot^2 2\phi_{1m} + (\mu_r \rho_1/\rho_2)^2}{\cot^2 2\phi_{1m} + 1}\right]$$

The relative permeability of the backing iron is likely to be within the range 500 to 2500 (see section 3.4.4). The ratio of resistivity, ρ_1/ρ_2, will be less than unity and normally greater than 0.15.

Consider the lower values first ($\mu_r = 500$, $\rho_1/\rho_2 = 0.15$). At zero frequency ϕ_{1m} will be zero and $|\zeta_m|$ will be 0.002; at infinite frequency ϕ_{1M} will be 45° and $|\zeta_m|$ will be 0.006. It

follows that, for all frequencies,

$$\frac{(1+\zeta_m)}{(1-\zeta_m)} \simeq 1$$

For higher values of μ_r and ρ_1/ρ_2 the approximation will be even better. Substituting $(1+\zeta_m)/(1-\zeta_m)=1$ in equation (3.39) gives

$$\xi_m = \frac{1}{1+e^{2\gamma_{1m}d}} \tag{3.41}$$

Substituting (3.41) into (3.35) to (3.38) we obtain

$$J_{x1} = \frac{\lambda}{2L} e^{j\left(\frac{2\pi x}{\lambda}-\omega t-\frac{\pi}{2}\right)} \sum_{m=1}^{\infty} \left[\frac{e^{\gamma_{1m}(2d-y)} + e^{\gamma_{1m}y}}{1+e^{2\gamma_{1m}d}}\right] m.\hat{J}_m \sin\frac{m\pi z}{L} \tag{3.42}$$

$$J_{z1} = e^{j\left(\frac{2\pi x}{\lambda}-\omega t\right)} \sum_{m=1}^{\infty} \left[\frac{e^{\gamma_{1m}(2d-y)} + e^{\gamma_{1m}y}}{1+e^{2\gamma_{1m}d}}\right] \hat{J}_m \cos\frac{m\pi z}{L} \tag{3.43}$$

$$J_{x2} = \frac{\rho_1}{\rho_2}\frac{\lambda}{2L} e^{j\left(\frac{2\pi x}{\lambda}+\omega t-\frac{\pi}{2}\right)} \sum_{m=1}^{\infty} \left[\frac{2e^{\gamma_{1m}d}}{1+e^{2\gamma_{1m}d}}\right] e^{\gamma_{2m}(d-y)}\, m.\hat{J}_m \sin\frac{m\pi z}{L} \tag{3.44}$$

$$J_{z2} = \frac{\rho_1}{\rho_2} e^{-j\left(\frac{2\pi x}{\lambda}-\omega t\right)} \sum_{m=1}^{\infty} \left[\frac{2e^{\gamma_{1m}d}}{1+e^{2\gamma_{1m}d}}\right] e^{\gamma_{2m}(d-y)}\, \hat{J}_m \cos\frac{m\pi z}{L} \tag{3.45}$$

These equations are a close approximation to the fundamental current-density distribution in the copper-faced drum.

3.3.5 Complete current-density distributions including harmonics.

So far only fundamental components of current-density have been considered. In a practical coupling, harmonic components will also be present, so it is necessary to incorporate these into the current-density equations.

Let the harmonic frequency and wavelength be ω_h and λ_h respectively, where h is the harmonic number, $\omega_h = h\omega$ and $\lambda_h = \frac{\lambda}{h}$.

Substituting these harmonic terms for the original fundamental terms in (3.40) gives

$$\gamma_h^2 = \left(\frac{2\pi h}{\lambda}\right)^2 + \left(\frac{m\pi}{L}\right)^2 + j\omega h\rho\mu \qquad (3.46)$$

In section 3.3.4, it was demonstrated that the approximation for ξ (3.41) was valid for all frequencies. Consequently (3.41) can be used for all harmonics.

Hence $$\xi_h = \frac{1}{1 + e^{2\gamma_{1h}d}} \qquad (3.47)$$

Substitution of (3.46) and (3.47) into (3.42) to (3.45) yields the h^{th} harmonic components of the current-densities. The complete equations of current-density distribution will be infinite series summed over h as follows:

$$J_{x1} = \frac{\lambda}{2L}\sum_{h=1}^{\infty}\sum_{m=1}^{\infty} e^{j\left(\frac{2\pi h}{\lambda}x - h\omega t - \frac{\pi}{2}\right)}\left[\frac{e^{\gamma_{1mh}(2d-y)} + e^{\gamma_{1mh}y}}{1 + e^{2\gamma_{1mh}d}}\right]\frac{m}{h}\,\hat{J}_{mh}\sin\frac{m\pi z}{L} \qquad (3.48)$$

$$J_{z1} = \sum_{h=1}^{\infty}\sum_{m=1}^{\infty} e^{j\left(\frac{2\pi h}{\lambda}x - h\omega t\right)}\left[\frac{e^{\gamma_{1mh}(2d-y)} + e^{\gamma_{1mh}y}}{1 + e^{2\gamma_{1mh}d}}\right]\hat{J}_{mh}\cos\frac{m\pi z}{L} \qquad (3.49)$$

$$J_{x2} = \frac{\lambda}{2L}\frac{\rho}{\rho_2}\sum_{h=1}^{\infty}\sum_{m=1}^{\infty} e^{j\left(\frac{2\pi h}{\lambda}x - h\omega t - \frac{\pi}{2}\right)}\left[\frac{2e^{\gamma_{1mh}d}}{1 + e^{2\gamma_{1mh}d}}\right]e^{\gamma_{2mh}(d-y)}\,\frac{m}{h}\,\hat{J}_{mh}\sin\frac{m\pi z}{L} \qquad (3.50)$$

$$J_{z2} = \frac{\rho}{\rho_2}\sum_{h=1}^{\infty}\sum_{m=1}^{\infty} e^{j\left(\frac{2\pi h}{\lambda}x - h\omega t\right)}\left[\frac{2e^{\gamma_{1mh}d}}{1 + e^{2\gamma_{1mh}d}}\right]e^{\gamma_{2mh}(d-y)}\,\hat{J}_{mh}\cos\frac{m\pi z}{L} \qquad (3.51)$$

Having derived the complete equations for current-density, it is useful to investigate the physical meaning of the radial distributions before proceeding with the analysis.

3.3.6 Variation of current-density with depth.

We shall first consider only fundamental components. From (3.42) and (3.43) in region 1 for any x, t, z and m, both J_{z1} and J_{x1} can be written as

$$J_1 \propto e^{\gamma_{1m}(2d-y)} + e^{\gamma_{1m}y}$$

Similarly for J_{z2} and J_{x2}, from (3.44) and (3.45),

$$J_2 \propto \frac{\rho_1}{\rho_2} . 2 . e^{\gamma_{1m}d} . e^{\gamma_{2m}(d-y)}$$

Now, writing $\gamma_m = \alpha_m + j\beta_m$, where from (3.40)

$$\alpha_m = \left\{ \left[\left(\frac{2\pi}{\lambda}\right)^2 + \left(\frac{m\pi}{L}\right)^2 \right]^2 + \left(\frac{N\mu}{\rho}\right)^2 \right\}^{1/4} \cos\phi_m , \qquad (3.52)$$

$$\beta_m = \left\{ \left[\left(\frac{2\pi}{\lambda}\right)^2 + \left(\frac{m\pi}{L}\right)^2 \right]^2 + \left(\frac{N\mu}{\rho}\right)^2 \right\}^{1/4} \sin\phi_m , \qquad (3.53)$$

and

$$\phi_m = \frac{1}{2} \tan^{-1} \left[\frac{N\mu/\rho}{\left(\frac{2\pi}{\lambda}\right)^2 + \left(\frac{m\pi}{L}\right)^2} \right] , \qquad (3.54)$$

we obtain

$$J_1 \propto e^{\alpha_{1m}(2d-y)} . e^{j\beta_{1m}(2d-y)} + e^{\alpha_{1m}y} . e^{j\beta_{1m}y}$$

and

$$J_2 \propto e^{\alpha_{2m}(2d-y)} e^{j\beta_{2m}(2d-y)}$$

The expression for J_1 contains both forward and backward travelling waves characteristic of diffusion equation solutions for bounded regions. The attenuation constant, α_{1m}, is the reciprocal of the skin depth for copper and the constant β_{1m} is a phase constant. The expression for J_2 contains only a forward travelling wave, there being no reflected wave, since the backing iron is assumed to be semi-infinite. Here α_{2m} is the reciprocal of the skin depth for iron and β_{2m} the phase constant for iron.

In terms of amplitude and argument,

$$J_1 \propto \left\{\left[e^{\alpha_{1m}(2d-y)}\cos\beta_{1m}(2d-y) + e^{\alpha_{1m}}\cos\beta_{1m}y\right]^2 + \left[e^{\alpha_{1m}(2d-y)}\sin\beta_{1m}(2d-y) + e^{\alpha_{1m}y}\sin\beta_{1m}y\right]^2\right\}^{1/2} \angle \tan^{-1}\frac{e^{\alpha_{1m}(2d-y)}\sin\beta_{1m}(2d-y) + e^{\alpha_{1m}y}\sin\beta_{1m}y}{e^{\alpha_{1m}(2d-y)}\cos\beta_{1m}(2d-y) + e^{\alpha_{1m}y}\cos\beta_{1m}y} \qquad (3.55)$$

and $$J_2 \propto e^{\alpha_{2m}(2d-y)} \angle \tan^{-1}\beta_{2m}(2d-y) \qquad (3.56)$$

Clearly the variation of current-density with depth depends wholly on the real and imaginary parts of γ_{1m} and γ_{2m}, i.e. α_{1m}, β_{1m} and α_{2m}, β_{2m}, respectively.

It will be shown later that it is only necessary, when calculating the performance of the copper-faced coupling, to consider the first few values of m and in many cases it is sufficient to consider only m = 1. Accepting this for the moment, the components of γ_1 and γ_2 will be calculated for m = 1 over the frequency range $0 \leqslant f \leqslant 10$ kHz* in accordance with equations (3.52) to (3.54).

To calculate the components the following values, taken from the experimental machine described in Chapter 4, are used:

$$\lambda = 8.31 \times 10^{-2} \text{ m},$$
$$L = 6.35 \times 10^{-2} \text{ m},$$
$$\rho_1 = 1.725 \times 10^{-8} \text{ m},$$
$$\rho_2 = 1.12 \times 10^{-7} \text{ m},$$
$$\mu_1 = \mu_0 .$$

---

* For fundamental quantities in the experimenatl machine discussed in Chapter 4, this frequency range corresponds to a slip speed range of $0 \leqslant n \leqslant 100\,000$ rev/min and thus encompasses all practical frequencies.

Also the backing iron permeability, μ_r, is assumed constant at 2000, with the result that $\mu_2 = 2000\mu_o$. (The error in such an approximation is discussed in detail in section 3.4.4).

The calculated components of γ_1 and γ_2 are given in tables 3.1 and 3.2.

Using tables 3.1 and 3.2 and equations (3.55) and (3.56), the variation of current-density with depth can be investigated. Since the constants of proportionality of (3.55) and (3.56) are different for J_x and J_z and for the different regions, the most general way to represent the variation of current-density with depth is to express the current-density amplitude at any depth as a per unit of the surface density amplitude. The phase angles calculated are then subtracted from the phase angle at the surface to indicate the change of phase with depth.

Using the α's and β's given in tables 3.1 and 3.2, the variation of current-density with depth was calculated for frequencies of 1, 10, 100, 1000 and 10 000 Hz. The depth of copper-facing, 'd', was taken as 4×10^{-4}m, from the specification of the experimental copper-faced coupling.

The variation of current-density amplitude is shown in Fig. 3.3. There is negligible amplitude variation with depth in the copper even at 1000 Hz. At 10 000 Hz the total attenuation at the copper iron interface is less than 5%.

The amplitude discontinuity at the interface is due to the continuity condition on the $\bar{E}$ vector, (3.25), which requires that $\left.\frac{J_1}{J_2}\right|_{y=d} = \frac{\rho_1}{\rho_2}$

In the backing iron, the current-density decays exponentially exhibiting typical skin-effect attenuation. At low frequencies (1 and 10 Hz) the current-density decays slowly with depth;

Table 3.1

f(Hz)	R_1	ϕ_1°	α_1	β_1
0	90.30	0.00	90.30	0.00
1	90.37	1.62	90.34	2.56
2	90.59	3.23	90.44	5.10
3	90.94	4.82	90.62	7.64
4	91.44	6.38	90.89	10.16
5	92.06	7.90	91.18	12.65
6	92.80	9.38	91.56	15.12
7	93.65	10.81	91.99	17.56
8	94.61	12.18	92.48	19.96
9	95.66	13.50	93.02	22.33
10	96.80	14.75	93.61	24.65
20	110.98	24.27	101.17	45.62
30	126.76	29.75	110.05	62.90
40	142.06	33.09	119.02	77.55
50	156.44	35.27	127.73	90.33
60	169.90	36.80	136.05	101.77
70	182.54	37.92	144.00	112.17
80	194.45	38.77	151.60	121.77
90	205.74	39.45	158.88	130,72
100	216.49	39.99	165.86	139.13
200	304.41	42.48	224.52	205.56
300	372.42	43.32	270.97	255.48
400	429.87	43.74	310.60	297.18
500	480.53	43.99	345.73	333.73
600	526.34	44.16	377.62	366.66
700	568.48	44.28	407.02	396.87
800	607.70	44.37	434.43	424.94
900	644.55	44.44	460.22	451.27
1000	679.41	44.49	484.64	476.15
2000	960.77	44.75	682.36	676.36
3000	1176.69	44.83	834.49	829.59
4000	1358.71	44.87	962.88	958.63
5000	1519.09	44.90	1076.05	1072.26
6000	1664.07	44.92	1178.41	1174.94
7000	1797.40	44.93	1272.56	1269.35
8000	1921.51	44.94	1360.21	1357.21
9000	2038.06	44.94	1442.54	1439.71
10000	2148.81	44.95	1520.42	1517.74

Components of γ_1 (copper region)
for m = 1

Table 3.2

f(Hz)	R_2	ϕ_2°	α_2	β_2
0	90.30	0.00	90.30	0.00
1	392.85	43.49	285.03	270.35
2	555.28	44.24	397.80	387.41
3	680.01	44.50	485.06	476.58
4	785.18	44.68	558.86	551.52
5	877.84	44.70	624.00	617.44
6	961.62	44.75	682.96	676.96
7	1038.66	44.78	737.21	731.66
8	1110.37	44.81	787.74	782.55
9	1177.72	44.83	835.22	830.33
10	1241.43	44.85	880.14	875.50
20	1755.64	44.92	1243.06	1239.78
30	2150.20	44.95	1521.76	1519.08
40	2482.84	44.96	1756.80	1754.47
50	2775.90	44.97	1963.90	1961.82
60	3040.85	44.98	2151.15	2149.26
70	3284.49	44.98	2323.36	2321.61
80	3511.28	44.98	2483.66	2482.02
90	3724.26	44.98	2634.23	2632.68
100	3925.72	44.99	2776.64	2775.17
200	5551.81	44.99	3926.29	3925.20
300	6799.55	44.99	4808.43	4807.58
400	7851.45	45.00	5552.18	5551.44
500	8778.20	45.00	6207.45	6206.80
600	9616.05	45.00	6799.87	6799.27
700	10386.51	45.00	7344.65	7344.09
800	11103.67	45.00	7851.74	7851.22
900	11777.21	45.00	8327.99	8327.50
1000	12414.30	45.00	8778.47	8778.00
2000	17556.56	45.00	12414.53	12414.20
3000	21502.53	45.00	15204.72	15204.45
4000	24829.07	45.00	17556.92	17556.69
5000	27759.94	45.00	19629.35	19629.14
6000	30409.80	45.00	21503.07	21502.89
7000	32846.57	45.00	23226.12	23225.95
8000	35114.83	45.00	24830.01	24829.85
9000	37244.83	45.00	26336.15	26338.99
10000	39259.84	45.00	27760.97	27760.83

Components of γ_2 (iron region)
for m = 1, μ_r = 2000

whilst at higher frequencies (100, 1000 and 10 000 Hz), corresponding to higher values of α_2, and lower values of skin depth, the reduction is much more severe.

For higher values of 'm', α_m will be increased and consequently the decay of current density in the iron will be more rapid, although the current-density in the copper will remain approximately constant until 'm' becomes large. At harmonic frequencies the attenuation constant, α_{mh} is increased and the current density decays more rapidly in the iron. Again, however, the current-density amplitude will remain approximately constant in the copper-facing until the frequency becomes very high (i.e. h becomes large).

To illustrate these points α_{hm} and β_{hm} were calculated for both regions for h = 7, m = 7 at 10 000 Hz. (These are much higher values of m and h than it is normally necessary to consider in practice. See section 3.4.2.2). The resulting values for α_{hm} and β_{hm} were used to derive a plot of current-density variation with depth (fig 3.4).

The variation of phase with depth is shown in fig 3.5. In the copper region, phase shift with respect to the surface wave is small. Even at 1000 Hz the total phase shift at the back of the copper is only a little more than 2°. In the backing iron, however, the phase shift is substantial, the rate of increase of phase rising with frequency. At low frequencies the phase discontinuity at the interface tends to 90°, which agrees with the results of the theory of wave propagation at the boundaries of dissimilar conducting material.

3.3.7 Approximations to the radial distribution of current-density.

From the results of the previous section it would seem that a suitable approximation would be to assume that, for all frequencies of any significance, the current-density does not vary in either amplitude or phase throughout the copper-facing. In the backing iron, however, the variation is substantial. Indeed at high frequencies the current-densities in the iron may be neglected altogether.

Thus, for that frequency range where there is little decrement in the copper-facing, but negligible current flowing in the iron, the coupling could be represented by copper sheet, carrying uniformly distributed eddy-currents, backed by a zero conducting, infinitely permeable slab. If this approximation is made, the current-density distributions in the copper-faced coupling drum conform with those discussed by Russell and Norsworthy[19] for screened-rotor induction motors.

From fig. 3.3 it would seem that such an approximation is only valid for frequencies greater than 100 Hz. For fundamental quantities in the 12 pole experimental coupling this frequency corresponds to a slip speed of 1000 rev/min. Since most eddy-current couplings are designed to give rated torque at less than 100 rev/min slip, it is clear that it is not permissible to use such an approximate distribution in design or when analysing machine performance.

In section 3.4, which deals with loss calculations, it is shown that although it is permissible to neglect the variation of current-density throughout the depth of copper, it is necessary to take some account of the eddy-currents in the iron and

the loss arising from them.

3.3.8 Determination of the current-density distribution from the airgap-flux-density distribution.

It has been shown that the solution of the diffusion equation in accordance with the boundary conditions laid out in section 3.3.1 contains a 'z' variation expressed as a Fourier series, the amplitude of each term in the series ($\hat{J}_m$) being required as a boundary condition. The current-density amplitude, $\hat{J}$, was initially defined as the amplitude of J_z at y = 0, z = 0 (section 3.3.1). To allow for all values of m, $\hat{J}$ was replaced by $\hat{J}_m$, which also conforms with the definition of an axially directed current-density amplitude at y = 0, z = 0.

The actual values of $\hat{J}_m$ can be determined directly from the known axial distribution of flux-density in the following manner. Consider first fundamental components only.

From Maxwell's equations,

$$\rho \nabla \wedge \bar{J} = -\frac{\partial \bar{B}}{\partial t}$$

But $\frac{\partial}{\partial t} = j\omega$,

therefore $\rho \nabla \wedge \bar{J} = j\omega \bar{B}$

which yields, for the 'y' component of flux-density,

$$B_y = j\frac{\rho}{\omega}\left(\frac{\partial J_z}{\partial x} - \frac{\partial J_x}{\partial z}\right)$$

Since $\hat{J}_m$ is defined for y = 0, it is necessary to consider J_x and J_z in region 1 only. Substituting for J_{x1} and J_{z2} from (3.42) and (3.43) gives

$$B_y = j\frac{\beta}{\omega}\left\{\frac{2\pi}{\lambda}e^{j\left(\frac{2\pi}{\lambda}x-\omega t+\frac{\pi}{2}\right)}\sum_m^{\infty}\left[\frac{e^{\gamma_{1m}(2d-y)}+e^{\gamma_{1m}y}}{1+e^{2\gamma_{1m}d}}\right].\hat{J}_m\cos\frac{m\pi z}{L}\right.$$

$$\left.+\frac{\lambda}{2L}e^{j\left(\frac{2\pi}{\lambda}x-\omega t+\frac{\pi}{2}\right)}\sum_m^{\infty}\left[\frac{e^{\gamma_{1m}(2d-y)}+e^{\gamma_{1m}y}}{1+e^{2\gamma_{1m}d}}\right]\frac{m^2\pi}{L}.\hat{J}_m\cos\frac{m\pi z}{L}\right\}$$

Setting $y=o$, $z = 0$, we obtain

$$B_y = -\rho_i \frac{2\pi}{\lambda} \sum_{m=1}^{\infty} J_m \left[1+\left(\frac{\lambda m}{2L}\right)^2 \right] e^{j\left(\frac{2\pi x}{\lambda} - \omega t\right)}$$

Consider the amplitude of a single term in the series:

$$\hat{B}_{ym} = \frac{2\pi}{\lambda} \rho_i \hat{J}_m \left[1+\left(\frac{\lambda m}{2L}\right)^2 \right]$$

Therefore

$$\hat{J}_m = \frac{\omega . \hat{B}_{ym}}{\frac{2\pi}{\lambda} \rho_i \left[1+\left(\frac{\lambda m}{2L}\right)^2 \right]} \qquad (3.57)$$

Thus if the axial variation of radially-directed flux-density is known and expressed as a Fourier series in the form,

$$B_y(z) = \sum_{m=1}^{\infty} \hat{B}_{ym} \cos \frac{m\pi z}{L}$$

then the current-density amplitudes can be found by substituting the corresponding flux-density amplitudes in (3.57).

The h^{th} harmonic component of current-density ($\hat{J}_{mh}$) is derived by replacing λ , ω and $\hat{B}_{ym}$ by $\frac{\lambda}{h}$, $h.\omega$ and $\hat{B}_{ymh}$ respectively in (3.57).

Thus

$$\hat{J}_{mh} = \frac{\hat{B}_{ymh} . \omega}{\frac{2\pi}{\lambda} \rho_i \left[1+\left(\frac{\lambda m}{2hL}\right)^2 \right]} \qquad (3.58)$$

The harmonic current-density amplitudes are then similarly found by expressing the axial variation of harmonic flux-density as a Fourier series of the form:

$$B_{yh}(z) = \sum_{m=1}^{\infty} \hat{B}_{ymh} \cos \frac{m\pi z}{L}$$

It should be noted that the series describing the axial variation of flux-density is the same for all harmonics except that the amplitude will be scaled down by the ratio of a particular

harmonic flux-density amplitude to the fundamental amplitude.

It is convenient at this point to examine the particular airgap flux-density distribution of a fully-interdigitated coupling and to derive particular relationships for the current-density amplitudes which will be used later in the prediction of the performance characteristics of the experimental copper-facedcoupling. Since there is no experimental data on the axial variation of flux-density in the copper-faced coupling, certain assumptions have to be made.

Using the same experimental coupling fitted with a homogeneous drum with copper end-rings, James[14] has experimentally determined that axial variation of airgap flux-density over a pole length (this is shown in fig. 3.6 , which is taken from ref.14). The variation of flux-density in a machine with a copper-faced drum will not be identical to this, but the same form of variation is to be expected. The simplifying approximate axial distributions developed from consideration of these results will be assumed to be equally valid for the copper-faced coupling.

James[14] has shown that the flux beyond the pole edges is negligible: "The fringing flux was less than 3% of the pole face flux, and it was considered reasonable to assume that it would have negligible effect on both the torque and end-region field."

In terms of the analytical model (fig. 3.1)

$$B = 0 \quad , \quad \frac{L_a}{2} \geq z \geq \frac{L_a}{2}$$

Thus the axial distribution of flux-density can be approximated by the form of curve shown in fig. 3.7. If this curve is then broken down into its harmonic components, the current-density

amplitudes can be found.

In fig 3.7 a table of values of $\hat{B}_{ym}$ is given for values of m up to m = 9. The harmonic analysis was carried out for the three cases shown in fig 3.6. Suppose now that the flux-density is averaged over the pole length to yield B_{av} (fig 3.7). The harmonic analysis of the resulting rectangular distribution is well known to be

$$B_y = \frac{4}{\pi} B_{av} \sum_{m=1}^{\infty} \frac{1}{m} \sin\left(\frac{m\pi L_a}{2L}\right) . \cos \frac{m\pi z}{L} \qquad (3.59)$$

Thus $$\hat{B}_{ym} = \frac{4}{\pi m} . B_{av} \sin \frac{m\pi L_a}{2L} \qquad (3.60)$$

Equation (3.60) was evaluated for each of the three flux-density distributions shown in fig 3.6. The resulting values for $\hat{B}_{ym}$ were then tabulated in fig 3.7 for comparison with the values obtained by analysing the actual distributions.

From fig 3.7 it can be seen that the worst deviation between the fundamental (m = 1) amplitudes of the actual and averaged distributions is less than 4%. The major discrepancy occurs for m = 5. Analysis of the approximate wave indicates $J_5 = 0$. In the following sections it is demonstrated that the loss due to the components of $\bar{J}$ corresponding to m = 5 (J_{5h}) are of the order of 1% of the total loss for the experimental machine. Consequently even a large error in this term will have an insignificant effect on the predicted performance of the machine.

Hence for the remainder of this work the axial flux-density distribution of the experimental copper-faced coupling will be assumed to be a chorded rectangular wave of height B_{av}. With this assumption, an experimental investigation of the axial distribution is not necessary since the various B_{av}'s, for

fundamental and harmonic terms, can be obtained by dividing the known flux/pole by the pole area. From the normal definition of flux/pole used in synchronous machines:

for fundamental quantities, $$B_{av} = \frac{\pi \phi_{ac}}{\lambda L_a} \qquad (3.61)$$

and for harmonics, $$B_{av} = \frac{\pi h \phi_{ach}}{\lambda L_a} \qquad (3.62)$$

The fundamental current-density amplitudes are now derived by substituting for $\hat{B}_{ym}$ from (3.60) into (3.57). This gives

$$J_m = \frac{2\omega\lambda B_{av} \sin\left(\frac{m\pi L_a}{2L}\right)}{m\pi^2 \rho_1 \left[1+\left(\frac{m\lambda}{2L}\right)^2\right]} \qquad (3.63)$$

For the harmonic components we have, from (3.58),

$$J_{mh} = \frac{2\omega\lambda B_{avh} \sin\left(\frac{m\pi L_a}{2L}\right)}{m\pi^2 \rho_1 \left[1+\left(\frac{m\lambda}{2Lh}\right)^2\right]} \qquad (3.64)$$

3.3.9 Summary of the results of section 3.3.

In section 3.3 the current-density distributions in the copper-faced drum were derived by developing a general solution of the three-dimensional diffusion equation and then solving for the arbitrary constants in terms of defined boundary conditions.

These resulting equations are biharmonic series which completely describe the current-density variations axially, peripherally and radially in both regions of the drum.

With the assumption that the performance characteristics of the coupling are largely dictated by these terms involving m = 1 (i.e. the fundamental axial harmonics), the radial variation of current-density was investigated over a frequency range which encompasses all practical slip speeds. The resulting curves of current-density against depth give a physical

picture of the radial distribution which, in the following sections, will enable a clear interpretation of coupling perfo-rmance over a wide slip speed range.

The development of an approximation to the axial distribu-tion of flux-density, the significant harmonic content of which conforms closely with the actual distribution, will be shown in the next section to lead to worthwhile simplifications in the procedure for calculating drum loss. Using this approximation, it will be shown that neglecting the influence of current-densities and flux-densities, for all but the first few values of 'm', is justified, (see section 3.4.2.2).

3.4 Power dissipated in the copper-faced loss drum.

3.4.1 The loss equation.

The total power dissipated in the drum is

$$P = \int_v \bar{E}\cdot\bar{J}\,\partial v = \int_v \rho J^2 \partial v \qquad (3.65)$$

where 'v' is the total drum volume.

The power dissipated in the copper skin is, for p pole pairs,

$$P_1 = \rho \int_{-\frac{L}{2}}^{\frac{L}{2}} \int_0^d \int_0^{p\lambda} \left(J_{x1}^2 + J_{z1}^2\right) \partial x\, \partial y\, \partial z \qquad (3.66)$$

and the power dissipated in the backing iron is

$$P_2 = \rho_2 \int_{-\frac{L}{2}}^{\frac{L}{2}} \int_d^{\infty} \int_0^{p\lambda} \left(J_{x2}^2 + J_{z2}^2\right) \partial x\, \partial y\, \partial z \qquad (3.67)$$

where $P = P_1 + P_2$.

For the purpose of deriving the loss equation, it is convenient to work only with the fundamental eddy-current distributions and then allow for harmonics later.

picture of the radial distribution which, in the following sections, will enable a clear interpretation of coupling perfo-rmance over a wide slip speed range.

The development of an approximation to the axial distribution of flux-density, the significant harmonic content of which conforms closely with the actual distribution, will be shown in the next section to lead to worthwhile simplifications in the procedure for calculating drum loss. Using this approximation, it will be shown that neglecting the influence of current-densities and flux-densities, for all but the first few values of 'm', is justified, (see section 3.4.2.2).

3.4 Power dissipated in the copper-faced loss drum.

3.4.1 The loss equation.

The total power dissipated in the drum is

$$P = \int_V \bar{E}\cdot\bar{J}\,\partial v = \int_V \rho J^2 \partial v \qquad (3.65)$$

where 'v' is the total drum volume.

The power dissipated in the copper skin is, for p pole pairs,

$$P_1 = \rho \int_{-\frac{L}{2}}^{\frac{L}{2}} \int_0^d \int_0^{P\lambda} \left(J_{x1}^2 + J_{z1}^2\right) \partial x\, \partial y\, \partial z \qquad (3.66)$$

and the power dissipated in the backing iron is

$$P_2 = \rho_2 \int_{-\frac{L}{2}}^{\frac{L}{2}} \int_d^{\infty} \int_0^{P\lambda} \left(J_{x2}^2 + J_{z2}^2\right) \partial x\, \partial y\, \partial z \qquad (3.67)$$

where $P = P_1 + P_2$.

For the purpose of deriving the loss equation, it is convenient to work only with the fundamental eddy-current distributions and then allow for harmonics later.

Substituting (3.42) and (3.43) in (3.66) gives for the loss in the copper skin

$$P_1 = \rho_1 p\frac{\lambda L}{8}\sum_{m=1}^{\infty} \hat{J}_m^2 \left[1+\left(\frac{m\lambda}{2L}\right)^2\right]\left[\frac{\frac{1}{\alpha_{1m}}\sinh 2\alpha_{1m}d + \frac{1}{\beta}\sin 2\beta_{1m}d}{\cosh 2\alpha_{1m}d + \cos 2\beta_{1m}d}\right] \quad (3.68)$$

Similarly substitution of (3.44) and (3.45) in (3.67) gives

$$P_2 = \frac{\rho_1^2}{4\rho_2} p\lambda L\sum_{m=1}^{\infty} \frac{\hat{J}_m^2}{\alpha_{2m}}\left[1+\left(\frac{m\lambda}{2L}\right)^2\right]\left[\frac{1}{\cosh 2\alpha_{1m}d+\cos 2\beta_{1m}d}\right] \quad (3.69)$$

for the values of 'd' usually encountered in practical copper-faced couplings (usually less than 1 mm) and for frequencies well beyond the operating range of these machines*

$$\begin{aligned} \sinh 2\alpha_{1m}d &\simeq 2\alpha_{1m}d \\ \sin 2\beta_{1m}d &\simeq 2\beta_{1m}d \\ \cosh 2\alpha_{1m}d &\simeq 1 \\ \cos 2\beta_{1m}d &\simeq 1 \end{aligned} \quad (3.70)$$

Substituting these approximate forms into (3.68) and (3.69) we obtain,

$$P_1 = \rho_1 p\frac{\lambda L}{4} d\sum_{m=1}^{\infty} \hat{J}_m^2\left[1+\left(\frac{m\lambda}{2L}\right)^2\right] \quad (3.71)$$

and

$$P_2 = \frac{\rho_1}{8\rho_2} p\lambda L\sum_{m=1}^{\infty} \frac{\hat{J}_m^2}{\alpha_{2m}}\left[1+\left(\frac{m\lambda}{2L}\right)^2\right] \quad (3.72)$$

The total fundamental power dissipated in the drum is thus

$$P = \rho_1 p\frac{\lambda L}{4}\sum_{m=1}^{\infty} \hat{J}_m^2\left[1+\left(\frac{m\lambda}{2L}\right)^2\right].\left[d+\frac{\rho_1}{2\rho_2\alpha_{2m}}\right] \quad (3.73)$$

---

*Taking values of d = 1 mm, (the maximum practical value) m = 1 and using table 3.1, it can be shown that even at 10 kHz (100 000 rev/min slip) the error in any one of these expressions is less than 6%. At 10 Hz (100 rev/min slip) the error is negligible.

The h^{th} harmonic loss, P_h, is found by replacing λ by $\frac{\lambda}{h}$, p by h.p, α_{2m} by α_{2mh} and $\hat{J}_m$ by $\hat{J}_{mh}$. The total drum loss is then given by the summation of the harmonic losses over h. Hence

$$P_{total} = \rho_1 p \frac{\lambda L}{4} \sum_{h=1}^{\infty} \sum_{m=1}^{\infty} \hat{J}_{mh}^2 \left[1 + \left(\frac{m\lambda}{2hL}\right)^2\right] \cdot \left[d + \frac{\rho_1}{2\rho_2 \alpha_{2mh}}\right] \qquad (3.74)$$

3.4.2 Drum loss in terms of airgap flux-density.

3.4.2.1 Loss equations.

The fundamental drum loss can be expressed in terms of B_y by substituting for J_m in (3.73) from (3.57). This gives

$$P = p \frac{\lambda^3 \omega^2 L}{16\pi^2 \rho_1} \sum_{m=1}^{\infty} \hat{B}_{ym}^2 \frac{\left[d + \rho_1/2\rho_2 \alpha_{2m}\right]}{\left[1 + \left(\frac{m\lambda}{2L}\right)^2\right]} \qquad (3.75)$$

Substituting for $\hat{J}_{mh}$ in (3.74) from (3.58) yields the total drum loss including harmonics:

$$P_{total} = p \frac{\lambda^3 \omega^2 L}{16\pi^2 \rho_1} \sum_{h=1}^{\infty} \sum_{m=1}^{\infty} \hat{B}_{ymh}^2 \frac{\left[d + \rho_1/2\rho_2 \alpha_{2mh}\right]}{\left[1 + \left(\frac{m\lambda}{2hL}\right)^2\right]} \qquad (3.76)$$

3.4.2.2 Contribution of higher order terms to the drum loss.

The series for fundamental loss is convergent due to the factor m^2 occurring in the denominator of each term. The rate of convergence clearly depends on the value of $\frac{\lambda}{2L}$.

In industrial couplings the ratio $\frac{\lambda}{2L}$ is normally within the range 3-1.* Taking the lowest value we have

$1 + \left(\frac{m\lambda}{2L}\right)^2 = 2$ for m = 1, 10 for m = 3, 26 for m = 5,
50 for m = 7, 82 for m = 9, etc.

---

*These figures were obtained by examining a range of couplings manufactured by Redman Heenan International Ltd.

Thus, even neglecting the reducing loss for high values of m due to the reducing value of $\hat{B}_{ym}$ and the increasing value of α_{2m}, it can be seen that all losses for m greater than 5 can be neglected. Indeed, even if B_{y3} and B_{y5} approach 50% of B_{y1}, the total loss contribution of B_{y3} is only 5% and that of B_{y5} less than 2% of the loss due to B_{y1}. If $\frac{\lambda}{2L}$ is greater than 1, these loss contributions will be even less.

The harmonic losses do not converge so rapidly with m, but again losses for m greater than 5 may be neglected.

3.4.2.3 The loss equations in terms of the approximate axial distribution.

For the particular case of the approximate rectangular distribution of flux-density discussed in section 3.3.8, we have for the fundamental loss, from (3.63) and (3.73)

$$P = \frac{p\lambda^3 L\omega^2}{\pi^4 \rho_1} B_{av}^2 \sum_{m=1}^{\infty} \frac{\sin^2\left(\frac{m\pi La}{2L}\right)}{m^2} \frac{\left[d + \rho_1/2\rho_2\alpha_{2m}\right]}{\left[1+\left(\frac{m\lambda}{2L}\right)^2\right]} \qquad (3.77)$$

From (3.64) and (3.74) the total loss is

$$P_{total} = \frac{p\lambda^3 L\omega^2}{\pi^4 \rho_1} \sum_{h=1}^{\infty}\sum_{m=1}^{\infty} B_{avh}^2 \frac{\sin^2\left(\frac{m\pi La}{2L}\right)}{m^2} \frac{\left[d + \rho_1/2\rho_2\alpha_{2mh}\right]}{\left[1+\left(\frac{m\lambda}{2hL}\right)^2\right]} \qquad (3.78)$$

In addition to the general discussion of section 3.4.2.2, an indication of the loss contribution of high values of m for this specific axial distribution can be obtained by considering one term in the series for fundamental loss:

$$P_m = \frac{p\lambda^3 L\omega^2}{\pi^4 \rho_1} B_{av}^2 \frac{\sin^2\left(\frac{m\pi La}{2L}\right)}{m^2} \frac{\left[d + \rho_1/2\rho_2\alpha_{2m}\right]}{\left[1+\left(\frac{m\lambda}{2L}\right)^2\right]}$$

Neglecting the increase in α_{2m} with m, which will reduce P_m,

$$\frac{P_m}{P_1} = \frac{\sin^2\left(\frac{m\pi La}{2L}\right)}{m^2 \sin^2\left(\frac{\pi La}{2L}\right)} \frac{\left[1+\left(\frac{\lambda}{2L}\right)^2\right]}{\left[1+\left(\frac{m\lambda}{2L}\right)^2\right]}$$

Taking values for the experimental copper-faced coupling of $L = 6.35 \times 10^{-2}$m, $L_a = 2.54 \times 10^{-2}$m, and $\lambda = 8.31 \times 10^{-2}$m, we have $\frac{P_{m=3}}{P_{m=1}} = 6.6\%$, $\frac{P_{m=5}}{P_{m=1}} = 0$, $\frac{P_{m=7}}{P_{m=1}} = 0.304\%$ ....

Thus, even for the case of the experimental copper-faced coupling where the ratio $\frac{\lambda}{2L}$ is untypically low (0.655), the vast majority of loss is contributed by B_1 and J_1.

In some machines, where it is not valid to assume a rectangular distribution of flux-density, it may well be nccessary to use the general loss equations, (3.75) and (3.76), to take account of loss components $P_{m=3}$ and $P_{m=5}$. However, at this stage, it would seem a worthwhile and justifiable simplification to neglect the effect of all those flux-density and current-density components corresponding to $m > 1$. Indeed, following the argument of section 3.4.2.2, even if the pole structure is such that the axial distribution departs radically from the approximation, the total loss contribution of those terms corresponding to $m > 1$ should not constitute a serious error.

Consequently for the remainder of this work only the fundamental (m=1) of the axial flux-density distribution will be considered to have any significant effect on the coupling performance.

3.4.2.4 The loss equation for limiting conditions.

Neglecting all terms containing $m > 1$ the fundamental loss is, from (3.75),

$$P = \frac{p\lambda^3 w^2 L}{16\pi^2 \rho_1} \hat{B}_y^2 \frac{\left[d + \rho_1/2\rho_2 \alpha_2\right]}{\left[1 + \left(\frac{\lambda}{2L}\right)^2\right]} \qquad (3.79)$$

For the limiting conditions where the drum length is much longer than the pole wavelength, and where $d \gg \rho_1/2\rho_2\alpha_2$

$$P = \frac{p\lambda^3\omega^2 L}{8\pi^2\rho_1}\hat{B}_y^2 d = \frac{\pi D^3\omega^2 L}{8p^2\rho_1}\hat{B}_y^2 d$$

This expression for dissipated power is identical to that given by Russell and Norsworthy[19] for the loss in the sleeve of a screened-rotor induction machine with no end effect. This is to be expected when the physical significance of imposing these limiting conditions is investigated.

Defining that $L \gg \lambda$ renders the problem effectively two-dimensional and eliminates end effects. If $d \gg \rho_1/2\rho_2\alpha_2$ then the majority of the loss is occurring in the copper sleeve. This condition is approached as α_2 becomes very large, i.e. as the frequency becomes very high and the backing-iron current-density becomes very small (see fig 3.3). The mathematical approximations (3.70) are equivalent to physically neglecting the variation of current-density throughout the copper sleeve.

Thus, with these approximations, not only do the eddy-current distributions in the copper-faced drum conform with those of Russell and Norsworthy, as discussed in section 3.3.7, but the two theories lead to the same loss equation.

This is encouraging support for the theory developed and the approximations introduced this far.

3.4.3 Comparison of dissipated powers in each region of the drum.

Neglecting all terms containing $m > 1$ we have; from (3.71), (3.72) and (3.79)

$$\frac{P_1}{P} = \frac{1}{1 + \dfrac{\rho_1}{2\rho_2\alpha_2 d}} \qquad (3.80)$$

and $$\frac{P_2}{P} = \frac{1}{1 + \frac{2\rho_2\alpha_2 d}{\rho}} \qquad (3.81)$$

Figure 3.8 shows the variations of the power ratios, (3.80) and (3.81), over the frequency range 0.1 to 1000 Hz (1 to 10 000 rev/min slip) for the parameters already given for the experimental copper-faced coupling. (see section 3.3.6)

Below approximately 0.57 Hz, 5.7 rev/min slip, the largest proportion of loss is in the backing iron. Above this frequency the larger loss contribution comes from the copper-face. At 10 Hz, 100 rev/min slip, the nominal rated speed of the experimental coupling, 81% of the total drum loss is occurring in the copper. The proportion of loss in the copper increases with frequency until at 150 Hz, 1500 rev/min slip, 94% of the loss is contributed by the eddy-currents in the copper-face.

Figure 3.8 shows clearly that, over the working speed range of the copper-faced coupling, it is not permissible to neglect the backing-iron loss, a procedure normally adopted in calculating the rotor loss in sleeve-rotor induction motors.

However this analysis does show that the predicted total drum loss is less sensitive to errors in the calculated backing iron loss than to errors in the loss in the copper-facing. For example, an error of 30% in the iron loss at 10 Hz would only result in an error of 6% in the total loss.

3.4.4 The validity of using a linear analysis.

The theory developed so far has been based on the assumption of constant resistivity and permeability in both regions of the drum. In reality this assumption is not valid and Gibbs[3] makes the following comments on the effects of variable

resistivity and permeability.

> "With regard to the value of ρ, any calculations will be based on the supposition that a steady state has been reached. Therefore, ρ is for the purpose constant, but since its value depends on the temperature of the material, it is necessary to adjust its value to suit the known or expected temperature at the load condition to be calculated.
>
> The case of μ is more complicated because its value varies with $\overline{H}$, and $\overline{H}$ has a different value at each point in the secondary (drum) as well as being periodic. μ depends too, for a given value of $\overline{H}$ on how and when this value was attained, i.e. on the history of the material; but this particular point can be disregarded as the effect is small compared with the principal changes of μ ".

In the copper-face, the problem of variable permeability does not arise since copper is a magnetically linear material. In the backing iron however, the permeability will vary axially, radially and peripherally throughout the drum volume. It is not feasible to take account of this spatial variation of permeability theoretically, but, as Gibbs[3] points out, "..... experience shows that reliable conclusions are possible by assuming μ to be single valued and results obtained .... show that the assumption is feasible". Davies[12] also followed this line of reasoning, "It is realised that the above theory assumes that once the value of μ at H_m is found, it applies for the whole sinusoidal excursion of the flux-density for all points in the drum. This can only be justified empirically by the

results that it gives in practice". Both Gibbs and Davies obtained excellent correlation between theory and experimental data and consequently it was decided to follow their method of attack and neglect the spatial variation of permeability.

As outlined in chapter 1, both Gibbs and Davies developed methods of incorporating the variation of μ with H into their respective theories and the author was faced with the decision of whether or not to attempt to use either of these methods to take account of variable permeability when calculating the backing iron loss in the copper-faced coupling.

The theory presented in this work involves two components of current-density, J_x and J_z, which give rise to three components of magnetic field strength, H_x, H_y and H_z. Consequently along each of the x,y and z axis the backing iron will have a different permeability.

To apply Gibbs semi-graphical method in this case would be inordinately complex. Davies' method, though completely analytical, would also be difficult to apply for the case of a three-dimensional field. Thus, bearing in mind the points made in section 3.4.3, where it was demonstrated that, over the working speed range of a copper-faced coupling, the backing iron only contributes the minor proportion of drum loss, it was decided to maintain the original, if incorrect, assumption that the backing iron permeability is constant.

The problem then arises: what level of permeability to use when calculating the backing iron loss.

Davies states that the drum in a conventional eddy-current coupling normally operates around and above the knee of the magnetisation curve of the drum iron (above 250 AT/m). Since

copper-faced couplings operate at flux-densities which are comparable with conventional couplings, it is reasonable to suppose that the backing iron operates over the same region of its magnetisation curve. The magnetic characteristics of a typical backing iron ('Armco' high grade electrical iron) are shown in fig 3.9. From this figure it can be seen that the operating region suggested by Davies corresponds to a relative permeability range of approximately 500 to 2500. However, since in section 3.4.3 it was shown that at high slip speeds the loss equation is relatively insensitive to errors in the assumed backing iron permeability, it is better to choose a value of permeability that conforms most closely to the true permeability at low slip speeds. At low slip speeds the effect of armature reaction on the airgap flux is a minimum and the level of average gap density does not depart radically from the standstill value. Consequently, a sensible choice of permeability would appear to be one corresponding to the flux-density at standstill.

Most eddy-current couplings are designed for average gap densities at standstill of between 0.7 and 1.2 Telsa. This corresponds to a relative permeability range of approximately 1600 to 2400 for a typical backing iron. Hence, for any illustrative calculations carried out in earlier sections, the average of this range of permeabilities was taken i.e. $\mu_r = 2000$.

The effect of different permeabilities on the power distribution is illustrated in fig 3.10 which shows the power ratios, equations (3.80) and (3.81), calculated over the frequency range of 0.1 to 1000 Hz (1 to 10 000 rev/min slip for fundamental quantities). The deviation of the power ratio curves from

the initial curve, fig 3.8, calculated with μ_r assumed to be 2000, is summarised in table 3.3. It is evident from this table that, as the slip frequency increases, the power ratios become less susceptible to the chosen value of permeability. Thus for slip frequencies greater than approximately 6 Hz (60 rev/min slip) it appears to be permissible to use a constant relative permeability of 2000 irrespective of the standstill excitation level. For lower slip frequencies it will be necessary to choose a value of permeability applicable to the given standstill average gap density.

Finally of course the only justification for using a particular constant relative permeability, whether based on standstill flux-density or any other value, is how closely the predicted performance approximates to the observed performance on test.

3.5 The torque equation in terms of resultant airgap flux-density.

The torque acting on the drum can be deduced from the equation of power balance:

Power input - Power output = Power dissipated in the drum

Therefore $$T.\left(\frac{\omega_{in}}{P} - \frac{\omega_{out}}{P}\right) = T.\frac{\omega}{P} = P$$

Thus, from (3.79) the fundamental torque is

$$T = \hat{B}_y^2 \frac{\omega \lambda^3 p^2 L}{16\pi^2 \rho_1} \frac{[d + \rho_1/2\rho_2\alpha_2]}{[1+(\frac{\lambda}{2L})^2]} \qquad (3.82)$$

Hence the total torque including harmonics is

$$T = \frac{\omega \lambda^3 p^2 L}{16\pi^2 \rho_1} \sum_{h=1}^{\infty} \hat{B}_{yh}^2 \frac{[d + \rho_1/2\rho_2\alpha_{2h}]}{[1+(\frac{\lambda}{2hL})^2]} \qquad (3.83)$$

TABLE 3.3.

	Percentage Deviation of Power Ratios			
f(Hz)	$\mu_r = 500$	$\mu_r = 1000$	$\mu_r = 1500$	$\mu_r = 2500$
·1	23	14	6·6	6
·5	47	22	8·5	4
1	41	16	5·5	5
5	24·5	10	4	2·5
10	32	19	1	1
50	9	4·7	1·1	1
100	2	1	0	0
500	1	0	0	0
1000	1	0	0	0

practical frequency range

practical permeability range

Equations (3.82) and (3.83) are the general torque equations of the copper-faced coupling, valid for any airgap field distribution so long as the loss contribution of the axial harmonics ($m > 1$) is negligible.

At this point it is convenient to express the torque in terms of the approximate rectangular distribution introduced earlier, since such an expression will be required when calculating the performance of the experimental copper-faced coupling. In terms of the approximate flux-density distribution, from (3.77) the fundamental torque is

$$T = \frac{\omega \lambda^3 p^2 L}{\pi^4 \rho_1} B_{av}^2 \sin^2\left(\frac{\pi}{2}\frac{L_a}{L}\right) \frac{\left[d + \rho_1/2\rho_2\alpha_2\right]}{\left[1+\left(\frac{\lambda}{2l}\right)^2\right]} \qquad (3.84)$$

whilst the torque including harmonics is

$$T = \frac{\omega \lambda^3 p^2 L}{\pi^4 \rho_1} \sin^2\left(\frac{\pi}{2}\frac{L_a}{L}\right) \sum_{h=1}^{\infty} B_{avh}^2 \frac{\left[d + \rho_1/2\rho_2\alpha_{2h}\right]}{\left[1+\left(\frac{\lambda}{2\pi L}\right)^2\right]} \qquad (3.85)$$

3.6 Armature reaction in the copper-faced coupling.

3.6.1 General effects of armature reaction.

The equations for torque in terms of the resultant airgap flux-density in section 3.5 are not directly useful in calculating the performance of a coupling, since they require that the resultant airgap flux-density be known for any given slip speed. In practice, armature reaction, due to the eddy-currents flowing in the loss drum, distorts the flux-density distribution and reduces the airgap flux as slip speed increases.[6,8,12] It is important, therefore, to be able to assess the variation of flux with speed over the whole working range of the coupling. To calculate the flux at any speed, it is necessary to investigate

the manner in which armature reaction varies with speed and the way in which it modifies the standstill flux-density distribution to produce the resultant dynamic flux-density distribution.

The total armature reaction m.m.f. will be due to the combined effect of the eddy-currents flowing in both regions of the drum, each region carrying both axial and peripheral components of current-density.

3.6.2 General equation for armature reaction m.m.f.

Figure 3.11 shows a section through the coupling and the contour a.b.c.e., chosen to calculate the m.m.f.

The line b.c. has arbitrary co-ordinates (x,z), but the line a.e. is chosen so that it has co-ordinates: $x = 0$, $z = \frac{L}{2}$. The line a.b. is within the rotor surface ($y < -g$), and the line c.e. is taken to be at $y = \infty$.

The nett m.m.f. acting on the contour a.b.c.e. is given by the integral of $\bar{H}$ around a.b.c.e. and also by the total current flowing through a.b.c.e.

In turn, the total current flowing through this contour will be equal to the sum of the currents flowing through the rectangles e.f.h.l. and c.f.h.m.

Thus the armature reaction m.m.f. is given by

$$F_R = \int_0^d \int_0^x J_{z1}\, dx\, dy + \int_0^d \int_z^{\frac{L}{2}} J_{x1}\, dz\, dy + \int_0^\infty \int_0^x J_{z2}\, dx\, dy + \int_d^\infty \int_z^{\frac{L}{2}} J_{x2}\, dz\, dy$$

where the first two terms denote the m.m.f. contribution

of the copper facing, F_{R1}, and the final two terms denote the m.m.f. contribution of the backing iron, F_{R2}.

Consider now the integral of $\bar{H}$ around the contour a.b.c.e:

$$F_R = \oint \bar{H} \cdot d\bar{l} = \int_a^b \bar{H} \cdot d\bar{l} + \int_b^c H_y \, dy + \int_c^e \bar{H} \cdot d\bar{l} + \int_e^a H_y \, dy$$

Now $\bar{H}$ must tend to zero as y tends to infinity and, since 'c' and 'e' are taken to be at $y = \infty$,

$$\int_c^e \bar{H} \cdot d\bar{l} = 0$$

Also, since the line a.e. is at $z = \frac{I}{2}$ and the armature reaction m.m.f. must fall to zero at this point, because no current can flow for $|Z| > \frac{L}{2}$,

$$\int_e^a H_y \, dy = 0$$

It is a reasonable assumption that only a very small portion of the total armature reaction m.m.f. will be used in driving flux through the rotor and hence we can say

$$\int_a^b \bar{H} \cdot d\bar{l} = 0$$

Thus

$$F_R = \int_b^c H_y \, dy$$

This means that the armature reaction m.m.f. can be considered to be totally consumed over b.c., which is a radial line whose position in the x.z. plane is defined by the co-ordinates x and z. Thus, although the armature reaction m.m.f. is a scalar quantity by definition, its amplitude is a point function of position in the x.z. plane.

It is convenient to consider the m.m.f. of each region, F_{R1} and F_{R2}, separately, and initially to consider only fundamental quantities. Harmonics are taken into account later.

3.6.3 Armature reaction m.m.f. due to eddy-currents in the copper-facing.

From section 3.6.2, we have

$$F_{R1} = \int_0^d \int_0^x J_{z1}\, dx\, dy + \int_0^d \int_z^{\frac{L}{2}} J_{x1}\, dz\, dy \Big]_{x=0}$$

Substituting from (3.42) and (3.43) for J_{x1} and J_{z1} we obtain

$$F_{R1} = \frac{\lambda}{2\pi} \hat{J} \frac{\tanh \gamma_1 d}{\gamma_1} \cos\frac{\pi z}{L}\, e^{j\left(\frac{2\pi x}{\lambda} - \omega t - \frac{\pi}{2}\right)}$$

Now for all practical depths of copper and for frequencies well beyond the operating range of eddy-current couplings (including significant harmonics),

$$\sinh \gamma_1 . d = \tanh \gamma_1 . d = \gamma_1 d$$

$$\cosh \gamma_1 . d = 1$$

The equation for F_{R1} thus reduces to

$$F_{R1} = \frac{\lambda}{2\pi} d \hat{J} \cos\frac{\pi z}{L}\, e^{j\left(\frac{2\pi x}{\lambda} - \omega t - \frac{\pi}{2}\right)} \qquad (3.86)$$

3.6.4 Armature reaction m.m.f. due to eddy-currents in the backing iron.

From (3.84) we have

$$F_{R2} = \int_d^\infty \int_0^x J_{z2}\, dx\, dy + \int_d^\infty \int_{\frac{L}{2}}^z J_{x2}\, dz\, dy$$

Substituting from (3.44) and (3.45) for the current-densities yields

$$F_{R2} = \frac{\rho_1}{\rho_2} \frac{\lambda}{2\pi} \frac{\hat{J}}{\gamma_2} \cos\frac{\pi z}{L}\, e^{j\left(\frac{2\pi x}{\lambda} - \omega t - \frac{\pi}{2}\right)}$$

However, since we can express γ_2 as $R_2 e^{j\phi_2}$

$$F_{R2} = \frac{\rho_1}{\rho_2} \frac{\lambda}{2\pi} \frac{\hat{J}}{R_2} \cos\frac{\pi z}{L}\, e^{j\left(\frac{2\pi x}{\lambda} - \omega t - \frac{\pi}{2} - \phi_2\right)} \qquad (3.87)$$

3.6.5 Total armature reaction m.m.f.

Equations (3.86) and (3.87) describe the fundamental armature reaction m.m.f.s set up by the eddy-currents flowing in each region of the drum.

These m.m.f.s are cophasal in their axial variation, both reaching a peak at the axial centre of the drum (z = 0), but the backing iron m.m.f. lags the copper-facing m.m.f. by ϕ_2 rad as the waves travel peripherally around the machine. The m.m.f. waves are radially displaced in the drum: the copper-facing m.m.f. appears as a wave travelling along the surface of the copper, whilst the backing iron m.m.f. may be considered to be a wave travelling along the copper-iron interface. This situation is illustrated schematically in fig 3.12a. However, since both m.m.f.s act on the same effective airgap, i.e. the physical airgap 'g' plus the depth of copper 'd', they can be considered to be acting at the same radius so long as the flux produced by the m.m.f.s is assumed to cross the effective airgap (g+d) radially. This assumption is reasonable for the copper since it has been shown that the attenuation of the current-densities in this region is negligible for all practical frequencies and this automatically implies radial flux penetration of the copper.

Also, since the physical airgap in an eddy-current coupling is small, there will be little error in assuming radial flux paths in the airgap. Consequently both F_{R1} and F_{R2} can be considered to act at the same arbitrary radius within the effective airgap (g+d) as illustrated in fig 3.12b.

The total armature reaction m.m.f, F_R, is then given by the vector addition of F_{R1} and F_{R2} as shown in fig 3.12c.

From fig 3.12c

$$F_R^2 = F_{R1}^2 + F_{R2}^2 - 2F_{R1}F_{R2}\cos(\pi - \phi_2)$$

Now from (3.54)

$$\phi_2 = \frac{1}{2}\tan^{-1}\left[\frac{\omega\mu_2/\rho_2}{(2\pi/\lambda)^2+(\pi/L)^2}\right]$$

For all practical cases

$$\omega\mu_2/\rho_2 \gg \left(\frac{2\pi}{\lambda}\right)^2+\left(\frac{\pi}{L}\right)^2$$

and consequently ϕ_2 tends to a limiting value of 45° as the frequency (ω) increases. Little error will, therefore, be introduced by considering ϕ_2 to be 45° over the whole working range of the coupling. This is shown clearly by table 3.2 which shows that, for the experimental copper-faced coupling, ϕ_2 is 43.5° at 1 Hz (10 rev/min slip), 44.8° at 10 Hz (100 rev/min slip), and for all practical purposes is 45° at higher frequencies.

If ϕ_2 is taken as 45° then

$$\gamma_2 = R_2 e^{j\frac{\pi}{4}} \qquad \text{and} \qquad \alpha_2 = \beta_2 = R_2/\sqrt{2}$$

For $\phi_2 = 45^\circ$, and $\omega\mu_2/\rho_2 \gg (2\pi/\lambda)^2+(\pi/L)^2$

$$\alpha_2 = (\omega\mu_2/2\rho_2)^{1/2}$$

where α_2^{-1} now conforms exactly with the classical definition of skin depth*

The armature reaction m.m.f. equation now simplifies to

$$F_R^2 = F_{R1}^2 + F_{R2}^2 + \sqrt{2}F_{R1}F_{R2} \qquad (3.88)$$

Substituting from (3.86) and (3.87) for F_{R1} and F_{R2} and replacing R_2 by $\sqrt{2}\alpha_2$, we have for the amplitude of F_R

$$\hat{F}_R = \left[\frac{\hat{J}\lambda}{2\pi}\, d^2 + \left(\frac{\rho_1}{\rho_2\sqrt{2}\alpha_2}\right)^2 + \frac{\rho_1 d}{\rho_2\alpha_2}\right]^{1/2}$$

---

* Table 3.2 shows these approximations to be valid.

As frequency increases and α_2 becomes very large (see table 3.2), $\rho_1/\rho_2\alpha_2$ becomes very small and the total armature reaction m.m.f. is almost equal to the m.m.f. generated by the eddy-currents in the copper-facing. This is to be expected, since in section 3.3.6 it was demonstrated that, at high frequencies, the backing-iron eddy-currents were very small and consequently the m.m.f. due to the backing-iron currents will also be small, compared to the m.m.f. generated in the copper-facing. Hence, due to the predominance of F_{R1} over F_{R2} with increasing frequency, in practice it is unnecessary to consider the vector sum of the armature reaction m.m.f.s, since simple arithmetic addition of F_{R1} and F_{R2} yields a conservative and sufficiently accurate estimate of the armature reaction m.m.f., F_R.

i.e. $$F_R = F_{R1} + F_{R2} \tag{3.89}$$

Hence $$\hat{F}_R = \frac{\hat{J}\lambda}{2\pi}\left[d + \rho_1/\sqrt{2}\rho_2\alpha_2\right] \tag{3.90}$$

In appendix 1 it is shown that the maximum error in the arithmetic addition of F_{R1} and F_{R2} is 7.6% and occurs when $F_{R1} = F_{R2}$. The condition for this is

$$d = \rho_1/\sqrt{2}\rho_2\alpha_2$$

In all copper-faced couplings this will occur at very low frequencies indeed. For the experimental machine the condition is satisfied when $\alpha_2 = 272$. From table 3.2 it can be seen that this corresponds to a frequency of less than 1 Hz (10 rev/min slip for fundamental quantities). The error involved at normal working slip will be much less.

At harmonic frequencies, arithmetic addition of the

armature reaction m.m.f.s is equally valid and, hence,

$$\hat{F}_{Rh} = \frac{\hat{J}_h \lambda}{2\pi h}\left[d + \rho_1/\sqrt{2}\rho_2\alpha_2\right] \qquad (3.91)$$

3.6.6 The relationship between armature reaction m.m.f., flux/pole and torque.

From (3.61) and (3.63) we have

$$\hat{J} = \frac{2\phi_{ac}\, w \sin(\frac{\pi}{2}\frac{L_a}{L})}{\rho_1 L_a \pi \left[1+(\lambda/2L)^2\right]} \qquad (3.92)$$

where ϕ_{ac} is defined as

$$\phi_{ac} = \frac{B_{av}\lambda L_a}{\pi} \qquad (3.93)$$

Substituting, from (3.92), for $\hat{J}$ in (3.90) gives

$$\hat{F}_R = \frac{\lambda w \phi_{ac} \sin(\frac{\pi}{2}\frac{L_a}{L})}{\rho_1 \pi^2 L_a\left[1+(\frac{\lambda}{2L})^2\right]}\left[d + \rho_1/\sqrt{2}\rho_2\alpha_2\right]$$

Therefore,

$$\hat{F}_R = C_1 \phi_{ac}(n + C_2 n^{\frac{1}{2}}) \qquad (3.94)$$

where $$C_1 = \frac{2d.D \sin(\frac{\pi}{2}\frac{L_a}{L})}{\rho_1 L_a\left[1+(\lambda/2L)^2\right]}$$

and $$C_2 = \frac{\rho_1}{d\sqrt{2\pi p \mu_2 \rho_2}}$$

From (3.84), (3.93) and (3.94),

$$T = \frac{L}{L_a}\sin\frac{\pi}{2}\frac{L_a}{L}\, p^2 \phi_{ac}\, \hat{F}_R \frac{\left[d+\rho_1/2\rho_2\alpha_2\right]}{\left[d+\rho_1/\sqrt{2}\rho_2\alpha_2\right]}$$

As slip frequency increases, $\rho_1/\rho_2\alpha_2$ becomes very small and little error is involved in writing

$$\frac{d+\rho_1/2\rho_2\alpha_2}{d+\rho_1/\sqrt{2}\rho_2\alpha_2} \simeq 1$$

(approximately 6% error at 100 rev/min slip for the experimental coupling).

The error involved in this approximation is of opposite sign to the error in the arithmetic addition of F_{R1} and F_{R2}. The two errors are not, therefore, cumulative.

The torque equation now simplifies to

$$T = \frac{L}{L_a} \sin\left(\frac{\pi}{2}\frac{L_a}{L}\right) p^2 \phi_{ac} \hat{F}_R$$

Defining F_{AR} as $\frac{\hat{F}_R}{C_3}$, where $C_3 = \frac{4}{\pi}\sin\left(\frac{\pi}{2}\frac{L_a}{L}\right)$ we have

$$T = C_3^2 \frac{L}{L_a} p^2 \phi_{ac} F_{AR} \frac{\pi}{4} \qquad (3.95)$$

(The significance of F_{AR} and C_3 and the reason for this step is explained in the next section).

By analogy with (3.95), for the h^{th} harmonic,

$$T_h = C_3^2 \frac{L}{L_a} p^2 h^2 \phi_{ach} F_{ARh} \frac{\pi}{4} \qquad (3.96)$$

where $F_{ARh} = \frac{\hat{F}_{Rh}}{C_3}$

From (3.94) and (3.95),

$$T = \frac{\pi}{4} C_1 C_3 \frac{L}{L_a} p^2 \phi_{ac}^2 (n + C_2 n^{1/2}) \qquad (3.97)$$

and $$T_h = \frac{\pi}{4} C_{1h} C_3 \frac{L}{L_a} p^2 h^2 \phi_{ac}^2 \left(n + C_2 \frac{n^{1/2}}{h^{1/2}}\right) \qquad (3.98)$$

where $$C_{1h} = \frac{1 + (\lambda/2L)^2}{1 + (\lambda/2hL)^2} \cdot C_1$$

3.7 Calculation of the excitation m.m.f.

Under zero slip conditions, the only m.m.f. acting on the airgap is F_g, the excitation m.m.f., supplied from the field winding. Under slip conditions the resultant m.m.f. is F_ϕ, where, for fundamental quantities,

$$\bar{F}_\phi = \bar{F}_g + \bar{F}_R$$

F_{R1} is 90° out of phase with B_y, whilst F_{R2} lags F_{R1} by ϕ_2 rad. So long as saturation effects do not predominate, F_ϕ is in phase with B_y. Hence the m.m.f. vector diagram is as shown in fig 3.13a, where 'δ' is the angle between F_ϕ and F_R.

Since, for all practical slip speeds, F_{R1} predominates over F_{R2}, only a small error will be introduced by assuming F_R to be in phase with F_{R1}. (This is implied by the arithmetic addition of F_{R1} and F_{R2}). The approximate vector diagram, fig 3.13b, then applies. The phase angle between F_R and F_ϕ is now 90° and hence $\hat{F}_g$ is given by

$$\hat{F}_g^2 = \hat{F}_\phi^2 + \hat{F}_R^2$$

Rather than work in these maximum values, it is best to convert to average pole values as shown in fig 3.14.

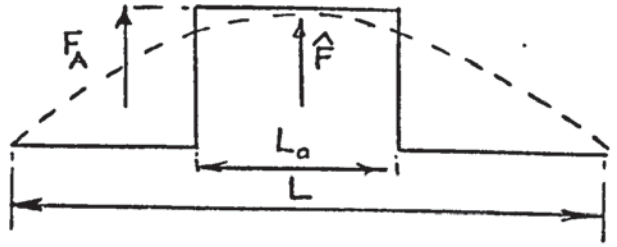

FIG 3.14

Denoting these average pole values as F_{Ag}, $F_{A\phi}$ and F_{AR}, we have, from the Fourier analysis of a chorded square wave given in section 3.3.8,

$$\hat{F}_g = C_3 F_{Ag}, \quad \hat{F}_\phi = C_3 F_{A\phi} \text{ and } \hat{F}_R = C_3 F_{AR} \qquad (3.99)$$

where $C_3 = \frac{4}{\pi} \sin\left(\frac{\pi}{2}\frac{L_a}{L}\right)$ (see (3.95) to (3.98))

Hence $$F_{Ag}^2 = F_{A\phi}^2 + F_{AR}^2 \qquad (3.100)$$

From section 3.6.6.

$$\Phi_{ac}^2 = \frac{4}{\pi} \frac{T L_a}{c_1 c_3 L p^2 (n + c_2 n^{1/2})}$$

and $$F_{AR}^2 = \frac{4}{\pi} T \frac{c_1 L_a}{c_3^3 L p^2} (n + c_2 n^{1/2})$$

Therefore, since $F_A = S \Phi_{ac}$

$$F_{Ag}^2 = \frac{4}{\pi} T \frac{L_a}{c_3 L p^2} \left[\frac{S^2}{c_1} \frac{1}{(n + c_2 n^{1/2})} + \frac{c_1}{c_3^2} (n + c_2 n^{1/2}) \right] \quad (3.101)$$

Equation (3.101) is the key equation to the performance of the copper-faced coupling. It gives the fundamental field m.m.f. required to support a given torque, T, at a given slip, n.

If (3.101) is rearranged as

$$T = \frac{\pi}{4} c_3 \frac{L}{L_a} p^2 F_{Ag}^2 \frac{n + c_2 n^{1/2}}{\frac{S^2}{c_1} + \frac{c_1}{c_3^2} (n + c_2 n^{1/2})^2} \quad (3.102)$$

then we have fundamental torque as a function of machine parameters, slip speed and excitation m.m.f.

The torque including harmonics will be

$$\Sigma T = \frac{\pi}{4} c_3 \frac{L}{L_a} p^2 \sum_{h=1}^{\infty} h^2 F_{Agh}^2 \frac{n + c_2 n^{1/2}/h^{1/2}}{\frac{S_h^2}{c_1} + \frac{c_1 h}{c_3^2} (n + c_2 n^{1/2}/h^{1/2})^2} \quad (3.103)$$

Equation (3.103) can now be used to calculate the torque-slip characteristic of a copper-faced coupling from the machine parameters and the known standstill m.m.f.

3.8 Slip speed for maximum torque.

Maintaining F_{Ag} constant, differentiating (3.101) and setting $\frac{\partial T}{\partial n} = 0$ yields*

$$\frac{\partial}{\partial n} \left[\frac{S^2}{c_1} \frac{1}{n_m + c_2 n_m^{1/2}} + \frac{c_1}{c_3^2} (n_m + c_2 n_m^{1/2}) \right] = 0$$

---

* 'm' denotes maximum not axial harmonic. For the remainder of the work 'm' will denote a maximum.

Therefore $$n_m + c_2 n_m^{1/2} = \frac{S c_3}{c_1} \qquad (3.104)$$

which gives, on solution,

$$n_m^{1/2} = -\frac{c_2}{2} \pm \left(\frac{c_2^2}{4} + \frac{S c_3}{c_1}\right)^{1/2}$$

One root implies that $n_m^{\frac{1}{2}}$ is imaginary, which, in a physical situation, it cannot be. Consequently we have

$$n_m = \left[\left(\frac{c_2^2}{4} + \frac{S c_3}{c_1}\right)^{1/2} - \frac{c_2}{2}\right]^2 \qquad (3.105)$$

By analogy the h^{th} harmonic torque reaches a maximum at

$$n_{mh} = \left[\left(\frac{c_2^2}{4h} + \frac{S_h c_3}{c_{1h}}\right)^{1/2} - \frac{c_2}{2h^{1/2}}\right]^2$$

Normally the harmonic torques will reach a maximum at much higher slip speeds than the fundamental.

Where backing-iron effects are small,

$$n_m \simeq \frac{S c_3}{c_1}$$

For a given machine, therefore,

$$n_m \propto \frac{g+d}{d} \qquad (3.106)$$

This is an important rule in the design of copper-faced couplings. In design studies, where the dimension (g+d) is fixed, it has been known for some time (see chapter 2) that n_m is inversely proportional to 'd'.

3.9 Equation for maximum torque.

Substituting (3.104) in (3.102) we have, for maximum fundamental torque,

$$T_m = \frac{\pi}{8} c_3^2 \frac{L}{L_a} \frac{p^2}{S} F_{Ag}^2 \qquad (3.107)$$

(It is interesting to note that at the peak torque condition the flux component of m.m.f., $F_{A\Phi}$, and the armature reaction component, F_{AR}, are equal. This was also found by Davies[6,8] in his analysis of conventional couplings).

For a given machine at fixed excitation,

$$T_m \propto \frac{1}{g+d} \qquad (3.108)$$

i.e. the maximum torque is not a function of the depth of copper 'd', only of the dimension (g+d). Hence, for a given machine with a total magnetic airgap of (g+d), the depth of copper deposited on the drum will only alter the speed at which maximum torque occurs and not the value of maximum torque.

It should be noted that this is only true, provided there is sufficient depth of copper to prevent the predominance of backing-iron effects. There would, however, be little point in manufacturing a copper-faced coupling with predominant backing-iron effect, since the performance obtained would be almost identical to that of a conventional machine with a homogeneous drum. Hence the statement is true (see chapter 2) for all practical machines.

As a function of excitation,

$$T_m \propto F_{Ag}^2 \propto I_f^2 \qquad (3.109)$$

3.10 Normalised torque-slip speed equation of the copper-faced coupling.

One of the most useful results of Davies' work[6,8,12] was the production of a single normalised equation which describes the behaviour of conventional eddy-current couplings under all conditions of steady-state load. In this section an analogous normalised equation is given for the copper-faced coupling. This equation is less general than Davies' equation since it produces not one normalised torque-slip curve, but a family of curves - each curve corresponding to one value of dimensionless

parameter 'G'. This is similar to the family of normalised curves given by Fitzgerald and Kingsley.[46]

From (3.101), since $F_{A\phi} = F_{AR}$ at peak torque,

$$2T_m \frac{C_1}{C_3^2}\left(n_m + C_2 n_m^{1/2}\right) = T.\left[\frac{S^2}{C_1(n + C_2 n^{1/2})} + \frac{C_1}{C_3^2}(n + C_2 n^{1/2})\right]$$

Hence

$$\frac{T}{T_m} = \frac{2\frac{C_1}{C_3^2}\left(n_m + C_2 n_m^{1/2}\right)}{\frac{S^2}{C_1(n + C_2 n^{1/2})} + \frac{C_1}{C_3^2}(n + C_2 n^{1/2})}$$

Substituting (3.104) gives

$$\frac{T}{T_m} = \frac{2}{\frac{n_m + C_2 n_m^{1/2}}{n + C_2 n^{1/2}} + \frac{n + C_2 n^{1/2}}{n_m + C_2 n_m^{1/2}}}$$

whence

$$\frac{T}{T_m} = \frac{2}{\frac{1 + C_2 n_m^{-1/2}}{\frac{n}{n_m} + C_2\left(\frac{n}{n_m}\right)^{1/2}} \quad \frac{\frac{n}{n_m} + C_2\left(\frac{n}{n_m}\right)^{1/2}}{1 + C_2 n_m^{-1/2}}}$$

Now $C_2 n_m^{-1/2}$ is a constant for a given machine and will be denoted by 'G', where, from (3.105),

$$G = \frac{2}{\left(1 + \frac{45 C_3}{C_1 C_2^2}\right)^{1/2} - 1} \tag{3.110}$$

Therefore

$$\frac{T}{T_m} = \frac{2}{\frac{1+G}{\left(\frac{n}{n_m}\right)^{1/2}\left[\left(\frac{n}{n_m}\right)^{1/2} + G\right]} + \frac{\left(\frac{n}{n_m}\right)^{1/2}\left[\left(\frac{n}{n_m}\right)^{1/2} + G\right]}{1+G}} \tag{3.111}$$

Equation (3.111) is the normalised torque equation of the copper-faced coupling. The exact shape of the curve it produces depends on the value of G.

For most practical couplings, it is permissible to approximate (3.110) to

$$G \simeq \left(\frac{C_1}{5C_3}\right)^{1/2} C_2$$

So, for a given machine,

$$G \propto \frac{1}{\sqrt{d\,(g+d)}}$$

i.e. as d tends to zero, G becomes infinite and as d tends to infinity, G tends to zero.

The condition d = ∞ corresponds to a homogeneous copper drum of infinite depth. The normalised torque equation for a coupling with a homogeneous copper drum is thus derived by setting G = 0 in (3.111), which yields

$$\frac{T}{T_m} = \frac{2}{\frac{n}{n_m} + \frac{n_m}{n}}$$

This is the classical normalised torque equation for an induction machine with zero stator resistance and is also that devised by Bahler and van der Hoek[13] for a coupling with a non-ferromagnetic drum.

The condition d = 0 corresponds to a homogeneous iron drum, the normalised torque equation of which should thus be given by (3.109) with G set to infinity. With G = ∞, (3.111) becomes

$$\frac{T}{T_m} = \frac{2}{\left(\frac{n}{n_m}\right)^{1/2} + \left(\frac{n_m}{n}\right)^{1/2}}$$

If the theory is correct the above equation should correlate with the normalised torque equation of a coupling with a solid iron drum given by Davies in reference 12.

From reference 12, section 2.6,

$$\frac{T}{(2+C)T_m} = \frac{Q}{1+CQ+Q^2}$$

where $C = -2\cos\delta$

and $$Q = \left(\frac{T}{T_m}\right)^{\frac{1-m}{m}} \cdot \left(\frac{n}{n_m}\right)^{1/2m}$$

The angle 'δ' has the same definition as the 'δ' used in this work, i.e., the angle between F_R and F_ϕ. The index 'm'

is defined by the magnetic characteristic of the drum iron in the following manner:

$$\mu^{1/4} H = K H^{m}$$

Davies takes $\delta = 135^{\circ}$, but in this work the angle δ has been taken as 90° due to the predominant effect of the copper region. So to correlate the (d = 0) condition with Davies' equation, 'C' must be set to zero. Since throughout this analysis a linear backing iron magnetic characteristic has been assumed, 'm' must be taken as unity.

Setting m = 1, Q becomes $\left(\frac{n}{n_m}\right)^{1/2}$.

Substituting this into Davies' equation with C = 0 yields:

$$\frac{T}{2T_m} = \frac{(n/n_m)^{1/2}}{1+\frac{n}{n_m}}$$

Therefore

$$\frac{T}{T_m} = \frac{2}{\left(\frac{n}{n_m}\right)^{1/2} + \left(\frac{n_m}{n}\right)^{1/2}}$$

which is identical to (3.111) for the particular case where $G = \infty$. This is convincing support for the theory developed in this chapter.

In general the value of G will be finite, normally up to a maximum value of 1.

The family of normalised torque-slip curves, derived from (3.111) is shown in fig 3.15. For higher values of G these curves will not be valid since they are derived from an analysis which assumes a constant angle of 90° between F_R and F_ϕ. This assumption is only valid if the effects of the copper region substantially dominate the performance of the coupling. Since higher values of G (lower values of d) denote increasing iron effects, and the backing iron component of F_R lags F_ϕ by

135°, the assumption of $\delta = 90^{\circ}$ will not be valid for large values of G.

As G increases the coupling becomes more and more like a solid iron coupling, the copper region having less influence on the torque. Consequently the curve corresponding to the upper limit of G should be Davies' normalised curve for solid iron couplings. Figure 3.16, shows the family of normalised curves up to G = 2, together with Davies' curve (This is Davies' curve for m = 0.77). From these curves it seems that the normalised torque equation (3.111) is quite valid up to G = 1, and Davies' curve is valid for $G > 2$. Between G = 1 and G = 2 it is difficult to say which would be the better curve to use. In this region the effective value of δ is somewhere between 90° and 135°.

The uncertainty in the normalised curves for $G > 1$ is not of any practical importance, since a commercial copper-faced coupling will almost invariably have a value of G less than 1 (G = 0.17 for the experimental copper-faced coupling). Indeed it would not be logical to manufacture couplings with larger values of G, since their performance would be little different from solid iron couplings. Figure 3.16 can be taken as the family of normalised torque-slip curves for the copper-faced coupling with the reservation that care must be taken in using the curves for $G > 1$.

3.11 Normalised flux and armature reaction m.m.f.

From (3.97)

$$\frac{T}{T_m} = \frac{\Phi_{ac}^2}{\Phi_{acm}^2}\left(\frac{n}{n_m}\right)^{1/2}\left[\frac{\left(\frac{n}{n_m}\right)^{1/2}+G}{1+G}\right]$$

Therefore

$$\frac{\Phi_{ac}}{\Phi_{acm}} = \frac{\sqrt{2}}{\left\{1+\left(\frac{n}{n_m}\right)\left[\frac{\left(\frac{n}{n_m}\right)^{1/2}+G}{1+G}\right]\right\}^{1/2}} \qquad (3.112)$$

Since

$$\frac{T}{T_m} = \frac{\Phi_{ac}\,F_{AR}}{\Phi_{acm}\,F_{ARm}},$$

$$\frac{F_{AR}}{F_{ARm}} = \frac{\sqrt{2}}{\left\{1+\left(\frac{n_m}{n}\right)\left[\frac{1+G}{\left(\frac{n}{n_m}\right)^{1/2}+G}\right]\right\}^{1/2}} \qquad (3.113)$$

The normalised flux and armature reaction curves are plotted in fig 3.17 for $2 \geq G \geq 0$, together with Davies' curves which, following the reasoning of section 3.10, should be used for $G > 2$.

A useful design point is that the flux remains substantially constant up to $\frac{n}{n_m} = 0.2$, which is higher than the normal rated slip of a commercial coupling. Consequently it is an excellent approximation to design the magnetic circuit of the machine for the standstill flux levels.

From (3.112) with n = 0, it would appear that standstill flux is $\sqrt{2}\,\Phi_{acm}$. However, at speeds approaching n = 0, backing-iron effects predominate and the machine performs like a standard coupling. Hence the standstill flux is given by Davies' curve, i.e. Φ_{aco} 1.85.Φ_{acm}, not the copper-faced coupling curve.

3.12 The validity of using the fundamental normalised equations for gross quantities.

The normalised torque, armature reaction and flux equations, (3.111), (3.112) and (3.113), were developed for fundamental quantities only and, therefore, are strictly not valid for gross torque, armature reaction or flux, since these may have significant harmonic contents. However, if the slip speed at which peak fundamental torque occurs is close to the slip speed at which peak gross torque occurs, i.e. $n_m \simeq n_{m\ (gross)}$, then the fundamental normalised equations will be good approximations to their counter equations normalised in terms of gross quantities.

For the vast majority of copper-faced couplings, the harmonic torques will reach their maximum values at much higher slip speeds than does the fundamental and, since the fundamental torque is the major portion of the gross torque, it is generally valid to use the normalised equation for gross quantities.

CHAPTER 4.

EXPERIMENTS WITH THE COPPER-FACED COUPLING.

4. Experiments with the copper-faced coupling.

4.1 Introduction.

This chapter discusses the results of tests on an experimental copper-faced coupling. Many of the tests were performed, under the authors supervision, by two honours students in the Department of Electrical Engineering. The test procedures are described in detail in their project reports.[51,52]

The experimental work on the copper-faced coupling was the standard sequence of tests[6,8,12,14] involving measurement of torque-slip curves and pole-face density distributions.

From the results of these tests, the theory of chapter 3 is shown to be valid and the main areas of uncertainty are identified.

4.2 The experimental copper-faced coupling

The experimental coupling was the stationary rotor coupling, used by Davies.[6,8] Complete details of the machine are given in references 6, 8 and 14. A sectional view of the machine and details of the pole member are given in figs 4.1 and 4.2.

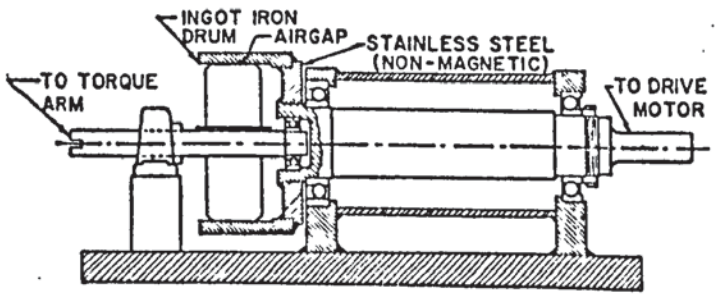

Fig 4.1 Sketch of experimental coupling, stationary field, rotating drum

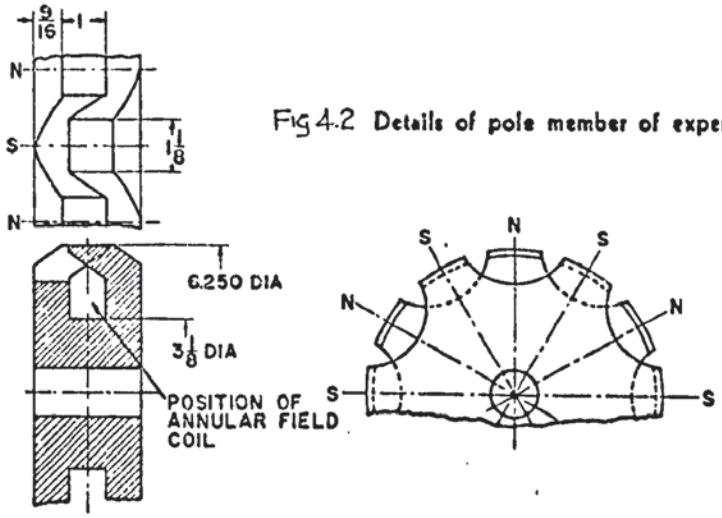

Fig 4.2 Details of pole member of experimental coupling

The original drum used by Davies was bored out and plated with copper to a nominal depth of 0.4 mm. The depth was checked on a travelling microscope and found to be 0.4 mm $\pm$0.02 mm. The eccentricity (5%) was considered negligible and for calculations the depth was taken to be 0.4 mm.

The parameters of the experimental machine are summarised in table 4.1.

TABLE 4.1

Loss drum:

length	=	63.5 mm
inside diameter	=	159.39 mm
outside diameter	=	185 mm
radial depth of copper	=	0.4 mm
resistivity of backing iron	=	11.2×10^{-8} Ω m
resistivity of copper face	=	1.725×10^{-8} Ω m

Rotor:

outside diameter	=	158.87 mm
radial airgap	=	0.254 mm
number of poles	=	12
fundamental wavelength	=	83.1 mm
length of pole	=	25.4 mm
pole arc/pole pitch	=	0.69
winding turns	=	2600

4.3 Instrumentation.

Search coils were fitted on the rotor to measure the cicumferential flux-density distribution across the pole face. These coils are described by James in section 2.6.1 and 2.6.3 of reference 14. Since the coils run the length of the pole, the flux-density values obtained from them will be axially averaged i.e. the coils give a direct indication of B_{av} (see section 3.3.8).

Torque was measured by the strain gauge bridge method.[6,14]

The coupling drive was a 3.75 kW induction motor-coupling unit (of the type shown in fig 1.3) with a tachometer incorporated on the output shaft.

Complete details of the experimental system and calibration are given in references 51 and 52.

4.4 Torque-slip curves.

The measured torque-slip curves are shown in fig 4.3. Each test run was commenced with the outer surface of the drum cooled to 50°C. The maximum temperature rise during a test was 20°C.

It can be seen that, for a given excitation, the torque-slip curve is unaffected by moving the rotor to either edge of the drum. This means that, as assumed in section 3.2, it is permissible to calculate the torque on the basis of axially symmetrical poles, whether the poles are positioned symmetrically or not.

4.5 Pole face flux-density distributions.

The measured flux-density distributions for excitations of 260, 520 and 780 AT/pole are shown in figs 4.4-4.6. Following previous work[6,8,12,14] the experimental flux-density values are plotted in the position along the pole arc corresponding to the centre of the search coil.

4.5.1 Harmonic analysis.

The flux-density waves were analysed up to the 50th harmonic using 49 ordinates per pole pitch.* The results of the analysis are summarised up to the 15th harmonic in table 4.2. The higher order harmonics were too small to warrent printing.

Fundamental flux per pole is defined by (3.93) as

$$\phi_{ac} = B_{av} \frac{\lambda L_a}{\wedge} \qquad (3.93)$$

Therefore from table 4.1 we have

$$\phi_{ac} = 0.67 \times 10^{-3} . B_{av}$$

The fundamental fluxes are summarised in table 4.3

TABLE 4.3

FUNDAMENTAL FLUX/POLE, ϕ_{ac}, mWb.

Excitation AT/Pole	Slip Speed, rev/min					
	50	100	200	400	1000	1470
260	0.382	0.363	0.345	0.322	0.212	0.14
520	0.67	0.61	0.541	0.52	0.35	0.275
780	0.825	0.75	0.725	0.64	0.465	0.37

*The validity of taking ordinates for the Fourier analysis from the constructed flux-density pattern is discussed in detail in section 8.2.5.

TABLE 4.2
HARMONIC ANALYSIS OF FLUX-DENSITY WAVES.

	FLUX - DENSITY, TESLAS.									
SLIP SPEED. REV/MIN.	EXCITATION CURRENT A.	FUNDAMENTAL	CORRECTION ANGLES (RAD)	THIRD HARMONIC.	FIFTH HARMONIC.	SEVENTH HARMONIC.	NINTH HARMONIC.	ELEVENTH HARMONIC.	THIRTEENTH HARMONIC.	FIFTEENTH HARMONIC.
STANDSTILL.	·6	1·398	·000038	·090	·220	·228	·085	·066	·126	·080
"	·4	1·16	·000757	·083	·180	·199	·079	·056	·111	·070
"	·2	·64	·00132	·0478	·100	·109	·043	·029	·061	·040
50	·6	1·23	·087	·168	·216	·233	·099	·072	·128	·085
"	·4	·996	·076	·135	·179	·192	·078	·058	·104	·068
"	·2	·569	·071	·074	·102	·109	·042	·032	·059	·038
100	·6	1·118	·384	·448	·330	·283	·176	·141	·138	·123
"	·4	·91	·144	·165	·174	·185	·084	·064	·100	·069
"	·2	·54	·161	·095	·102	·106	·054	·040	·060	·042
200	·6	1·08	·159	·214	·219	·231	·114	·084	·128	·089
"	·4	·809	·386	·337	·248	·215	·135	·104	·117	·089
"	·2	·5159	·239	·127	·118	·117	·067	·052	·067	·051
400	·6	·956	·314	·306	·257	·249	·159	·124	·142	·112
"	·4	·779	·277	·220	·169	·190	·117	·092	·107	·080
"	·2	·483	·434	·227	·159	·141	·095	·076	·078	·061
1000	·6	·694	·420	·315	·260	·246	·170	·135	·139	·110
"	·4	·521	·468	·254	·207	·201	·149	·119	·118	·095
"	·2	·316	·419	·193	·110	·136	·140	·063	·086	·106
1470	·6	·553	·525	·300	·232	·199	·139	·110	·106	·085
"	·4	·410	·558	·235	·194	·166	·122	·089	·091	·076
"	·2	·212	·519	·147	·122	·104	·132	·085	·099	·094

4.5.2 Armature reaction phase angle.

The phase angle of armature reaction, which is assumed to be 90° (see fig 3.13), was obtained by Davies' method[6,8] using the computed "correction angles". The measured phase angles are summarised in table 4.4.

TABLE 4.4

ARMATURE REACTION PHASE ANGLE, ELECTRICAL DEGREES.

Excitation AT/pole	Slip Speed, rev/min 50	100	200	400	1000	1470
260	126	121	115	101	110	110
520	130	126	113	114	113	111
780	124	103	120	101	115	110

The theory predicts that the phase angle should tend from 135° to 90° as slip speed increases. The measured angles are close to 135° at low slip (50 rev/min) but are nearer to 90° at higher slips, so the general trend, suggested in chapter 3, is obeyed. However the variation of the measured phase angle is uneven due, almost certainly, to error in the method of measurement.[8]

The measured angles are, however, sufficiently close to theory to allow the use of 90°. Even if the phase angle is at its maximum possible value of 135°, only a very small error will result in assuming it to be 90° (see section 3.7 and appendix 1).

4.5.3 Estimation of fundamental armature reaction m.m.f., F_{AR}.

Davies' method of estimating the armature reaction m.m.f. assumes that harmonics higher than the third are negligible. However, as shown in table 4.2, in the copper-faced coupling, the fifth and seventh harmonics are of the same order of magnitude as the third and, hence, large errors can be expected in the measurement of F_{AR}, which is very approximate, even where the higher harmonics are very small.[8,14]

It is not, therefore, possible to test the armature reaction equation, (3.94), fairly, from the measured values of F_{AR}.

However, if the normalised torque and flux relationships, (3.111) and (3.112), and the excitation equation, (3.101), can be shown to be valid, then it follows that the armature reaction equation is correct, since that relationship is implicit in each of the others.

For these reasons, armature reaction m.m.f. is not considered explicitly again in this chapter. However, the curves of measured armature reaction are available for inspection in references 51 and 52.

4.6 Variation of torque with excitation m.m.f. (field current).

The relationship between torque and excitation is given by (3.103). Now, neglecting saturation effects, the harmonic content of the excitation m.m.f. wave will be the same as the standstill flux-density pattern. Since the harmonic content of the standstill flux-density pattern is small, we have, approximately, $T \propto I_f^2$, for constant slip speed.

Figure 4.7 shows a log-log plot of torque against excitation current for the slip speed range 100-1000 rev/min. The

measured current indices are very close to 2, the worst error occurring at 100 rev/min where the index is 1.86. The torque-current curves deviate from a straight line at the higher excitations due to saturation effects. However, at 1000 rev/min, where the flux levels are lower, the curve is linear over the whole excitation range.

4.7 Variation of torque with fundamental flux.

Neglecting harmonics,

$$T \propto \Phi_{ac}^2 (n + C_2 n^{1/2})$$

Since C_2 is normally less than unity, we have, for high slips,

$$T \propto \Phi_{ac}^2 n$$

As shown in fig 4.8, this relationship holds true over a surprisingly wide speed range.

4.8 Peak torque conditions.

The equation for maximum fundamental torque is (3.107). Using (3.107), together with*

$$S = \frac{2(g+d)}{\mu_0 \lambda L_a \cdot \frac{4}{\pi} \sin(\frac{k\pi}{2})} \qquad (4.1)$$

and $F_{Ag} = \frac{4}{\pi} N I_f \sin(\frac{k\pi}{2})$, which neglects saturation, (4.2)

we obtain $T_m = 0.975 . I^2$ (4.3)

The measured and calculated values of T_m are summarised in table 4.5.

Up to 520 AT/pole excitation, the correlation is excellent. For higher excitations the theory predicts peak torques too high, the error increasing with excitation. The reason for this

---

* $k = \frac{\text{pole arc}}{\text{pole pitch}}$.

TABLE 4.5

MEASURED AND CALCULATED PEAK TORQUES AT VARIOUS EXCITATIONS.

Excitation AT/Pole	Field Current (A)	T_m (Calc) (Nm)	T_m (Exp) (Nm)
260	0.2	3.9	4
390	0.3	8.8	9
520	0.4	15.4	15
650	0.5	24.4	21.7
780	0.6	35	28.2
910	0.7	47.8	35.2
1040	0.8	62.5	41.2

error is that, as shown in fig 4.9, the magnetic circuit of the coupling begins to saturate at about 400 AT/pole. The reluctance, given by (4.1), will thus be too low,because an increasing proportion of the excitation m.m.f. is used up in driving flux through saturated iron.

Using (3.105) and assuming a drum temperature of 70°C (see section 4.3) we obtain

$$n_m = 9 \text{ rev/s} = 540 \text{ rev/min.}$$

The measured values of n_m (see fig 4.3) vary from approximately 500 rev/min (at 260,390 and 520 AT/pole), which is excellent correlation, to 780 rev/min (at 1040 AT/pole). Once again this is due to saturation: in section 3.8 it is shown that n_m is proportional to reluctance; so, as the reluctance increases with saturation, n_m will increase also.

By taking the ratio of n_m at an excitation in the saturated region to the "unsaturated n_m" we can obtain the ratio of airgap reluctance to saturated reluctance. Then, if the

calculated values of T_m given in table 4.4 are multiplied by this ratio, they should correspond closely to the measured data. The T_m values obtained are as follows:

780 AT/pole: T_m = 27.4 Nm (compare 28.2 Nm measured)

910 AT/pole: T_m = 32.4 Nm (compare 35.2 Nm measured)

1040 AT/pole: T_m = 40.2 Nm (compare 41.2 Nm measured).

The correlation is now quite precise, indicating that the source of error is indeed the reluctance calculation.

4.9 Harmonic torque contribution

"Harmonic torque" is taken to imply the torque contribution of the excitation m.m.f. harmonics, not the resultant flux-density harmonics as is usual.[6,14]

From (3.103) it is difficult to make any general deductions regarding harmonic torque. However at slip speeds less than n_m it is good approximation to write

$$\frac{T_h}{T_1} = h^2\left[\frac{F_h}{F_1}\cdot\frac{S_1}{S_h}\cdot\frac{C_{1h}}{C_1}\right]^2 = \frac{F_h^2}{F_1^2}\,\frac{1+(\lambda/2L)^2}{1+(\lambda/2L_h)^2}$$

i.e, for the experimental machine,

$$\frac{T_h}{T_1} = \frac{F_h^2}{F_1^2}\,\frac{1\cdot4}{1+0\cdot4/h^2}$$

If we assume that $F_h = .15.F_1$ for the 3rd, 5th and 7th harmonics, which is untypically high, then the torque contribution of these harmonics is approximately 6.5%

Thus, as indicated by the correlation between measured T_m and calculated fundamental T_m, in the previous section, it is reasonable to neglect harmonic torque for slip speeds up to and including n_m. At higher slips, where the torque is reducing, the harmonic torque will increase but should still be

only a small proportion of the fundamental torque.

In design studies it will therefore be permissible to neglect the torque due to the excitation harmonics, provided the $\frac{\text{pole arc}}{\text{pole pitch}}$ ratio is within practical limits.

4.10 Calculation of torque-slip curves.

The torque-slip curves were calculated using (3.102), with the calculated airgap reluctance, from (4.1), and assuming a relative backing-iron permeability of 2000 to estimate C_2.

Calculated points for excitations of 260, 520 and 780 AT/pole are compared with the measured curves in fig 4.10. The correlation is excellent at the two lower excitations but there is a considerable error between the calculated and measured torque-slip curves at 780 AT/pole. This is due to the influence of saturation on the airgap reluctance, 'S', discussed in section 4.8. If a higher empirical value of reluctance is used in (3.102), a much closer fit to the experimental curve can be obtained. However, the purely theoretical points are shown in fig 4.10, to indicate the sort of accuracy to be obtained from the theory in a design excercise and the importance of obtaining a reliable estimate of S.

4.11 Normalised curves.

The value of G for the experimental machine is 0.17. The normalised flux and torque curves calculated using this value are compared with the experimental normalised curves in fig 4.11.

The correlation is almost exact, indicating the correctness of the theory. Note that the error associated with the reluctance does not affect the normalised curves.

4.12 Conclusions.

This part of the thesis has presented a theory of the copper-faced coupling, together with adequate experimental evidence to demonstrate the correctness of the theory.

The most important features of the work are:

(a) the first three-dimensional analysis of a double region loss drum,

(b) a general method of calculating armature reaction m.m.f,

(c) the family of normalised torque-slip curves characterised by the parameter 'G'.

The objectives of the study were to enable the design of copper-faced couplings and to gain understanding of the way in which performance varies with machine parameters. It is considered that these objectives have been achieved.

CHAPTER 5.

THE TRANSIENT PERFORMANCE OF EDDY-CURRENT COUPLINGS.

5. The transient performance of eddy-current couplings.

5.1 Introduction.

The application of eddy-current couplings in control systems is growing rapidly and it is becoming increasingly important to view the coupling in a new perspective i.e. as a control element. The most important area of investigation is the transient performance of the machine, upon which there is no published literature.

Information is required which will not only allow the analysis of the transient performance of couplings, but which will also provide guidance in the synthesis of high response machines. At the present time, in industry, transient performance is predicted by ad hoc methods based on previous test results. Design for transient performance progresses on a trial and error basis, apart from the obvious procedure of reducing winding time constants and output inertias. The influence of basic design parameters such as diameter, length, number of poles, type of field member, pole arc/pole pitch, drum material etc. is not understood.

An investigation of a fundamental nature, examining the transient processes within the machine is thus required.

5.2 The eddy-current coupling as a control element.

The coupling is a three terminal control element (fig 5.1) belonging to a class of system components including friction clutches, magnetic particle couplings, pilot-operated

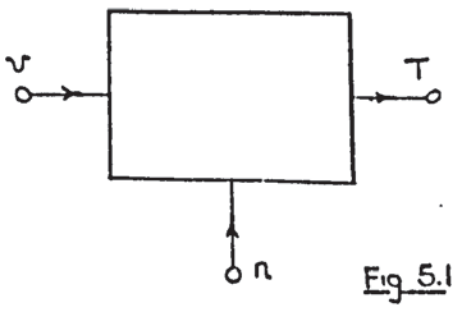

Fig 5.1

hydraulic couplings etc.

The response of torque and slip speed to a voltage control signal depends on the system of which the coupling is a part. To assess the dynamic performance of the machine, the general control situation is reduced to two variables by holding one quantity constant. The three conditions usually considered are:

(a) slip speed response to a torque disturbance at constant field voltage,

(b) torque response to a voltage signal at constant slip speed, and, occasionally,

(c) slip speed response to a voltage signal at constant load torque.

In each case the problem is to identify the relationship between reference and control variable.

5.2.1 Slip speed response to a torque disturbance at constant voltage.

The information obtained from this test is useful in closed loop system design since, for given control equipment, it enables an estimate of system recovery time. The transient speed-torque relationship depends on the load that the coupling is driving. Hence in any analysis it is important to include the load parameters.

In the authors experience, analytical methods are limited to predicting the approximate form of response, rather than absolute response, due to non-linearities in the drive system.

When the slip is small ($n < n_m$), useful approximations to the form of response can sometimes be obtained if the machine is represented by a single mechanical network as shown in

fig 5.2a.

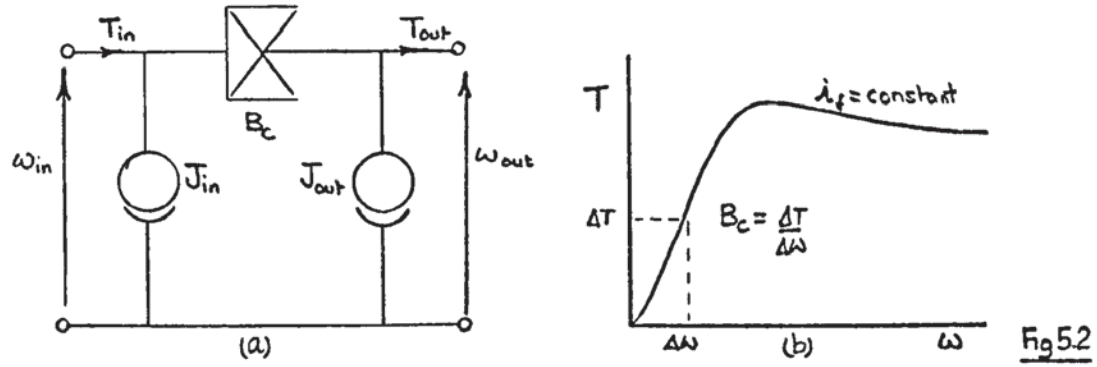

Fig 5.2

The damping coefficient B_c is the ratio of torque to slip speed taken from the steady-state torque-slip curve (fig 5.2b).

This model neglects the transient reduction in coupling field current following a sudden speed change.

5.2.2 Slip speed response at constant torque.

This condition may also be analysed approximately because of non-linearity. Usually the steady-state torque-slip curve is assumed to apply. During the transient period the machine progresses through a series of steady-state conditions, corresponding to the instantaneous values of field current. The voltage-to-current transfer function is usually assumed to be single order and the time constant is determined experimentally.

Whilst it is true that approximately correct results can be obtained for many applications, this method gives unduly optimistic predictions of acceleration time in fast response systems with low output inertias.

5.2.3 Torque response at constant slip speed.

This is the most important of the three transient conditions. It is a situation which occurs often in practice, particularly in conveyor and multi-machine applications. It is also

unnecessary complication.

The assumption of a transfer function of the form of (5.1) or (5.2) is dubious for the following reasons. The torque of an electrical machine depends on the product of two airgap fields, usually stator and rotor m.m.f.s. In a multiply excited machine one field may be independent of the other (e.g. separately excited d.c. machine) and the torque can be considered to be proportional to only one airgap field. The voltage-torque relationship can then be written as a simple transfer function, i.e. as (5.1) or (5.2), where the independent field is included in the amplification constant K. The coupling, however, is a singly excited machine where both rotor and drum m.m.f.s are functions of field voltage. $\bar{T}$ and $\bar{v}$ will hence be related by a convolution integral and not by a simple transfer function.

Even though the coupling is clearly not a single order linear system, torque response is usually specified in terms of the "torque time constant", i.e. the time to reach 63% of steady-state torque, following a step of rated field voltage. The torque time constant of a commercial coupling ranges from 0.20 s for a fractional kilowatt machine to approximately 10 s for a large dynamometer.

5.3 Objectives of the work on transient performance.

The remainder of this thesis is devoted to the investigation of transient response at constant slip speed (the term "transient response" will be taken to imply constant slip).

The objectives of the work are:

(a) to obtain an understanding of the factors that govern transient response,

(b) to determine the variation of the machine time constants with basic design parameters and slip speed,

(c) to develop a practical method of predicting transient response from design data,

(d) to develop simple guidelines for the design of high response machines.

5.4 Analytical approach.

5.4.1 Lumped and distributed parameter methods.

The transient analysis of electrical machines is normally based on the assumption of constant lumped parameters. In the eddy-current coupling, however, where the 'armature' is not an arrangement of discrete conductors, but a continuous structure, this assumption can hardly be justified. The need for a more fundamental approach in the transient analysis of electrical machines was expressed by Say[39] in a recent discussion on the transient performance of induction motors. His comments are quite applicable to couplings:

> "Linearised circuit parameters and sinusoidal distributions, however justified for the steady-state, fail when the conditions are those of transience. What, for example, is the transient current-density in the rotor conductors and how does this influence the torque? What is the process of shock exciting a magnetic flux following a switching operation, con-

sidering the complex local B-H relationships and the eddy-current reactions? Constant reactance, inductance and mutual inductance seem inadequate".

It was hence concluded that the traditional lumped parameter approach is not applicable to the transient analysis of the coupling. However this is not to say that the results of a more fundamental theoretical method cannot be interpreted in terms of conventional concepts, only that conventional concepts do not themselves lead to the correct results. For example it is a simple matter to develop the steady state equivalent circuit of the coupling, shown in fig 5.4, from Davies' work.[6,8] However the equations, from which it is deduced, have first to be derived from a field theory (i.e. a distributed parameter) approach.

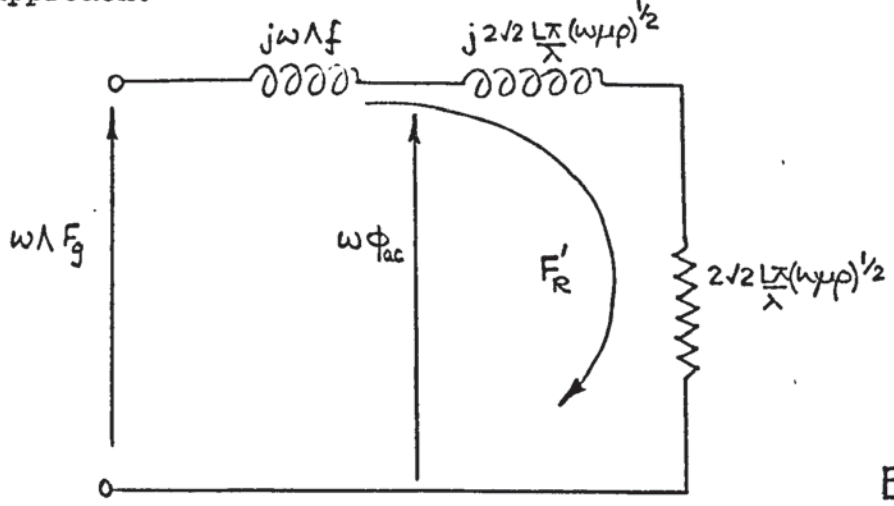

Fig 5.4

There is a dearth of published work dealing with the transient performance of machines from a distributed parameter standpoint, the most notable exception being the papers of Concordia and Poritsky[37] and Concordia[38] on solid rotor synchronous machines. In the field of thermodynamics, however, Carslaw and Jaeger[41] have broached certain analogous problems which could well be applied to electrical machines: their study

of the transient temperature distribution in a massive heat conducting slab is a perfect analogy of the flux-forced solid rotor induction motor. Much of the work carried out in transient thermodynamics, especially that based on variational principles, could be used effectively to deal with transient effects in solid iron. The main difference in the two fields is eddy-current armature reaction, which is not paralleled in heat conduction.

The authors approach to the problem of the transient response of the coupling was to treat the machine as a distributed parameter system.

5.4.2 Factors affecting torque response.

In general $T \propto \Phi_{ac}^{r}$, where $3 > r > 2$. The index is 3 for fully saturated iron and 2 where the B-H curve of the drum is linear.[12] Torque response therefore depends on flux response and the state of saturation of the drum iron. These are not independent factors.

From engineering experience it is easy to produce a list of factors which may influence transient flux response:

(a) slip speed at which transient occurs,

(b) natural time constant of field winding (L/R),

(c) eddy-current damping on the field member (if solid),

(d) transient distribution of eddy-currents in the drum,

(e) leakage flux,

(f) harmonic content of airgap flux,

(g) end effects,

(h) saturation,

(i) hysteresis,

(j) extraneous factors such as eddy-current induction in endbells, main frame and shaft, flexion of parts under impact, transient heating effects, commutation etc.

Considered as a problem of formal mathmatics, a theoretical account of all these effects is impossible. The only practicable method is to carry out a rigorous linear analysis, the results of which are then modified to approximate the effects of non-linearity (as with the steady state theory[8]).

Consequently the initial linear theory includes factors (a) to (f) and then the results are modified to take account of saturation. Transient end effects and hysteresis are beyond the scope of this work. Extraneous factors, as defined above, are neglected in the theory and eliminated as far as possible in the experimental machine.

5.5 Presentation of the work on transient response.

The work on transient performance will be presented in the following order:

Chapter 6: Theory of transient response.

Chapter 7: The experimental machine.

Chapter 8: Experiments with the salient-pole rotor.

Chapter 9: Experiments with the partially-interdigitated rotor.

This is not however the chronological order of the work. Before the theory was developed, early exploratory experiments were carried out. The machine was fitted with a solid partially-

interdigitated rotor, since this is the standard rotor fitted to commercial couplings of up to 100 kW. These experiments indicated considerable eddy-current damping lags in the response of airgap flux. It was thus decided to build a laminated rotor and model laminated drum, in order to allocate the total damping effect between solid rotor and drum. At the same time the opportunity was taken to use a salient-pole design for the rotor with a new type of winding, so that, for the first time, a reliable comparison between the steady-state performance of salient-pole and partially-interdigitated machines could be made.

The tests on the laminated rotor machine suggested a simplification to the general F_Φ - F_R transfer function (see section 6.11) which enabled the derivation of the machine time constants and the flux and current differential equations.

With the theory established, a series of tests on the experimental machine were carried out for both rotors. These tests constitute chapters 8 and 9.

CHAPTER 6.

THEORY OF TRANSIENT RESPONSE.

6. Theory of transient response.

6.1 Introduction.

The theory is basically a solution of the diffusion equation under general conditions of forcing, but at constant frequency. Apart from the usual analytical difficulties of coupling theory, discussed in chapter 1, there is an additional problem to be overcome in the transient analysis, a brief discussion of which will clarify the approach.

The object of the study is to relate the transient airgap flux, and hence the torque, to the voltage signal applied to the field winding. The differential equation relating field voltage and flux should, therefore, be formulated in rotor co-ordinates. However the transient airgap flux is modified by the transient eddy-currents in the drum. To analyse the transient eddy-currents, we use Maxwell's equations, embodied in the diffusion equation, which are defined for co-ordinates rigidly fixed in the conducting medium[20,42] (drum co-ordinates). In general Maxwell's equations are not invarient to the Galilean transformation, used for quasi-static field solutions, and it is necessary to solve the diffusion equation in drum co-ordinates. Then, after solution, the resulting airgap field equations are transferred into rotor co-ordinates.

6.2 Assumptions.

The assumptions on which the following theory is based are:

(a) Current-density is everywhere axial.

(b) Current-density is sinusoidally distributed in time and space at the surface of the drum.

(c) Curvature effects are negligible and cartesian co-ordinates may be used.

(d) The drum is composed of semi-infinite homogeneous iron.

(e) Permeability is constant (for the moment).

(f) End effects are negligible.

(g) Slip speed is constant during the transient period.

(h) Initial conditions are zero (for the moment).

Assumptions, (a) to (f) are the 'classical' assumptions of coupling theory, discussed critically in chapter 1. Assumption (g) is necessary for tractability and (h) is introduced to simplify the solution. Initial conditions and variable permeability can be conveniently introduced later.

6.3 Current-density weighting function.

The eddy-current density in the drum is governed by the diffusion equation*:

$$\nabla^2 \underline{J} = \frac{\mu}{\rho} \frac{\partial \underline{J}}{\partial t}$$

In terms of the co-ordinates defined in fig 6.1, $J = J_z$ and

$$\frac{\partial^2 J}{\partial x^2} + \frac{\partial^2 J}{\partial y^2} = \frac{\mu}{\rho} \frac{\partial J}{\partial t} \qquad (6.1)$$

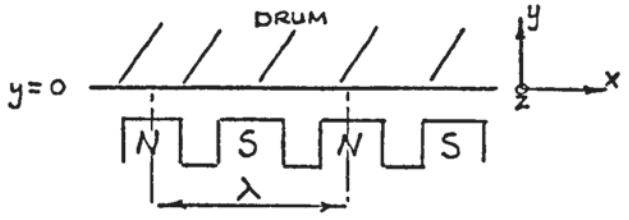

FIG 6.1

*To avoid confusion with transform notation, in this part of the thesis, "$\underline{A}$" denotes the vector "A", whilst "$\bar{A}$" denotes the Laplace transform of "A".

Under steady-state conditions a solution of (6.1) can be obtained by the method of separable variables. Under conditions of general forcing this is not possible. In co-ordinates fixed rigidly on the drum, J is defined as

$$J = Re.\ \sigma(y,t)\, e^{j(\omega t - \frac{2\pi x}{\lambda})} \qquad (6.2)$$

Removing the 'Re' for the moment and substituting (6.2) into (6.1) gives

$$\left[\left(\frac{2\pi}{\lambda}\right)^2 \sigma(y,t) + \frac{\partial^2 \sigma(y,t)}{\partial y^2}\right] e^{j(\omega t - \frac{2\pi x}{\lambda})} = \left[j\omega\frac{\mu}{\rho}\sigma(y,t) + \frac{\mu}{\rho}\frac{\partial \sigma(y,t)}{\partial t}\right] e^{j(\omega t - \frac{2\pi x}{\lambda})}$$

Cancelling the exponential and taking Laplace transforms with respect to 't', we obtain

$$-\left(\frac{2\pi}{\lambda}\right)^2 \bar{\sigma}(y,s) + \frac{d^2}{dy^2}\bar{\sigma}(y,s) = j\omega\frac{\mu}{\rho}\bar{\sigma}(y,s) + \frac{\mu s}{\rho}\bar{\sigma}(y,s) - \frac{\mu}{\rho}\sigma(y,0)$$

Discarding the initial condition and solving the resulting ordinary differential equation yields

$$\bar{\sigma}(y,s) = \bar{\sigma}(0,s)\, e^{-y\left[\left(\frac{2\pi}{\lambda}\right)^2 + j\omega\frac{\mu}{\rho} + s\frac{\mu}{\rho}\right]^{1/2}}$$

$\sigma(0,t)$ is the surface amplitude of current-density and $\bar{\sigma}(0,s)$ the transform of this. The inversion of this equation when $\sigma(0,t) = \delta(t)$ i.e. $\bar{\sigma}(0,s) = 1$, is the weighting function, $^{*}W^{\sigma(y,t)}_{\sigma(0,t)}$, relating $\sigma(y,t)$ to the surface boundary condition $\sigma(0,t)$:

$$W^{\sigma(y,t)}_{\sigma(0,t)} = e^{-\left[\left(\frac{2\pi}{\lambda}\right)^2\frac{\rho}{\mu} + j\omega\right]t} \cdot \frac{y}{2}\left(\frac{\mu}{\rho}\right)^{1/2}\frac{e^{-\frac{y^2\mu}{4\rho t}}}{\sqrt{\pi t^3}}$$

Thus the current-density response to an impulse of surface current-density amplitude, and the weighting function relating

---

*The notation of the weighting function is

$$\epsilon(t) = \int_0^t W^{\epsilon}_{\phi}(\tau).\,\phi(t-\tau).\,d\tau$$ where W^{ϵ}_{ϕ} is the weighting function relating $\epsilon(t)$ and $\phi(t)$.

$\sigma(0,t)$ and $J(x,y,t)$, is

$$W^{J}_{\sigma(0,t)} = e^{-(2\pi/\lambda)^2 \rho_\mu t}\, e^{-j\frac{2\pi}{\lambda}x}\, \frac{y}{2}\left(\frac{\mu}{\rho}\right)^{1/2} \frac{e^{-y^2/4\rho t}}{\sqrt{\pi t^3}} \qquad (6.3)$$

6.4 Armature reaction weighting function.

The equivalent drum current sheet is

$$I = \int_0^\infty J.dy$$

Hence $$W^{I}_{\sigma(0,t)} = \int_0^\infty W^{J}_{\sigma(0,t)}.dy$$

The armature reaction m.m.f. is given by

$$F_R = \int I.dx$$

and so $$W^{F_R}_{\sigma(0,t)} = \int\left(\int_0^\infty W^{J}_{\sigma(0,t)}.dy\right).dx$$

Substituting for $W^{J}_{\sigma(0,t)}$ from (6.3) gives

$$W^{F_R}_{\sigma(0,t)} = \frac{\lambda}{2\pi}\left(\frac{\rho}{\mu}\right)^{1/2} \frac{e^{-(2\pi/\lambda)^2 \rho_\mu t}}{\sqrt{\pi t}}\, e^{j(\pi/2 - \frac{2\pi}{\lambda}x)} \qquad (6.4)$$

which is the weighting function relating surface current-density and armature reaction m.m.f.

6.5 Airgap flux-density weighting function.

Since the airgap in a coupling is small (less than 1 mm), the radial flux-density may be written as

$$B = b(t)\, e^{j(\omega t - \frac{2\pi}{\lambda}x)} \qquad (6.5)$$

Since curl $\underline{E} = -\frac{\partial \underline{B}}{\partial t}$ and $\underline{E} = \rho \underline{J}$,

$$-j\frac{2\pi}{\lambda}\rho \cdot \sigma(0,t) = \frac{\partial b}{\partial t} + j\omega b$$

Taking Laplace transforms and discarding the initial condition, $b(0)$, gives

$$-j2\pi\rho\, \bar{\sigma}(0,s) = (s + j\omega)\bar{b}$$

For $\sigma(0,t) = \delta(t)$, $\bar{\sigma}(0,s) = 1$,

$$\bar{b} = -j\frac{2\pi\rho/\lambda}{s+j\omega}$$

Hence, inverting this,

$$W^{b}_{\sigma(0,t)} = -j\,2\pi\rho/\lambda\, e^{-j\omega t}$$

whence $$W^{B}_{\sigma(0,t)} = -2\pi\rho/\lambda\, e^{j(\pi/2 - \frac{2\pi x}{\lambda})} \qquad (6.6)$$

(Note the weighting function $W^{B}_{\sigma(0,t)}$ is not time dependent. This is logical, since a step of B would be associated with an impulse of surface density).

6.6 Transformation to rotor co-ordinates.

The weighting functions (6.4) and (6.6) are now transformed into rotor co-ordinates by the Galilean transformation:

$$x^{d} = x^{r} + \frac{\omega\lambda}{2\pi}t\,, \quad y^{d} = y^{r}\,, \quad t^{d} = t^{r}$$

where the 'd' and 'r' superscripts refer to drum and rotor respectively.

It is unnecessary to work in mixed co-ordinates and the superscripts are omitted in the transformed equations:

$$W^{F_z}_{\sigma(0,t)} = \frac{\lambda}{2\pi}\left(\frac{\rho}{\mu}\right)^{1/2}\frac{e^{-(\frac{\pi}{\lambda})^2\frac{\rho}{\mu}t}}{\sqrt{\pi t}}\, e^{j(\frac{\pi}{2} - \frac{2\pi x}{\lambda} - \omega t)} \qquad (6.7)$$

and $$W^{B}_{\sigma(0,t)} = -\frac{2\pi\rho}{\lambda}\, e^{j(\pi/2 - \frac{2\pi x}{\lambda} - \omega t)} \qquad (6.8)$$

For the remainder of the thesis, unless otherwise specified, all quantities are written in rotor co-ordinates.

6.7 Airgap m.m.f. - armature reaction m.m.f. transfer function.

The transfer functions relating F_R to $\sigma(0,t)$ and B to $\sigma(0,t)$ are given by

$$\frac{\bar{F}_R}{\bar{\sigma}(0,s)} = \mathcal{L}\{Re.W^{F_R}_{\sigma(0,t)}\} = Re.\mathcal{L}\{W^{F_R}_{\sigma(0,t)}\}^*$$

and

$$\frac{\bar{B}}{\bar{\sigma}(0,s)} = \mathcal{L}\{Re.W^{B}_{\sigma(0,t)}\} = Re.\mathcal{L}\{W^{B}_{\sigma(0,t)}\}^*$$

Hence, from (6.7),

$$\frac{\bar{F}_R}{\bar{\sigma}(0,s)} = \frac{\lambda}{2\pi}\left(\frac{\rho}{\mu}\right)^{1/2}\frac{1}{(a^2+\omega^2)\sqrt{2}}\left\{\left[(a^2+\omega^2)^{1/2}-a\right]\cos\frac{2\pi x}{\lambda}+\left[(a^2+\omega^2)^{1/2}+a\right]\sin\frac{2\pi x}{\lambda}\right\},$$

where $a = s+(2\pi/\lambda)^2\rho/\mu$.

In practice $\omega \gg (2\pi/\lambda)^2\rho/\mu$, (rated value of ω is 60 rad/s and $(2\pi/\lambda)^2\rho/\mu$ is about 0.5), so the above equation can be simplified with little error to

$$\frac{\bar{F}_R}{\bar{\sigma}(0,s)} = \frac{\lambda}{2\pi}\left(\frac{\rho}{\mu}\right)^{1/2}\frac{\sin(2\pi x/\lambda+\theta)}{(s^2+\omega^2)^{1/4}} \qquad (6.9)$$

where $\theta = \tan^{-1}\left\{\frac{(s^2+\omega^2)^{1/2}-s}{(s^2+\omega^2)^{1/2}+s}\right\}^{1/2}$

This approximation is the same as that made by Davies[8,12] in his steady-state theory of the coupling (see chapter 1, equation (1.15)).

From (6.8),

$$\frac{\bar{B}}{\bar{\sigma}(0,s)} = -\frac{2\pi\rho}{\lambda}\frac{\sin(\frac{2\pi x}{\lambda}+\tan^{-1}\frac{\omega}{s})}{(s^2+\omega^2)^{1/2}} \qquad (6.10)$$

The F_R-B transfer function is generated by dividing (6.10) and (6.9). This is permissible since $W^{F_R}_{\sigma(0,t)}$ is independent of $W^{B}_{\sigma(0,t)}$

i.e. $$\frac{\bar{F}}{\bar{B}} = -\left(\frac{\lambda}{2\pi}\right)^2\frac{1}{(\mu\rho)^{1/2}}\frac{(s^2+\omega^2)^{1/4}.\sin(\frac{2\pi x}{\lambda}+\theta)}{\sin(\frac{2\pi x}{\lambda}+\tan^{-1}\omega/s)} \qquad (6.11)$$

---

*This is valid because of the commutative property of the Laplace transform with real and imaginary transformations.[47]

In general B(t) will be of the form

$$B(t) = b(t) \cos 2\pi x/\lambda$$

and hence the general form of $\bar{F}_R$ is

$$\bar{F}_R = -\bar{b}\left(\frac{\lambda}{2\pi}\right)^2 \frac{1}{(\mu\rho)^{1/2}} (s^2+\omega^2)^{1/4} \left[\frac{\cos(2\pi x/\lambda) \cdot \sin(2\pi x/\lambda + \theta)}{\sin(2\pi x/\lambda + \tan^{-1}\frac{\omega}{s})} \right] \qquad (6.12)$$

The trigonometrical term in the square brackets governs the transient phase relationship between F_R and B: at time $s=\infty$ (when the amplitude of F_R is theoretically infinite) B and F_R are in exact antiphase; at time $s=0$ (steady-state), F_R lags B by 135°*. This term does not modify the relationship between the amplitudes of F_R and B which is

$$\frac{\hat{\bar{F}}_R}{\hat{\bar{B}}} = \left(\frac{\lambda}{2\pi}\right)^2 \frac{1}{(\mu\rho)^{1/2}} (s^2+\omega^2)^{1/4} \qquad (6.13)$$

Flux density and resultant airgap m.m.f., F_ϕ , are related by $B = \mu_0/g \, F_\phi$

so $$\frac{\hat{\bar{F}}_R}{\hat{\bar{F}}_\phi} = \left(\frac{\lambda}{2\pi}\right)^2 \frac{\mu_0}{g} \frac{1}{(\mu\rho)^{1/2}} (s^2+\omega^2)^{1/4}$$

To relate the excitation, reaction and resultant m.m.f.s (i.e. F_g, F_R and F_ϕ) the phase lag between F_R and F must be known at every instant in time. But, even for the simplest of flux-density variations, it is not possible to invert (6.12) analytically and the transient phase is generally incalcuable.

However it is known that the phase angle reduces from 180° to 135° during the transient period. Therefore the worst error in F_g, incurred by assuming F_R and F_ϕ to be in antiphase during

---

*If b(t) is specified as a step function, the steady-state F_R-B relationship, produced by applying the final value theorem to (6.12), is the same as that given by Davies.[8] This is a valuable check on the theory.

the transient period, will be 7.6% (see appendix 1 and the discussion of chapter 8). In practice the error will be much less because, as experimental evidence indicates (see reference 14 and chapter 8 of this thesis), the phase angle is more than 135° - typically about 150° (see table 8.5). So, to render the problem tractable, it is assumed that F_R and F_ϕ are in antiphase during the transient period.

Thus

$$\frac{\bar{F}_R}{\bar{F}_\phi} = -\left(\frac{\Delta}{2\pi}\right)^2 \frac{\mu_0}{g} \frac{1}{(\mu\rho)^{1/2}} (s^2+\omega^2)^{1/4} = -A(s,\omega) \qquad (6.14)$$

This transfer function is the key relationship in the transient theory: it characterises the action of the drum during the transient period. As far as the author is aware, it is original and may be of use in the solution of kindred problems.

6.8 Block diagram of the airgap m.m.f.s.

The resultant m.m.f., F_ϕ , is the sum of the excitation m.m.f., F_g , and the armature reaction m.m.f., F_R:

$$\underline{F}_\phi = \underline{F}_g + \underline{F}_R \qquad (6.15)$$

Therefore, from (6.14),

$$\frac{\bar{F}_\phi}{\bar{F}_g} = \frac{1}{1+A} \qquad (6.16)$$

The relationships between the m.m.f.s can be represented conveniently in block diagram form (fig 6.2).

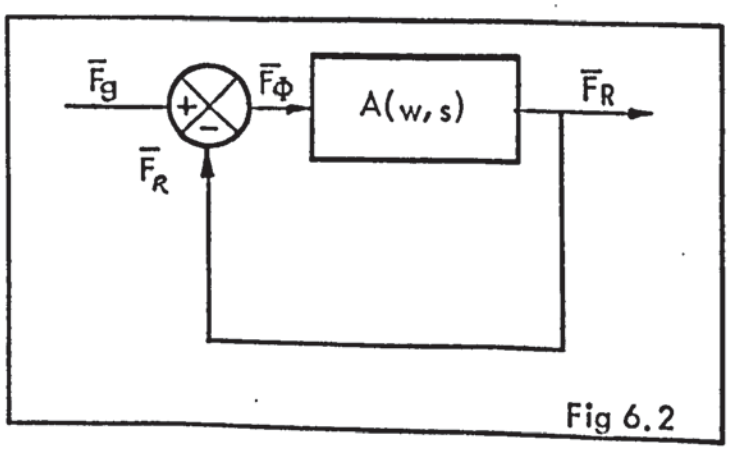

Fig 6.2

This block diagram will be later interconnected to the rotor block diagram to form the complete 's' domain model of the coupling.

6.9 Rotor block diagram.

The inclusion of rotor damping at this stage poses no problem but, for the purposes of deriving the differential equation of the coupling, it is an unnecessary complication. For the moment, then, rotor damping will be neglected.

The mesh voltage equation for the field winding is

$$v = iR + \frac{d}{dt}\psi_f,$$

where ψ_f is the total flux linkages of the field. ψ_f can be separated into leakage and mutual flux linkage as

$$\psi_f = L_l i + \psi_g ,$$

where L_l is the leakage inductance of the field. ψ_g is the mutual flux linkage between field and drum, given by

$$\psi_g = 2pN\,(\text{flux per pole}),$$

where N is a winding turns factor which depends on the type of rotor winding (e.g. $N = \frac{\text{turns}}{2}$, for the standard cylindrical winding[48] and for a serpentine winding; but N = turns, for a salient-pole machine with individually wound poles). N may be quantitatively defined as the numerical value of the m.m.f. per pole when 1 A flows in the field winding. Davies[6,12] has shown that $(\frac{\text{flux per pole}}{\Phi_{ac}})$ is approximately constant for a given machine. For well designed couplings, the ratio will be in the range 0.95 (Lundell or salient pole) to 1.2 (inductor).* Denoting the ratio as r_ϕ, we have

$$\psi_g = 2pN\Phi_{ac}r_\phi , \qquad (6.17)$$

---

*The validity of this under transient conditions is investigated in chapter 8.

and, hence,

$$v = i.R + L_l \frac{di}{dt} + 2pN r_\phi \frac{d\phi_{ac}}{dt} \qquad (6.18)$$

Taking Laplace transforms and discarding initial conditions, (6.18) becomes

$$\bar{v} = \bar{i}(R + sL_l) + 2pN r_\phi s \bar{\phi}_{ac} \qquad (6.19)$$

This is represented by the block diagram shown in fig 6.3,

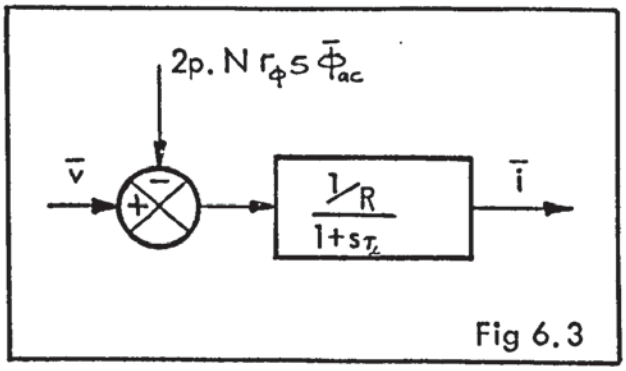

Fig 6.3

where τ_l is the leakage time constant, $\frac{L_l}{R}$.

6.10 Complete block diagram and transfer functions.

The block diagrams shown in figs 6.2 and 6.3 can be combined into the complete block diagram of the coupling after the introduction of two constitutive relationships:

$$\phi_{ac} = \Lambda F_\phi \qquad F_g = Ni$$

The resulting block diagram is shown in fig 6.4

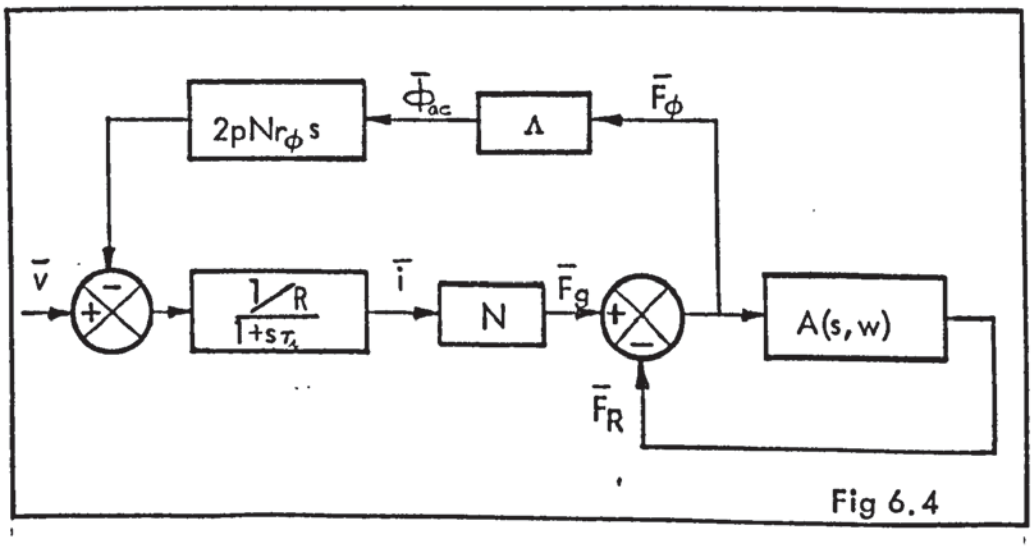

Fig 6.4

From this block diagram, the transfer function relating any two quantities in the machine can be deduced. The three most significant transfer functions are given below.

$$\frac{\bar{i}}{\bar{v}} = \frac{\frac{1}{R}\left\{1+\left(\frac{\lambda}{2\pi}\right)^2\frac{\mu_0}{g}\frac{1}{(\mu\rho)^{1/2}}(s^2+w^2)^{1/4}\right\}}{(1+s\tau_1)\left\{1+\left(\frac{\lambda}{2\pi}\right)^2\frac{\mu_0}{g}\frac{1}{(\mu\rho)^{1/2}}(s^2+w^2)^{1/4}\right\}+s\tau_{go}} \qquad (6.20)$$

$$\frac{\bar{\phi}_{ac}}{\bar{v}} = \frac{N\Lambda/R}{(1+s\tau_1)\left\{1+\left(\frac{\lambda}{2\pi}\right)^2\frac{\mu_0}{g}\frac{1}{(\mu\rho)^{1/2}}(s^2+w^2)^{1/4}\right\}+s\tau_{go}} \qquad (6.21)$$

$$\frac{\bar{\phi}_{ac}}{\bar{i}} = \frac{N\Lambda}{1+\left(\frac{\lambda}{2\pi}\right)^2\frac{\mu_0}{g}\frac{1}{(\mu\rho)^{1/2}}(s^2+w^2)^{1/4}} \qquad (6.22)$$

τ_{go} is the standstill coupled time constant, given by

$$\tau_{go} = 2pN\tau_\phi\frac{\phi_{aco}}{\bar{i}} = 2p\tau_\phi N^2\frac{\Lambda}{R}, \qquad (6.23)$$

where ϕ_{aco} is the standstill fundamental flux per pole.

The flux and current responses from (6.20) and (6.21) would have to be inverted numerically because of their complexity. However, if numerical inversion is required, then it is arguable that a wholly numerical solution of the problem is appropriate. Numerical solutions give little insight into the physical phenomena involved, nor, except in the statistical analysis of a large number of individual solutions, do they give guidance in design. The main objectives of this work are to determine the machine parameters that dictate transient response and to establish a basis for the design of fast response couplings. An analytical approach is thus to be preferred.

In the next section the transfer function 'A' is simplified by an approximation which modifies (6.20) to (6.22) and renders them tractable. The experimental work described later, investigates the validity of the approximation and shows it to

be valid for most practical situations.

6.11 Simplified transfer functions and differential equations.

The current-density induced in the drum can be separated into two parts: one part due to the motion of the airgap flux-density pattern relative to the drum, and one part due to the rate of change of flux-density amplitude. By analogy with classical machine theory, these effects can be termed 'motional induction and transformer induction' respectively.

The approximation we now introduce is that the motion induced component of current-density is much greater than the transformer induced component. In quantitative terms this implies that $\omega b \gg \frac{\partial b}{\partial t}$ (see section 6.5) and hence $\omega \gg s$.

For $\omega \gg s$, (6.14) simplifies to

$$A = (\lambda/2\pi)^2 \frac{\mu_0}{g} \frac{1}{(\mu\rho)^{1/2}} \omega^{1/2} \qquad (6.24)$$

Hence 'A' can be regarded as a constant in the transfer functions (6.20) to (6.22):

$$\frac{\bar{\imath}}{\bar{V}} = \frac{1/R}{1 + s(\tau_1 + \tau_{g0}/1+A)} \qquad (6.25)$$

$$\frac{\bar{\Phi}_{ac}}{\bar{V}} = \frac{N\Lambda/(1+A)R}{1 + s(\tau_1 + \tau_{g0}/1+A)} \qquad (6.26)$$

$$\frac{\bar{\Phi}_{ac}}{\bar{\imath}} = \frac{N\Lambda}{1+A} \qquad (6.27)$$

The flux-current transfer function contains no 's' term and hence $\Phi_{ac}(t) \propto i(t)$. This provides the basis for checking the assumption of negligible transformer induction. If the assumption is valid then, in a coupling with no rotor damping or saturation,

$$\Phi_{ac\,pu} = i_{pu} \qquad (6.28)$$

where $\Phi_{ac\,p.u}$ and $i_{p.u}$ are per units of the steady-state flux and current. If saturation is present, then transient flux and current should be related by the steady-state $\Phi_{ac} - i$ curve for the given slip speed.

The flux and current time constant is comprised of two parts: a constant part, τ_l, which depends on the leakage flux of the field winding, and a variable part, $\tau_{go}/1+A$, which depends on the mutual standstill flux and the slip speed. For zero slip, A = 0 and (6.25) reduces to

$$\frac{\bar{I}}{\bar{V}} = \frac{1/R}{1+S(\tau_l+\tau_{go})}$$

Hence $(\tau_l+\tau_{go})$ is the standstill time constant of the field winding.

From (6.25) and (6.26) the flux and current differential equations can be written:

$$V = R\left[i + (\tau_l+\tau_g)\frac{di}{dt}\right] \qquad (6.29)$$

and

$$V = \frac{(1+A)R}{N\Lambda}\left[\Phi_{ac} + (\tau_l+\tau_g)\frac{d\Phi_{ac}}{dt}\right] \qquad (6.30)$$

where τ_g is the coupled time constant at slip 'n' i.e.

$$\tau_g = \tau_{go}/1+A \qquad (6.31)$$

So far initial conditions have been neglected to simplify the derivation of the basic equations. However, having arrived at (6.29) and (6.30), initial conditions may be included in their solution in the usual way.

6.12 Eddy-current damping in solid iron rotors.

The vast majority of eddy-current couplings are manufactured with solid iron rotors. During the transient period, eddy-currents are induced in the rotor, the field of which tends to delay the change in airgap flux. Because of the interdependence of the inducing flux and the distribution of eddy-currents, a

rigorous analysis of the problem is impossible without certain assumptions regarding the current contours within the solid structure.

For very simple geometries, i.e. iron rings of circular cross-section,[27,28] the problem can be analysed satisfactorily since the eddy-current contours are obvious. However, even in such idealised cases, the analytical and computational effort is formidable.[28]

Most publications on eddy-current damping deal with iron cores of rectangular cross-section,[e.g. 30-32, 34-36] where it is assumed that the shape of the iron boundary precisely defines the eddy-current contours in the core. This assumption is unlikely to be valid for coupling rotors because of their complex magnetic geometry.[8] Kevasamurthy and Rajagopalan[34] reviewed various methods of calculating the rise of flux in a rectangular iron core of constant permeability. They used Phol's published experimental results[29] to verify both the theory of Dunaevski[31,32] and their own method of approximating the $\bar{J}$ contours in the core. In neither case was the correlation significantly better than that originally obtained by Phol with his considerably simpler 'damping ring' theory.[29]

Phol's theory is based on the assumption that the damping effect of eddy-currents may be accounted for by considering the iron to be ideally laminated, but embraced by a short-circuited winding or damping ring. The flux response may then be found using the theory of mutual induction in circuits at rest.[30(chapter 8)] The main problem in this approach lies in determining the parameters of the damping winding.

This method of modeling eddy-current damping has been used

successfully for many years,[e.g. 26] but Phol's work represented the first serious attempt to calculate the parameters of the damping winding. However, Phol's theory is limited in practice to simple magnetic geometries; so, for the analysis of real machines, Fegley[33] suggests purely experimental determination of the winding parameters. Recently, Johnson[45] used the damper winding method successfully in a sophisticated digital simulation of the dynamic performance of a d.c. machine.

Although Dunaevski's theory has been applied successfully to a practical rotating machine,[32] it is difficult to visualise the way in which the theory could be applied to coupling field members, with the inherent complexities of partial interdigitation, tapered poles etc. It was thus decided to represent the effect of rotor eddy-currents by a fictious damper winding as shown in fig 6.5.

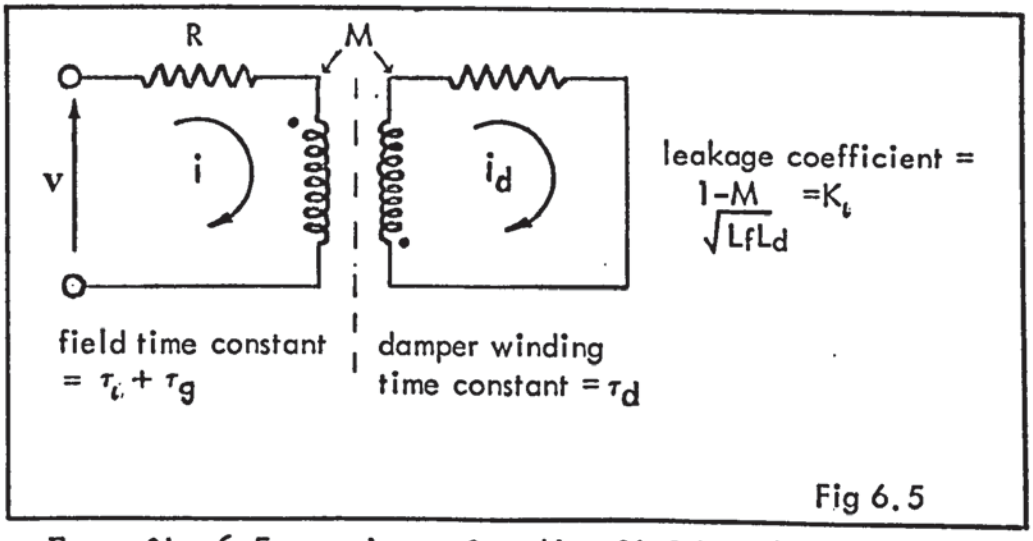

Fig 6.5

From fig 6.5, we have for the field and damper current transfer functions,

$$\frac{\bar{i}}{\bar{v}} = \frac{1}{R} \cdot \frac{1+s\tau_d}{1+s(\tau_g+\tau_t+\tau_d)+s^2(\tau_g+\tau_t)\tau_d - K_t(2-K_t)}$$

and $$\frac{\bar{i}_d}{\bar{V}} = \frac{Ms}{R_1 R_2 \left[1 + s(\tau_g+\tau_f+\tau_d) + s^2(\tau_g+\tau_f)\tau_d - K_f(2-K_f)\right.}$$

The common poles of the transfer functions are given by solution of the quadratic denominator. Let the two real roots be $-1/\tau_a$ and $-1/\tau_b$, where τ_b is the leakage time constant, then we have,

$$\frac{\bar{i}}{\bar{V}} = \frac{1}{R} \cdot \frac{1+\tau_d s}{(1+\tau_a s)(1+\tau_b s)}$$

Hence $$1+(\tau_a+\tau_b)s+\tau_a\tau_b s^2 \equiv 1+(\tau_f+\tau_g+\tau_d)s + \tau_d(\tau_f+\tau_g)s^2 - K_f(2-K_f)$$

So $$\tau_a+\tau_b = \tau_g+\tau_f+\tau_d$$

and $$\tau_a\tau_b = \tau_d(\tau_f+\tau_g) - K_f(2-K_f)$$

It is reasonable to assume that the leakage between field and damper winding is small, and consequently that τ_b is much less than τ_a

i.e. $$\tau_a = \tau_f+\tau_g+\tau_d \qquad (6.32)$$

and $$\tau_b = \frac{\tau_d(\tau_f+\tau_g)K_f(2-K_f)}{\tau_d+\tau_g+\tau_f} \qquad (6.33)$$

Substituting for τ_a and τ_b in the damper-current transfer function and using (6.27) gives

$$\frac{\bar{\Phi}_{ac}}{\bar{V}} = \frac{N\Lambda/(1+A)R}{1+s(\tau_f+\tau_g+\tau_d)} \qquad (6.34)$$

Thus, for small leakage between damper winding and field, the sole effect of the damper is to increase the flux time constant by τ_d .

6.13 Introduction of variable μ.

The previous sections of this chapter have traced the development of the fundamental transient equations, (6.29) to (6.34), which are based on the important assumption that transformer induction in the drum is negligible. This assumption implies that, during the transient period, the drum is progressing through a series of steady-state modes and that conditions

in the drum are described by the steady-state field equations,[6,8,12] where the steady-state field amplitudes are replaced by instantaneous values.

So far the calculation of transient torque has not been discussed. Linear theory suggests that $T \propto \Phi_{ac}^{2}$, but this is not true in practice because of saturation in the drum. Davies' steady-state theory of the coupling[12] shows that torque is greatly influenced by the index, 'm', of the drum magnetisation curve (see chapter 1). Therefore, since the drum is assumed to be in a pseudo-steady-state condition during the transient period, the value of 'm' will affect transient torque according to the equation,[12]

$$T \propto \Phi_{ac}^{\frac{2m}{2m-1}}$$

The introduction of variable μ means that 'A' is no longer a constant, but is now a function of Φ_{ac}. Equations (6.29) to (6.34) hence become non-linear.

It is realised that the blending of the linear theory and the non-linear substitution for μ is not mathematically rigorous and that the approach shares the weakness of Gibbs',[3] Davies',[8] and James'.[14] However, the combination of linear theory and a non-linear relationship for μ has provided valid steady-state performance relationships (see chapter 1), and it is shown in the following chapters of the thesis that the approach correlates well with experimental transient data.

6.14 Transient torque calculation.

Using the drum permeability equation,

$$\mu^{1/4} H = K_1 H^{m} \qquad (6.35)$$

Davies[12] shows that

$$\Phi_{ac} = K_2 M \frac{T^{\frac{2m}{2m-1}}}{n^{1/4m}} \qquad (6.36)$$

where $$K_2 = 1{\cdot}8\pi^{1/4m}\left(\frac{K_1}{2}\right)^{1/m}$$

and $$M = \frac{\rho^{1/4m} L^{1/2m}}{P^{\frac{4m-1}{4}} D^{\frac{2m-1}{2}}}$$

Hence $$T = \Phi_{ac}^{\frac{2m}{2m-1}} \; n^{\frac{1}{4m-2}} \; (K_2 M)^{\frac{2m}{1-2m}} \qquad (6.37)$$

So, for a transient at constant speed,

$$T_{p.u.} = \Phi_{ac\,p.u.}^{\frac{2m}{2m-1}} \qquad (6.38)$$

where $T_{p.u.}$ and $\Phi_{ac\,p.u.}$ are per-units of the steady-state torque and flux.

The per-unit representation is very convenient, since the constant term, $(k_2.M)$, is difficult to determine exactly because of its extreme sensitivity to variations in 'm'. Since the object of this work is to investigate the transient response of the machine, it is best to work in per-unit, since this eliminates the uncertainty in $(k_2.M)$.

The calculation of transient torque depends on the prediction of flux response, $\Phi_{ac\,p.u}(t)$. The key equation to the transient response of the coupling is therefore the transient flux equation, (6.30):

$$V = \frac{(1+A)R}{N\Lambda}\left[\Phi_{ac} + (\tau_l' + \tau_g)\frac{d\Phi_{ac}}{dt}\right] \qquad (6.30)$$

(As shown in section 6.13, rotor damping adds an extra time constant, τ_d, but does not change the form of the differential equation. Since τ_d is assumed constant, it may be considered as simply increasing the effective leakage time constant, τ_l').

Now, from (6.23) and (6.31),

$$\frac{(1+A)R}{N\Lambda} = \frac{2p r_\phi N(1+A)}{\tau_{go}} = \frac{2p r_\phi N}{\tau_g}$$

Hence (6.30) can be written

$$v = \frac{2p r_\phi N}{\tau_g}\left[\phi_{ac} + (\tau_l' + \tau_g)\frac{d\phi_{ac}}{dt}\right] \qquad (6.39)$$

The analytic solution of (6.39) is limited to the region of the load magnetisation curve where τ_g is constant (i.e. where $\frac{d\phi_{ac}}{di}$ is constant). This implies that the analysis is limited to voltage signals corresponding to relatively low excitation currents. However, in the low slip regions (up to 100 rev/min), where the machine will usually be rated, little error will be involved in assuming a constant mean value of τ_g for excitation signals corresponding to rated field current.*

For transients at high slips, it will be necessary to solve (6.39) on a piecewise-linear basis, holding τ_g constant over a given current range. The number of steps required will normally be small* (a maximum of three steps would be required for the experimental couplings used in this work).

The solution of (6.39) with constant τ_g and τ_l' is straightforward for any transformable voltage signal. The major problem remaining is the calculation of τ_g for the slip speed at which the transient occurrs. For the method to be of practical value, τ_g must be determined from design data and the standstill magnetisation curve, even though it's variation with slip is non-linear because of drum saturation. The linear relationship,

---

*See the magnetisation curves given in references 6,8,12 and 14 and chapters 8 and 9 of this thesis.

(6.31), is inadequate since it neglects saturation.

A method of calculating τ_g which takes saturation into account is developed in the next section.

6.15 Normalised coupled time constants.

6.15.1 Basic method.

The standstill coupled time constant, τ_{go}, can be determined from design data with little difficulty. The problem is then to relate τ_{go} to the coupled time constant at slip speed, τ_g.

The linear theory gives

$$\tau_g = \frac{\tau_{go}}{1+A} = \frac{\tau_{go}}{1+(\lambda/2\pi)^2/\mu_0 (\omega/\mu\rho)^{1/2}}$$

Therefore

$$\tau_g = \frac{\tau_{go}}{1+\frac{D^2}{p^{3/2}}\cdot\frac{1}{g}\cdot\frac{\mu_0}{2}\cdot\left(\frac{\pi n}{2\mu\rho}\right)^{1/2}}$$

This equation is useful because it indicates the machine parameters that dictate τ_g. It is interesting to note that the relationship between τ_{go} and τ_g is independent of axial length. This may not be true when end effects are taken into account.

From the above expression,

$$\frac{\tau_{go}}{\tau_g} - 1 \propto n^{1/2} \quad , \quad \text{neglecting variable } \mu.$$

But

$$\frac{\tau_{go}}{\tau_g} = \frac{\phi_{aco}}{\phi_{ac}}$$

and so

$$\frac{\phi_{aco}}{\phi_{ac}} - 1 \propto n^{1/2}$$

Experience has shown this to be untrue in general, except at very high slip speeds, the speed range changing with different couplings. However, it is known that

$$\frac{\phi_{aco}}{\phi_{ac}} - 1 \propto n^{x}, \text{ where } 0.75 > x > 0.6,$$

over speed ranges of approximately $0.2 > \frac{n}{n_m} > 0.05$. This is shown in the experimental results given by Davies, for Lundell[8] and inductor[12] couplings, and by James,[14] for a Lundell endring machine (e.g. see fig 3.8 of reference 14).

The expression given above correlates well with the normalised flux curve for couplings with wrought iron drums[12] (m=0.77), using which Davies demonstrated that $\Phi_{acm} = 0.54\ \Phi_{aco}$ and hence that

$$\frac{\Phi_{ac}}{\Phi_{aco}} = 0.54 \frac{\Phi_{ac}}{\Phi_{acm}}$$

Thus, from non-linear theory,

$$\frac{\tau_g}{\tau_{go}} = 0.54 \frac{\Phi_{ac}}{\Phi_{acm}} \qquad (6.40)$$

where (Φ_{ac}/Φ_{acm}) is taken from the normalised flux curve.

This method of calculating τ_g, used in conjunction with (6.38) and (6.39), has been found to give adequate predictions of the step response of torque. The method does however neglect the change in n_m, and hence the value of $\left(\frac{\Phi_{ac}}{\Phi_{acm}}\right)$, with current during the transient period. The choice of n_m to be used in obtaining $\left(\frac{\Phi_{ac}}{\Phi_{acm}}\right)$ is discussed in section 6.15.3.

It should also be remembered that the use of a single normalised curve to estimate τ_g at all slips and excitations is not strictly valid, because n_m will vary with excitation and slip speed.[12] However, the normalised flux curve is insensitive to changes in 'm' and, hence, little error will be involved in using the normalised curve corresponding to m = 0.77 for all practical cases. The normalised flux curve for m = 0.77 is reproduced from reference 12 in fig 6.6.

6.15.2 Incremental time constants.

It is assumed that changes in flux and current are limited to a region of the load magnetisation curve, (Φ_{ac1}, i_1) to (Φ_{ac2}, i_2), where the curve may be approximated by a straight line. The incremental time constant, $\tau_{g\Delta}$, for this excursion range, is proportional to the slope of the straight line:

i.e. $$\tau_{g\Delta} = \frac{2p\tau_\phi N}{R} \cdot \frac{\Phi_{ac2} - \Phi_{ac1}}{i_2 - i_1} \qquad (6.41)$$

The standstill incremental time constant for the same excursion range is

$$\tau_{go\Delta} = \frac{2p\tau_\phi N}{R} \cdot \frac{\Phi_{aco2} - \Phi_{aco1}}{i_2 - i_1} \qquad (6.42)$$

Therefore, $$\frac{\tau_{g\Delta}}{\tau_{go\Delta}} = \frac{\Phi_{ac2} - \Phi_{ac1}}{\Phi_{aco2} - \Phi_{aco1}} \qquad (6.43)$$

But

$$\Phi_{ac1,2} = 0{\cdot}54 \left(\frac{\Phi_{ac}}{\Phi_{acm}}\right) \cdot \Phi_{aco1,2}$$

and so $$\frac{\tau_{g\Delta}}{\tau_{go\Delta}} = 0{\cdot}54 \frac{\Phi_{ac}}{\Phi_{acm}} \qquad (6.44)$$

Thus, theoretically, the normalised time constant method of calculating τ_g, developed in section 6.15.1, is directly applicable to incremental time constants.

In practice (see section 8.6.3) this method predicts values of $\tau_{g\Delta}$ about 30% too high, particularly at high slips. However at high slips, the leakage time constant, τ_ℓ, is of the same order of magnitude as $\tau_{g\Delta}$ and, consequently, the error in the nett calculated time constant ($\tau_{g\Delta} + \tau_\ell$) is reduced to 10-15% at high slip. Since the flux and torque response depend on the total time constant, not the coupled time constant, the error in $\tau_{g\Delta}$ may be acceptable in design studies, particularly since

the error is pessimistic.

If the incremental time constants can be found for the whole excitation range, then the flux response to voltage signals which force the machine into saturation can be computed by considering each excursion range as a different linear regime. The analytical techniques involved are straightforward and well known, but a study of such large scale transients is beyond the scope of this work.

The transient experiments described in the following chapters are concerned mainly with transients in the linear region of the load magnetisation curve. The load magnetisation curve of a coupling at rated slip (approx 100 rev/min) will be linear over a wide excitation range, usually up to about 80% of rated excitation m.m.f. The analysis of transients in the linear region of the load magnetisation curve will thus cover a great many practical situations and is not an unjustifiably idealised condition.

However, to show that the theory is extendable to large scale transients at high slip, it is sufficient to demonstrate that incremental variations of torque in the high slip - high excitation region can be predicted with reasonable accuracy. Experiments to demonstrate this are described in section 8.6.3.

6.15.3 Selection of n_m for the calculation of the normalised coupled time constant.

The analysis is limited to linear or piecewise-linear regions of the load magnetisation curve where τ_g may be considered constant. We are not concerned with taking account of variable τ_g; the problem is to choose the value of n_m to obtain $\frac{\phi_{ac}}{\phi_{acm}}$

from the normalised flux curve.

In practice, n_m changes gradually with excitation m.m.f.[6,14] and may be considered constant over a wide excitation range. Hence, for the incremental time constants discussed in section 6.15.2, little error will be involved in taking a value of n_m corresponding to the mean value of current for the excursion range.

For transients in the linear region it is suggested that a value of n_m corresponding to the final steady-state current is chosen. Although tending to give an optimistic estimate of τ_g, this choice of n_m has been found to give adequate predictions of the step response of torque (see chapters 8 and 9).

Finally, of course, any choice of n_m is only pragmatically justified by the answers it gives in practice.

6.16 Response of flux and torque to a step of field voltage.

The solution of (6.39) for a voltage step of amplitude 'V' is

$$\phi_{ac}(t) = \frac{V\tau_g}{2p\tau_\phi N}\left[1 - e^{-\frac{t}{\tau_1'+\tau_g}}\right] + \phi_{ac}(0)\, e^{-\frac{t}{\tau_1'+\tau_g}} \qquad (6.45)$$

The general solution can be written as

$$\phi_{ac}(t) = \phi_{ac2} - (\phi_{ac2} - \phi_{ac1})\, e^{-\frac{t}{\tau_1'+\tau_g}} \qquad (6.46)$$

where ϕ_{ac2} is the final steady-state fundamental flux,

$$\phi_{ac2} = \frac{V\tau_g}{2p\tau_\phi N}$$

and ϕ_{ac1} is the initial steady-state flux.

The torque response is obtained from

$$T_{p.u.} = \phi_{ac\,pu}^{\frac{2m}{2m-1}} \qquad (6.38)$$

Thus

$$T_{p.u.}(t) = \left[1 - \frac{\phi_{ac2} - \phi_{ac1}}{\phi_{ac2}} \cdot e^{-\frac{t}{\tau_1'+\tau_g}}\right]^{\frac{2m}{2m-1}} \qquad (6.47)$$

where $T_{p.u}$ is a per-unit of the final steady state torque.

The torque response for zero initial conditions is obtained by setting $\phi_{ac1} = 0$ in (6.47).

6.17 Procedure for calculating the step response of torque.

The following sub-sections outline the procedure that is used to calculate the step response of torque for correlation with experimental data in chapter 8.

6.17.1 Voltage steps in the linear region of the load magnetisation curves with zero initial conditions.

(a) Calculate τ_{go} and τ_t.

(b) Choose n_m and obtain $\left(\frac{\phi_{os}}{\phi_{acm}}\right)$ from the normalised flux curve for the slip speed at which transient occurs.

(c) Calculate τ_g from (6.40).

(d) Estimate τ_d (if the rotor is solid) and add this to τ_t to give τ_t'.

(e) Use (6.47), with $\phi_{ac1} = 0$, to calculate the per-unit torque response.

6.17.2 Incremental voltage steps in the non-linear region of the load magnetisation curve.

(a) Calculate the nett change in current due to the voltage step.

(b) Obtain the corresponding change in standstill flux $(\phi_{aco2} - \phi_{aco1})$ from the standstill magnetisation curve.

(c) Calculate τ_L and $\tau_{g\Delta}$ from (6.42).

(d) Choose n_m and obtain $\left(\frac{\phi_{ac}}{\phi_{acm}}\right)$ from the normalised flux curve.

(e) Calculate $\tau_{g\Delta}$ from (6.44).

(f) Calculate the nett change in fundamental flux $(\phi_{ac2}-\phi_{ac1})$ from (6.43), and, from this, the final steady-state flux, ϕ_{ac2}.

(g) Estimate τ_d (if the rotor is solid) and add this to τ_L to give τ_L'.

(h) Use (6.47) to calculate the per-unit torque response.

6.18 Harmonic effects.

One of the basic assumptions, upon which the analysis of this chapter is based, is that the current-density is sinusoidally distributed in time and space (see section 6.2). In reality, the current-density, and hence the flux-density, will have a significant harmonic content and it is important to consider the effect of harmonic flux on the transient response of the coupling.

Harmonics are included in the transient flux equation (6.39) because fundamental flux, ϕ_{ac}, is related to total pole flux (including harmonics) by the constant, τ_ϕ, and τ_L is based on total leakage flux. Harmonic effects should therefore introduce no error in the calculation of flux response.

However, the neglect of harmonics may introduce error into the torque calculation, since harmonic flux will contribute to the torque. It is shown in chapter 8, section 8.2.5.2, that, in the experimental salient pole coupling, harmonic torque may be

neglected except at high slip speeds. The transient response tests (chapters 8 and 9) indicate that good correlation with experimental results is obtained if harmonic torques are neglected. Thus, whilst it is not claimed that harmonic effects are negligible in all eddy-current couplings, it is reasonable to assume that they are negligible in most industrial couplings, except at very high slips.

In machines where harmonic effects are prevalent, e.g. couplings with very low ($\frac{\text{pole arc}}{\text{pole pitch}}$) ratios, it may be necessary to calculate a range of torque multipliers by which the fundamental torque is multiplied to yield gross torque. (This is analogous to the factor 'f_3' introduced by Gibbs[3]).

6.19 Conclusions.

This chapter has given a theory of the constant slip transient performance of the eddy-current coupling. From an analysis of the transient airgap and drum fields, the block diagram of the coupling (fig 6.4) was developed. The form of the $F_\phi - F_R$ transfer function, 'A', rendered the transfer functions, obtained from the block diagram, intractable. The assumption of negligible transformer induction in the drum was thus introduced to simplify the problem (section 6.11).

The validity of the analysis contained in the sections following 6.11 hinges on this assumption, the verification of which is an important part of the experimental work described in chapter 8.

It follows, from the assumption of negligible transformer induction, that the drum may be considered as progressing through a sequence of steady-state modes during the transient period

and, hence, that the steady-state $T(\phi_{ac}, n)$ relationship applies to transient torque and flux (section 6.14).The relationship between T, ϕ_{ac} and n is taken from Davies' work[8,12], in which the author also derives the normalised flux curve, which is used to calculate the coupled time constant, τ_g (section 6.15).

The use of the normalised curve method of calculating τ_g is not a complete rejection of the linear equation for 'A',(6.31). The linear equation is important in the design of eddy-current couplings, since it describes the effect of changes in machine parameters on the response time of a coupling.

An experimental investigation of the basic theory given in this chapter is described in chapters 7-9.

CHAPTER 7.

THE EXPERIMENTAL MACHINE.

7. The experimental machine.

7.1 Introduction.

Rather than building a coupling suitable for an investigation of transient performance and little else, it was deceided to design and build a precision experimental coupling, which could be used by later research workers in the Electrical Machines Centre. In the light of previous experience with experimental couplings,[6,14] the following general specification was drawn up for such a machine:

(a) Provision to be made for the fitting of a variety of sizes and types of rotor and drum.

(b) Provision to be made for the substitution of various rotors and drums and for the mounting of search conductors, probes etc, with the minimum of dismantlement.

(c) Provision to be made for dynamic and steady-state measurement of torque and speed.

(d) The construction to be such to ensure long-term mechanical stability.

(e) Both rotor and drum to be concentric with their own shafts and with each other; the residual eccentricity to be less than 5% of the radial airgap.

(f) Axial and radial play in all rotating parts to be eliminated as far as possible.

(g) To reduce magnetic leakage, all shafting, mechanical couplings, endbells etc to be of non-magnetic material.

(h) To reduce compliance under transient loading, mechanical coupling to be rigid.

The design and building of the experimental coupling to this specification took up a major part of the time for this work. The result, however, is a precision laboratory coupling which can be used for a wide variety of experimental investigations in the future. A set of engineering drawings for the experimental coupling are filed in the Electrical Machines Centre.

7.2 Design.

7.2.1 Primary dimensions.

It was decided that the most convenient rating of machine for the transient experimental work was twice the rating of Davies' coupling[6] (nominally 0.75 kW). The new machine was therefore nominally rated at 1.5 kW. Assuming output to vary as $D^2.L$, the dimensions of the rotor/drum region of Davies' coupling were linearly scaled up in the proportion $\sqrt[3]{2}$:1 (1.26:1). The resulting interior dimensions (inside diameter of drum = 200 mm, length of drum iron = 72 mm) set the scale of the experimental machine.

7.2.2 General mechanical arrangement.

Figures 7.1 and 7.2 show the general arrangement of the experimental coupling. Figure 7.1 shows the coupling in the closed position, ready to run, whilst fig 7.2 shows how the two halves are drawn apart to allow work on the interior.

The drum and rotor are overhung from massive bearing housings, which slide on the ground bedplate when the locking bolts are removed. To ensure concentricity of rotor and drum, two extra bearings were provided: a small pilot bearing in

the specified magnetisation curve for hydrogen annealed pure iron and correlated exactly with Davies' equation, $\mu^{1/4} H = 0.97 H^{0.77}$ for flux-densities in excess of 0.8 T. This means that the weld did not alter the magnetisation curve of the iron and that m = 0.77 can be confidently used in calculations.

7.2.4 The model laminated drum.

A model laminated drum of the same internal diameter, but slightly longer (76 mm) than the iron part of the loss drum, was built so that the rotor time constants could be measured without the effect of eddy-current damping on the drum. This drum was made from 0.381 mm (.015") laminations of 'Losil 90' bonded together with epoxy resin and is shown in fig 7.4.

7.2.5 The partially-interdigitated rotor.

The partially-interdigitated (p.i) rotor, shown in fig 7.4, was designed to be representative of the rotors fitted to commercial machines of less than 100 kW: the poles are 50% interdigitated with a pole arc/pole pitch of 0.69. The dimensions of the rotor are given in table 7.1. Each half of the rotor was machined from a mild steel billet. The teeth were formed last by milling scollops on the outside of the billet.

The excitation coil was wound with 1000 turns of 0.4572 mm diameter, (26 S.W.G.) Lewmex wire, insulated with cotton tape and varnished. It is rated at 0.6 A (300 AT/pole) and has a d.c. resistance of 41Ω.

7.2.6 The laminated salient-pole rotor.

The majority of the experimental work was carried out with the salient-pole (s.p) rotor fitted in the experimental machine. It is designed to avoid rotor eddy-current damping and saturation, since these will obscure the experimental results, but is also a commercially viable design.[16]

The rotor stack was built of 0.5 mm mild steel disc laminations. To avoid creating low resistance paths for the rotor eddy-currents, by bolting or welding the stack together, the laminations were bonded together with 'Loctite 310' which also formed an excellent inter-lamination insulation. As an extra precaution, four 6.35 mm (0.25") diameter bolts were used to support the stack at a low p.c.d. well away from the teeth.

When the disc laminations were firmly bonded together, the slots were milled out using a pre-formed cutting tool. A rotor at this stage of development, fitted with 'Tufnol' end laminations, is shown with the cutting tool in fig 7.5. The teeth were then cut back 14 mm each side, at the tooth root diameter to allow for the endwinding (see fig 7.3). Before winding, the rotor was treated with 'deburring' fluid. The dimensions of the rotor are summarised in table 7.1 and the tooth profile is shown in fig 7.9.

The rotor was wound with two identical serpentine windings as shown in fig 7.6.

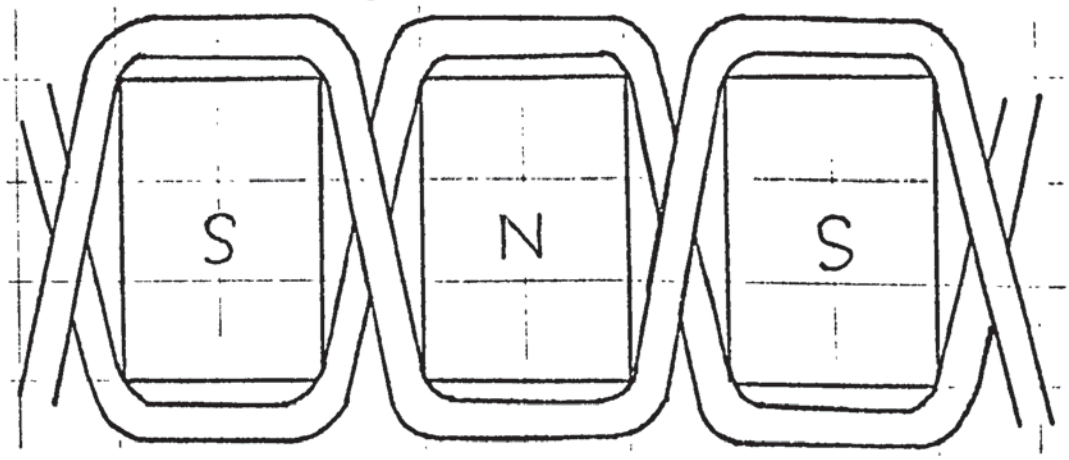

Fig 7.6

The reasons for having two serpentine windings, rather than one, are:

(a) Since the windings are very tightly coupled, one winding can be used as a search coil to measure the total flux linking the other.

(b) The effectiveness of the second winding as a search coil for total winding flux can be determined by feeding the two windings, connected in opposing magnetic polarity, with the same current, when there should be zero pole flux.

(c) With one winding short-circuited, eddy-current damping on the rotor can be simulated.

Each winding comprises 200 turns of 0.508 mm diameter (25 S.W.G.) Lewmex wire, insulated with cotton tape and then varnished after being wound in the rotor slots. The slots carried a 0.5 mm leatheroid liner and a fibre wedge. Each winding is rated at 1.5 A (150 AT/pole/winding) and has a d.c. resistance of 23.3 Ω. 2.75 ?

7.2.7 Parameters of the experimental machine.

The parameters of the experimental coupling are given in table 7.1.

7.3 The coupling drive.

The drive machine was a 12 kW level-compound d.c. motor with a high inertia rotor. The armature was fed from a 3-phase full wave, bridge-connected rectifier supplied from the mains through a motorised variable autotransformer driven at 1 rev/min, which enabled the motor to be run up smoothly. The

Table 7.1

Loss drum:

length of iron	=	72 mm
inside diameter	=	200 mm
outside diameter	=	232 mm
resistivity of iron	=	$11.2 \times 10^{-8} \Omega.m$

Rotors:

outside diameter	=	199.36 mm
radial airgap	=	0.32 mm
number of poles	=	12

p.i. rotor:

length of pole	=	48 mm
length of Lundell region	=	24 mm
length of inductor region	=	24 mm
pole arc/pole pitch	=	0.69
length of drum spanned by poles	=	72 mm
winding turns	=	1000
winding resistance	=	41 Ω

s.p. rotor:

length of pole	=	68 mm
pole arc/pole pitch	=	0.7
winding turns	=	200 per coil
winding resistance	=	23.3 Ω per coil
number of coils	=	2

shunt field was separately excited through a full-wave rectifier connected across two lines of the supply. A schematic diagram of the drive system is shown in fig 7.7.

The coupling excitation was taken from a 150 V,6 A stabilised d.c. power supply, capable of operating in either a constant-voltage or constant-current mode.

7.4 Instrumentation.

7.4.1 Torque measurement.

Torque was measured by a strain gauge transducer. The gauges are connected in a full bridge circuit fed from a stabilised d.c. supply and arranged on the transducer shaft so that shaft strains, due to bending and axial thrust, are self cancelling. Also, since the gauges have a common temperature coefficient of resistance, the calibration of the transducer is insensitive to changes in temperature. The output signal from the bridge is fed via a system of silver sliprings and silver graphite brushes, to a drift-compensated amplifier, the gain of which is adjusted so that the output voltage is 1 V at maximum torque. The unit containing the amplifier stack has signal outlets for ultra-violet recorders and oscilloscopes.

The torque measuring system has a bandwidth of 8 kHz and is hence ideally suited to the measurement of transient torque. The specification of the system is given below:

load range = 0-135.5 Nm (0-100 lb.ft)

speed range = 0-6000 rev/min

bridge input voltage = 20 V d.c. or a.c.

bridge sensitivity = 2.226 mV/V at full load.

error due to non linearity = $\pm$ 0.07%

no-load output = 10 μV/V

The transducer is shown mounted between the rotor shaft and locking bracket in fig 7.1.

7.4.2 Speed measurement.

The torque transducer had an integral photo-electric tachometer which was not used because of its poor signal/noise ratio at low speeds. Instead, a permanent magnet d.c. tacho-generator was used, mounted on the drive machine. The tacho-generator has an output of 0.1 V/rev/min.

7.4.3 Flux measurement.

7.4.3.1 Search coils.

7.4.3.1.1 Partially - interdigitated rotor.

Search coils were provided to measure total pole flux, Lundell-region pole flux, inductor-region pole flux, core flux and axial leakage flux. A total pole flux search coil was wound on every pole so that the airgap eccentricity could be checked. The search coils are shown in fig 7.8.

The search coils on the pole face comprised a single turn of 0.152 mm diameter (38 S.W.G.) Lewmex wire. The core flux and axial leakage flux coils comprised two turns of 0.254 mm diameter (33 S.W.G.) Lewmex wire. All the coils were adhered with epoxy resin.

The search coil leads were carefully twisted together to avoid 'pick-up' and soldered to the miniature terminal board, mounted behind the rotor teeth (see fig 7.4). The terminals were then connected, by screened cable, to the rotary switch mounted on the rotor main bearing housing (see figs 7.1 and 7.2). It was then possible to 'dial' any individual search

coil to the switch output terminals.

7.4.3.1.2 Salient-pole rotor.

The s.p. rotor search coils were installed to measure the total pole flux and the circumferential flux-density distribution across the pole. The search coil arrangement is shown in fig 7.9.

To measure the total pole flux and the airgap eccentricity, a single turn search coil was wound on each pole. The flux-density distribution was measured by six coils on the pole face, each spanning 3.5^{o} (6.1 mm). All the coils comprised a single turn of 0.1 mm diameter (42 S.W.G) Lewmex wire, and were adhered with epoxy resin.

The search coil leads were brought out to the rotary switch in an identical manner to the p.i. rotor.

7.4.3.2 Flux meters.

Steady-state flux was measured by the method of reversals using a 'Norma' ballistic flux meter.[6,14] The instrument was critically damped via a precision decade resistance in series with the input terminals.

Transient flux was measured using an integrating flux meter with a direct read-out facility. The output from the flux meter was fed to an ultra-violet recorder or storage oscilloscope as required. The input impedance of the flux meter is a minimum of 50 kΩ on the most sensitive range and, hence, any error due to finite search coil resistance (approximately 6Ω maximum) is negligible. The instrument has a drift compensation control, using which, the drift rate on the most sensitive range was held to less than 2.5 μWb/min.

The calibration of both flux meters was checked against a 'Hibbert' magnetic standard and found to be within 1% of the standard over the entire range.

7.5 Preliminary equipment tests.

7.5.1 Airgap concentricity.

The following test was carried out for both rotors.

The rotor was locked in position with a pole lined up in the vertical axis. The outside of the loss drum was marked at 30° increments around the outer periphery; the first increment marked directly over the weld. With the rotor winding carrying rated current, the flux per pole of all 12 poles, was measured as each increment on the drum was lined up in the vertical axis, making 144 measurements in all. Expressed as a percentage of the mean pole flux, the maximum difference between flux readings was found to be 3.3% for the p.i. rotor and 2.9% for the s.p. rotor. For every position of the drum, this was the difference between the flux of the pole under the drum weld and the adjacent pole.

Mechanical measurements of airgap eccentricity showed a variation of less than 1% for each rotor and hence the flux variation was attributed to the heterogeneous nature of the drum weld.

The flux variation test was repeated at twice rated current, to examine the effects of unbalanced magnetic pull. The flux variations were 3.7% for the p.i. rotor and 3.1% for the s.p. rotor.

In view of the small flux variation, it was decided that the degree of eccentricity was small enough to neglect.

7.5.2 Effectiveness of rotor and drum laminations.

The laminated rotor was positioned concentrically in the laminated drum and a steady-state curve of flux per pole and excitation current was taken. The response of current and flux to a step of rated field voltage were then recorded. A flux response curve was constructed from the measured current response and the steady-state magnetisation curve.

Since there was negligible difference between the constructed and measured flux responses, it was assumed that the laminations were effective in eliminating eddy-current damping.

7.5.3 Effectiveness of one serpentine field winding as a search coil.

The s.p. rotor was fitted in the experimental machine and the two field windings were connected in opposing magnetic polarity. Each coil was fed with 2.5 A. The measured flux per pole was 44 μWb; less than 2% of the flux obtained when the coils are connected in assisting magnetic polarity. It was therefore decided that, for all practical purposes, the windings could be assumed to be perfectly coupled and that it was valid to use one as a search coil to measure the flux of the other (i.e. the field flux).

7.5.4 Endbell and shaft leakage fluxes.

Search coils comprising 5 turns of 0.254 mm diameter (33 S.W.G.) Lewmex wire were wound on the outer surface of the trunnion housing and endbell, on the shaft directly behind the drum endbell and behind the slip rings. With maximum m.m.f. applied to the field winding (500 AT/pole) the measured leakage

fluxes were negligible. The maximum flux reading was obtained from the shaft coil behind the slip rings, with the p.i. rotor fitted i.e. 1.33μ Wb.

It was hence assumed that the endbell and shaft leakage flux was negligible and would have no influence on the performance of the coupling.

7.5.5 Torque transducer and tachometer calibration.

The tachogenerator calibration was checked with a stroboscope and found to be within 1.5% of the manufacturers specification over the speed range 0-2000 rev/min.

The output voltage of the torque measuring system was calibrated against a precision balance ($\pm$5 gm) and found to correspond, within the accuracy of the balance, to the manufacturers specification.

7.6 Conclusions.

The experimental machine and associated instrumentation has been described in this chapter together with various preliminary tests. The results of these tests indicate the accuracy of measurement to be expected from the rig and encourage confidence in the experimental results given in the following chapters.

CHAPTER 8.

EXPERIMENTS WITH THE SALIENT-POLE ROTOR.

8. Experiments with the salient-pole rotor.

8.1 Introduction.

Before proceeding to investigate the transient response of the coupling, the steady-state performance must be determined. This is necessary because the data required to calculate the transient response has first to be determined (or at least checked) by steady-state measurement. Since the torque response equations assume the validity of Davies theory[12] in the steady-state, it is important to verify this for the experimental machine. The steady-state experiments are thus described first.

The transient experiments described in the later sections of this chapter are concerned with measuring current, flux and torque responses to changes in field voltage. Prior to this, however, the assumption that transformer effects in the drum are negligible is investigated and its range of validity established.

8.2 Steady-state experiments.

8.2.1 Torque-slip curves.

Torque-slip curves were obtained by maintaining the field current constant, whilst increasing the slip speed of the coupling from zero to a maximum by running up the drive motor (see section 7.3). The speed and torque signals were fed to the axes of an x-y, plotter, so that the torque-slip curves were plotted automatically as the drive ran up. To ensure that the field current remained constant during the test, the excitation power supply was set in the constant-current mode.

At high excitations the temperature of the outer surface of the drum increased significantly during the test. The rise in

drum resistivity caused a reduction in torque which was apparent when the drive was run down. To minimise the effects of drum heating, each run was commenced with the outer surface of the drum cooled to 45°C. The maximum temperature rise during a run was 10°C at 500 AT/pole. This represents an increase in resistivity and a consequent reduction in torque of 5%.

The measured torque-slip curves are shown in fig 8.1.

8.2.2 Variation of flux with excitation m.m.f. and slip speed.

Curves of measured field flux and pole flux were plotted against excitation m.m.f. for a range of slip speeds from standstill to 1500 rev/min.

The field flux curves are shown in fig 8.2. The flux levels are reduced to a per-pole basis to compare with the pole flux curves shown in fig 8.3.

By subtracting the field and pole fluxes, we obtain the leakage flux per pole. The leakage flux curves are also shown in fig 8.2, from which it is clear that leakage flux and excitation m.m.f. are related by a constant, which is independent of slip except at high slips and excitations.

The leakage flux is 8.2% of the standstill field flux over the linear region. When saturation sets in, the leakage rises to about 13% (at 500 AT/pole).

8.2.3 Time constants.

The time constants τ_{go} and τ_{ℓ}, can be found from the slopes of the standstill pole flux and leakage flux magnetisation curves and the winding parameters, i.e. for one field coil τ_{go} = 38 ms and τ_{ℓ} = 3.42 ms. This means that the standstill time constant of the

field winding should be 41.42 ms with no eddy-current damping on the drum. (see section 8.5.1).

The linear coupled time constant τ_g can also be determined from fig 8.3. The values of τ_g for various slip speeds will only be valid up to about 150 AT/pole, beyond which the load magnetisation curves are non linear. However these values will be useful for comparison with the measured time constants and the time constants obtained from the normalised flux curves.

The coupled time constants for a single field coil, obtained from fig 8.3, are given below in table 8.1.

TABLE 8.1

COUPLED TIME CONSTANTS FROM FIG 8.3.

n, rev/min	τ_g , ms.
50	27
100	22.8
200	17.6
400	13.7
1000	10.4
1500	7.25

8.2.4 Pole face flux-density distribution.

The search coils used to measure the flux-density distribution are described in section 7.4.3.1.2. The measurements were carried out, for a range of slip speeds and excitations, by the method of flux reversals. The exact test procedure is described in detail by Davies[6] and James.[14]

The flux-density distributions are plotted in figs 8.4-8.8. Following Davies and James, the experimental points are plotted in a position along the pole arc, corresponding to the centre

of the search coil.[14]

Armature reaction effects are apparent in all of the flux-density waves. In common with James' results for a Lundell endring machine, the reduction in flux at the leading pole edge is seen to be more severe than in a coupling with a solid iron drum.[6]

8.2.5 Fourier analysis of the flux-density waves.

8.2.5.1 Accuracy of computation.

Six experimental points are known for each wave, but, to ensure accurate computation of the harmonics, many more ordinates are required. These are taken from the flux-density plots shown in figs 8.4-8.8. This is equivalent to graphical interpolation of the ordinates from the six experimental values. From a purely mathematical point of view, this might be expected to produce errors in the Fourier analysis, because of the small number of experimental points. However, Gibbs[3] has shown the equivalence of the $J_z(t)$ and $B_y(x)$ distributions at the surface of the drum; so, by comparing the constructed flux-density wave with a measured surface current-density wave, at the same slip speed and excitation, the accuracy of the construction can be verified.

Davies' flux-density and surface current-density waveforms* have identical shapes. It is, therefore, reasonable to conclude that the flux-density waves, produced by joining the experimental points with a smooth curve, are good approximations to the physical waves in the machine. Consequently the ordinates for

---

*c.f. figs 12-16 and 31a-31b of reference 6.

the Fourier analysis may confidently be taken from figs 8.4-8.8, provided that caution is exercised with regard to the computed values of the higher harmonics.

The flux-density waves were analysed up to the 15th harmonic using a computer program which required a minimum of 29 ($2.h_{max}$-1) samples. To assess the effect of variations in the curve joining the experimental points, a second set of ordinates was linearly interpolated from the experimental values at 1000 rev/min, 400 AT/pole, and used for the harmonic analysis. Comparing the computed harmonics with those obtained from fig 8.8, it was found that there was negligible difference in the first four harmonics (order 1-7), but significant variations in the higher harmonics (order 9-15). Hence it was concluded that the harmonics computed from figs 8.4-8.8 are reliable up to the 7th (and possibly the 9th) but that the amplitudes of the higher harmonics should be treated with discretion, although the orders of magnitude should be correct.

It should be remembered that we are primarily interested in the fundamental flux-density and the first few harmonics, since these produce the torque. Any errors in the higher harmonics do not matter much.

8.2.5.2 Harmonic flux-densities and the torque produced by them.

The transient theory of the coupling includes the assumption that the torque response can be deduced with adequate accuracy from the fundamental flux response. Before proceeding to make use of the data on fundamental flux, it is important to confirm that the harmonic fluxes do not make a major contribution to the torque. Otherwise the relationship between T, ϕ_{oc} and n

will be obscured.

In general (see section 6.14)

$$\frac{T_h}{T_1} = \left(\frac{B_h}{B_1}\right)^{\frac{2m}{2m-1}} \cdot \frac{1}{h^{4m-2}}$$

where $1 > m > 0.75$.

As shown in fig 8.9, the two extreme values of m represent the limiting forms of the B-H curve for the drum: linear and fully saturated.

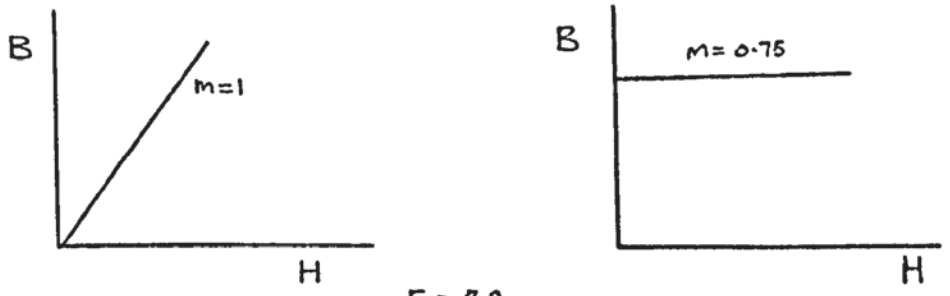

FIG 8.9

To estimate harmonic torque contributions, Davies[12] uses m = 0.75, which gives

$$\frac{T_h}{T_1} = \left(\frac{B_h}{B_1}\right)^3 \cdot \frac{1}{h}$$

James,[14] however assumes m = 1:

i.e. $$\frac{T_h}{T_1} = \left(\frac{B_h}{B_1}\right)^2 \frac{1}{h^{1/2}}$$

The truth lies somewhere between the two.

Except for very low excitations and slips, James' equation cannot be expected to give the correct results. In the later sections of his thesis, he demonstrates that his endring machine obeys Davies' theory i.e. that the drum is saturated ($m < 1$). There is, therefore, no justification for using m = 1, which assumes no saturation, to calculate the harmonic torque. James' calculated harmonic torque of $0.36 \cdot T_1$ at maximum slip must hence be considered an overestimate.

Davies' approach, on the other hand, will underestimate the harmonic torque, but should give more correct answers than James' method, because the B-H curve assumed corresponds more

closely, although crudely, to the physical situation. Using James' data, Davies' method produces a harmonic torque estimate of $0.09.T_1$, as compared with $0.36.T_1$ calculated by James.

All that can be said for certain is that the harmonic torque lies somewhere between the two extreme values produced by the two methods. As a compromise solution, the measured value of m for the drum iron (m = 0.77) was used to estimate the harmonic torque, although the choice of m for any harmonic is arbitrary.

The Fourier analysis of the flux-density waves is summarised in table 8.2 up to the 7th harmonic. Typical computed values of the higher harmonics, which are relatively insensitive to excitation, are given in table 8.3.

TABLE 8.3

TYPICAL HIGHER HARMONICS
AS P.U. OF FUNDAMENTAL

h \ n	50	100	200	400	1000	1500
9	0.08	0.09	0.10	0.14	0.19	0.25
11	0.12	0.12	0.15	0.17	0.17	0.22
13	0.12	0.10	0.10	0.10	0.15	0.19
15	0.03	0.05	0.07	0.10	0.12	0.14

To estimate the harmonic torque at each slip speed, the flux wave containing the maximum harmonic content was chosen. A torque contribution of 1% ($0.01.T_1$) was allowed for the higher harmonics (9+). Using m = 0.77 and rounding up to the second decimal, we obtain table 8.4.

TABLE 8.4

HARMONIC TORQUE

$\frac{\sum T_h}{T_1}$	0.03	0.05	0.07	0.09	0.13	0.16
n	50	100	200	400	1000	1500

TABLE 8.2

HARMONIC CONTENT OF FLUX-DENSITY WAVES EXPRESSED AS PER UNIT OF FUNDAMENTAL

50 AT/POLE

h \ n	50	100	200	400	1000	1500
3	0.16	0.21	0.28	0.34	0.49	0.51
5	0.18	0.19	0.23	0.25	0.38	0.39
7	0.19	0.21	0.24	0.25	0.32	0.32

100 AT/POLE

h \ n	50	100	200	400	1000	1500
3	0.19	0.28	0.33	0.40	0.52	0.53
5	0.18	0.23	0.27	0.32	0.43	0.46
7	0.20	0.24	0.27	0.32	0.41	0.41

200 AT/POLE

h \ n	50	100	200	400	1000	1500
3	0.29	0.32	0.42	0.52	0.56	0.61
5	0.24	0.25	0.31	0.40	0.52	0.51
7	0.23	0.25	0.32	0.39	0.50	0.51

300 AT/POLE

h \ n	50	100	200	400	1000	1500
3	0.31	0.39	0.46	0.54	0.60	0.62
5	0.25	0.30	0.36	0.41	0.48	0.53
7	0.23	0.29	0.33	0.37	0.48	0.49

400 AT/POLE

h \ n	50	100	200	400	1000	1500
3	0.32	0.40	0.42	0.49	0.54	0.59
5	0.26	0.30	0.31	0.36	0.42	0.50
7	0.26	0.28	0.32	0.35	0.41	0.43

(n = slip speed, rev/min)
(h = harmonic order)

It can be seen that the assumption of negligible harmonic torque is reasonable at the lower slip speeds, but begins to fall down as slip speed increases. Thus, for higher slip speeds the relationship between T, Φ_{ac} and n may have to be adjusted to allow for the harmonic torques. In practice, however, interest is centred around the region of rated speed (100 rev/min) where it seems perfectly valid to neglect the harmonic torques.

8.2.5.3 Fundamental flux.

Figure 8.10 shows the variation of computed fundamental flux per pole, Φ_{ac}, with slip speed for various excitation m.m.f.s. Values of total pole flux, from fig 8.3, are also plotted on fig 8.10, from which it can be seen that Φ_{ac} and the pole flux are almost equal over the whole speed range for all of the excitations. The ratio of $(\frac{\text{flux per pole}}{\Phi_{ac}})$, i.e. '$r_\Phi$' varies from 0.93 to 0.97. From Davies[12] the calculated ratio is 0.97. This is excellent correlation and supports his claim[6] that the ratio is independent of speed.

The constancy of r_Φ is crucial to the transient theory, because it enables the rotor voltage equation (6.21) to be written in terms of the torque producing flux, Φ_{ac}.

8.2.5.4 Armature reaction m.m.f. and its phase.

Although the measurement of armature reaction m.m.f. and its phase are not essential to the investigation of transient performance, experimental results are included here for completeness and because no data has been previously published on salient-pole couplings.

The armature reaction m.m.f. is obtained from the flux-

density waves by Davies' method.[6,8] The method neglects harmonics higher than the third, which is assumed to have the same zero as the fundamental. It is thus very approximate, as Davies points out: "Since, emphatically, this is an approximation, not too much faith should be placed in the exact numerical value of this F_R measurement. However its variation with torque and speed should be correct".

The measured variation of F_R with speed is shown for a range of excitations in fig 8.11. The values of F_R from these curves will be used later as a check on Davies' normalised curves.

The armature reaction phase angle, which should theoretically tend to 45° as slip speed increases, was measured by Davies' method, using the computed "correction angles".[8] The variation of measured phase angle with slip speed and excitation is summarised in table 8.5.

TABLE 8.5

MEASURED PHASE ANGLE ø
(DEG ELEC)

Fg \ n	50	100	200	400	1000	1500
50	34	40	38	35	39	36
100	32	32	33	33	28	29
200	25	30	30	26	27	30
300	24	26	26	28	27	27
400	21	24	28	35	32	32

The angles are much lower than those obtained by Davies[8] for a homogeneous iron drum, but compare well with those obtained by James[14] for an endring drum. This tends to substantiate James' claim that endring drums produce lower phase angles due to the reduction in 'drum impedance'.[14] However table 8.5 must be treated with discretion because of the very approximate nature of the measurements.

8.2.6 Relationship between torque, fundamental flux and slip speed.

The transient torque equation, (6.41), is based on Davies' steady-state theory:

i.e. $T \propto \Phi_{ac}^{\frac{2m}{2m-1}} . n^{\frac{1}{4m-2}}$ (see chapter 6)

It is therefore essential to verify this expression under steady-state conditions before applying the transient theory.

Torque versus fundamental flux, at constant slip, is plotted on a log-log scale in fig 8.12. The measured index of flux varies from 2.6 at 100 rev/min to 2.7 at 1000 rev/min. This is good correlation with the calculated index of 2.85 ($m = 0.77$). The reduced indices in the low slip - low excitation regions (2.35 at 50 rev/min) are to be expected, since the iron may not be operating in the region of the magnetisation curve where $m = 0.77$.

Torque versus slip speed, at constant fundamental flux, is plotted in fig 8.13. The index of flux varies from 0.85 at 0.4 mWb to 0.93 at 1.0 mWb, which is good correlation with the calculated value of 0.93.

The results summarised in figs 8.12 and 8.13 show that, even in the region where significant harmonic torque might be expected, the theoretical $T(\Phi_{ac}, n)$ relationship is valid. The form of the relationship is valid at low slips and excitations where the drum is less saturated i.e. where $m > 0.77$. (The flux index at 50 rev/min implies $m = 0.87$).

The experimental results obtained by Davies[6,8,12] and James,[14] coupled with the results of this chapter, show that Davies' theory can be applied with confidence to both endring and solid drum machines with any type of rotor. This, in turn,

implies that, if the transient theory can be verified for the salient-pole coupling, it may be expected to apply to other types of coupling also.

8.2.7 Normalised curves.

As outlined in chapter 1, Davies derived normalised curves of torque, flux, armature reaction m.m.f. and drum loss.[12] In this section the calculated curves for m = 0.77 are compared with the curves obtained by normalising the experimental results. (Drum loss is not considered explicitly, since, if the normalised torque curve is valid, it naturally follows that the loss curve is valid also[12]).

The normalised speed range, $0.1 < \frac{n}{n_m} < 6.0$, corresponds to an absolute range of approximately $25 < n < 1500$ rev/min, and covers the practical operating range of the coupling.

Normalised torque, flux and armature reaction m.m.f. are plotted in figs 8.14a, 8.14b and 8.14c respectively. The overall correlation between experimental and theoretical values is very good, the worst errors occurring in the armature reaction curve, which is to be expected (see section 8.2.5.4).

The experimental normalised torques and fluxes deviate from the theoretical curves by only a few percent, except at very low and very high slips, where the errors increase to about 10%. The errors at low slip are almost certainly due to the skin depth reaching a value where the approximation, $\sqrt{2\alpha} \gg 2\pi/\lambda$, is invalid. The high slip errors can be reasonably attributed to harmonic torque.

The maximum errors in both torque and flux occur for an m.m.f. of 400 AT/pole, where the shape of the curves[12] suggests that 'm' is slightly less than 0.77.

The errors in the normalised armature reaction curve rise to around 20 or 30% at low slips, but are negligible at high slip. In view of the uncertainty in the F_R measurement, the correlation is surprisingly good.

8.3 Comments on the steady-state experimental results.

The steady-state tests described in this chapter have demonstrated that Davies' theory applies to the salient-pole coupling and, consequently, that it will be valid to use the torque equation,

$$T_{p.u} = \Phi_{ac\,p.u}^{\frac{2m}{2m-1}},$$

and the normalised flux curve to calculate torque response, provided that it can be conclusively shown that transformer induction is negligible (see chapter 6).

For the sake of completeness, the experiments were extended to consider armature reaction and its phase and the complete set of normalised curves. These tests show that, generally, Davies' theory agrees very well with the experimental data.

The main deviations from the theory are the measured values of phase angle and armature reaction m.m.f. The method of measuring armature reaction has always been in some doubt,[8] so errors in this quantity are not unexpected. The measured phase angles, however, deviate from the theoretical angle of 45° by up to 24°. This together with James' results,[14] suggests strongly that, in endring couplings, it is invalid to use $\phi = 45^{\circ}$.

In practice, the phase angle error will be unimportant because the final performance relationships (e.g. torque - flux - speed equation, generalised curves etc) still correlate well with test results.

8.4 Experiments to investigate the assumptions of the transient theory.

Apart from the "classical" assumptions of coupling theory which are listed in section 6.2, the current and flux (and hence torque) differential equations are based on two important assumptions:

(a) $\frac{\text{flux per pole}}{\Phi_{ac}}$ = a constant, i.e. Γ_{ϕ}, under transient conditions. (see section 6.9).

(b) There is negligible transformer induction on the drum i.e. $\Phi_{ac\,pu} \approx i_{pu}$ (see section 6.11).

Since these assumptions are not based on prior experimental evidence they must be verified before applying the theory. If the first assumption can be verified for a certain slip speed range, it implies that the transient airgap flux-density distribution is the same as the steady-state distribution and consequently that the second assumption is also valid over the same speed range. However, because (b) is such an important assumption, it is verified by a completely separate experiment which provides a valuable cross check on both assumptions. (see section 8.4.3).

8.4.1 Variation of slip speed during the transient period.

In order to check the assumptions in a reliable way, it was essential that the slip speed of the experimental machine remained substantially constant during the transient period. A number of step response tests were thus carried out for a range of excitations and slips.

The drive machine was a level-compound 12 kW d.c. motor with a high inertia rotor, specially chosen to give a stable

running speed without closed loop control. The response tests showed that there was negligible speed regulation of the motor during the transient period, except for large voltage steps at low slip (e.g. 60 V at 20 rev/min).

Figure 8.15 shows the results of a typical test at 50 rev/min slip. The excitation coils were connected in parallel and subject to a voltage "step" which produced rated steady-state current. (Although the "step" has a finite slope and an overshoot of about 3%, the voltage signal is a close approximation to an ideal step function, which it will be assumed to be for correlation with the theory). The final steady-state speed, after the transient, was 41.5 rev/min; a regulation in speed of 17%. However, as shown in fig 8.15, by the time the current had effectively reached steady-state, the speed had only fallen to 47 rev/min; a regulation of 6%. A further 0.94 s was required for the speed to reach steady-state.

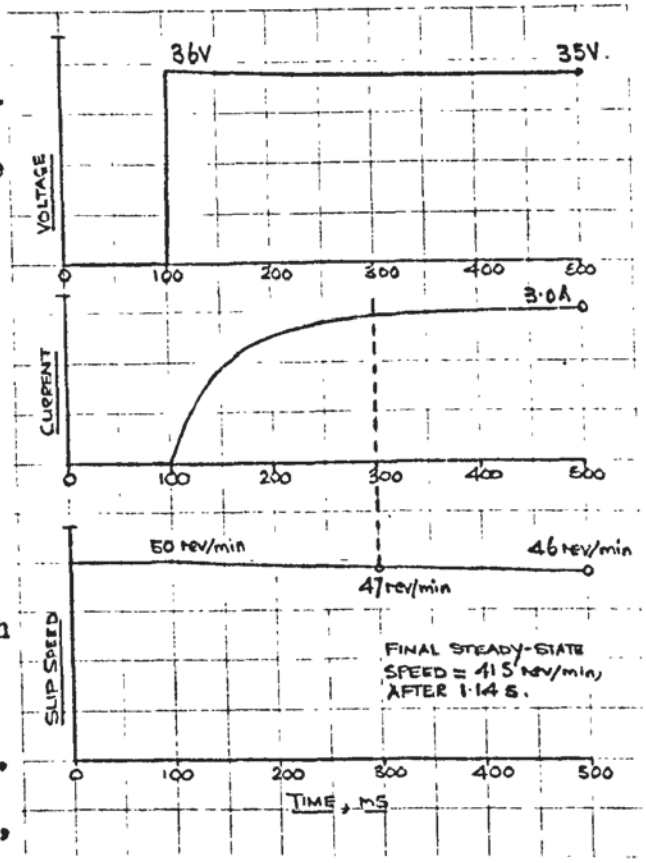

Fig 8.15

For lower voltage steps (i.e. smaller torque disturbances on the drive motor) the change in slip during the transient period was much less and the assumption of constant speed was valid for lower slips, (e.g. 11.65 V at 20 rev/min).

For higher slip speeds (i.e. increased kinetic energy of

the drive) the change in slip was similarly reduced, and steps of maximum overload voltage could be applied without excessive speed regulation during the transient period (e.g. 8% regulation for 70 V at 400 rev/min).

In the transient tests described in this chapter the speed regulation during the transient period was a maximum of 6% (typically about 3%). Neglecting the increase in flux due to the speed reduction, which will tend to offset any reduction in torque, this will introduce an error of less than 6% in torque. The experiments should hence approximate closely to the ideal constant speed situation.

8.4.2 Transient flux-density distribution.

The transient distribution of flux-density was measured in the following manner. The response of the flux linking a pole face search coil was measured simultaneously with the field current response on a storage oscilloscope. After the test the magnetic circuit of the coupling was returned to the same cyclic state by rapidly reversing the field current several times. This experiment was then repeated five times until the flux response of all six pole face search coils was obtained.

Thus, at a given instant in time, and for a given instantaneous value of field current, the mean flux-density of each search coil can be found and the transient distribution of flux-density plotted.

To check that the results were not obscured by hysteresis effects, a sample distribution was repeated several times. It was found that the curve was reproduceable to within 3%, the

maximum error occurring at the trailing pole edge where the flux densities are highest.

The theory of chapter 6 assumes that, 'drum damping' is negligible and hence that the transient distribution, corresponding to an instantaneous value of field current, is the same as the steady-state distribution for the same field current and slip speed. It is, however, logical to expect the maximum discrepancy between the steady-state and transient distributions,

(a) early in the transient period when the transient wave should be almost in antiphase with the pole centre line (see section 6.7).

(b) at low slips, where $\frac{\partial b}{\partial t}$ may be of the same order as ωb (see section 6.11).

Figure 8.16 shows the transient flux-density distribution at different instants in time, following the application of a 58 V step to the field winding. The field current response, also shown in the figure, is not a pure exponential because of saturation effects. The test was carried out at 100 rev/min (i.e. rated slip). The curves shown in dotted outline on fig 8.15 are the steady-state distributions for the same values of field current taken from figs 8.4-8.8.

The 0.5 A transient distribution, occurring at 5.6 ms, is almost in antiphase with the pole centre, as theory predicts. The 1 A curve (11.2 ms) is similarly phase-shifted with respect to the steady-state distribution, but the shift is less than at 0.5 A. At 2.0 A (34 ms) the phase shift is further reduced and is negligible by the time the current has reached 3.0 A (61 ms).

A similar test at 1000 rev/min showed virtually no phase lag for any of the current values. This is to be expected since, at high slips, the effect of drum damping will be negligible compared to the motional induction effect.

The experiments summarised in fig 8.16 were carried out at 100 rev/min. To check that the steady-state and transient distributions were similar over the full operating range of the machine, a second series of experiments was carried out. The transient distribution corresponding to rated field current (3 A) was measured at slip speeds of 50, 100, 200, 400 and 1000 rev/min. The transient was caused by the application of a 47 V step to the field winding (this was the maximum voltage step that could be applied, without exceeding 6% speed regulation at 50 rev/min - see section 8.4.1).

The transient and corresponding steady-state distributions are shown in fig 8.7. For the higher slip speeds, the steady-state and transient curves are identical. At 50 and 100 rev/min, however, there is a small amplitude lag at the leading pole edge.

It was fairly obvious from figs 8.16 and 8.17 that the assumption ($\frac{\text{flux per pole}}{\Phi_{ac}}$ = constant) was approximately valid during the transient period. To check this, the transient curves showing the greatest deviation from the steady-state distribution (i.e. 0.5 A curve on fig 8.16 and 50 rev/min curve on fig 8.17) were Fourier analysed to give transient Φ_{ac}. This was then compared with the corresponding transient pole flux measured with a total pole flux search coil. In each case the value of k_Φ was within the range 0.93-0.97, determined from steady-state measurement. It was thus concluded that the calculated value of k_Φ (0.97) was valid during the transient period.

8.4.3 Investigation of the frequency range where transformer induction is negligible.

In section 6.11 it was shown that, provided

$$\omega b \gg \frac{db}{dt} \qquad \text{i.e.} \quad \omega \phi_{ac} \gg \frac{d\phi_{ac}}{dt}$$

in a coupling with no saturation or rotor damping,

$$\phi_{ac\,p.u.} = \lambda_{p.u.} \tag{6.28}$$

In section 8.4.2 it was verified that

$$\text{flux per pole} = \tau_\phi \phi_{ac}$$

So, for the laminated salient-pole rotor, in the linear region of the load magnetisation curve,

$$(\text{flux per pole})_{p.u.} = i_{p.u.} \tag{8.1}$$

Normally the field time constant of a commercial coupling running at rated slip (50-100 rev/min) will be greater than 0.1 s* and, consequently, the largest value of $\frac{d\phi_{ac}}{dt}$ will be $10.\ \phi_{ac}(\text{steady-state})$. So if the assumption ($\omega\phi_{ac} \gg \frac{d\phi_{ac}}{dt}$) can be verified, over a certain slip frequency range, for a coupling with a much lower field time constant and, hence, a much higher rate of change of flux, then it is reasonable to expect the assumption to apply to all commercial machines over the same frequency range.

From section 8.2.3, the field time constant of the salient-pole rotor at 100 rev/min will be approximately

$$(\tau_\ell + \tau_g) = (4.4 + 22.8) = 27.2 \text{ ms},$$

for a single field winding. (If the two field coils are connected in parallel this value is doubled: i.e. 54.4 ms). The maximum rate of change of flux will thus be $36.7.\ \phi_{ac}(\text{steady-state})$. Hence, if the assumption can be verified for the experimental

---

*The figure of 0.1 s is obtained by assuming $T \propto \phi_{ac}^3$ and the torque time constant to be 0.2 s - see chapter 5.

machine with the salient-pole rotor, using one field coil, it will also be valid for the experimental Lundell rotor, which has a much higher field time constant, as well as most other commercial machines.

An experiment was designed to investigate the frequency range over which (8.1) is valid. The step response of excitation current and pole flux was recorded simultaneously on a multi-channel storage oscilloscope for a range of slip speeds, with the input amplifier gains so adjusted that the steady-state traces of flux and current were of equal amplitude. If the height of the steady-state trace is taken as unity then this gives a direct indication of per-unit flux and current.

To avoid saturation and excessive speed regulation at low slip, the field voltage step was limited to 11.65 V (0.5 A steady-state field current).

Figure 8.18 shows the per-unit flux and current response over the slip range 0-1000 rev/min (0-100 Hz)*. At standstill there is a considerable time lag between flux and current due to the damping effect of the solid iron drum. The current response curve is not exponential but exhibits the well known "current jump"[26,30,33] at the instant of applying the voltage step. The 10, 20 and 50 rev/min (1,2 and 5 Hz) traces show a continuous reduction in lag until, at 100 rev/min (10 Hz), the flux and current traces are almost co-incident. The 400 and 1000 rev/min (40 and 100 Hz) response curves show no trace of drum damping whatsoever.

From fig 8.18 it is clear that the assumption of negligible transformer induction is valid for slip frequencies in

---

*For a 12 pole machine the frequency of drum currents is $\frac{n}{10}$.

excess of 5 Hz for the salient-pole coupling. For commercial machines with larger field time constants the assumption may be valid for lower frequencies.

The way in which drum damping reduces as frequency increases can be qualitatively explained in terms of the "drum time constant". As frequency increases, the depth to which flux penetrates the drum, and hence the permeance of the drum flux path, reduces. Hence the drum self inductance, which depends on this permeance, reduces with frequency. On the other hand, the resistance of the drum will increase with frequency, because of the reduction in the sectional area of the eddy-current paths. The "drum time constant", which may be defined as the ratio of drum inductance and resistance, will thus reduce rapidly with increasing frequency. This time constant is a measure of the drum damping and, hence, it can be seen that the amount of drum damping will be reduced as the frequency increases.

8.5 Measurement and calculation of linear time constants.

8.5.1 Standstill time constants.

Because of the simple magnetic geometry of the salient pole rotor, it is easy to calculate the linear standstill time constants, τ_{go} and τ_{ℓ}, directly from design data.[48]

The calculated time constants of a single coil are

$$\tau_{go} = 37.4 \text{ ms} \quad \text{and} \quad \tau_{\ell} = 3.18 \text{ ms.}$$

The standstill time constant of the field winding, neglecting drum damping, is thus

$$(\tau_{go} + \tau_{\ell}) = 40.58 \text{ ms.}$$

Before fitting the laminated rotor in the experimental machine, the rotor was fitted inside the model laminated drum

(see section 7.2.4)to test the effectiveness of the system of laminations. At the same time the time constant of a single coil was measured from an oscillogram of the field current response and found to be

$$(\tau_{go} + \tau_{\ell}) = 42.5 \text{ ms.}$$

The external resistance of the excitation circuit was 0.65 mΩ. This will introduce errors in the measured time constant of 0.31% and 0.62% respectively for the single coil and parallel coil field connections. Since the time constants are obtained from recorded response curves where the possible experimental error is about 3%, the effect of the external resistance was ignored.

In section 8.23 the standstill time constant was calculated from the measured standstill magnetisation curves as

$$(\tau_{go} + \tau_{\ell}) = 41.42 \text{ ms.}$$

This is a convincing cross-check on the measured value: the difference of 2.7% is almost certainly due to experimental error.

The calculated value of 40.58 ms (4.5% error) indicates the accuracy with which it is possible to design salient-pole rotors, using Phol's method for estimating the leakage permeance.[48]

The measured time constant with two coils in parallel was 83.7 ms. Assuming perfect coupling between the field windings, we would expect a value of 85 ms from the measured time constant of the single coil. This is excellent correlation and supports the results of section 7.5.3, where the coils were found to be effectively 100% coupled from the results of a d.c. test where the coils were connected in opposite magnetic polarity.

8.5.2 Variation of the linear coupled time constant, τ_g, with slip speed.

The field time constant ($\tau_g + \tau_\ell$), at a given slip speed, was obtained from the recorded step response of pole flux. A voltage step was applied to one of the field coils with the other open-circuited. The step was limited to 23.3 V (1 A steady-state current) to avoid saturation.

The leakage time constant, τ_ℓ, obtained from the stand-still magnetisation curves (i.e. 3.42 ms from section 8.2.3), was subtracted from the measured field time constant to give τ_g.

The tests were carried out over the slip speed range, 50-1500 rev/min, using a storage oscilloscope to record the flux response.

The coupled time constant, τ_g, was calculated over the same speed range by the normalised curve method of section 6.15.1. The value of n_m used was that corresponding to a field current of 1 A (i.e. 320 rev/min). τ_{go} was taken as the calculated value of 37.4 ms.

The calculated and measured time constants are plotted in fig 8.19, together with the time constants obtained from the load magnetisation curves which are summarised in table 8.1.

Although the predicted variation of τ_g with slip is correct, the calculated values of τ_g are approximately 15-25% pessimistic, the error increasing with slip. Now the chosen value of n_m will tend to produce a low estimate of τ_g, but the measured values of τ_g are lower than the calculated values. The error does not therefore lie in the choice of n_m. Since the shape of the τ_g -n curve is correct, the error does not lie with the normalised flux curve. The calculated standstill

time constant, τ_{go}, has been shown to correspond closely (within 2%) to the measured value; so the error is not in τ_{go}. Hence the source of error must be the constant (0.54) in (6.40):

$$\frac{\tau_g}{\tau_{go}} = 0.54 . \frac{\phi_{ac}}{\phi_{acm}} \qquad (6.40)$$

From the results summarised in fig 8.10 it is apparent that the average experimental ratio of $\frac{\phi_{acm}}{\phi_{aco}}$ over the excitation range is 0.5, rather than the theoretical value of 0.54. If (6.40) is now modified to

$$\frac{\tau_g}{\tau_{go}} = 0.5 . \frac{\phi_{ac}}{\phi_{acm}} \qquad (8.2)$$

and used to calculate τ_g, with the values of τ_{go} and n_m used previously, we obtain the curve shown in dotted outline in fig 8.19.

The correlation with the measured time constants is now more precise: the error is within the range 6-13%, with the maximum error at high slip speed.

Considering the complexity of the problem and the simplicity of the method of calculating τ_g, the correlation between theory and experiment must be considered good, particularly when it is remembered that the theoretical curve (solid line in fig 8.19) was calculated purely from design data, with no experimental information whatsoever. The best correlation is obtained at low slip, which is the operating region of practical importance.

Considerably better results are obtained if (8.2) is used to calculate the time constants. Although there is no general experimental justification for using a constant of 0.5 rather than 0.54, James' work[14] (fig 3.8) on a Lundell endring coupling, shows that $\frac{\phi_{acm}}{\phi_{aco}}$ is closer to 0.5 than 0.54. Also, from unpublished data on low excitation transients in commercial

couplings without endrings,* it would seem that (8.2) gives consistently better results than (6.40) in practice.

The experimental time constants correlate closely with those taken from table 8.1, except for one bad point at 1500 rev/min. The author is unable to explain this sudden divergence at 1500 rev/min, but in view of the close and consistent correlation over the rest of the speed range, it is unlikely that the discrepancy represents any unaccounted source of damping.

8.6 Torque response experiments.

8.6.1 Linear transients.

With the field coils connected in parallel, the response of torque to a 11.65 V step of field voltage (1 A steady-state field current) was recorded at slip speeds in the range 50-1000 rev/min.

The torque response curves were recorded on an ultra-violet (u.v) recorder. To enable the use of a galvanometer with adequate frequency response, it was necessary to amplify the torque signal at the stage between the torque indicator unit and the recorder. The step response of the torque measuring system was obtained by applying a 10 mV voltage step to the input terminals of the indicator unit. The resulting u.v. recording showed a very small overshoot which persisted for less than 1 ms. It was thus decided that the system was capable of accurately recording the transient torque response. However, as a check, the torque response was also recorded simultaneously on a storage oscilloscope. No significant differences were observed.

---

*Redman Heenan Froude Technical Library.

The measured torque response curves are plotted in figs 8.20 a-f with the instantaneous torque as a per-unit of the steady-state torque. Calculated torque response is also plotted in the same figures for comparison. The torque response was calculated by the procedure outlined in section 6.17.1. Since the field was connected in parallel, the time constant, τ_f, was obtained by doubling the values taken from the curve of calculated time constants (using the theoretical constant of 0.54) in fig 8.9. The leakage time constant was taken as double the value calculated in section 8.5.1. i.e. τ_l = 6.36 ms. The flux index was the theoretical value for m = 0.77 i.e. $\frac{2m}{2m - 1}$ = 2.85. The predicted response curves are therefore derived on a purely theoretical basis.

The overall correlation between predicted and measured torque response is good. The theoretical responses have the correct shape and predict the 'torque lag' (see chapter 5) which persists for about 10 ms. In every case the predicted response is slower than the measured response. For design studies this inherent pessimism is preferable to an optimistic response prediction.

An indication of the error in the predicted response can be obtained by comparing the measured and predicted 'torque time constants' (i.e. the time for the per-unit torque to reach 0.632). These are given in table 8.6.

The two sources of error in the torque response calculation are the time constant ($\tau_f + \tau_l$) and the flux index ($\frac{2m}{2m - 1}$). Although the two errors are related, since τ_f is obtained from the normalised flux curve for m = 0.77, they can be considered separately since the normalised flux curve is relatively insensitive to the value of 'm'.

TABLE 8.6

MEASURED AND CALCULATED
'TORQUE TIME CONSTANTS'

n, rev/min	Time Constant; ms	
	Measured	Calculated.
50	108	128
100	100	113
200	80	100
400	68	80
800	56	65
1000	46	53

At low slips the error due to the flux index may be appreciable, since the steady-state experimental work (see section 8.2.6) has shown that the index is significantly less than the theoretical value of 2.85 (e.g. index = 2.35 at 50 rev/min). At high slips, however, the measured index is close to the theoretical value and the error in torque response should then be small.

In section 8.5.2. it was shown that the error in the calculated time constant increased with slip. Thus, conversely to the error associated with the flux index, the error due to the time constant will predominate as slip increases.

It is thus logical to expect significant 'index error' in the torque response at low slip and significant 'time constant error' at high slip.

To investigate these errors, the torque response curves at 50 and 1000 rev/min were recalculated, first using the measured indices (from fig 8.12) and the theoretical time constants, and then using measured indices and measured time constants.

The 50 rev/min response, calculated with the measured index of 2.35 and the theoretical time constant, is shown in dotted outline in fig 8.20a. The predicted curve now corresponds much more closely to the experimental curve, indicating a significant index error in the theoretical curve. The calculated response, using the measured values of both index and time constant, is almost identical to the measured response. (Calculated points are shown on fig 8.20a).

The equivalent calculated responses for 1000 rev/min are shown in fig 8.20f. Substituting the measuring index of 2.7 for the theoretical index of 2.85 affects only a small improvement to the theoretical curve. However, when the measured time constant is used, the calculated points fall almost exactly on the measured response curve.

These results prove conclusively that the discrepancy between the theoretical and experimental responses is due to the combined effect of index error and time constant error. They also show that, at low slip, index error is the dominant effect whilst, at high slip, time constant error predominates.

In practice, interest is centred on the low slip operating region where a commercial drive will normally be rated. The index error at low slip is due to uncertainty in the value of 'm'. Both Davies[12] and James[14] suggest that m = 0.77 should be used for $\frac{n}{n_m} > 0.2$. For lower normalised slips, "Judgement is needed in deciding ..... (the value of 'm') ..... to use; experience of the type of coupling must be used, taking into account the value of n_m for which it has been designed".[12]

8.6.2 Large scale linear transients at low slip.

The low slip load magnetisation curves are approximately linear up to much higher excitation currents than are the high slip magnetisation curves. Thus, at low slip speeds, the normalised time constant method can be applied to large scale transients, without resorting to a piecewise linear solution of the flux differential equation.

The response of torque to a voltage step of 29.1 V (2.5 A steady-state field current), at 50 rev/min, and 23.3 V (2.0 A steady-state field current), at 100 rev/min, was recorded and compared with the theoretical response. The measured response curves and calculated points are shown in fig 8.21.

The correlation between the theoretical and experimental responses is excellent. In the case of the transient at 100 rev/min, the correlation is almost exact.

The reason for the improved correlation, compared with the results of the previous section, at these higher voltage signals (compare fig 8.21 with figs 8.20a and 8.20b) is that the values of n_m used in the calculations are lower, since they correspond to higher excitation currents.[12] The increased value of $\frac{\eta}{n_m}$ reduces $\frac{\phi_{ac}}{\phi_{acm}}$ and, hence, reduces the calculated coupled time constant, τ_g. The experimental and theoretical time constants are

50 rev/min: τ_g = 55.6 ms (theoretical), 54 ms (measured)

100 rev/min: τ_g = 46.4 ms (theoretical), 45 ms (measured).

The only significant errors in the predicted response curves occur early in the transient period, when the excitation current is low and it is not valid to use m = 0.77.

8.6.3 Incremental variations of torque.

The response of pole flux and torque to a voltage step between 29 and 41 V was recorded over the slip speed range of 50 to 1000 rev/min. The field coils were connected in parallel.

Torque response was predicted by the procedure outlined in section 6.17.2. The field current excursion range was 2.5-3.5 A and so n_m was chosen corresponding to 3.0 A i.e. n_m = 125 rev/min.

The calculated and measured coupled time constants and total time constants are summarised in table 8.7. The experimental coupled time constants were obtained by subtracting the measured leakage time constant (6.8 ms from section 8.2.3) from the measured flux time constant.

TABLE 8.7

MEASURED AND CALCULATED INCREMENTAL TIME CONSTANTS

n, rev/min	Coupled time constants, ms		Total time constant, ms	
	Experimental	Calculated	Experimental	Calculated
50	28.2	23.1	35	29.4
100	14.2	19.4	21	25.8
200	11.7	14.8	18.5	21.2
400	7.7	11.2	14.5	17.6
1000	6.2	7.6	13	14

The correlation between measured and calculated coupled time constants is not very good (up to 45% error). However the leakage time constant is of the same order of magnitude as the coupled time constant and, when they are added to produce the total time constant, the error in the total time constant is much less.

Typical incremental torque responses are shown in fig 8.22.

The incremental torque responses are subject to the same errors as the linear torque responses (i.e. time constant error and index error) plus error in the p.u. initial torque. However the correlation between measured and calculated response is good and demonstrates that the theory is extendable to the piecewise linear solution of large scale transients.

8.7 Conclusions.

The experimental work described in this chapter has proven that the theory of torque response is valid for a machine with no eddy-current damping on the rotor.

The accuracy with which torque response can be predicted is adequate for design studies and is certainly superior to that obtained using any existing technique.

It has been shown that the drum has negligible effect on response time and that attention should, therefore, be focused on the rotor parameters, when designing a coupling to meet predefined response times.

The fact that the drum has little effect on transient performance means that copper-faced couplings should have the same response times as otherwise identical conventional machines. This is borne out in practice (see section 2.2) and so the methods of calculating torque response, outlined in chapter 6, will be equally applicable to copper-faced couplings or machines with similar drum constructions.

CHAPTER 9.

EXPERIMENTS WITH THE P.I. ROTOR.

9. Experiments with the p.i. rotor.

9.1 Introduction.

The main objectives of this chapter are to compare the performance of the experimental coupling, when fitted to the s.p. and p.i. rotors, and to assess the effect of the eddy-currents induced in the solid p.i. rotor during the transient period.

The flux response tests, to measure the eddy-current damping time constant, τ_d , are limited to the linear regions of the load magnetisation curves, for which the various machine time constants are defined.

Because of the complex magnetic geometry of the p.i. rotor, it is beyond the scope of this work to attempt torque response calculations in the manner of chapters 6 and 8. This would require an investigation into the effect of the complicated inductor permeance pattern on the response of the machine; each permeance term will be associated with a different time constant. In addition to this it would be essential to analyse the end effects of the p.i. rotor. These are extremely complex, since the end region of one pole pattern (Lundell or inductor) overlaps the active region of the other. One of the basic assumptions of Gibb's end effect theory[3] is that end region currents are linked only by their own flux (see chapter 1), but the end region currents of the inductor pattern will be linked by the flux of the Lundell poles; the overlapping end regions will not, therefore, be Laplacean and Gibbs' analysis will not apply. No other theory of end-effects is apparently extendable to p.i. machines and so, at the present time, we must conclude that the transient theory of chapter 6 is not directly

applicable to p.i. couplings.

The comparison of the torque response of the s.p. and p.i. rotors is, therefore, on a purely experimental basis.

9.2 Steady-state experiments.

9.2.1 Torque-slip curves.

The recorded torque-slip curves are shown in fig 9.1 As with the measurement of the s.p. rotor torque-slip curves (section 8.2.1), each test was commenced with the outer surface of the drum at a temperature of 45°C. The maximum temperature rise during a run was again 10°C, representing a torque reduction of 5% due to temperature effects.

9.2.2 Variation of flux with excitation m.m.f. and slip speed.

Core flux, pole flux, Lundell region and inductor region flux were measured over a range of excitations and slips, using the search coils described in chapter 7. Leakage flux was obtained by subtracting the measured pole flux from the core flux.

Curves of core flux and leakage flux are shown in fig 9.2. As with the s.p. rotor, the leakage flux and excitation m.m.f. are related by a constant which is effectively independent of slip. The leakage flux is 17% of the core flux over the linear region. When saturation sets in, the leakage rises to about 28%.

Figures 9.3 and 9.4 show curves of Lundell and inductor region flux respectively. At standstill the inductor flux is 27% higher than the Lundell flux. Since the poles are 50% interdigitated and parallel, this means that the inductor

flux-density is 1.27 times the Lundell flux-density. This initial unbalance is due to the radial taper of the rotor teeth, causing saturation in the Lundell part of the poles.

The degree of unbalance increases with slip speed until the inductor flux is about twice the Lundell flux at 1500 rev/min. This is because the inductor flux is less efficient in inducing eddy-currents in the drum and is, therefore, subject to a lower demagnetising (armature reaction) m.m.f. than the Lundell flux.

9.3 Comparison of the steady-state performance of the s.p. and p.i. rotors.

Figure 9.5 shows that, at standstill, for the same m.m.f. per pole, the s.p. rotor produces roughly 25% more flux per pole than the p.i. rotor. The p.i. rotor utilizes this flux less effectively because of the 50% interdigitation and hence developes less torque, for a given slip, than the s.p. rotor. This is shown in fig 9.6 which shows torque-slip curves at rated excitation (300 AT/pole) and 40% of rated excitation.

At rated excitation and slip (100 rev/min) the s.p. rotor torque is 50% more than the p.i. rotor torque; at 60 rev/min slip (a preferable working point) the s.p. torque is 80% more than the p.i. torque.

As slip speed increases, the s.p. torque falls off more rapidly than the p.i. torque, but is still more than the p.i. torque at 1400 rev/min (typical 50 Hz, 4 pole drive speed).

The reason that the p.i. torque remains more constant is that the inductor part of the pole is subject to less armature reaction than a salient pole of the same $\frac{\text{pole arc}}{\text{pole pitch}}$. The

inductor pole flux therefore 'flattens out' the p.i. rotor torque-slip curve. In addition to this, the Lundell part of the p.i. poles will have an end effect which will also tend to flatten the p.i. rotor torque-slip curve.

However, even at 2200 rev/min slip (the maximum speed of the d.c. drive machine), the s.p. torque was still slightly more than the p.i. torque. Thus, over the practical slip range of the coupling, the performance of the s.p. rotor is significantly superior to the p.i. rotor. In the low slip region, which is the most important, the performance of the s.p. rotor is dramatically superior.

9.4 Time constants of the p.i. rotor.

The nett flux time constant, with zero drum damping, can be written as

$$\sum\tau = \tau_{gp} + \tau_{\ell} + \tau_{d}$$

where τ_{gp} here signifies the time constant associated with the total flux per pole (i.e. Lundell plus inductor). τ_{gp} and τ_{ℓ} can be found from the slopes of the load magnetisation curves:

$$\tau = \frac{2pN}{R} \frac{\text{flux per pole}}{i}$$

Having found $(\tau_{gp} + \tau_{\ell})$, τ_{d} can be obtained by measuring the core flux time constant with zero drum damping (i.e. $\sum\tau$) and subtracting $(\tau_{gp} + \tau_{\ell})$ from this.

To simulate the condition of zero drum damping, the p.i. rotor was mounted concentrically in the model laminated drum (see section 7.4.2).

A steady-state core flux magnetisation curve was measured and found, over the linear region, to correspond, within 2%, to the core flux curve shown in fig 9.2. The winding time constant

($\tau_{gp} + \tau_{\ell}$), from this curve, was 0.6 s.

The response of core flux to a voltage step of 15 V was then recorded. From the recording, the core flux time constant ($\sum\tau$) was found to be 0.71 s.

The damper time constant was thus (0.71 - 0.6 = 0.11 s).

It is assumed that τ_d is independent of slip, so this value can be used to estimate the nett flux time constant under slip conditions. The expression used to calculate the nett time constant was:

$$\sum\tau = \frac{2pN}{R} \cdot \frac{\text{core flux per pole}}{i} + 0.11 \qquad (9.1)$$

The p.i. rotor was mounted in the experimental coupling and the core flux response to an 8 V step of field voltage was recorded at slip speeds over the range 50-1500 rev/min.

The time constants, obtained from the core flux response curves, are compared with the predicted time constants, obtained from (9.1), in table 9.1.

TABLE 9.1

PREDICTED AND MEASURED CORE FLUX TIME CONSTANTS AT VARIOUS SLIPS

n, rev/min	Measured time constant, s	Predicted time constant, s
50	0.61	0.59
100	0.54	0.51
200	0.48	0.46
400	0.39	0.40
1000	0.33	0.35
1500	0.29	0.32

The correlation is good, indicating that the assumptions of negligible drum damping and constant τ_d are substantially valid for the p.i. coupling. It is, however, interesting to examine the trend of table 9.1: at low slips the measured time constant is greater than the predicted value, indicating a possible small drum damping effect; in the middle of the slip range, correlation is almost exact, indicating no extra source of damping; at high slips the measured value is less than the predicted value, which suggests that the damper time constant is reducing, due, possibly, to armature reaction effects.

Response curves of field current were also recorded over the same slip speed range to test the assumption that the equivalent damper winding is perfectly coupled with the field winding. Figures 9.7a and 9.7b show the current responses at 50 and 400 rev/min. In each case the "current jump" is quite distinct, indicating that there is negligible leakage between the field current and the damper currents.

The current responses can also be used as a check on the measured damper time constant, since the per-unit amplitude of the current jump is related to the damper and field time constants:

$$\frac{i_f(0)}{i_f(\infty)} = \frac{\tau_d}{\sum \tau}$$

From figs 9.7a and 9.7b we have,

$$\text{50 rev/min:} \quad \frac{i_f(0)}{i_f(\infty)} = 0{\cdot}2$$

$$\text{400 rev/min:} \quad \frac{i_f(0)}{i_f(\infty)} = 0{\cdot}25$$

Multiplying these values by the measured time constants given

in table 9.1 we obtain,

$$50 \text{ rev/min: } \tau_d = 0.2 \times 0.61 = 0.12 \text{ s.}$$

$$400 \text{ rev/min: } \tau_d = 0.25 \times 0.39 = 0.098 \text{ s.}$$

The correlation with the measured value of 0.11 s is quite good, considering the possible errors involved in reading off the response oscillograms.

9.5 Comparative torque response experiments.

The linear torque response tests, described in section 8.6.1 were repeated for the p.i. rotor. The field voltage signal was a 8.2 V step (100 AT/pole steady-state field m.m.f.).

The measured per-unit torque responses for the p.i. rotor are shown together with those for the s.p. rotor, taken from fig 8.20, in figs 9.8 a-d. The measured torque time constants are compared in table 9.2.

TABLE 9.2

TORQUE TIME CONSTANTS FOR
THE P.I. AND S.P. ROTORS.

n, rev/min	Time Constant, s	
	S.P. Rotor	P.I. Rotor
50	0.108	0.90
100	0.100	0.85
400	0.068	0.60
1000	0.046	0.54

The torque response of the s.p. rotor is dramatically superior to the p.i. rotor. There are two main reasons for this: the field windings have different time constants and the p.i. rotor is subject to eddy-current damping.

The major influence on the torque response is the winding time constant (430 and 55.2 ms respectively, for the p.i. and s.p. rotors at 100 rev/min) and it could be argued that the improved transient response of the s.p. rotor was achieved simply at the expense of extra I^2R loss in the s.p. rotor field coil. However, at 100 rev/min, the p.i. rotor damping time constant alone is twice the time constant of the s.p. rotor; so, even if the winding time constants of the two rotors were equal, the nett time constant of the p.i. coupling would be much greater than that of the s.p. coupling.

It can thus be seen that the eddy-currents induced in the solid rotor during the transient period have a significant effect on the transient response of the coupling.

The standstill winding time constant of a coupling is directly related to the power rating of the winding (and hence the power rating of the controller[49]) and the steady-state peak torque which the machine is required to deliver.

$P_f = I^2R \propto F_g^2 \frac{R}{N^2}$, where P_f is the power rating of the field, and $\tau_{go}+\tau_L = \frac{N^2\Lambda}{R}$

Therefore $P_f \propto \frac{F_g^2\Lambda}{\tau_{go}+\tau_L}$

But[8] $F_g^2\Lambda \propto T_m$,

and hence $P_f \propto \frac{T_m}{\tau_{go}+\tau_L}$

So, for a given T_m, the minimum response time that can be achieved is limited by the rating of the excitation coil and it's controller. This means that fast response couplings will have inherently highly rated field windings. It is not, therefore,

possible, without resorting to forcing techniques, to design a coupling for both fast response and low control power. However, this is not a practical limitation on the design of fast response couplings, since the field power will only be a fraction of the drive power, even when designed to give very low response times.[49]

9.6 Suggestions for further work on the transient performance of eddy-current couplings.

Much work needs to be done on the transient performance of couplings with inductor or partially-interdigitated rotors. The effect on torque of the different components of flux produced by these rotors must be evaluated. However it seems clear, even at this stage, that inductor type machines must have an inherently poor transient response, since they will have a time constant associated with a component of flux (the mean airgap flux) which produces no torque. The effect of the mean gap flux time constant will depend on the "flux utilisation factor",[3] ϵ, for which the rotor has been designed. An analysis which relates torque response to ϵ would be extremely valuable.

The theory of chapter 6 neglects end-effects. An investigation into transient end effects may therefore be required in the future. However, since it has been shown that the drum may be considered as progressing through a series of steady-state modes, it is logical to expect that the usual end-effect treatment[3] will be adequate for transient conditions. This could be verified simply by fitting the experimental coupling with a homogeneous iron drum (i.e. without endrings).

This thesis has dealt only with transients at constant

slip speed. The next stage in developing a complete mathematical model of the machine will be an investigation of speed transients under various load constraints. This work, together with the accurate definition of load parameters (e.g. friction coefficients, compliance etc), should then enable the accurate simulation of a coupling drive.

The techniques required for the digital simulation of a coupling drive should be broadly the same as those demonstrated by Johnson[45] in the simulation of a single axis d.c. machine. However, a major difficulty in predicting the performance of the machine at low slip will be the simulation of transfer functions of the type given in (6.20) to (6.22), where drum effects are included.

The development of a reliable mathematical model for the machine will enable the prediction of control strategies for complex duty cycles. The index of performance can be defined as a surface in control space with dimensions of torque, slip speed and reference signal. The optimisation technique described by Johnson[45] would then seem to lend itself admirably to the prediction of control strategy.

9.7 Conclusions.

The part of the thesis dealing with transient performance has presented a theory of torque response at constant slip and the results of a programme of experiments designed to test the theory.

The results have shown that the theory is substantially valid and predicts torque response in the linear region of the load magnetisation curve with sufficient accuracy for most

engineering problems. It has been demonstrated (in section 8.6.3) that the method of predicting torque response is extendable, on a piecewise linear basis, to large scale transients which force the rotor into magnetic saturation. The theory should thus form a sound basis for design and simulation studies.

REFERENCES.

References

1. Rudenburg, R. :"Energie der Wirblestrome in elektrischen Bremsen und Dynamomaschinen", Sammlung Elektrotechnischer Vortrage, 1906, p 269.

2. Rosenburg, E.:"Wirblestrome in massiven Eisen", Elektrotechnik und Maschinenbau, 1923, V41, No.49, p 1055.

3. Gibbs, W.J.:"The theory and design of eddy-current slip couplings", BEAMA Journal, 1946, pp 123,172,219.

4. Sharov, V.:"Armature reaction of massive iron in electromagnetic slip couplings", Elektrichestvo, 1956, No.10, p 42.

5. Glazenko, T.A.:"Some design problems of an asynchronous clutch with a solid mass rotor", Arotomatika i Telemekhanita, 1958, V19, No.8 p 800.

6. Davies E.J.:"Two experimental studies in dynamoelectric machinery", part one, Ph.D. thesis, University of Bristol, 1961.

7. Erdelyi, E.A., and Kolatorowicz, E.E.:"Model laws of eddy-current couplings for aircraft alternator drives", Trans I.E.E.E., P.A.S, V79, 1961, p 438.

8. Davies, E.J.:"An experimental and theoretical study of eddy-current couplings and brakes", ibid, V82, 1963, p 401.

9. Malti, M.G., and Ramakumar, R.:"Three dimensional theory of the eddy-current coupling", ibid p 793.

10. Hansen, A., and Timmler, W.R.:"Theory of eddy-current couplings - unidirectional flux type", ibid p 436.

11. Gonnen, D., and Striker, S.:"Analysis of an eddy-current brake", ibid, V84, 1965, p 357.

12. Davies, E.J.:"General theory of eddy-current couplings and brakes", Proc I.E.E., V133, 1966, p 825.

13. Bahler, W., and van der Hoek, W.:"An eddy-current coupling used as a variable speed drive", Phillips Technical Review, V27, 1966, p 15.

14. James, B.:"Eddy-current couplings with and without endrings", M.Sc. thesis, University of Aston in Birmingham, 1969.

15. Kundu, P.:"Analysis of saturation and end effects in variable speed solid secondary couplings", Trans I.E.E.E., P.A.S, V90, 1971, p 548.

16. Davies, E.J., James, B., and Wright, M.T.:"High performance, low cost, simple eddy-current couplings",I.E.E. Conf. Publ. Oct.1972.

17. Ollendorf, F.:"Das Eindringen elektromagnetischer Wellen usw", Z.Tech. Phys. V12, 1931, p 39.

18. Fillmore, R.L.:"Calculation of eddy-current paths in drag-cup induction motor rotor", Trans. A.I.E.E. V75, III, 1956, p 922.

19. Russell, R.L., and Norsworthy, K.H.:"Eddy-currents and wall losses in screened rotor induction motors", Proc. I.E.E., 105A, 1958, p 163.

20. Guilford, E.C.:"Theory of the induction motor with conducting sleeve rotor", Trans. I.E.E.E., P.A.S., V81, 1962, p 1129.

21. West, J.C., and Hesmondhalgh, D.E.:"Analysis of thick cylinder induction motors", Proc. I.E.E., 109C, 1962, p 172.

22. Piggot,L.S.:"Theory of cylindrical rotor induction motors", ibid, p 270.

23. Jayawant, B.V., and Parr, P.J.:"Sleeve rotor induction motors for control applications", Trans. I.E.E.E., P.A.S., V88, 1969 p 1103.

24. Schelkunoff, S.A.:"The impedance concept and its application to reflection, refraction, shielding and power absorption", Bell. Tech. Journal., V17, 1938, p 17.

25. Cullen, A.L., and Barton, T.H.:"A simplified electromagnetic analysis of the induction motor using the concept of wave impedance", Proc. I.E.E., V105C, 1958, p 331.

26. Hill, B.H.:"The damping effect of solid rotors", The Electrician, V42, 1924, p 511.

27. Weber, E.:"Field transients in magnetic systems partially laminated, partially solid", Trans. A.I.E.E., V50, 1931, p 1234.

28. Wagner, C.F.:"Transients in magnetic systems", ibid, V53, 1934, p 418.

29. Phol, R.:"Rise of flux due to impact excitation: retardation by eddy-currents in solid iron parts", Proc. I.E.E., V96, II, 1949, p 57.

30. Rudenburg, R.:"Transient performance of electric power systems", McGraw Hill, 1950, Chapters 8 and 10.

31. Dunaevski, S.Y.:"The effect of eddy-currents on magnetic flux", Elektrichestvo, V8, 1951, p 55.

32. Brockman, J.J., and Linkous, C.E.:"D.C. machines: response to impact excitation", Trans. A.I.E.E., V74, 1955, p 500.

33. Fegley, K.A.:"Determining the parameters of a short-circuited winding that represents eddy-current paths", ibid, V75, 1956, p 143.

34. Kevasamurthy, N., and Rajagopalan, P.K.:"Effects of eddy-currents on the rise and decay of flux in magnetic cores", Proc. I.E.E., 109C, 1962, p 63.

35. Subba Rao, V.:"Equivalent circuit of solid iron core for impact excitation problems", ibid, III,(2), 1964, p 349.

36. Subba Rao, V., and Bhate, B.E.:"Voltage impact excitation of rectangular solid iron core, ibid, 114,(3), 1967, p 411.

37. Concordia, C., and Poritsky, H.:"Synchronous machine with solid cylindrical rotor", Trans. A.I.E.E., P.A.S., V56, 1937, p 49.

38. Concordia, C.:"Synchronous machine with solid cylindrical rotor - part II", Trans. A.I.E.E., P.A.S., V78, 1959, p 1650.

39. Say, M.G.:"Transient effects in induction motors", discussion, Proc. I.E.E., V115,(1), 1968, p 128.

40. Hamilton, H.B.:"Magnetic saturation and eddy-current effect in d.c. machine voltage build-up", Trans. I.E.E.E., P.A.S.

41. Carslaw, H.S., and Jaeger, J.C.:"Conduction of heat in solids", Oxford University Press, 1947.

42. Cullwick, E.G.:"Electromagnetism and relativity", second edition, Longmans Ltd, 1959.

43. Whittaker, E.T., and Watson, S.N.:"A course of modern analysis", fourth edition, Cambridge University Press, 1963.

44. Roberts, G.E., and Kaufman, H.:"Table of Laplace Transforms", W.B. Saunders Co., 1966.

45. Johnson, R.C.:"The single axis d.c. machine as a control system element",Ph.D. thesis, University of Aston in Birmingham, 1969.

46. Fitzgerald, A.E., and Kingsley Jr., C.:"Electric machinery", 2nd edition, McGraw Hill Book Co. Ltd, 1961.

APPENDICES.

Appendix 2

Supporting papers

"Eddy-current coupling as an industrial variable speed drive" (reference 49), Proc I.E.E., V119, (8), 1972 p 1149.

"High performance, low cost, simple eddy-current couplings" (reference 16), I.E.E., Conf. Publ. Oct. 1972.

"Economic aspects of eddy-current coupling variable speed drives" (reference 50), ibid.

FIGURE FOR CHAPTER 1.


Aston University
Illustration removed for copyright restrictions

FIGURE 1.3

FIGURES FOR CHAPTER 3.

Figure 3.1

ANALYTICAL MODEL

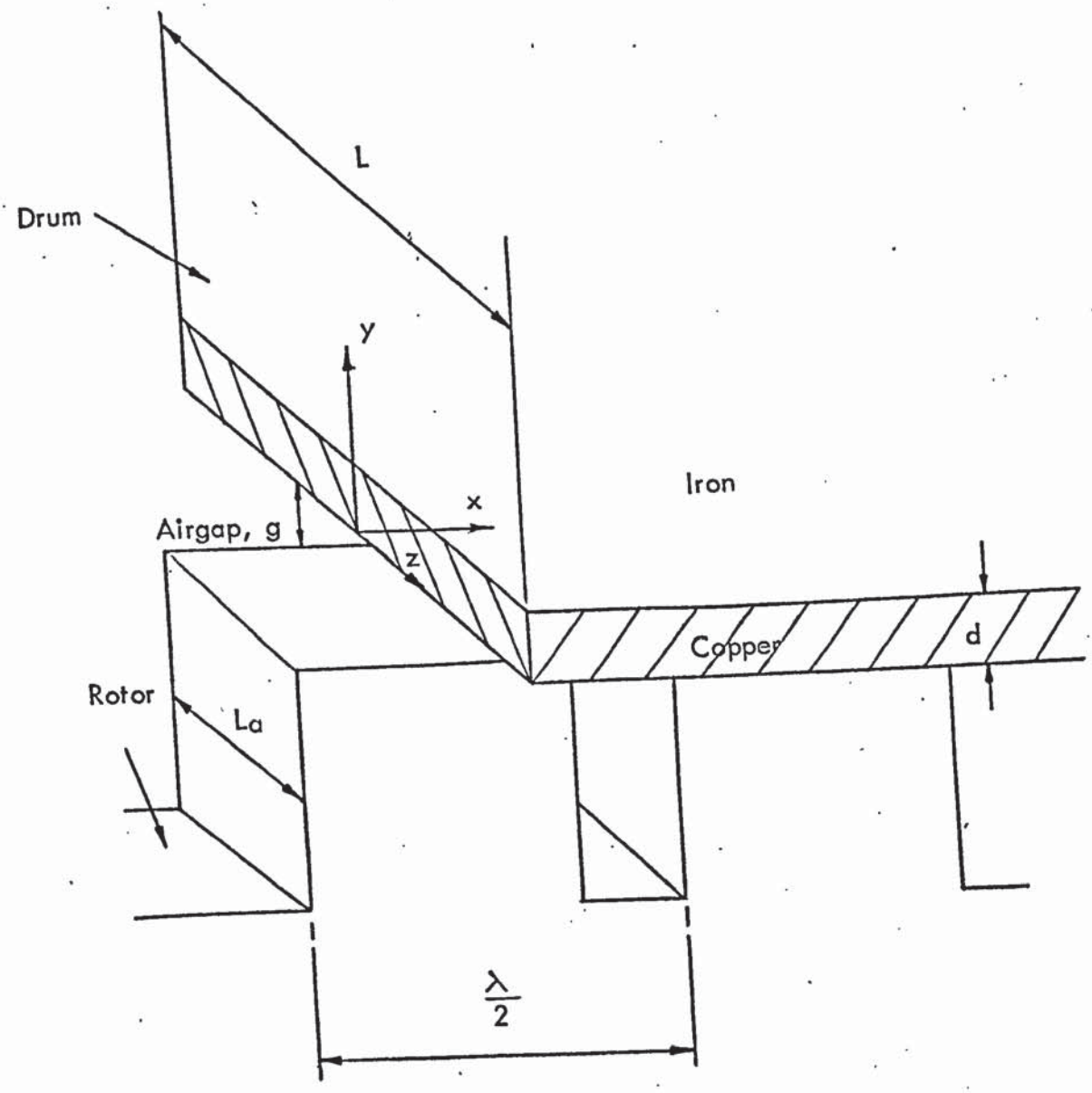

Figure 3.2

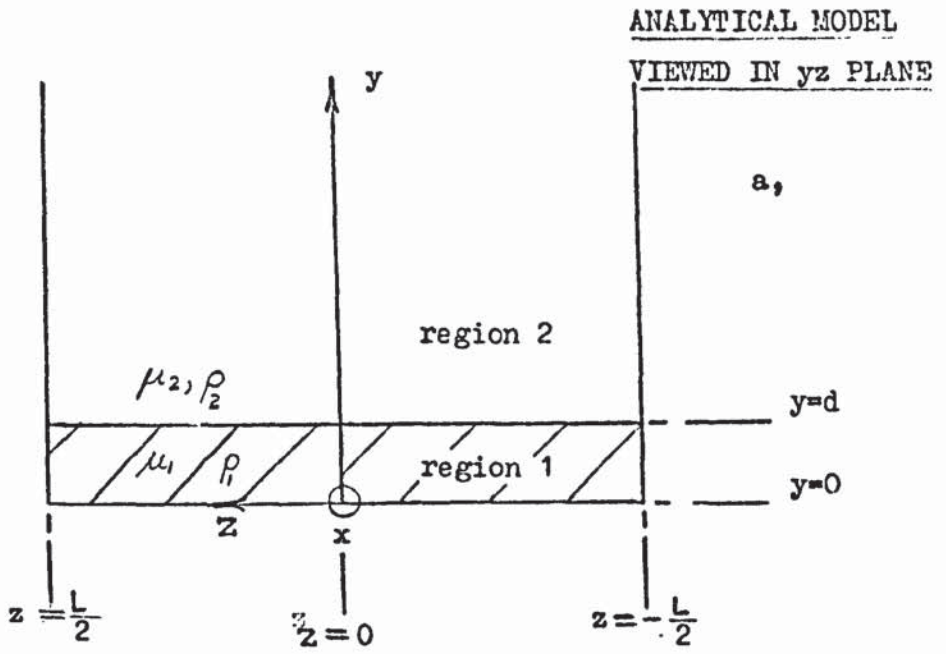
ANALYTICAL MODEL
VIEWED IN yz PLANE
a,
y
region 2
μ_2, ρ_2
y=d
μ_1 ρ_1
region 1
y=0
z
x
$z = \frac{L}{2}$
$z = 0$
$z = -\frac{L}{2}$

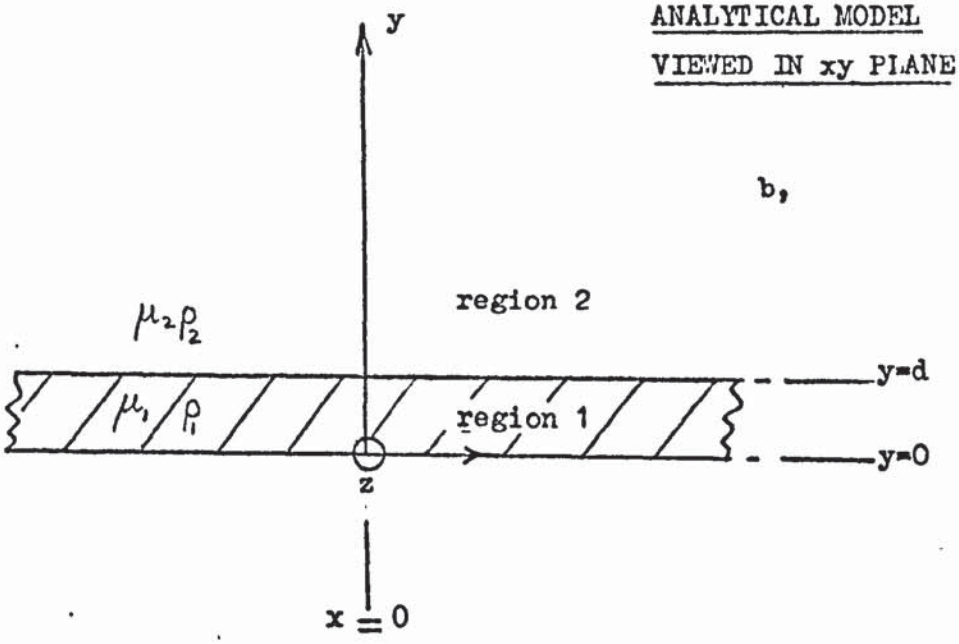
ANALYTICAL MODEL
VIEWED IN xy PLANE
b,
y
region 2
$\mu_2 \rho_2$
y=d
μ_1 ρ_1
region 1
y=0
z
x = 0

Figure 3.3

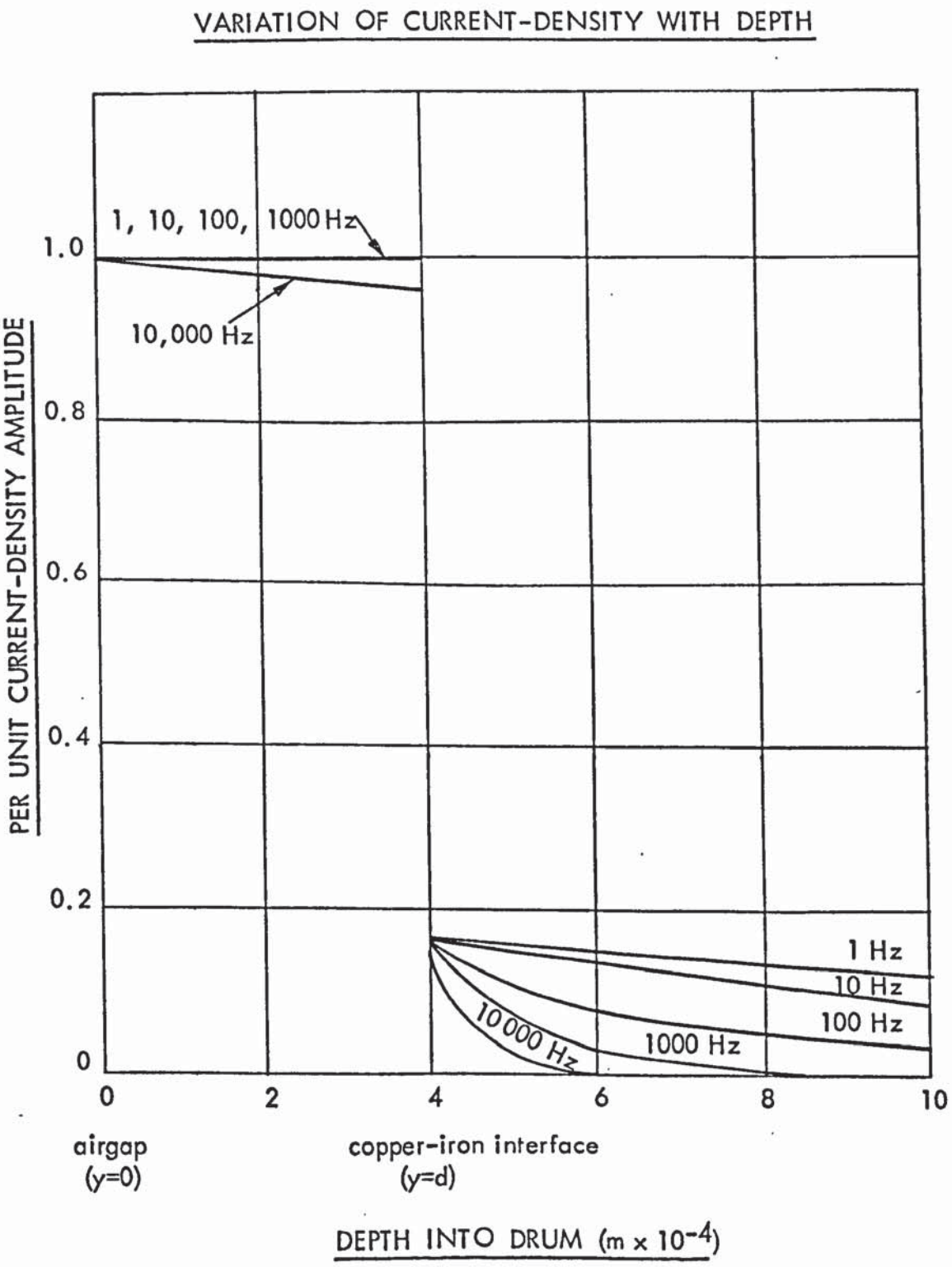
VARIATION OF CURRENT-DENSITY WITH DEPTH
PER UNIT CURRENT-DENSITY AMPLITUDE
1.0
0.8
0.6
0.4
0.2
0
1, 10, 100, 1000 Hz
10,000 Hz
1 Hz
10 Hz
100 Hz
1000 Hz
10 000 Hz
0
2
4
6
8
10
airgap
(y=0)
copper-iron interface
(y=d)
DEPTH INTO DRUM (m x 10⁻⁴)

Figure 3.4

VARIATION OF CURRENT-DENSITY WITH DEPTH FOR m = h = 7 at 10 000 Hz.

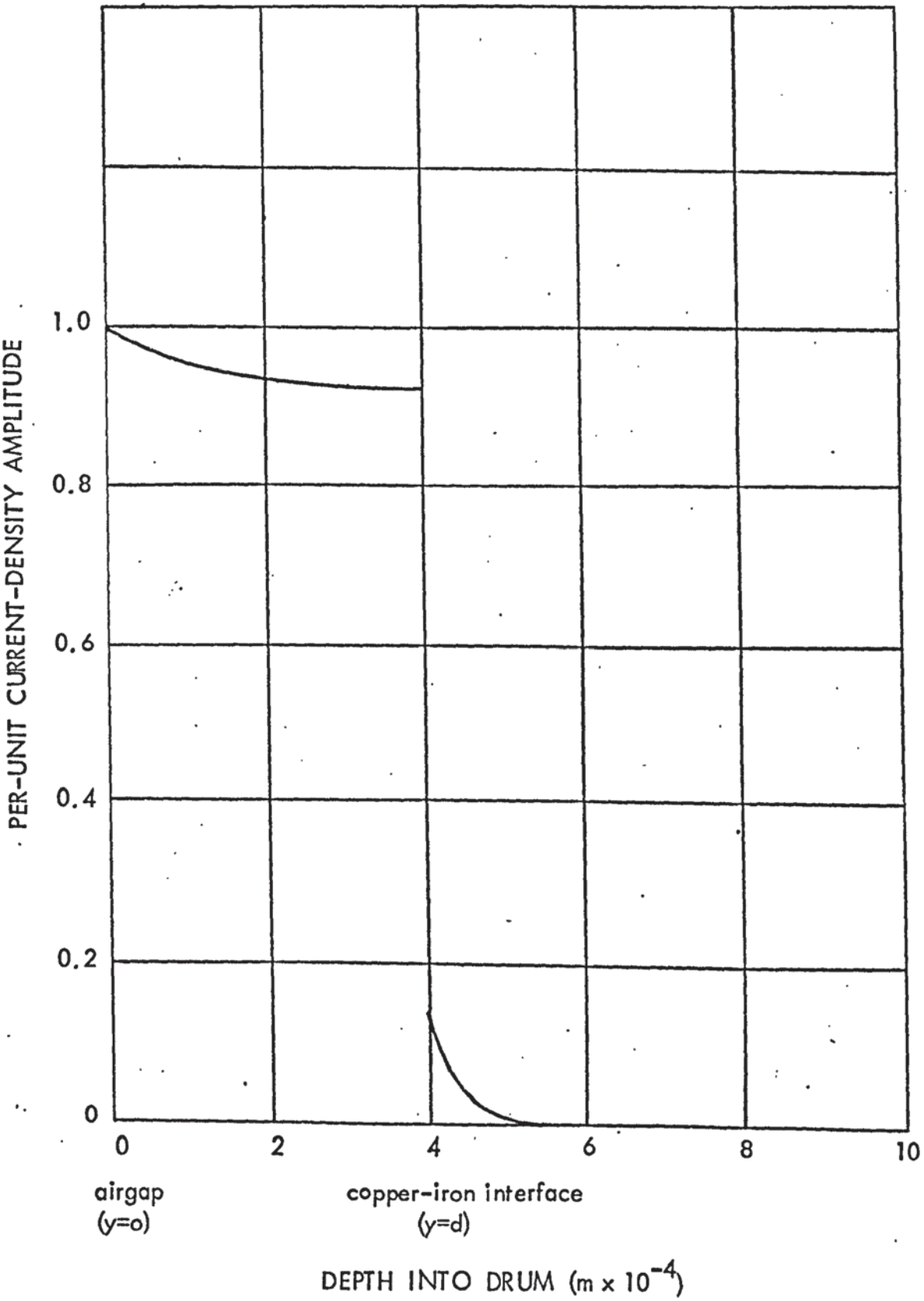

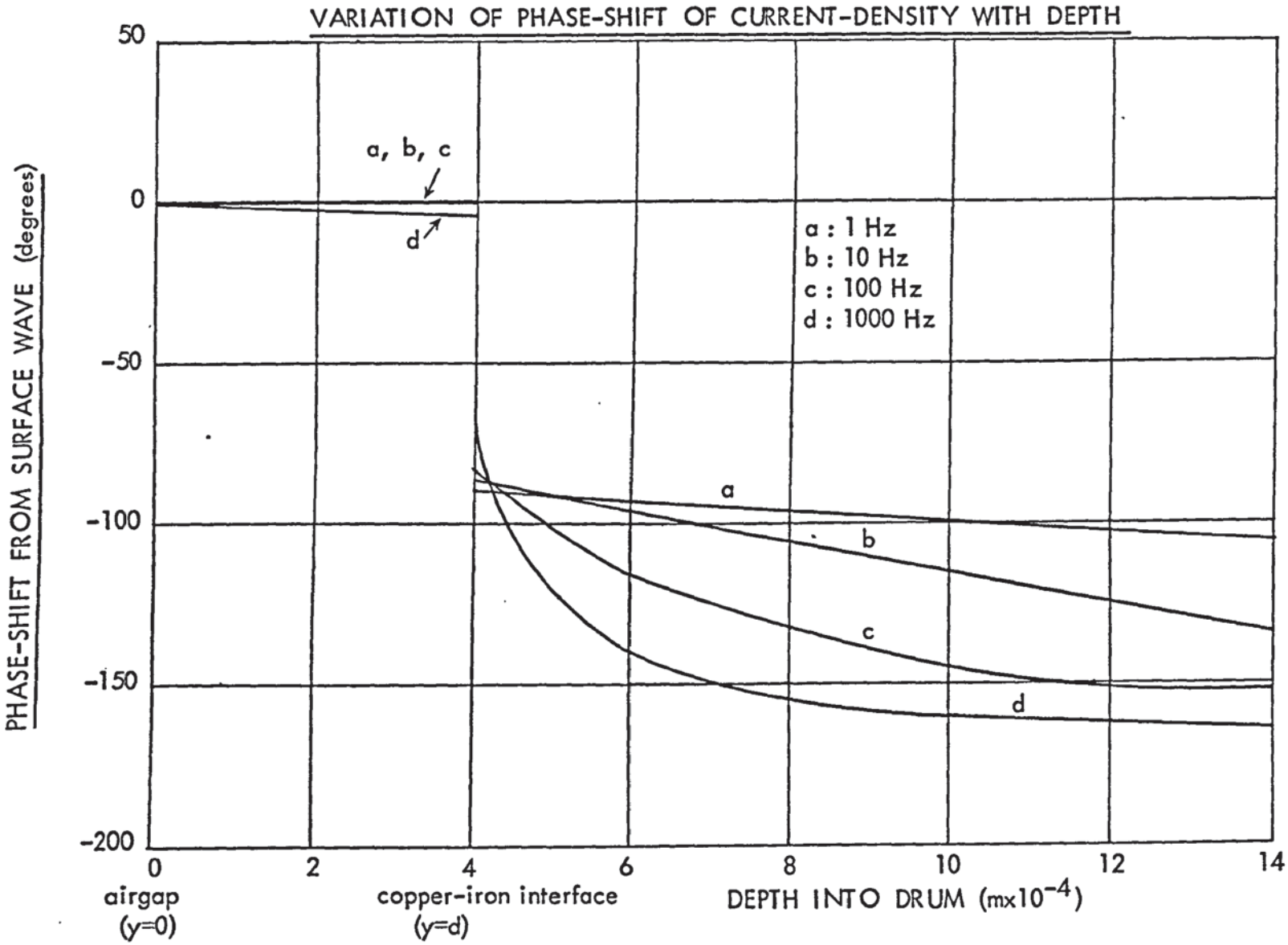
VARIATION OF PHASE-SHIFT OF CURRENT-DENSITY WITH DEPTH
PHASE-SHIFT FROM SURFACE WAVE (degrees)
50
0
-50
-100
-150
-200
a, b, c
d
a : 1 Hz
b : 10 Hz
c : 100 Hz
d : 1000 Hz
a
b
c
d
0
2
4
6
8
10
12
14
airgap
(y=0)
copper-iron interface
(y=d)
DEPTH INTO DRUM (mx10^{-4})

Figure 3.5

Figure 3.6

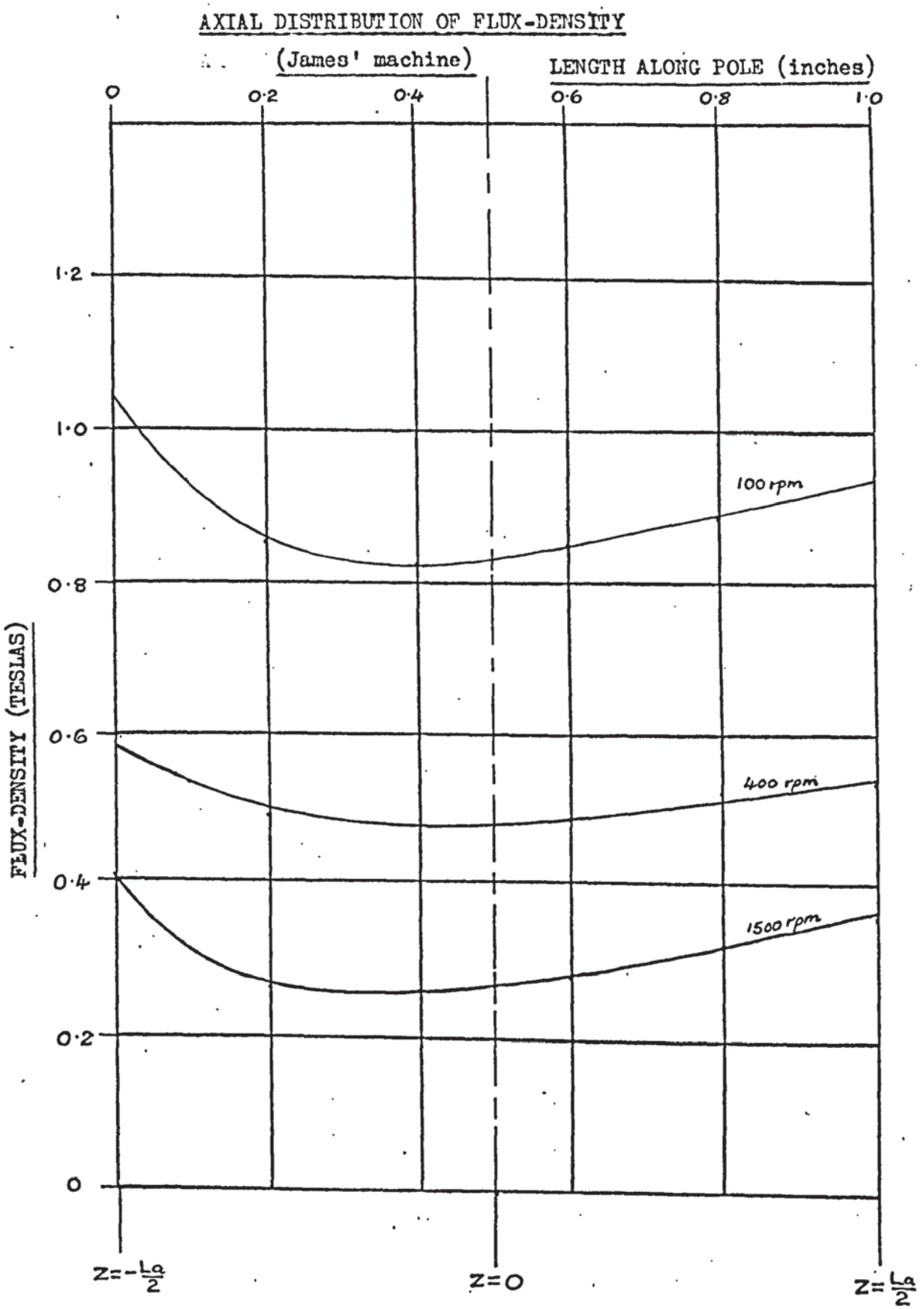
AXIAL DISTRIBUTION OF FLUX-DENSITY
(James' machine)
LENGTH ALONG POLE (inches)
0
0·2
0·4
0·6
0·8
1·0
1·2
1·0
0·8
0·6
0·4
0·2
0
FLUX-DENSITY (TESLAS)
100 rpm
400 rpm
1500 rpm
z=-La/2
z=0
z=La/2

Figure 3.7

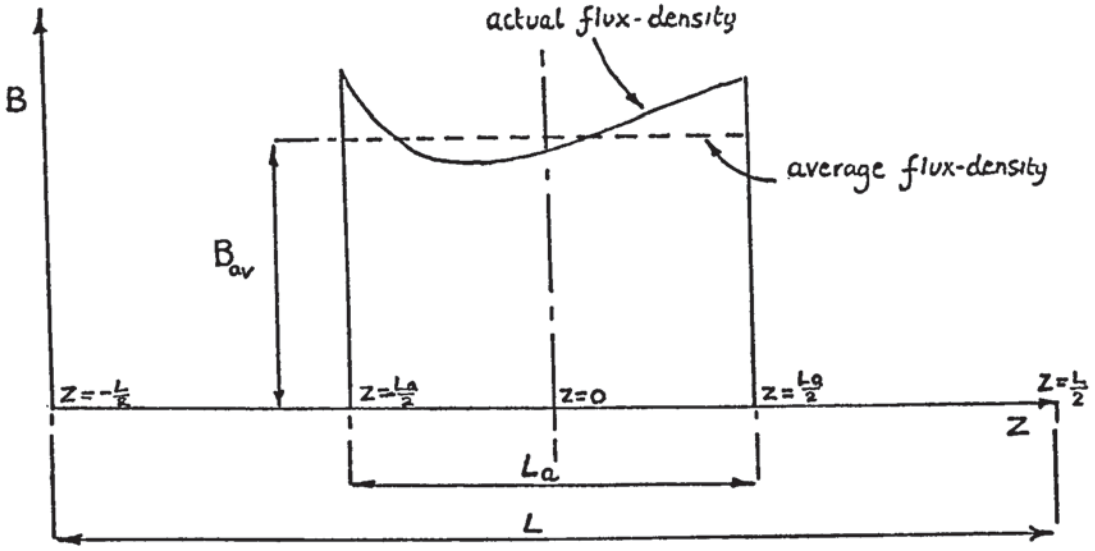

		Flux-Density Amplitude (T)				
Slip Speed	Variation	m=1	m=3	m=5	m=7	m=9
100 rpm	Actual	·617	·36	·0256	·173	·061
	Averaged	·642	·351	0	·148	·071
400 rpm	Actual	·3546	·208	·0173	·0945	·0602
	Averaged	·368	·1975	0	·085	·0408
1500 rpm	Actual	·2131	·122	·0078	·0643	·061
	Averaged	·2194	·121	0	·051	·0245

Ordinates for the harmonic analysis are taken from fig. 3.6

Figure 3.8

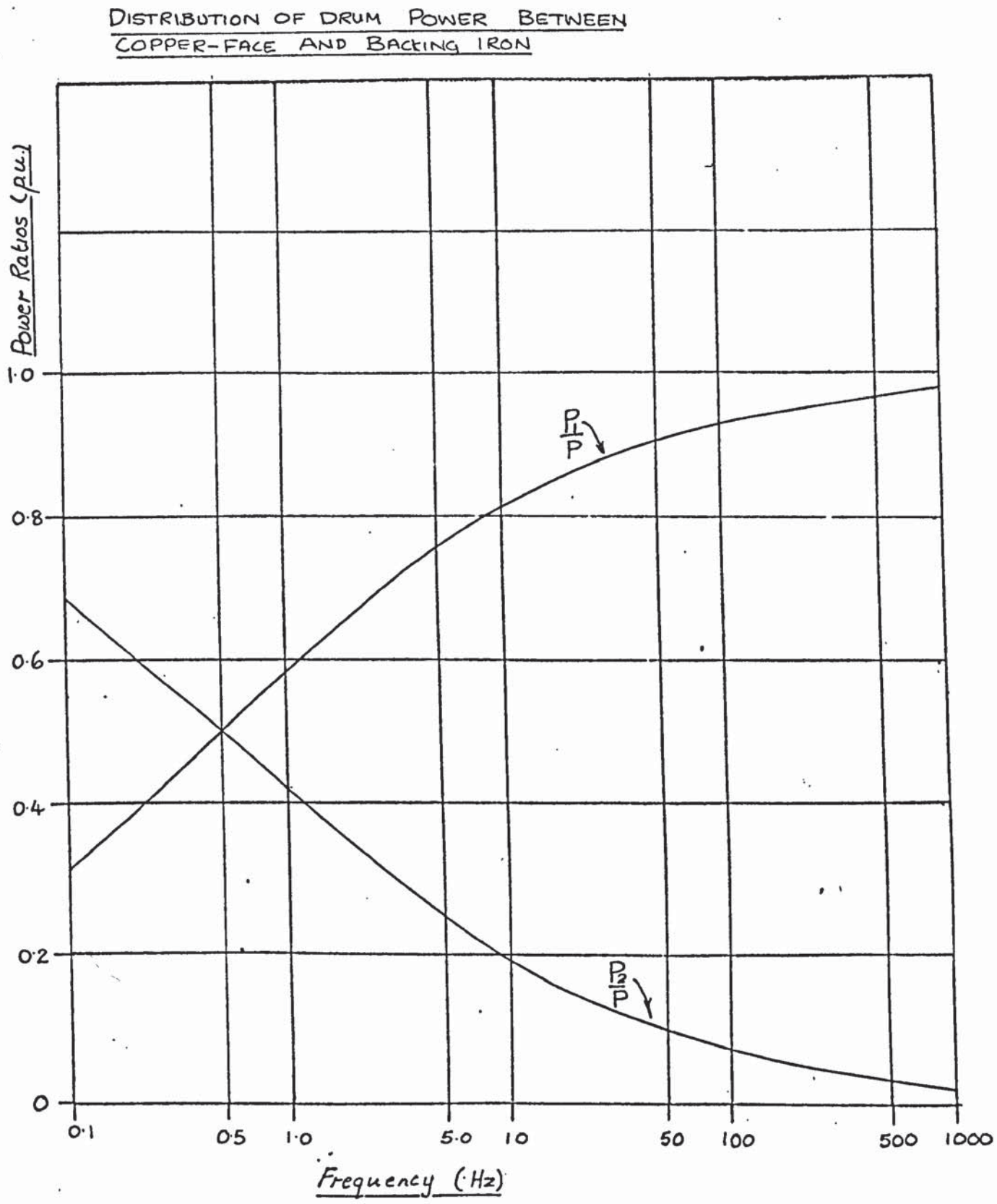
DISTRIBUTION OF DRUM POWER BETWEEN COPPER-FACE AND BACKING IRON
Power Ratios (p.u.)
1·0
0·8
0·6
0·4
0·2
0
P1/P
P2/P
0·1
0·5
1·0
5·0
10
50
100
500
1000
Frequency (Hz)
curves calculated for μr = 2000

MAGNETIC CHARICTERISTICS OF TYPICAL DRUM BACKING IRON Figure 3.9

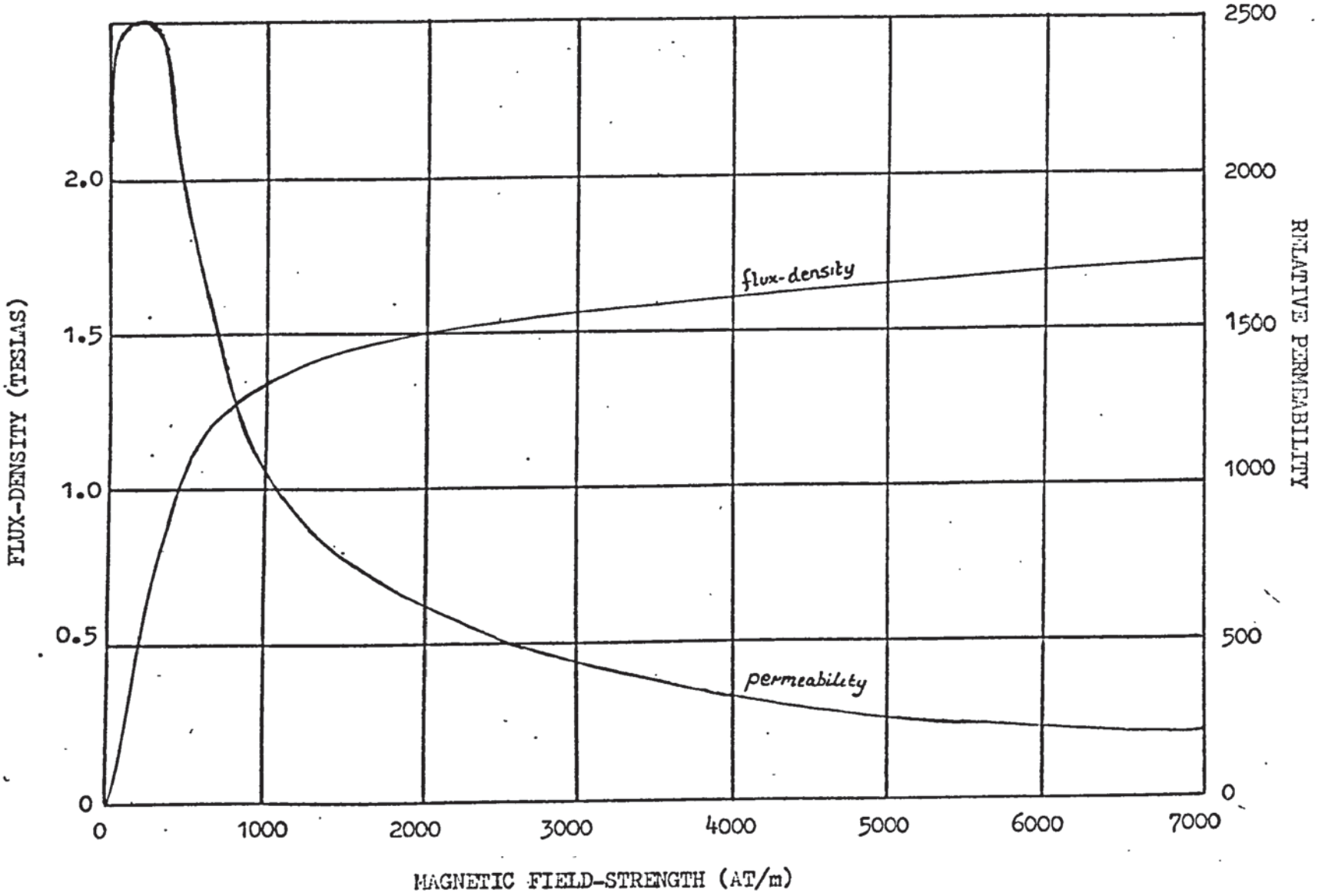

Figure 3.10

VARIATION OF THE POWER RATIOS WITH FREQUENCY AND BACKING-IRON RELATIVE PERMEABILITY

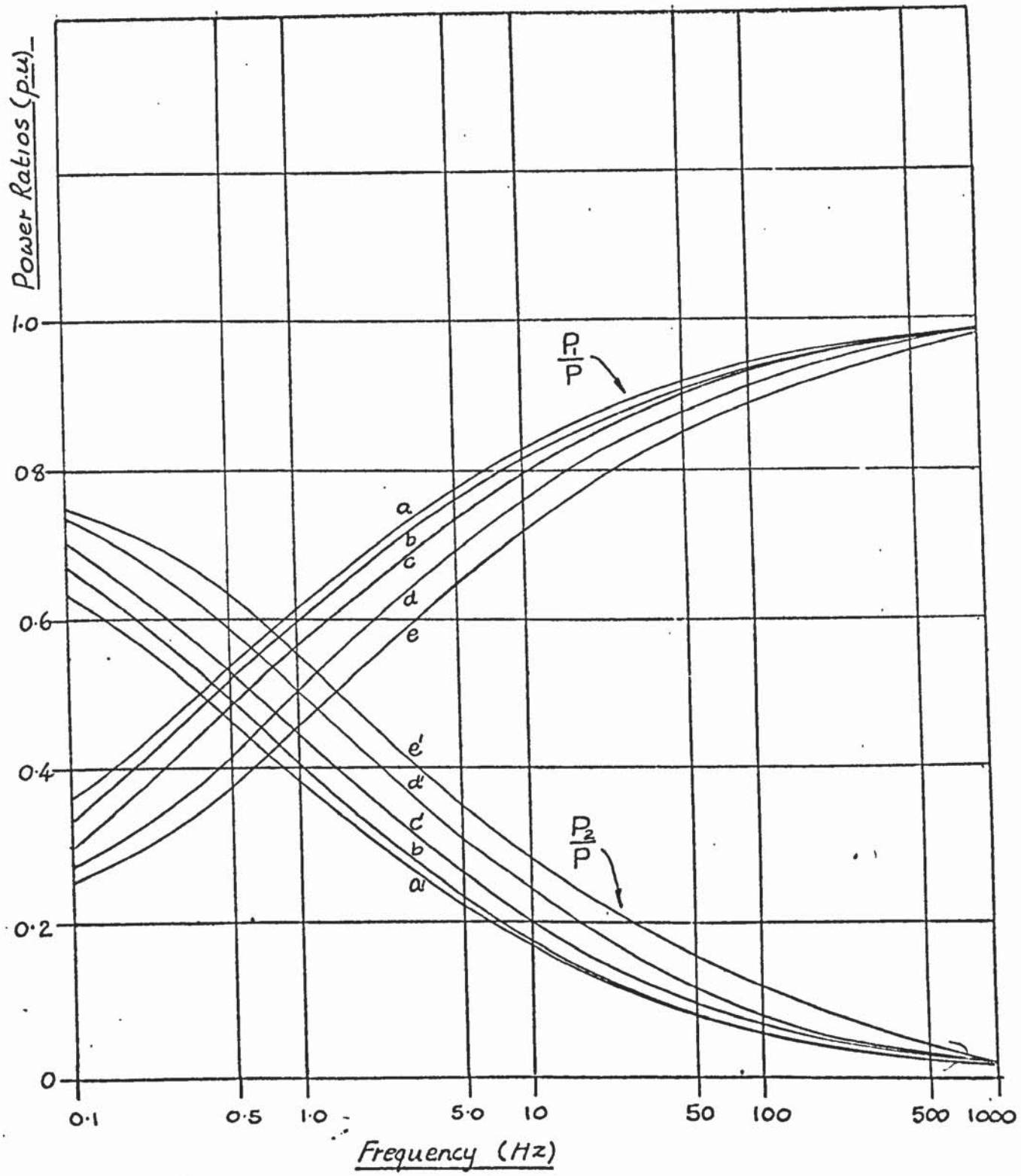

a & a': μ_r = 2500
b & b': μ_r = 2000
c & c': μ_r = 1500
d & d': μ_r = 1000
e & e': μ_r = .500

Figure 3.11

CONTOUR USED TO CALCULATE ARMATURE REACTION M.M.F.

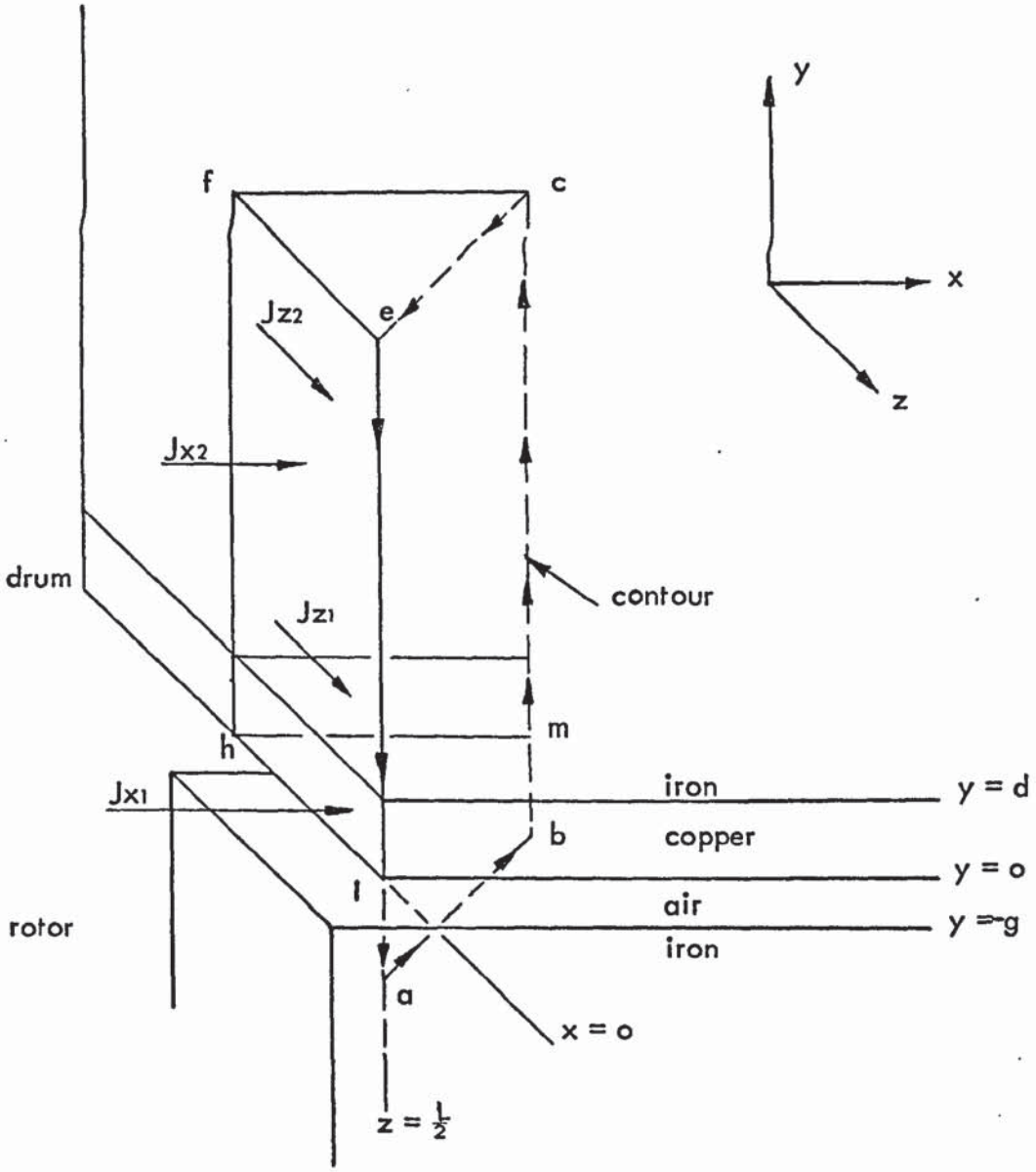

Points 'a' and 'b' are within the rotor surface

Points 'e', 'f' and 'c' are at $y = \infty$

Figure 3.12

ARMATURE REACTION M.M.F. WAVES

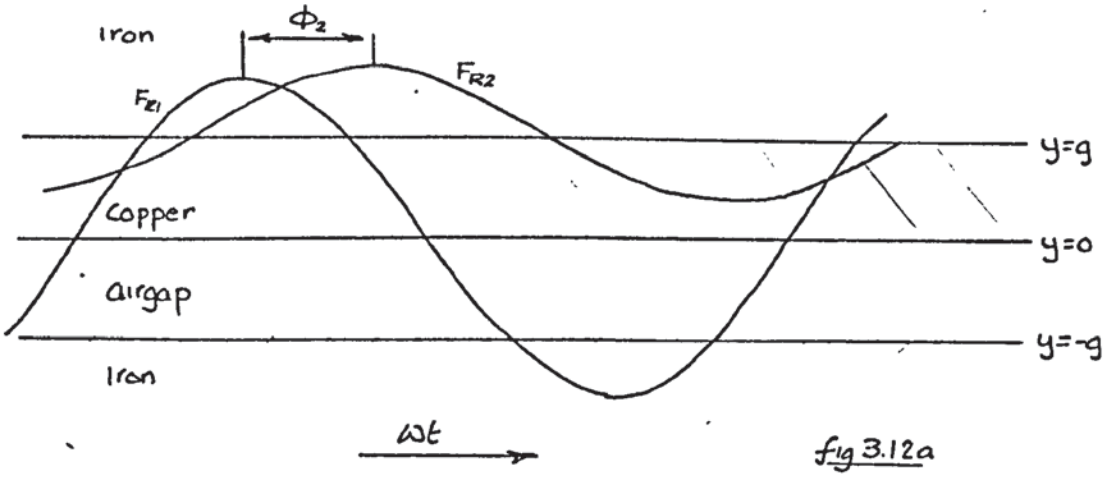

fig 3.12a

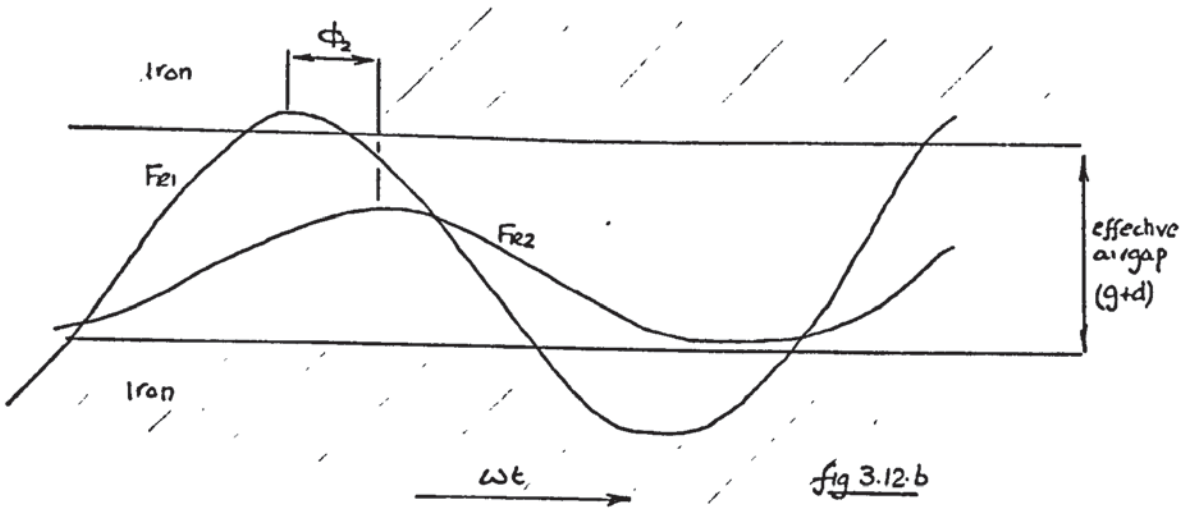

fig 3.12.b

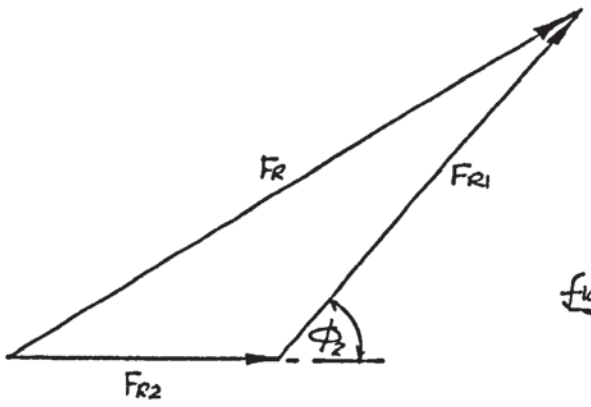

fig 3.12c

Figure 3.13

M.M.F. VECTOR DIAGRAMS OF THE COPPER-FACED COUPLING

complete vector diagram

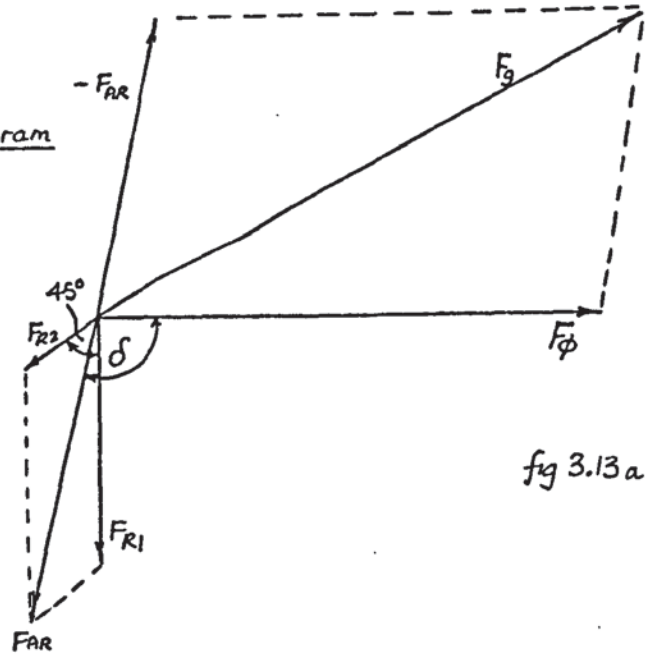

fig 3.13a

approximate vector diagram

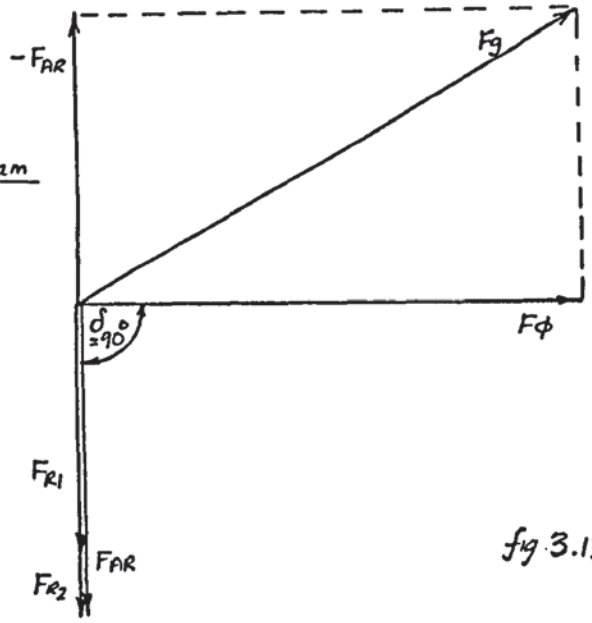

fig 3.13b

THEORETICAL FAMILY OF NORMALISED TORQUE-SLIP CURVES Figure 3.15

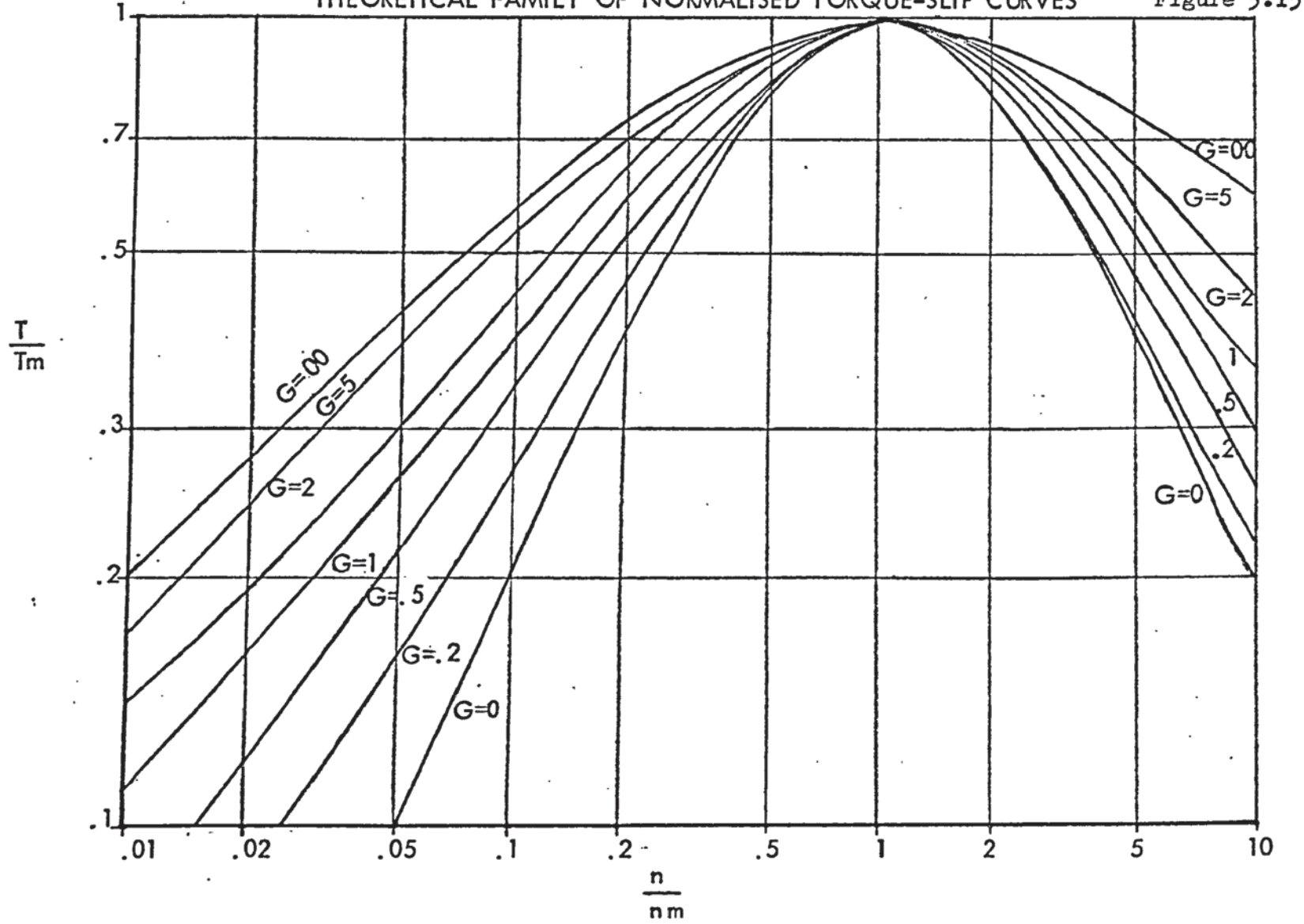

NORMALISED TORQUE-SLIP CURVES FOR THE COPPER FACED COUPLING

Figure 3.16

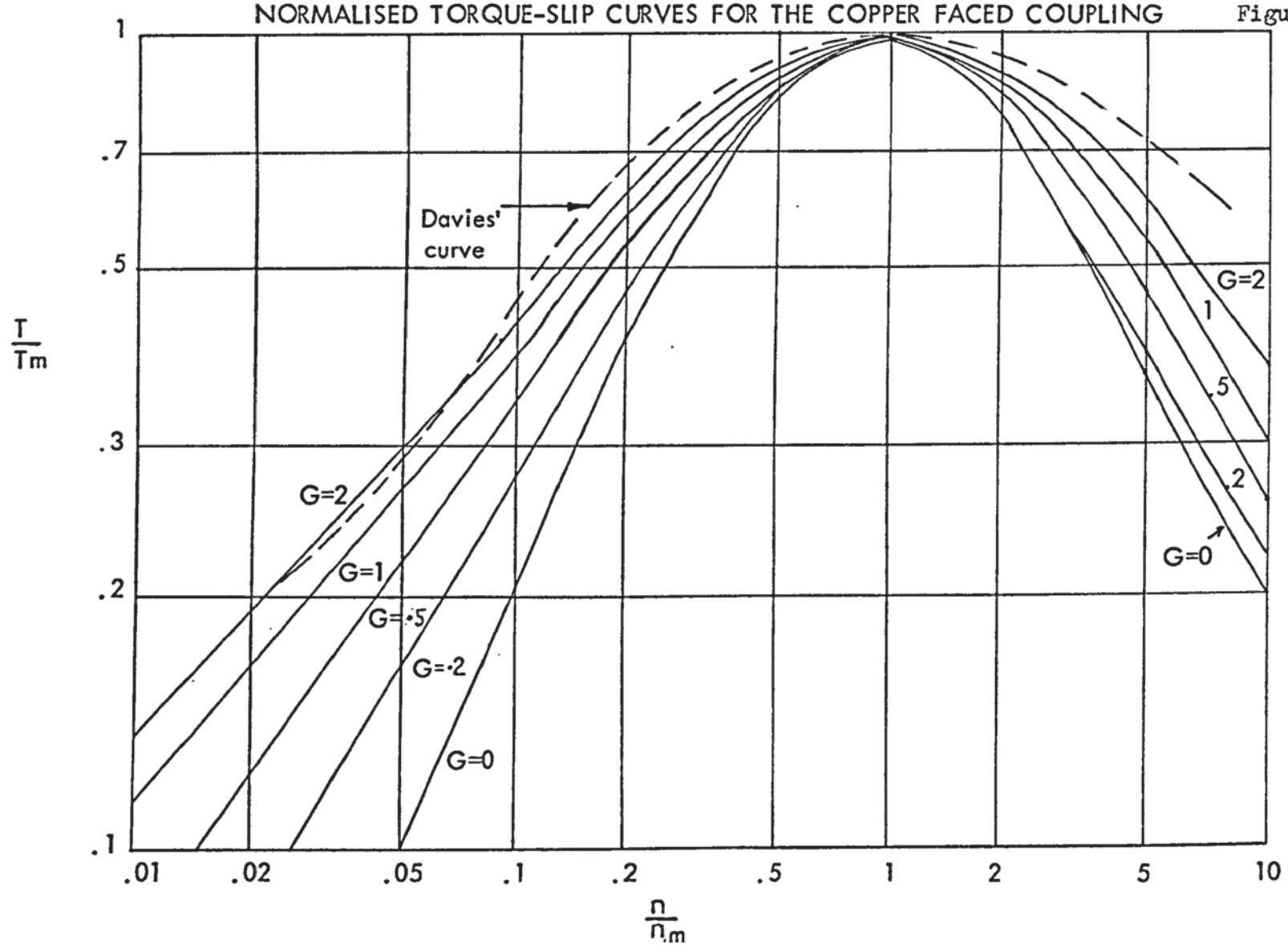

NORMALISED FLUX AND ARMATURE REACTION M.M.F. Figure 3.17

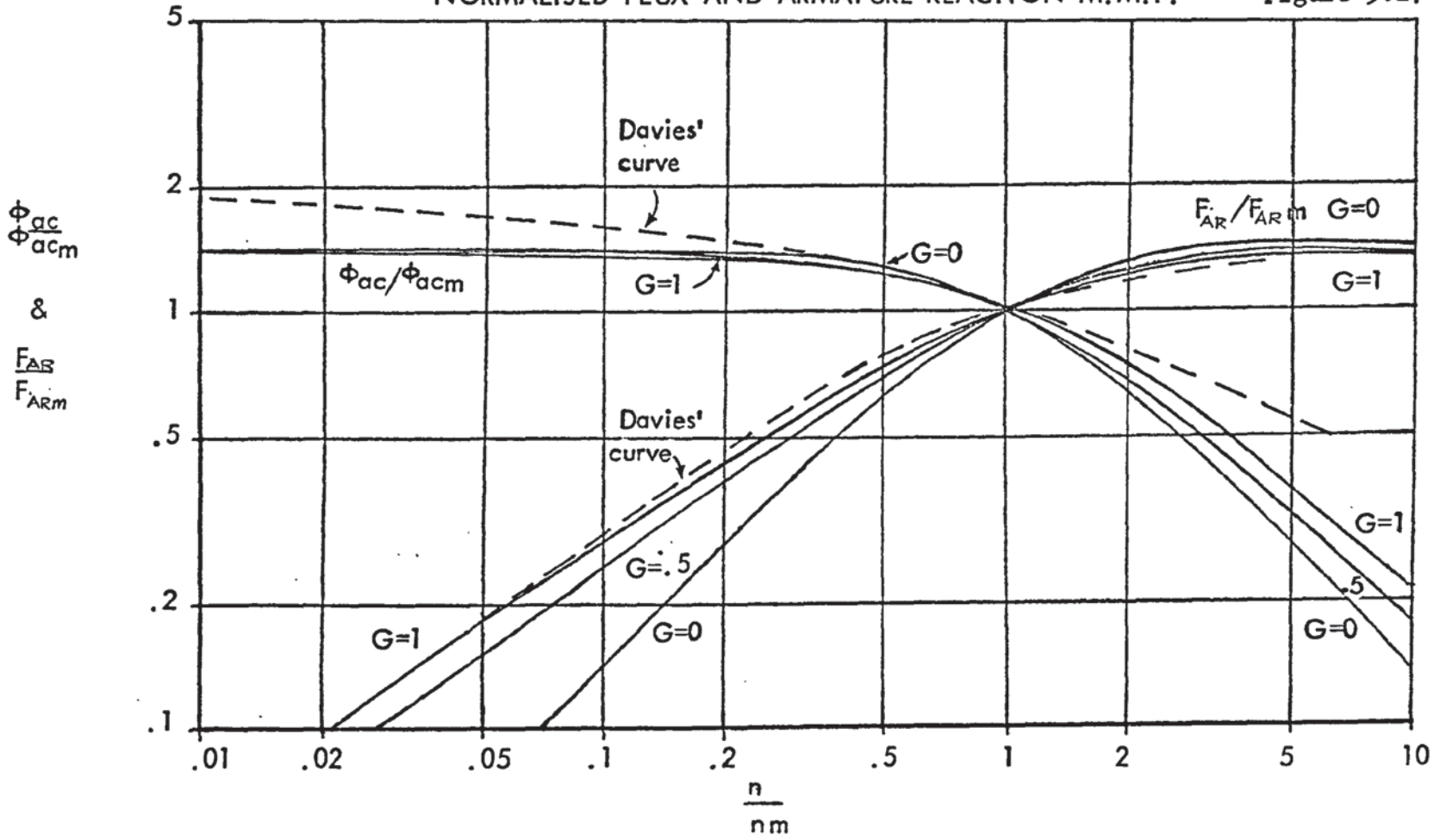

FIGURES FOR CHAPTER 4.

Figure 4.3

EXPERIMENTAL TORQUE-SLIP CURVES
OF THE COPPER-FACED COUPLING

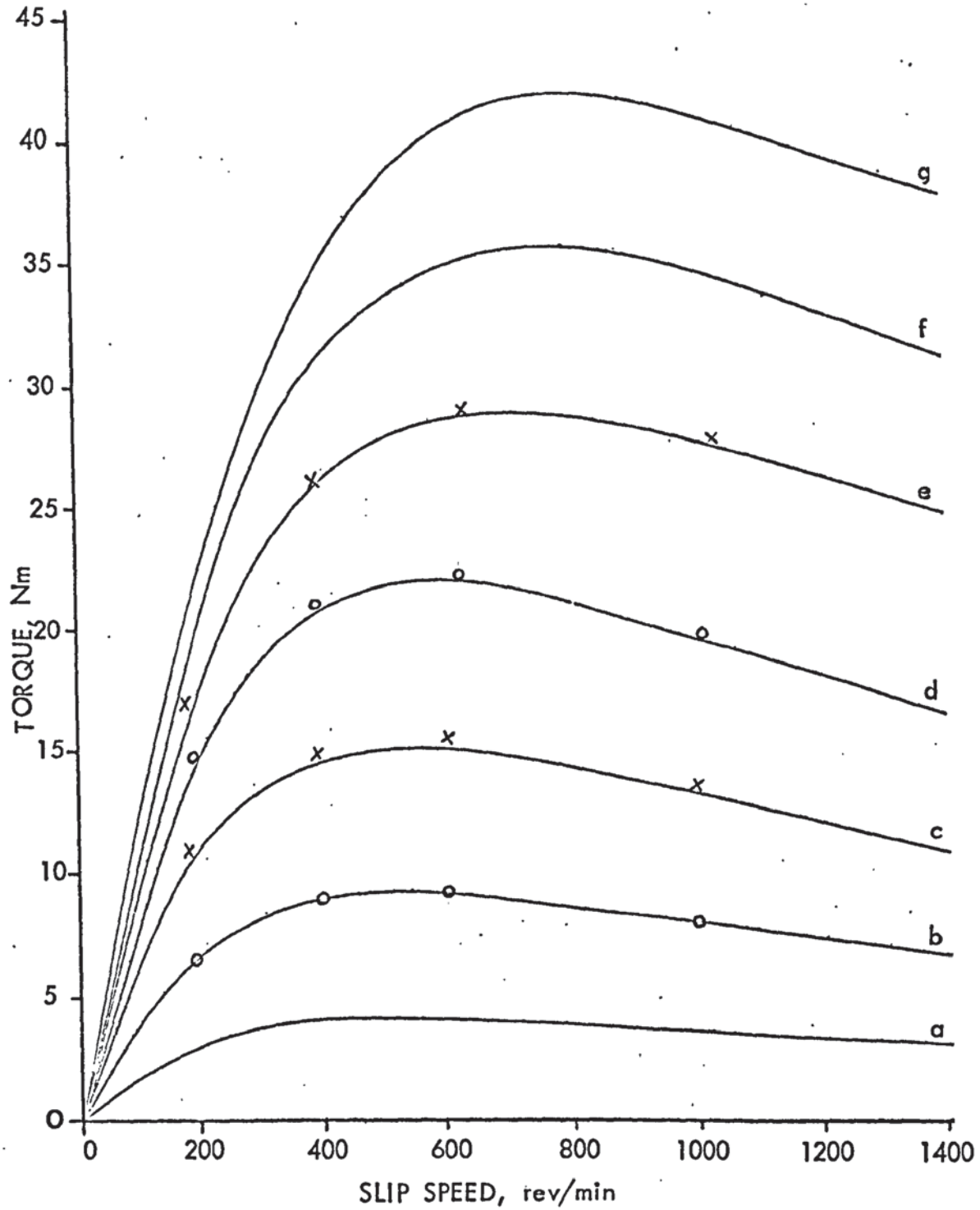

Excitations: a : 260 AT/POLE, d : 650 AT/POLE,
b : 390 AT/POLE, e : 780 AT/POLE, g : 1040 AT/POLE
c : 520 AT/POLE, f : 910 AT/POLE

O : Measured points with rotor at the open edge of the drum
X : Measured points with rotor near backing plate

Figure 4.4

POLE FACE FLUX-DENSITY DISTRIBUTION
AT VARIOUS SLIP SPEEDS
EXCITATION M.M.F. = 260 AT/POLE

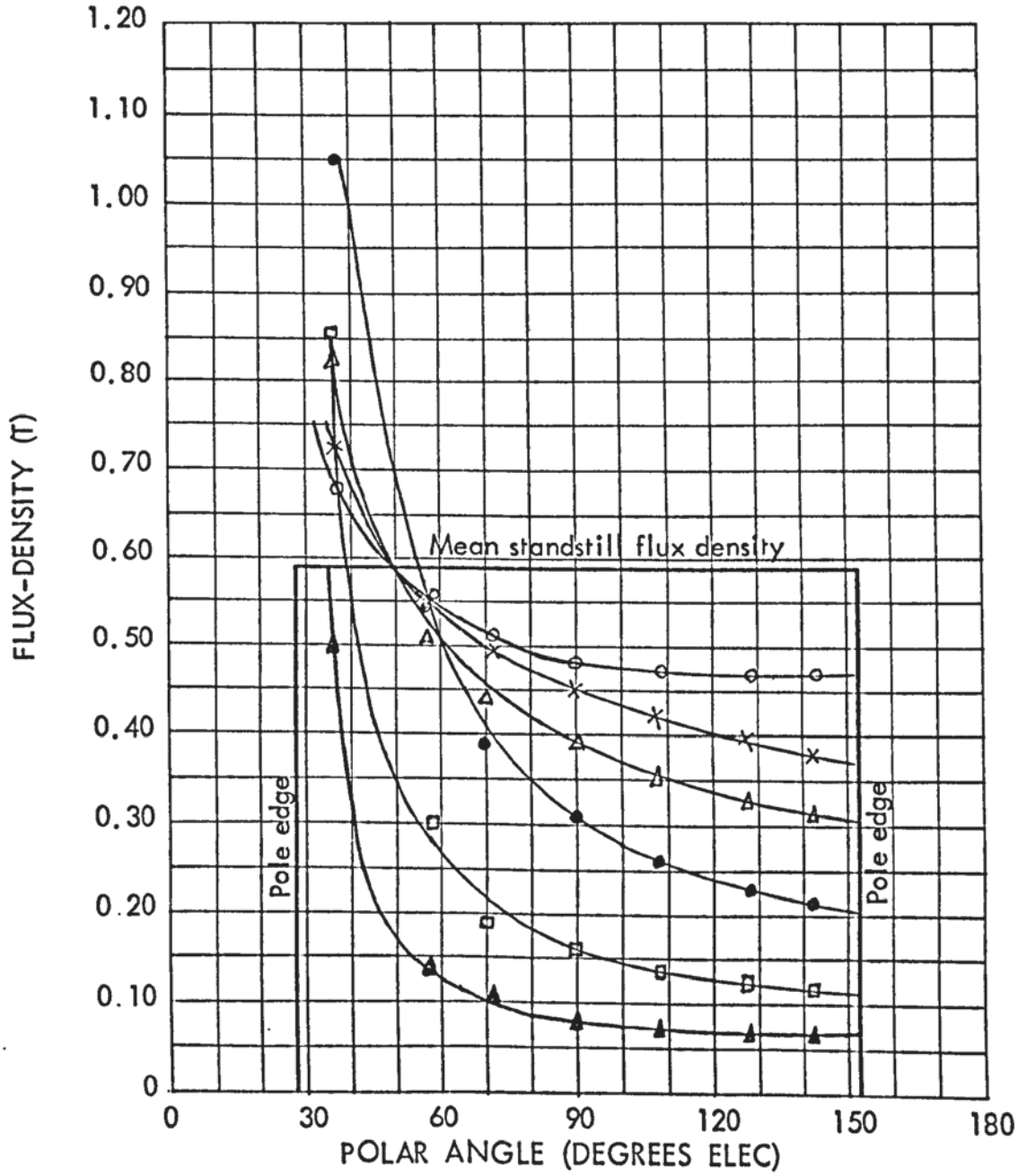

Slip Speeds:

0 : 50 rev/min
X : 100 rev/min
△ : 200 rev/min
● : 400 rev/min
□ : 1000 rev/min
▲ : 1400 rev/min

Figure 4.5

POLE-FACE FLUX-DENSITY DISTRIBUTION
AT VARIOUS SLIP SPEEDS
EXCITATION M.M.F. = 520 AT/POLE

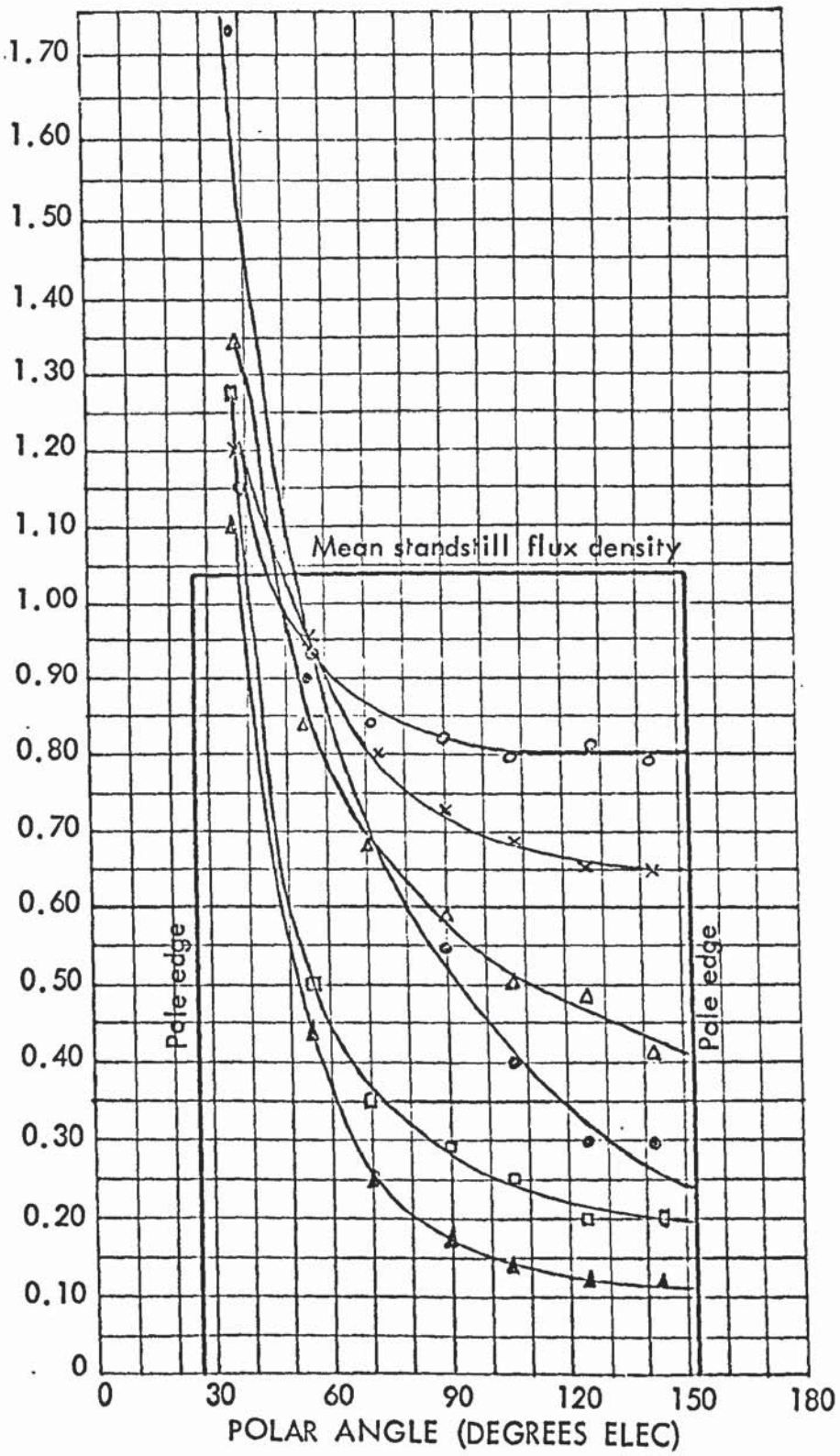

Slip Speeds:

0 : 50 rev/min	● : 400 rev/min
X : 100 rev/min	□ : 1000 rev/min
△ : 200 rev/min	▲ : 1400 rev/min

Figure 4.6

POLE FACE FLUX-DENSITY DISTRIBUTION
AT VARIOUS SLIP SPEEDS
EXCITATION M.M.F. = 780 AT/POLE

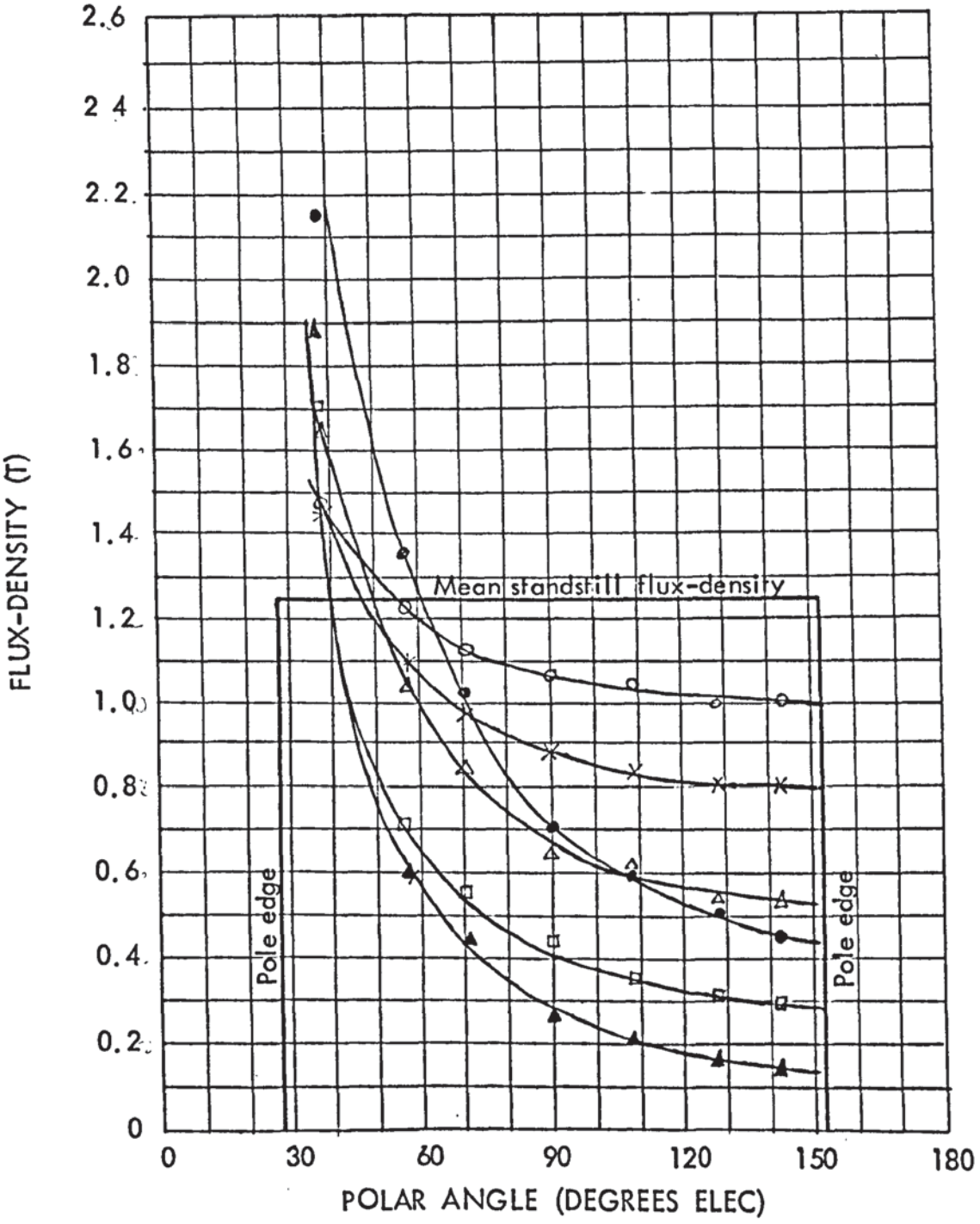

Slip Speeds

0 : 50 rev/min
X : 100 rev/min
Δ : 200 rev/min
● : 400 rev/min
□ : 1000 rev/min
▲ : 1400 rev/min

Figure 4.7

VARIATION OF TORQUE WITH FIELD CURRENT
AT VARIOUS SLIP SPEEDS

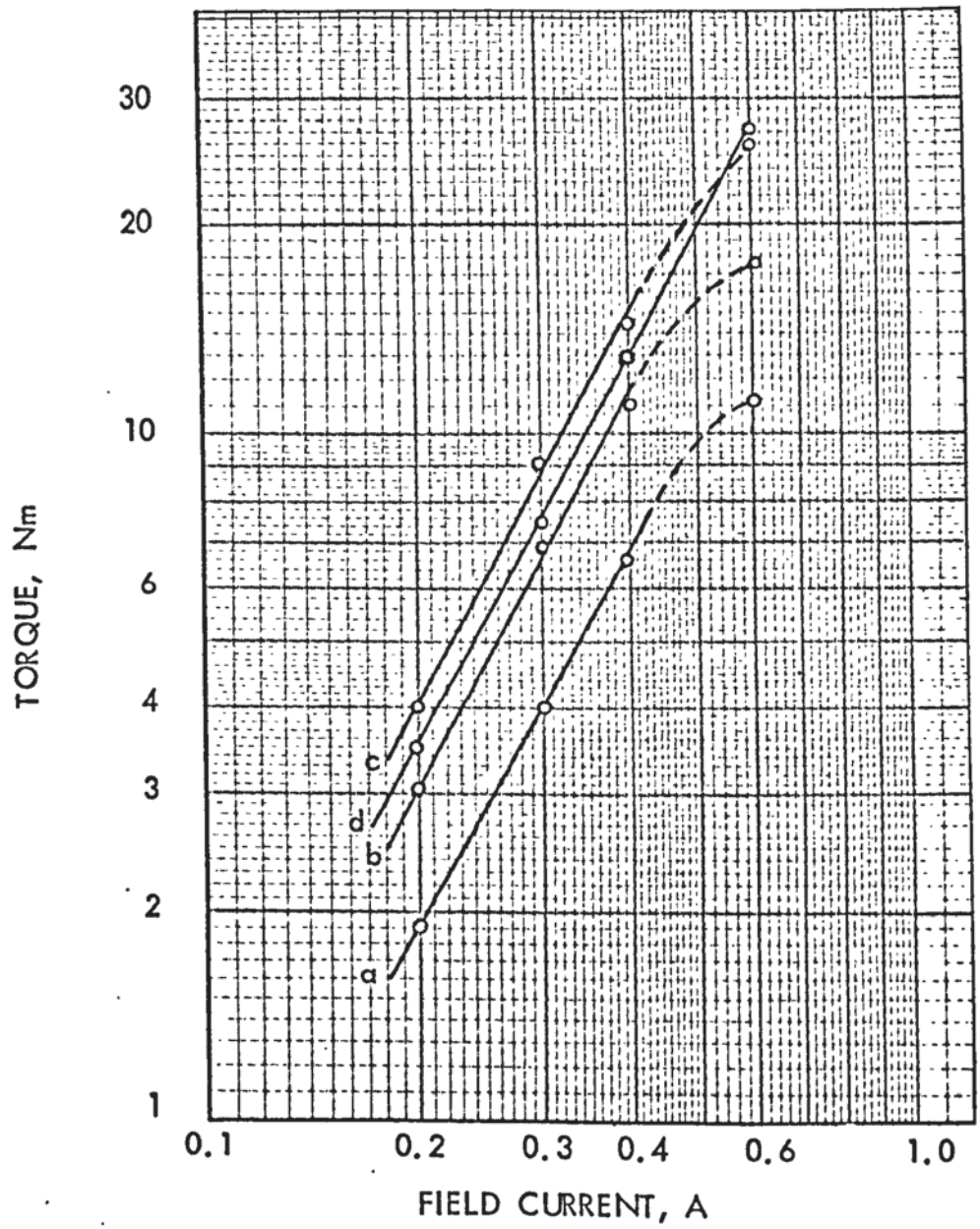

a : 100 rev/min, slope = 1.86
b : 200 rev/min, slope = 1.93
c : 400 rev/min, slope = 1.95
d : 1000 rev/min, slope = 1.95

Figure 4.8

VARIATION OF TORQUE WITH FUNDAMENTAL FLUX AND SLIP SPEED.

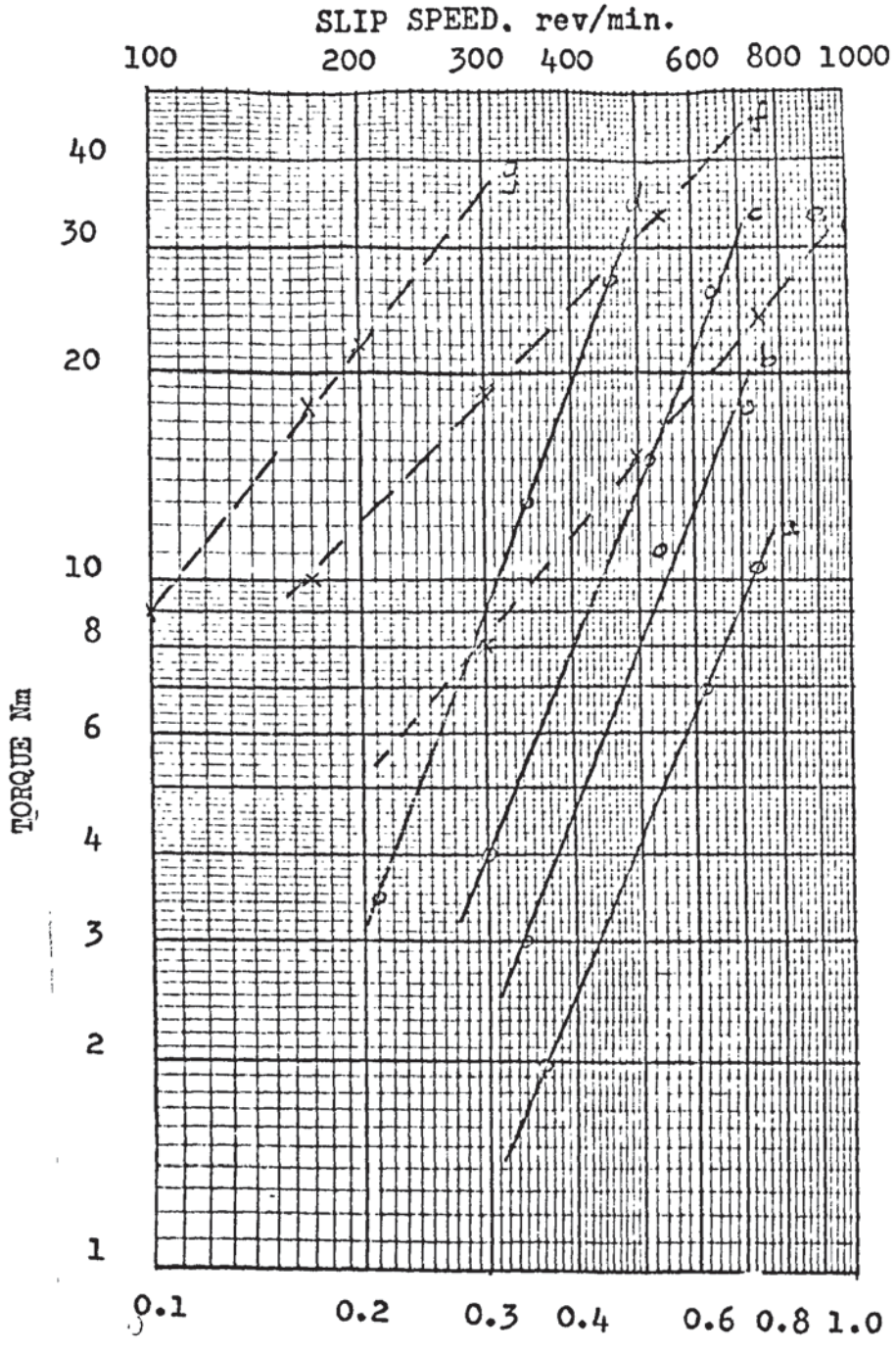

Constant slip curves:

a: 100 rev/min, slope = 2.2 b: 200 rev/min, slope = 2.3

c: 400 rev/min, slope = 2.3 d: 1000 rev/min, slope = 2.4

Constant flux curves:

e: 0.4 mWb, slope = 1.15 f: 0.6 mWb, slope = 1.1

g: 0.8 mWb, slope = 1.2

Figure 4.9

POLE-FLUX MAGNETISATION CURVE

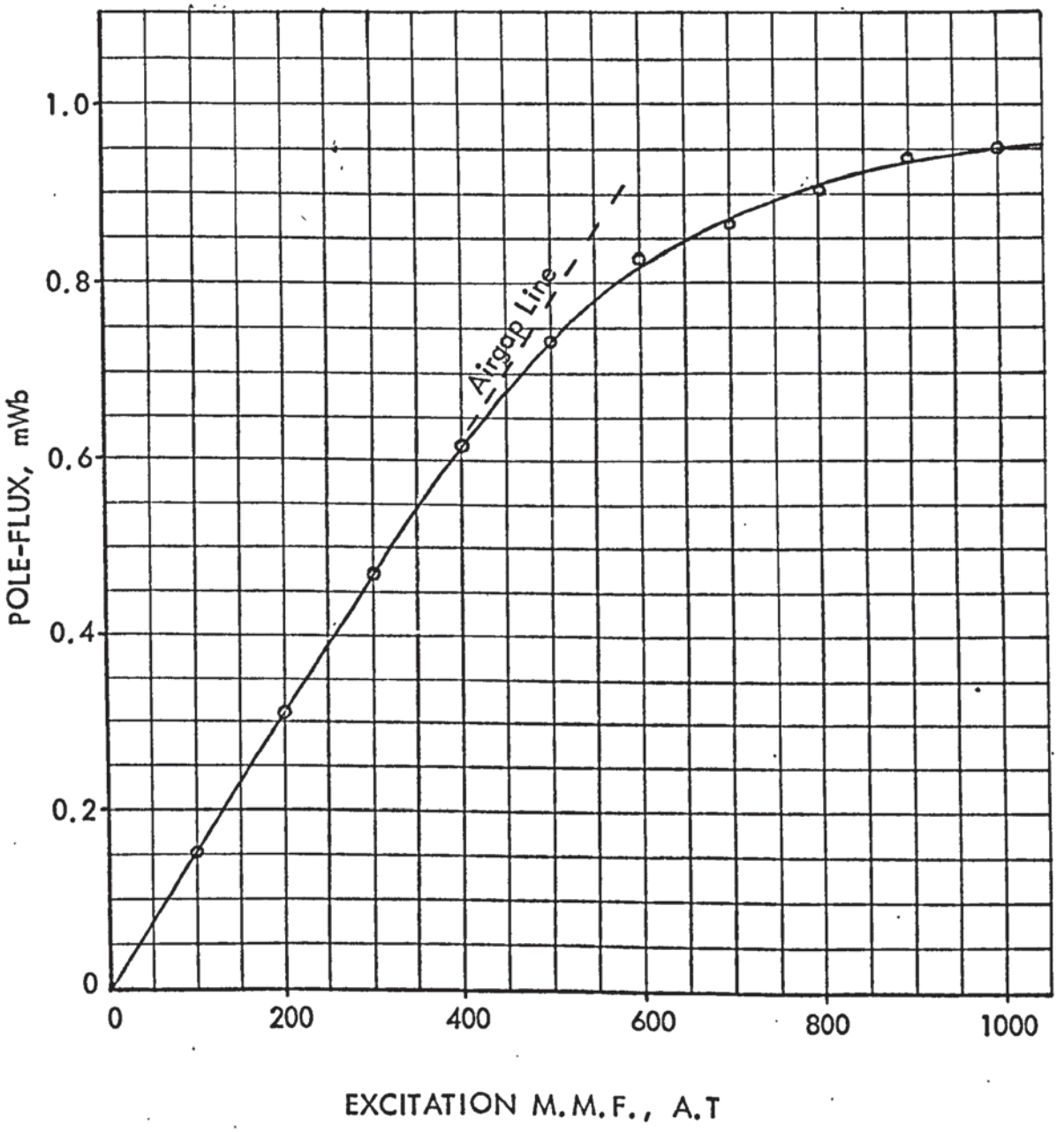

Figure 4.10

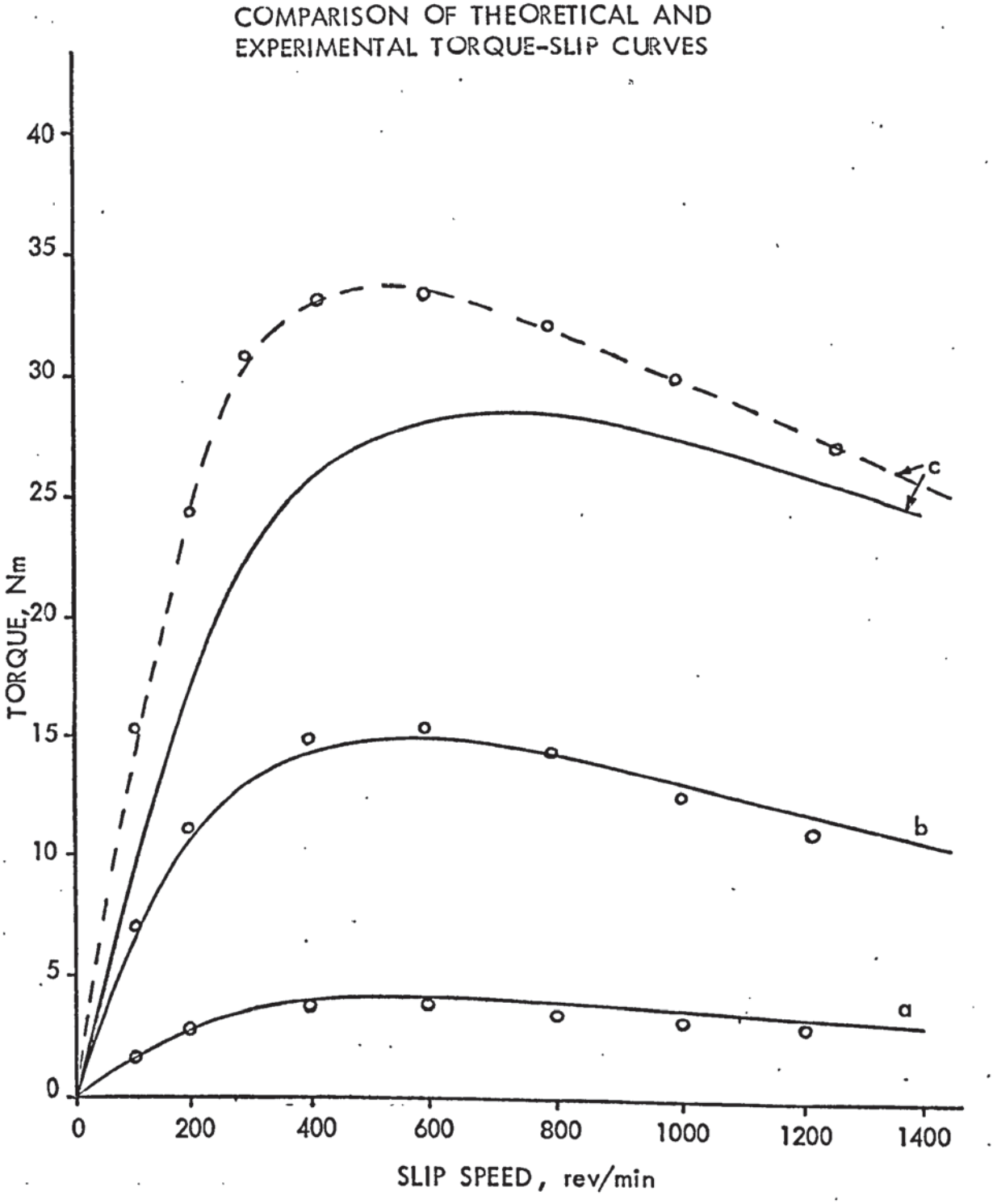
COMPARISON OF THEORETICAL AND
EXPERIMENTAL TORQUE-SLIP CURVES
TORQUE, Nm
SLIP SPEED, rev/min
0
5
10
15
20
25
30
35
40
0
200
400
600
800
1000
1200
1400
a
b
c
—— : Experimental Curves
--- : Calculated Curve for 780 AT/POLE
0 : Calculated Points
Excitations:
a : 260 AT/POLE
b : 520 AT/POLE
c : 780 AT/POLE

Figure 4.11

MEASURED AND CALCULATED NORMALISED CURVES

OF THE COPPER-FACED COUPLING.

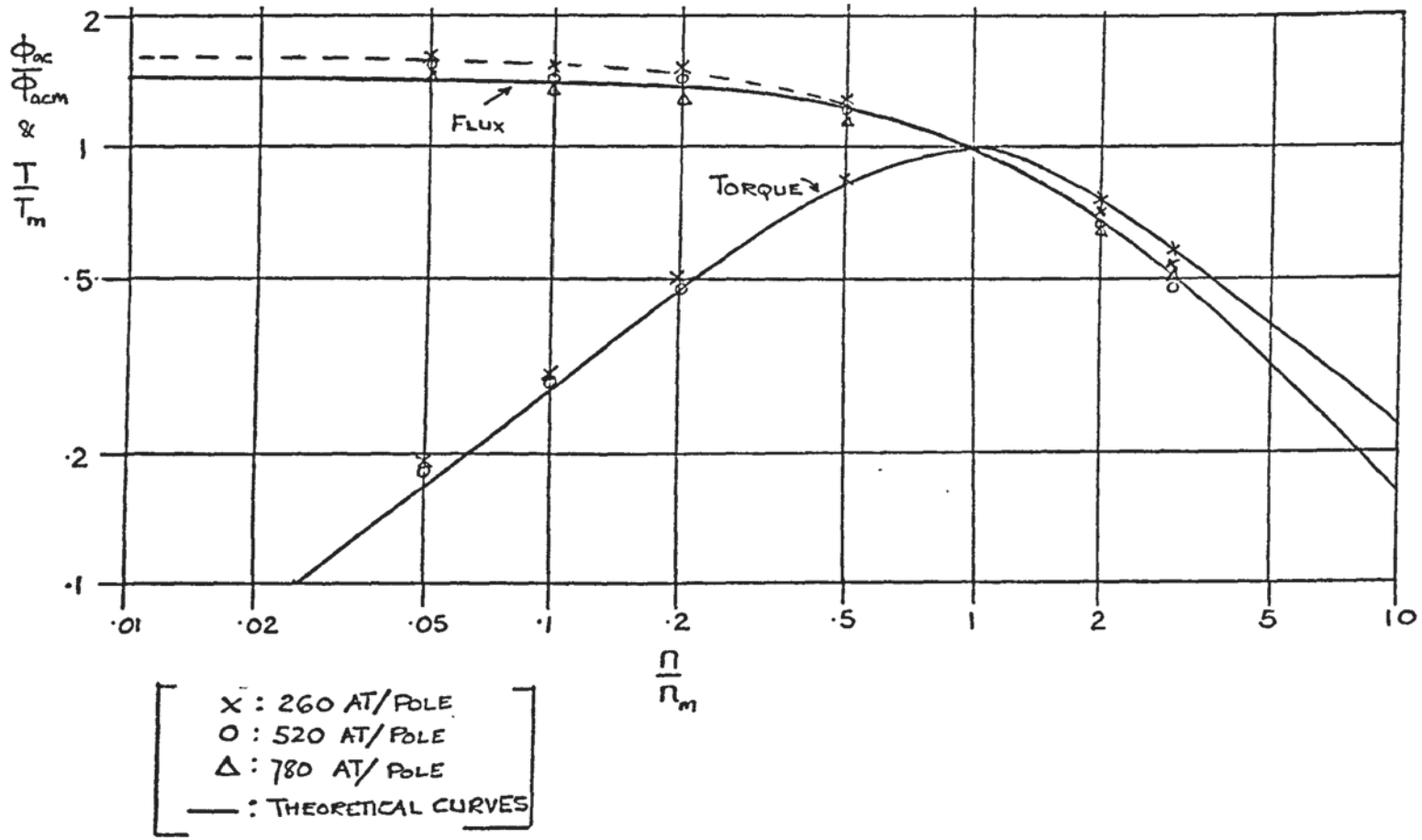

FIGURE FOR CHAPTER 6.

Figure 6.6

NORMALISED FLUX CURVE FOR m = 0.77

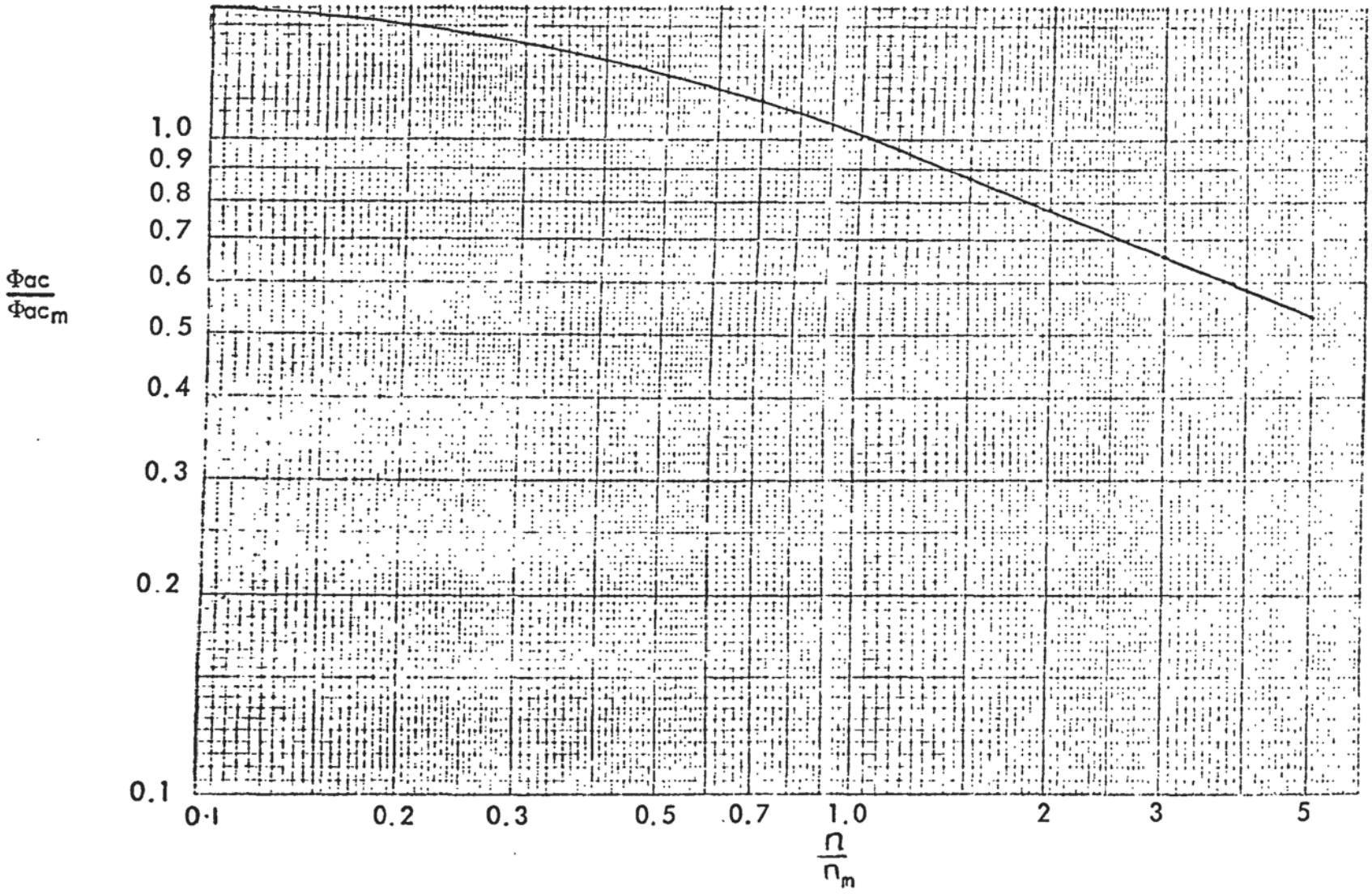

FIGURES FOR CHAPTER 7.

FIGURE 7.1

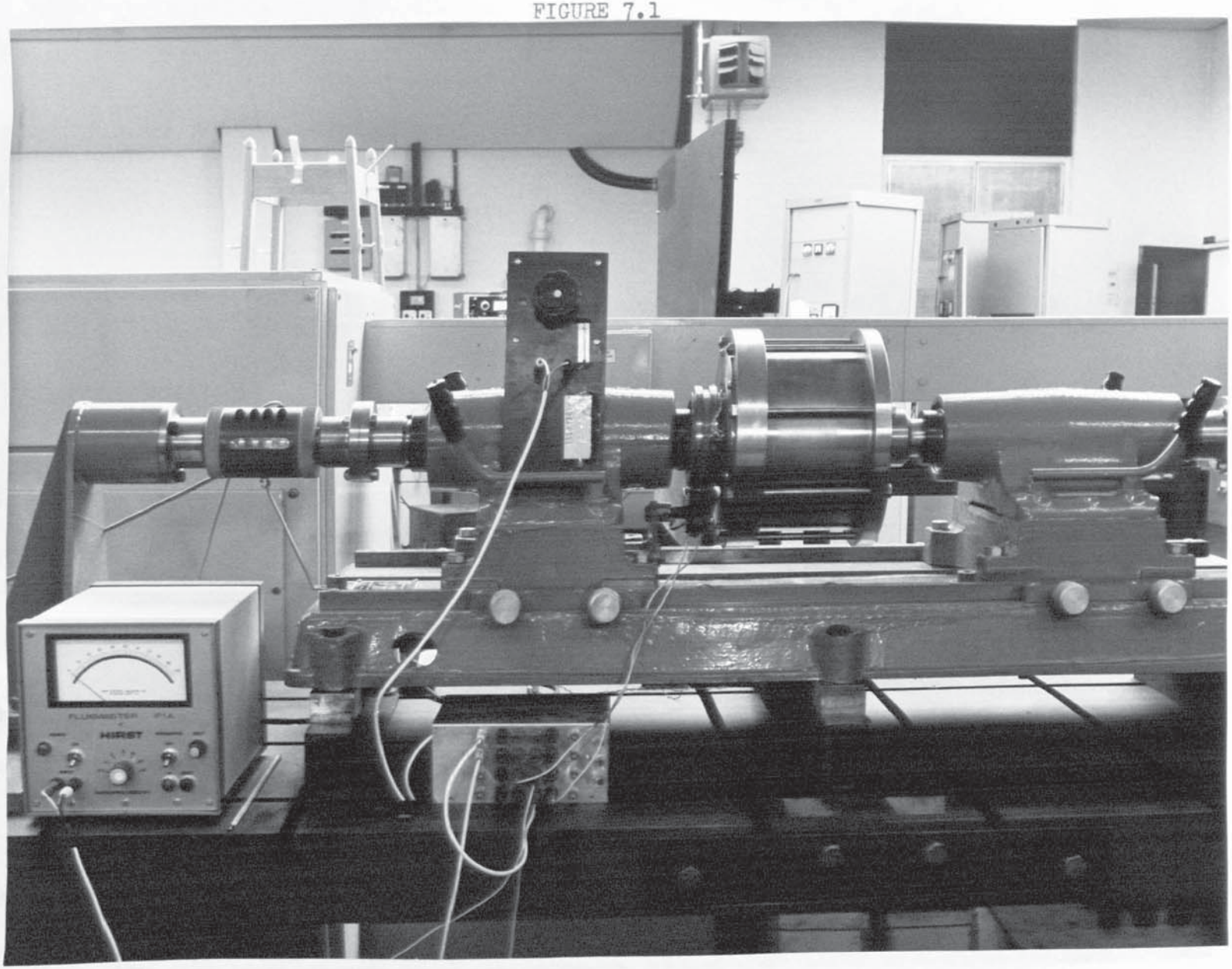

FIGURE 7.2

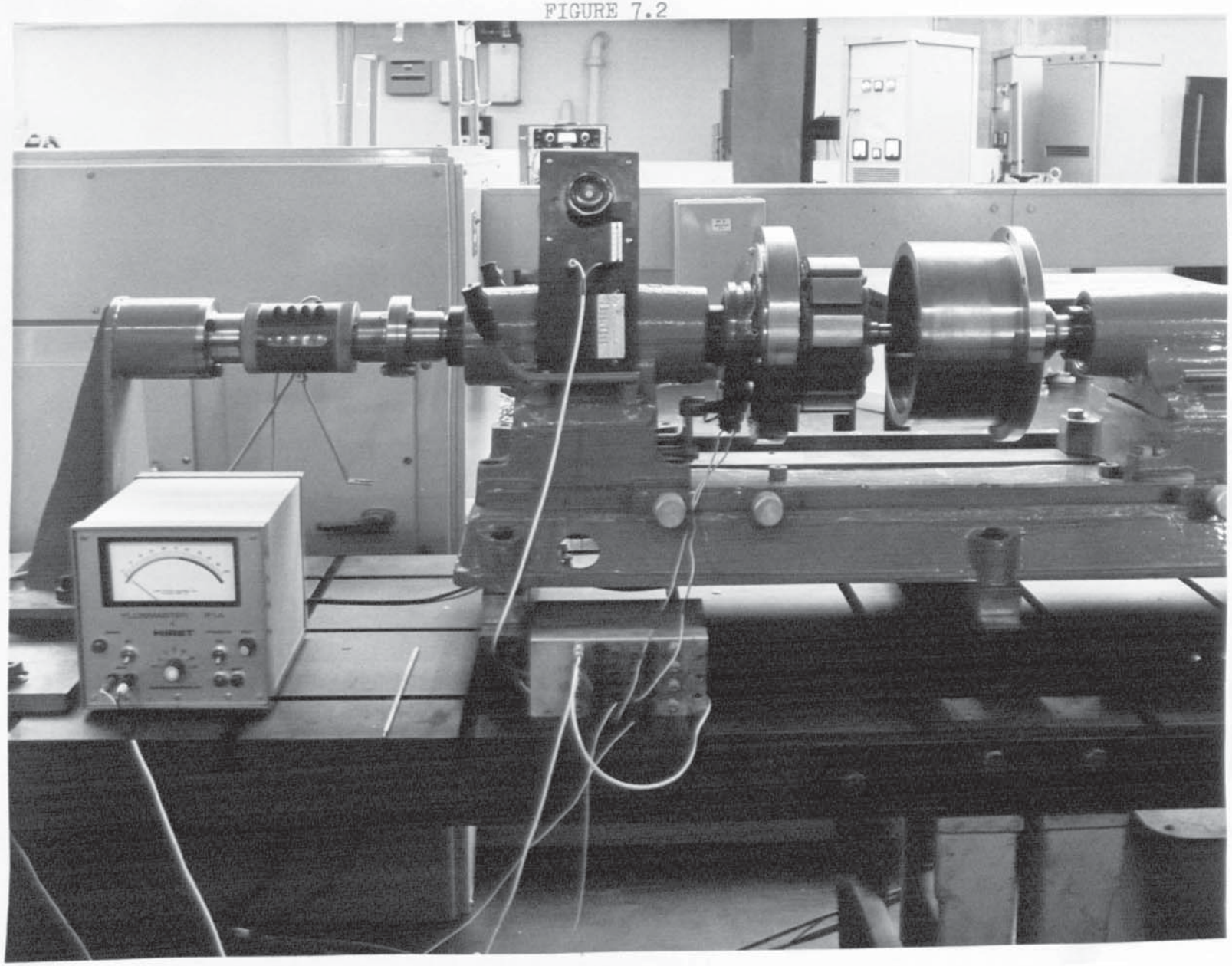

FIGURE 7.3

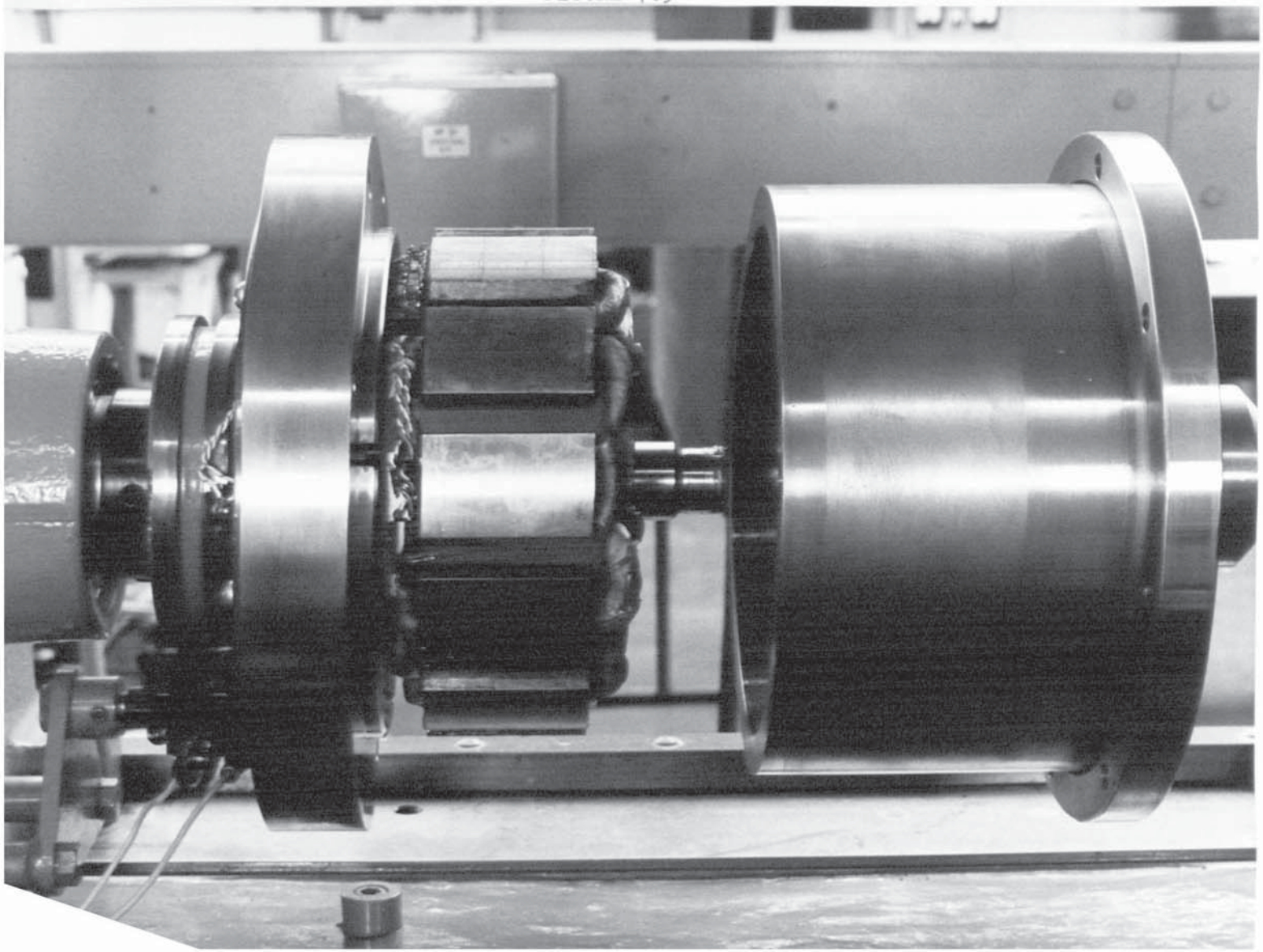

FIGURE 7.4

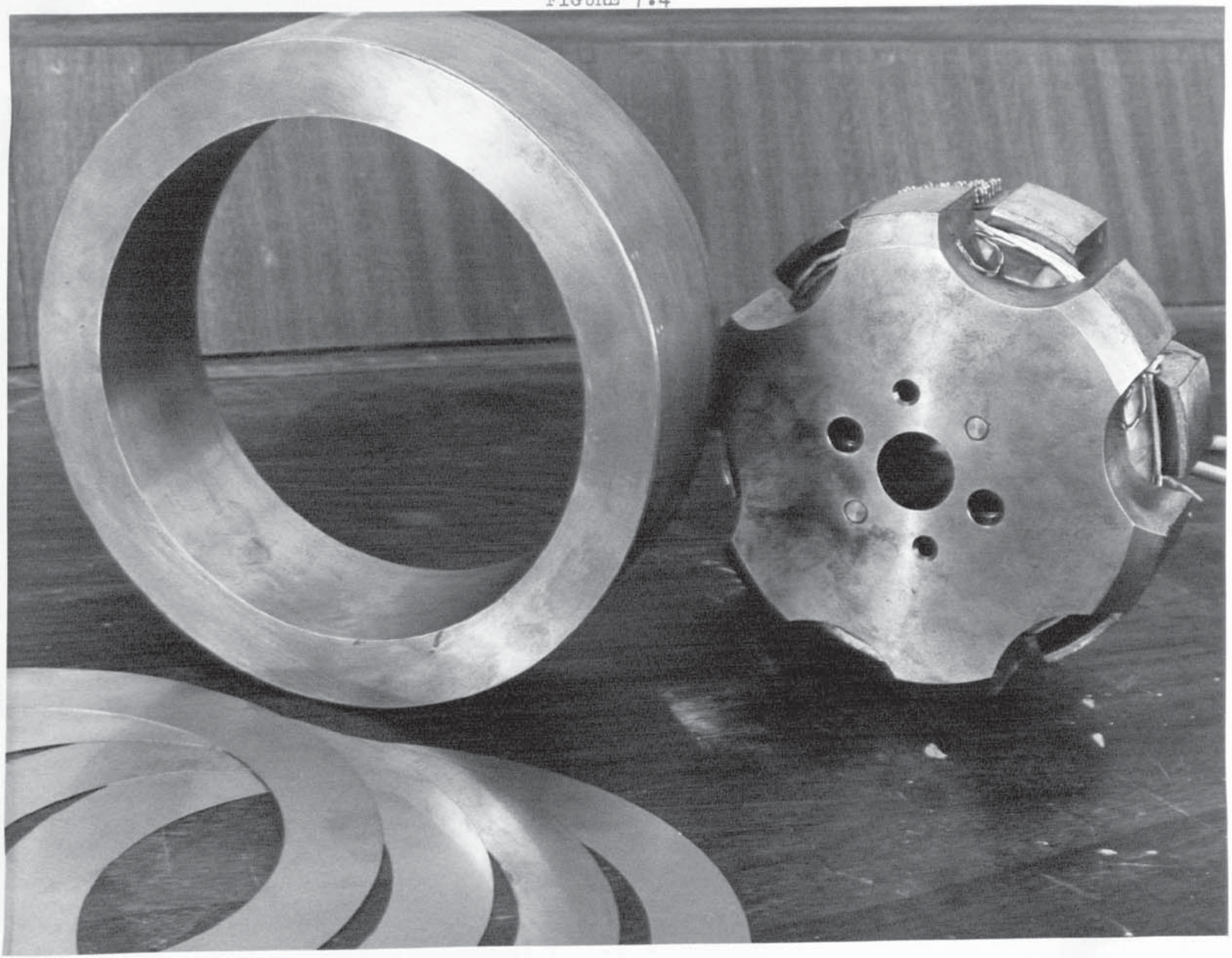

FIGURE 7.5

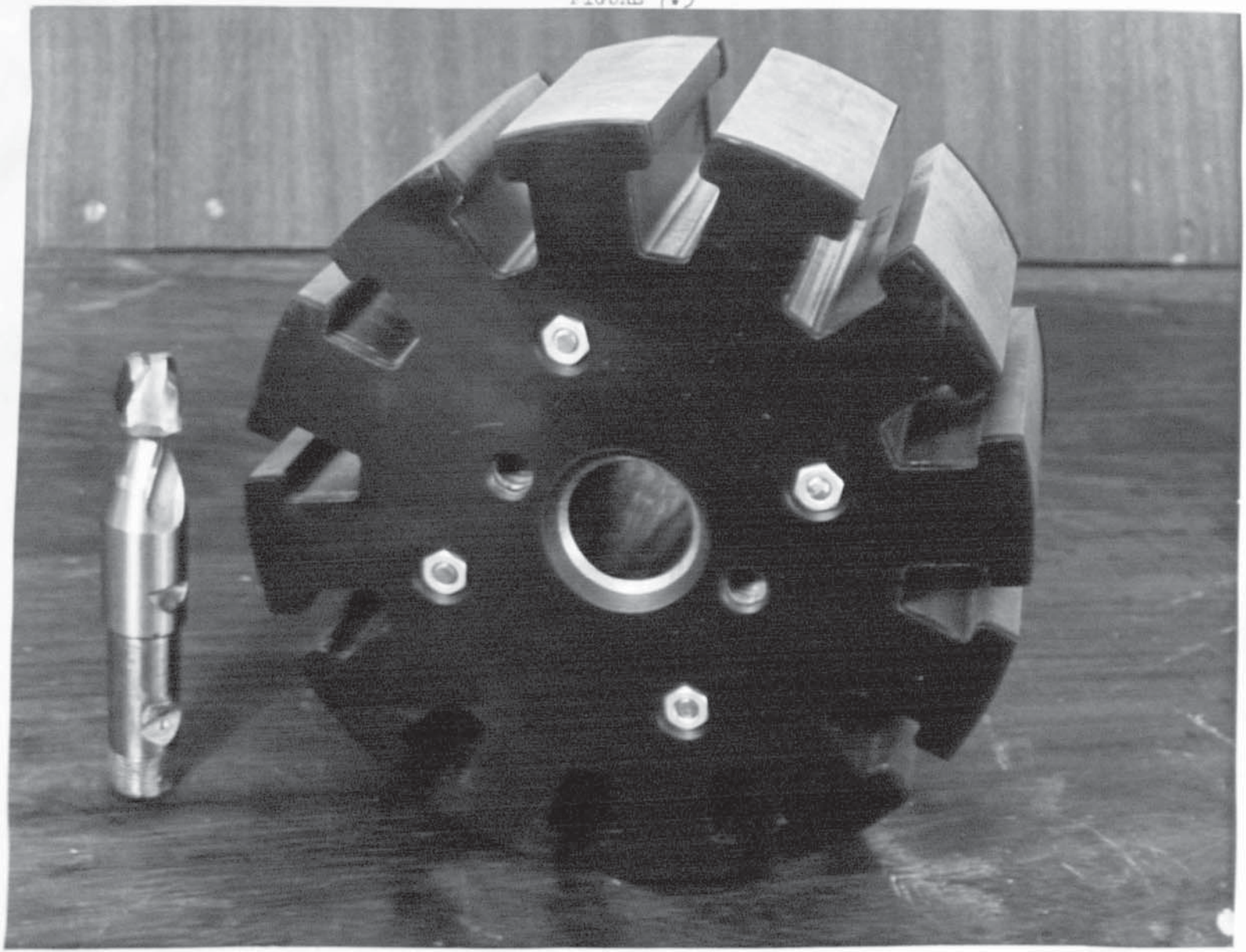

Figure 7.7

EXPERIMENTAL DRIVE SYSTEM

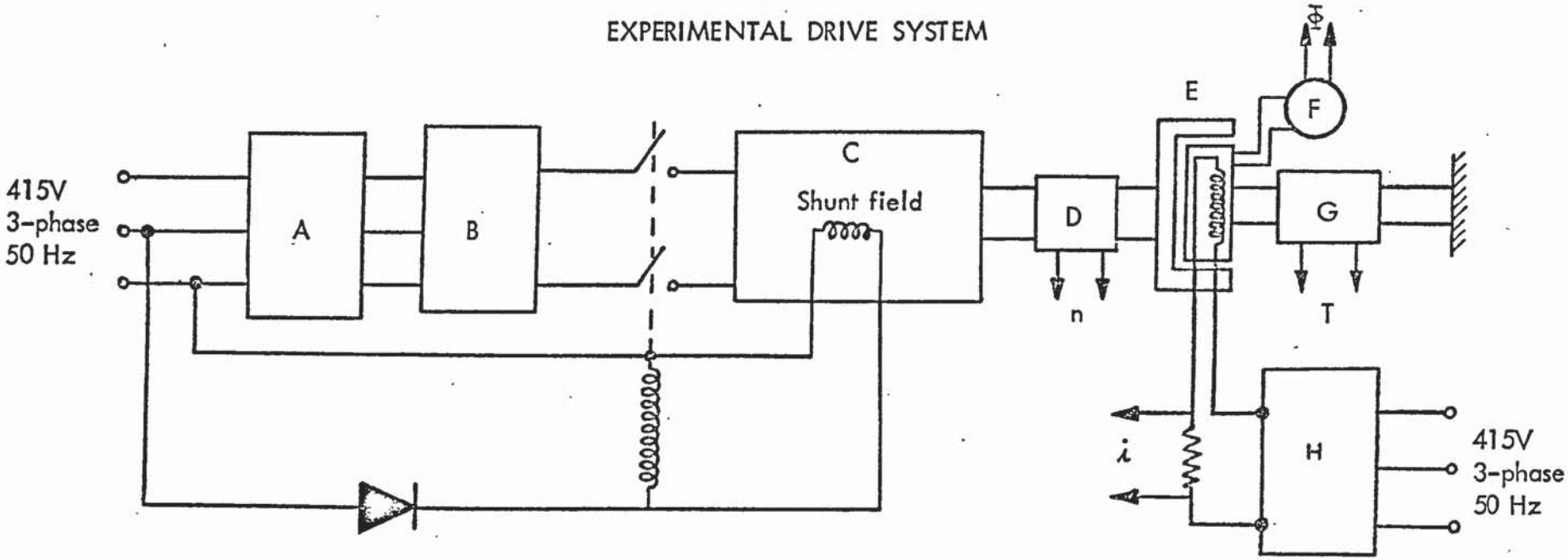

A : Motor-driven autotransformer
B : 3-phase rectifier stack
C : D.C. Drive machine
D : D.C. Tachogenerator

E : Experimental coupling
F : Rotary switch for search-coils
G: Torque Transducer
H: Power supply for coupling

Figure 7.8

SEARCH COIL ARRANGEMENT
FOR PARTIALLY INTERDIGITATED ROTOR

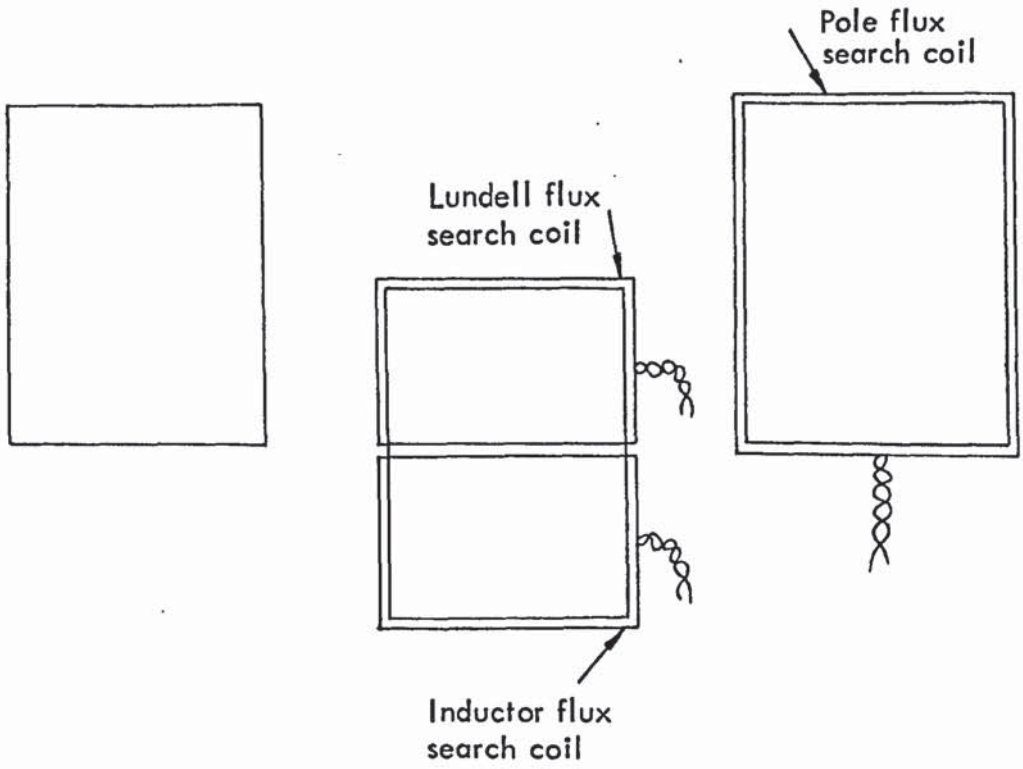

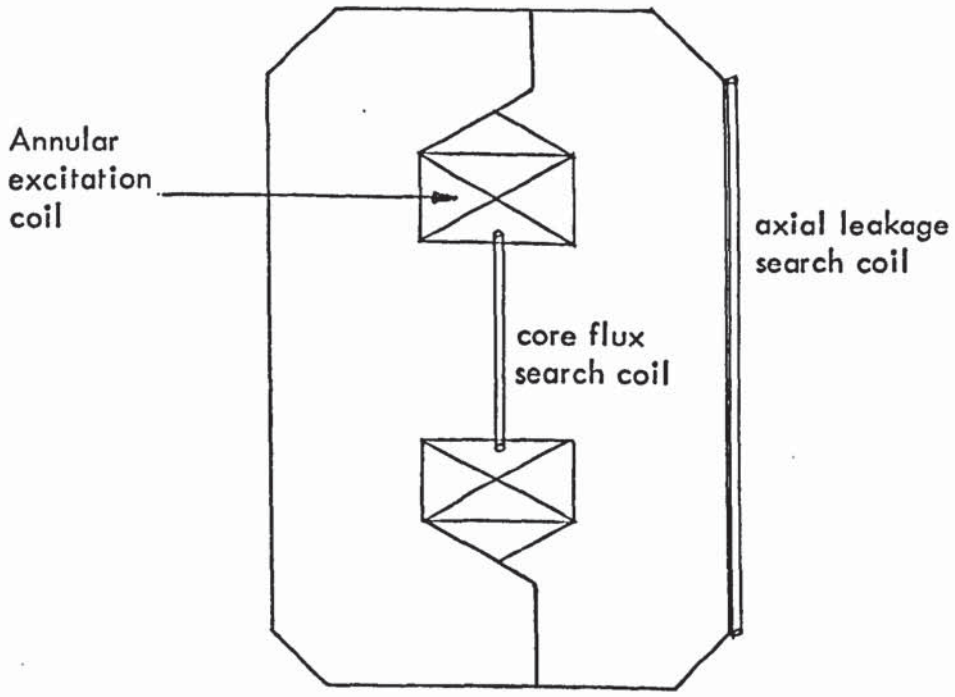

Figure 7.9

SEARCH COIL ARRANGEMENT
FOR SALIENT POLE ROTOR

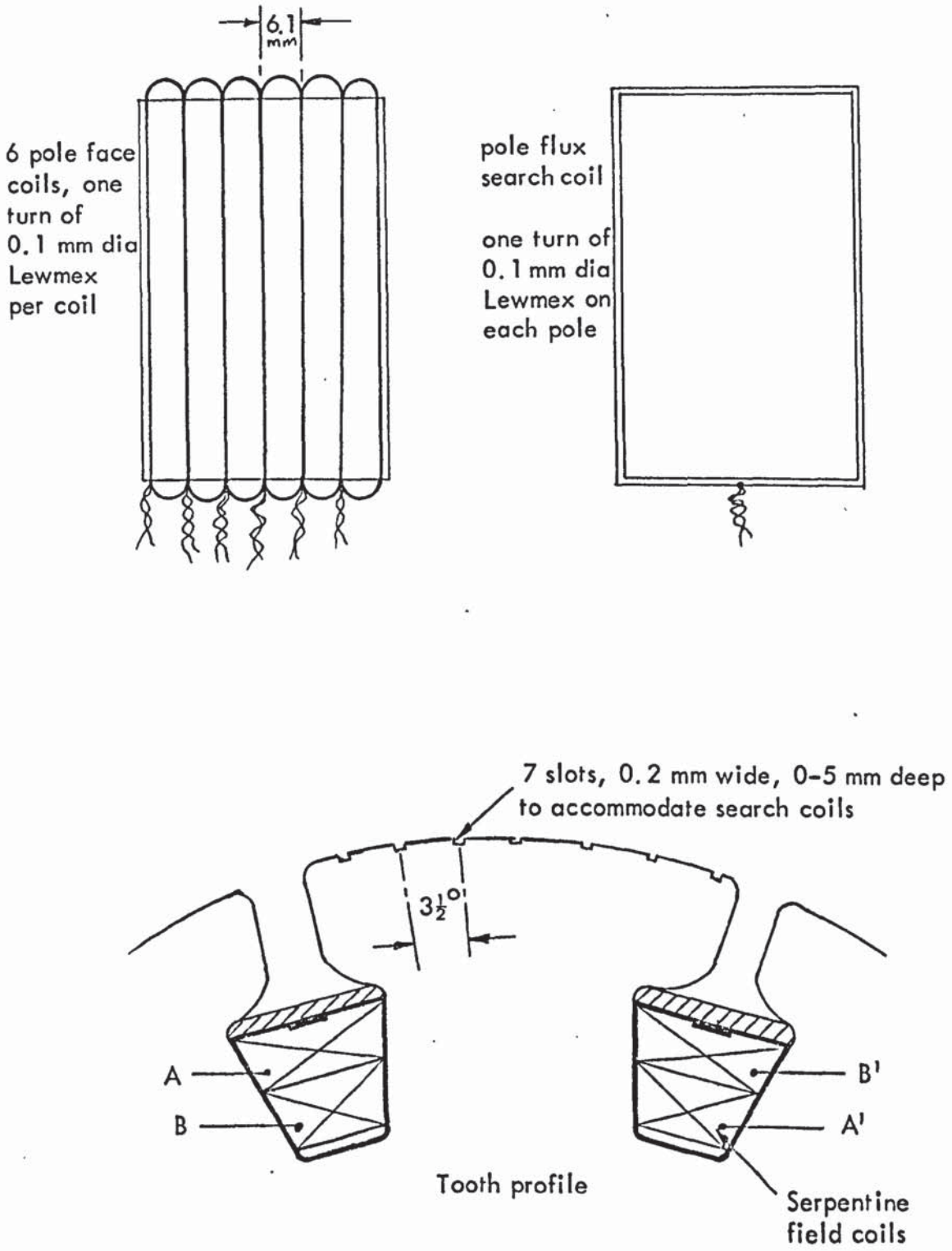

FIGURES FOR CHAPTER 8.

EXPERIMENTAL TORQUE-SLIP CURVES OF SALIENT POLE COUPLING Figure 8.1

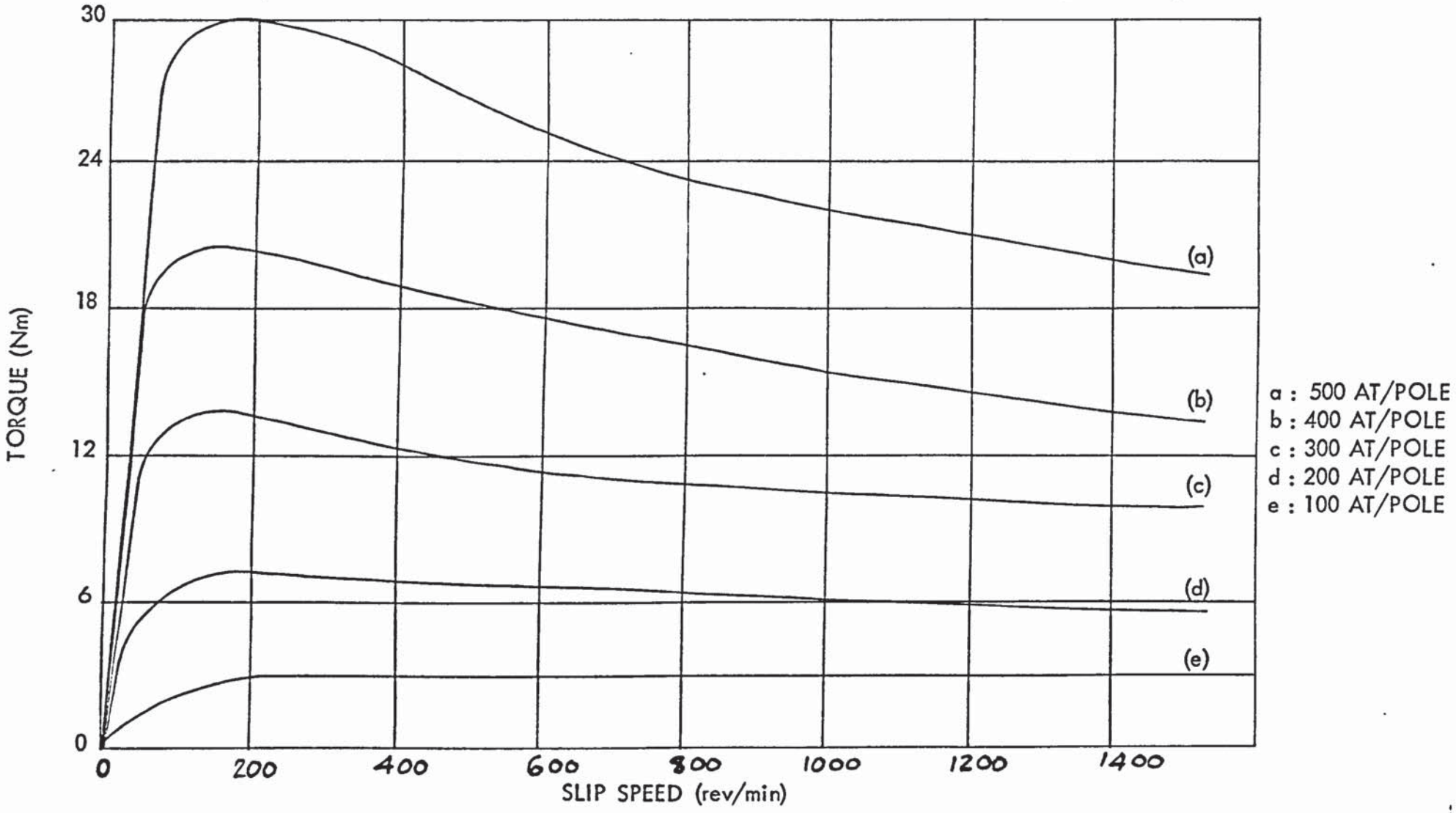

Figure 8.2

FLUX LINKING FIELD WINDING AND LEAKAGE FLUX AS A FUNCTION OF EXCITATION M.M.F. AT VARIOUS SLIP SPEEDS.

(Fluxes are reduced to a per-pole basis)

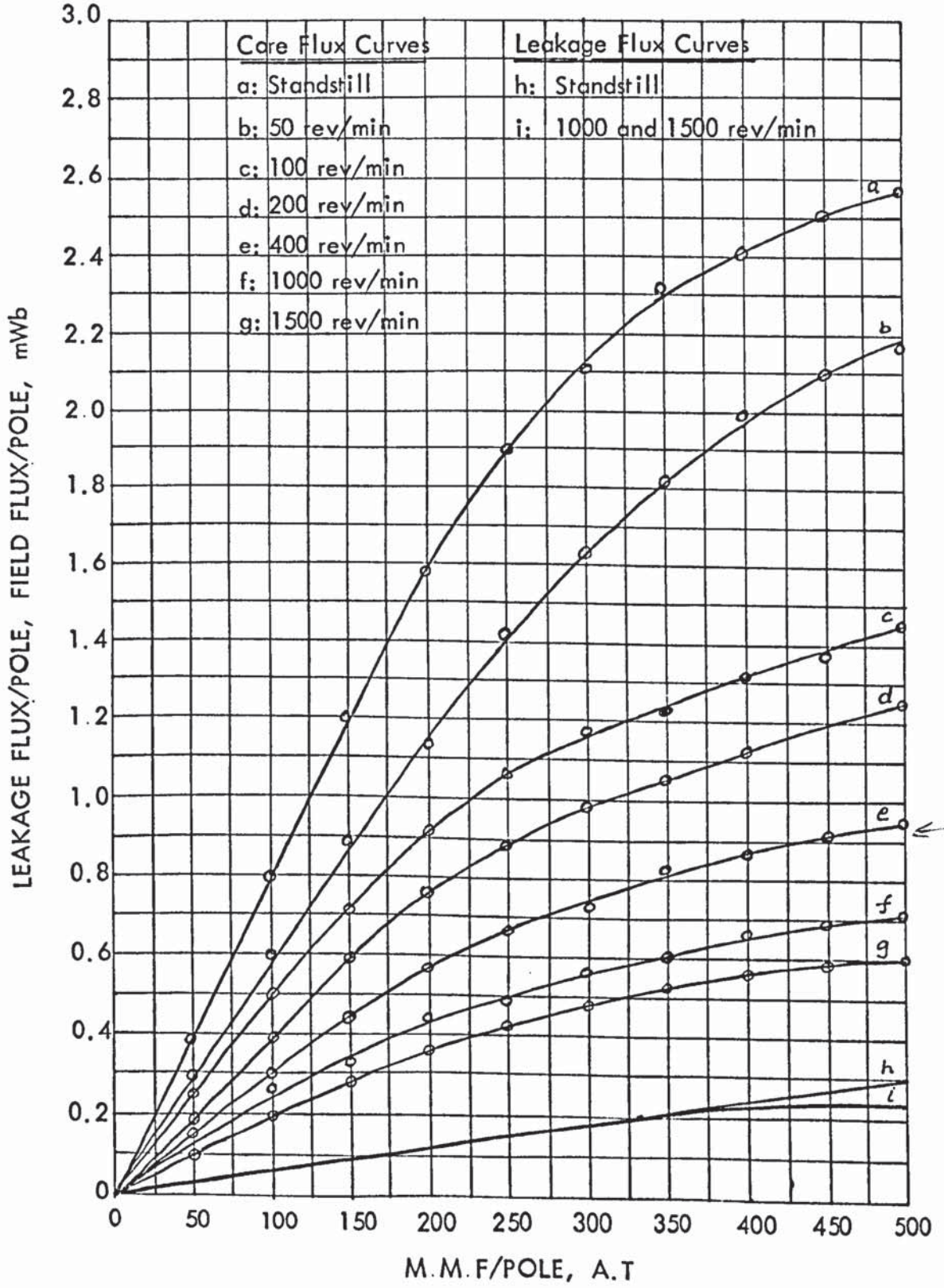

Figure 8.3

AIRGAP FLUX/POLE AS A FUNCTION OF
EXCITATION M.M.F. AT VARIOUS SLIP SPEEDS

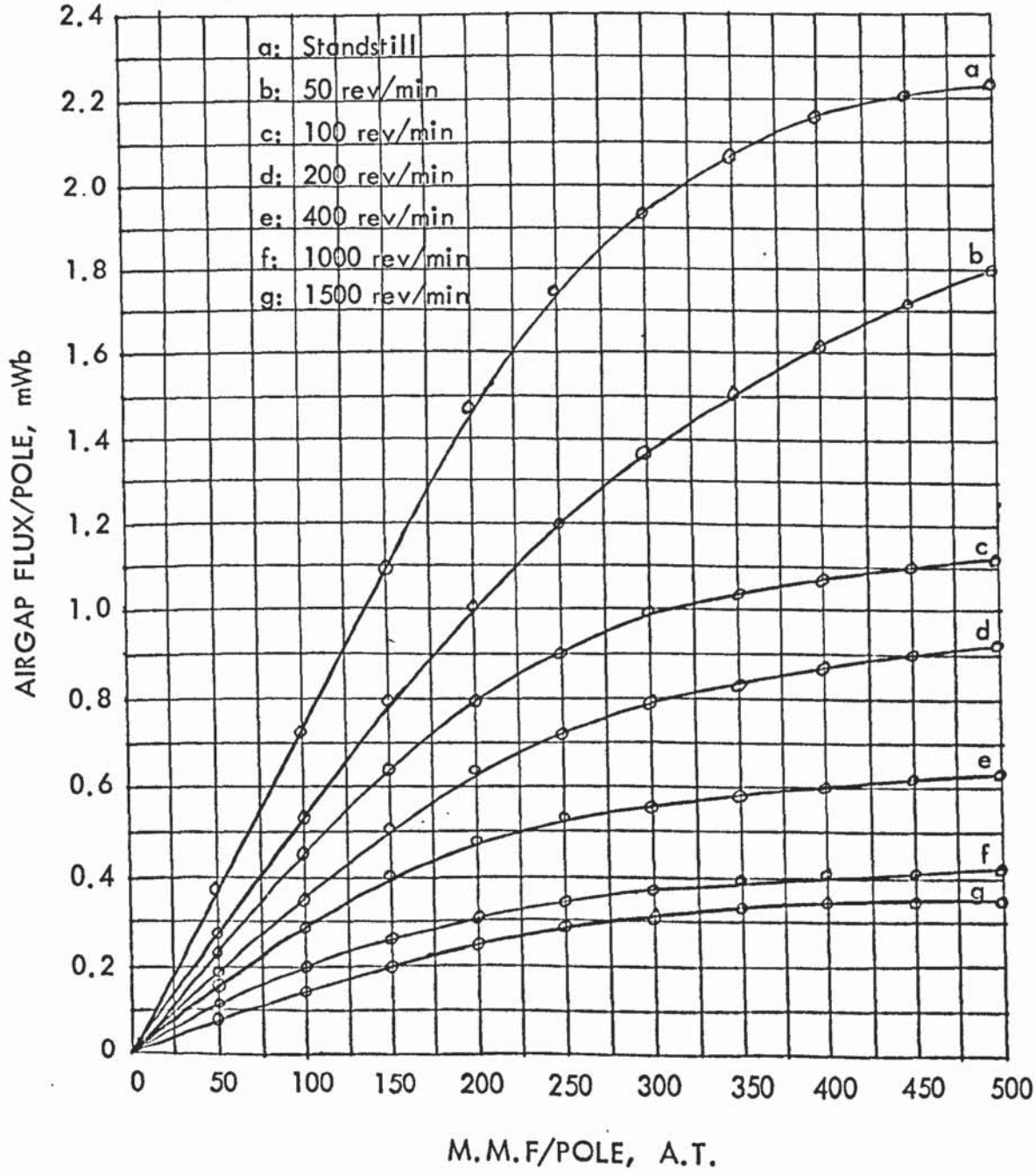

Figure 8.4

Pole face flux-density distribution
at various slip speeds
Excitation M. M. F. = 50 AT/POLE

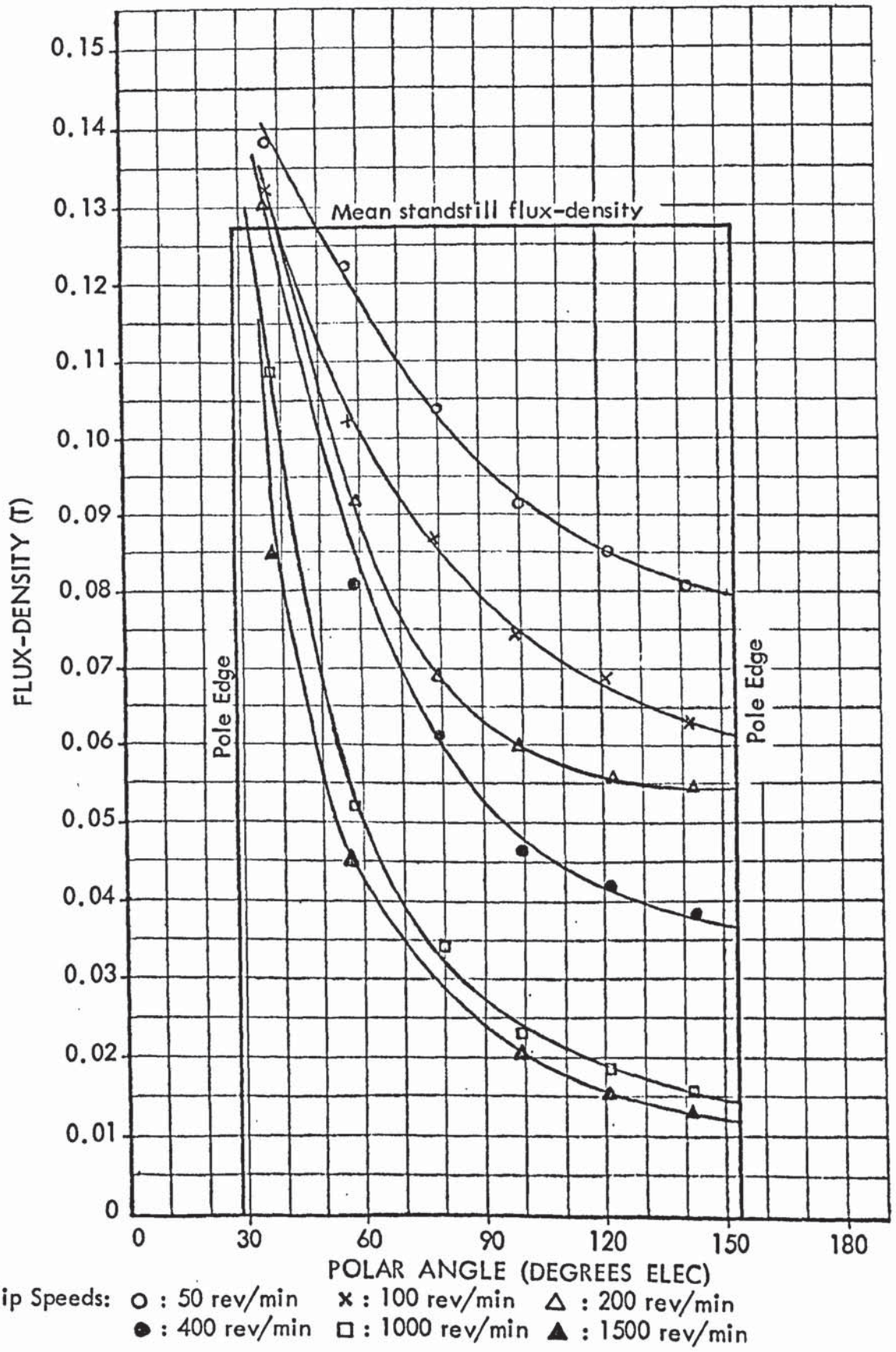

Figure 8.5

Pole face flux-density distribution
at various slip speeds
Excitation M.M.F. = 100 AT/POLE

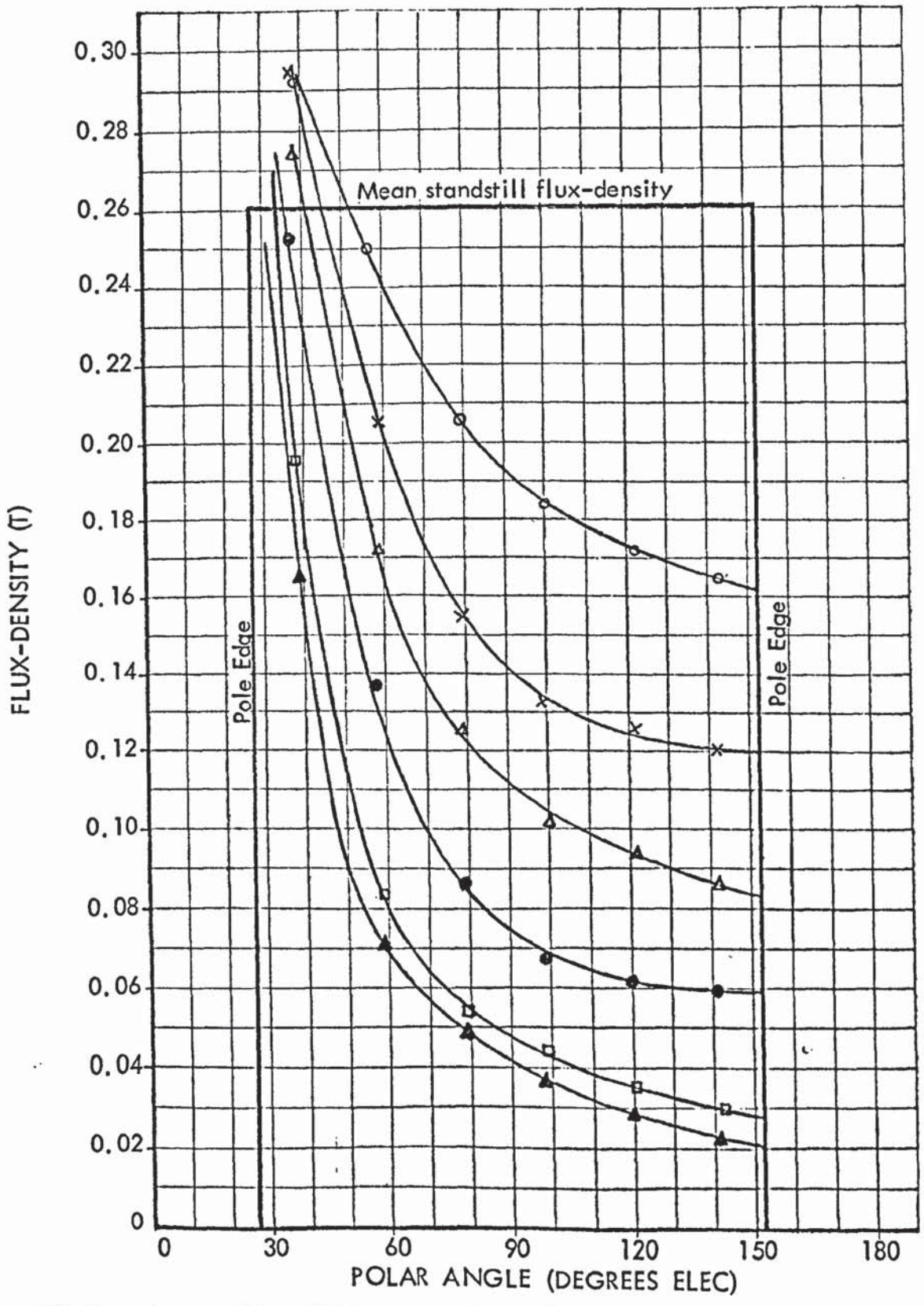

Figure 8.6

Pole face flux-density distribution
at various slip speeds
Excitation M M F = 200 AT/POLE

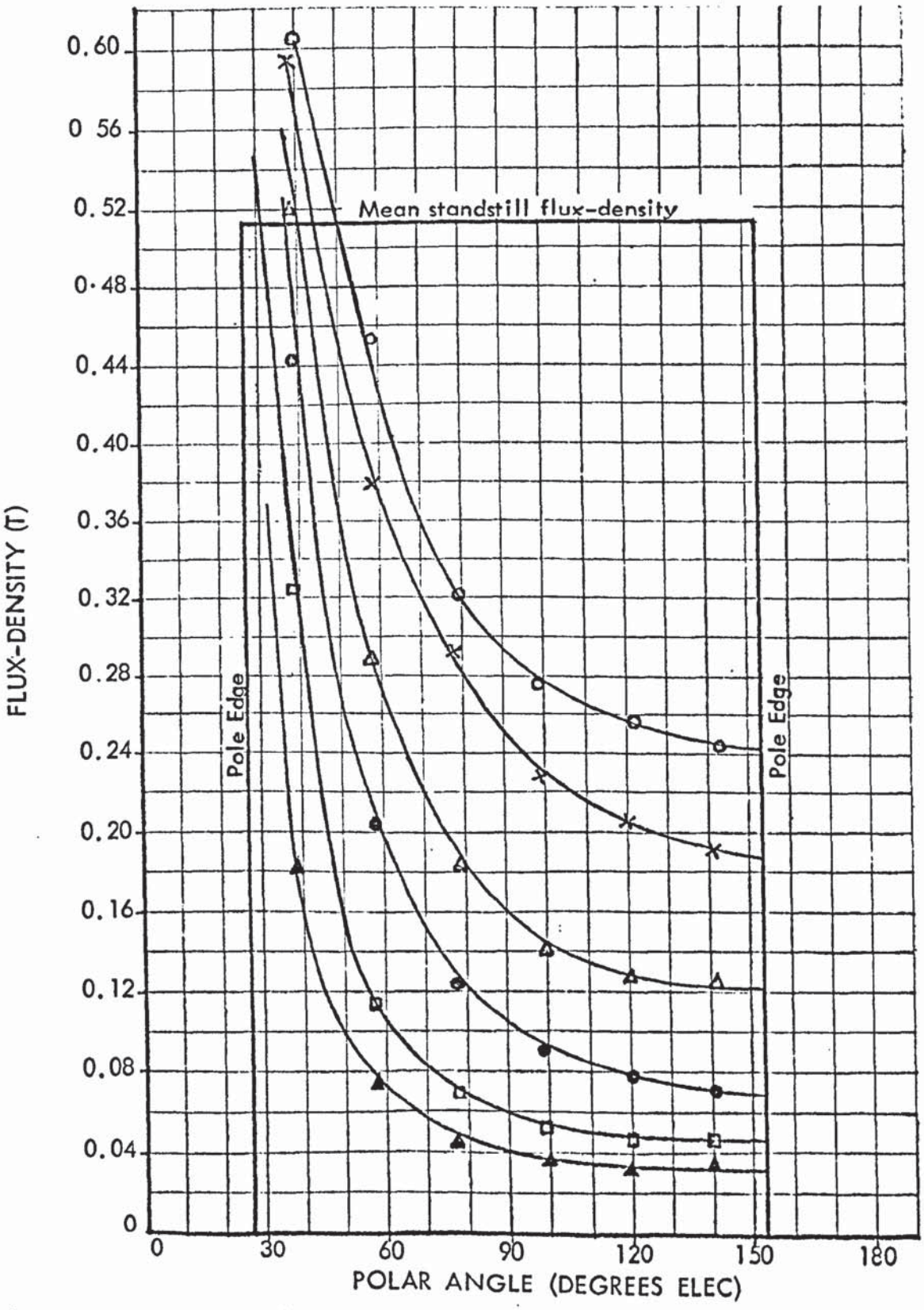

Slip Speeds: o : 50 rev/min × : 100 rev/min △ : 200 rev/min
● : 400 rev/min □ : 1000 rev/min ▲ : 1500 rev/min

Figure 8.7

Pole face flux-density distribution
at various slip speeds
Excitation M.M.F. = 300 AT/POLE

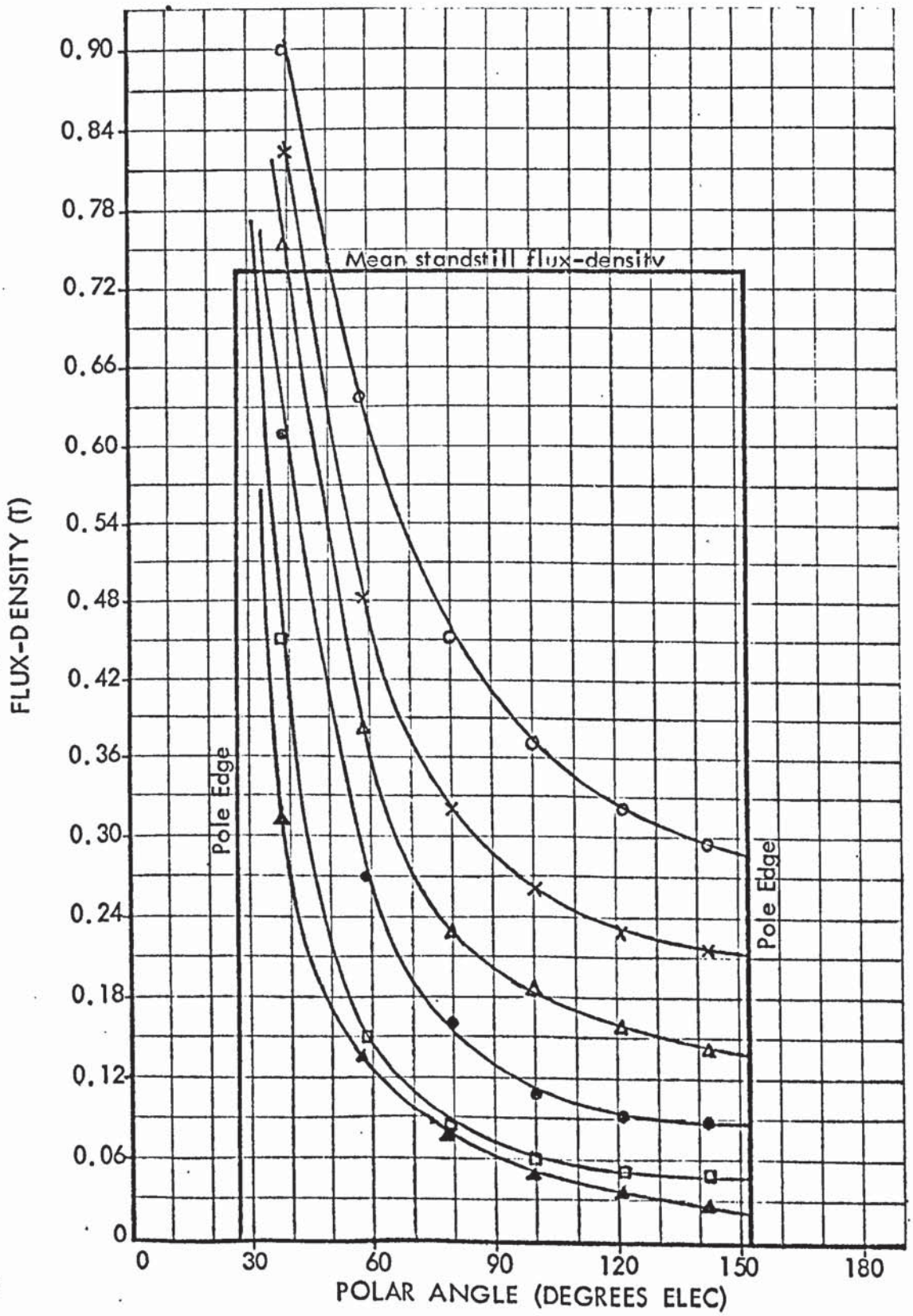

Slip Speeds: o : 50 rev/min x : 100 rev/min Δ : 200 rev/min
● : 400 rev/min □ : 1000 rev/min ▲ : 1500 rev/min

Figure 8.8

Pole face flux-density distribution
at various slip speeds
Excitation M.M.F = 400 AT/POLE

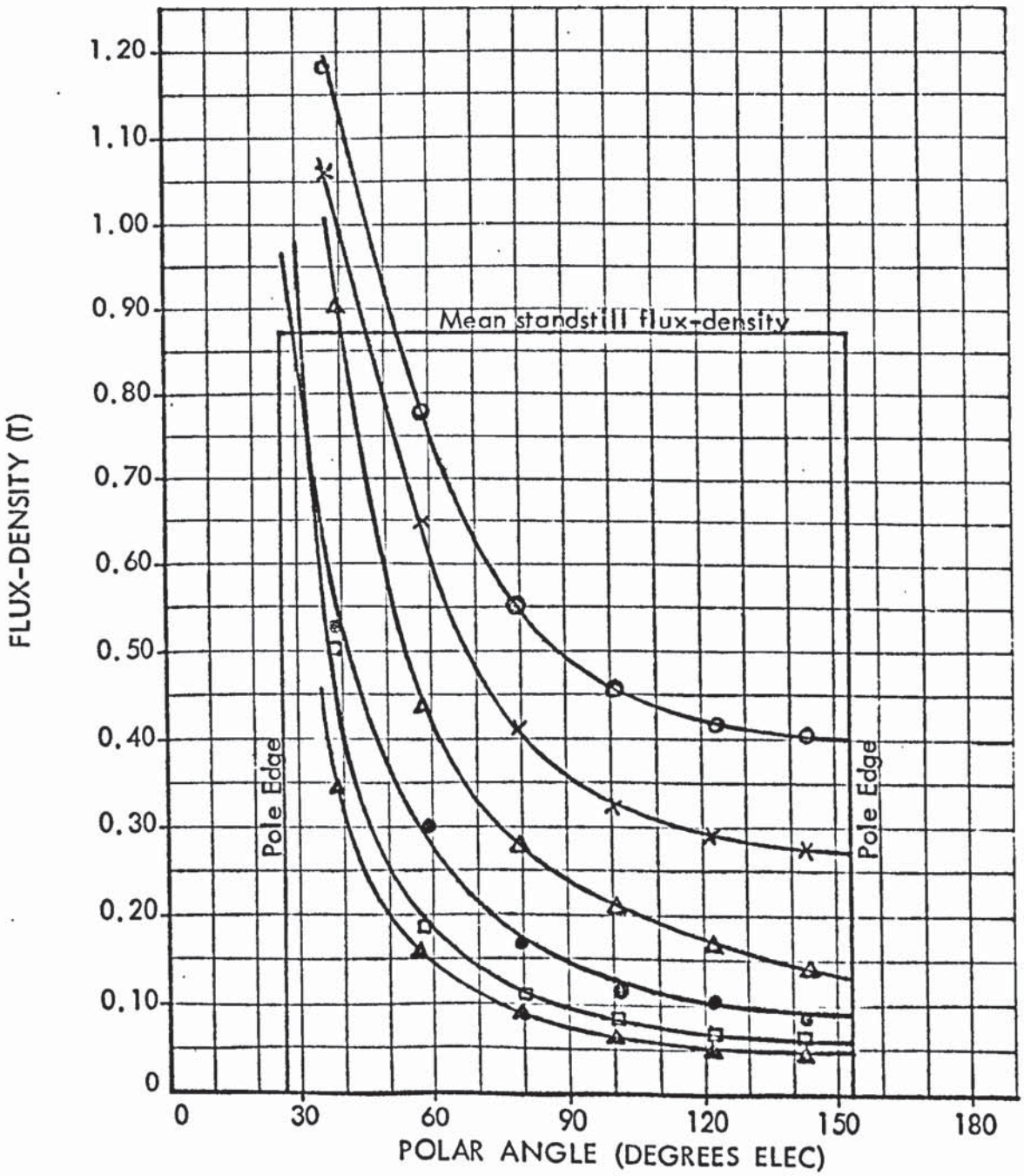

Slip Speeds: O : 50 rev/min × : 100 rev/min △ : 200 rev/min
● : 400 rev/min □ : 1000 rev/min ▲ : 1500 rev/min

FIGURE 8.10

VARIATION OF FUNDAMENTAL FLUX WITH SLIP SPEED

FOR VARIOUS EXCITATIONS.

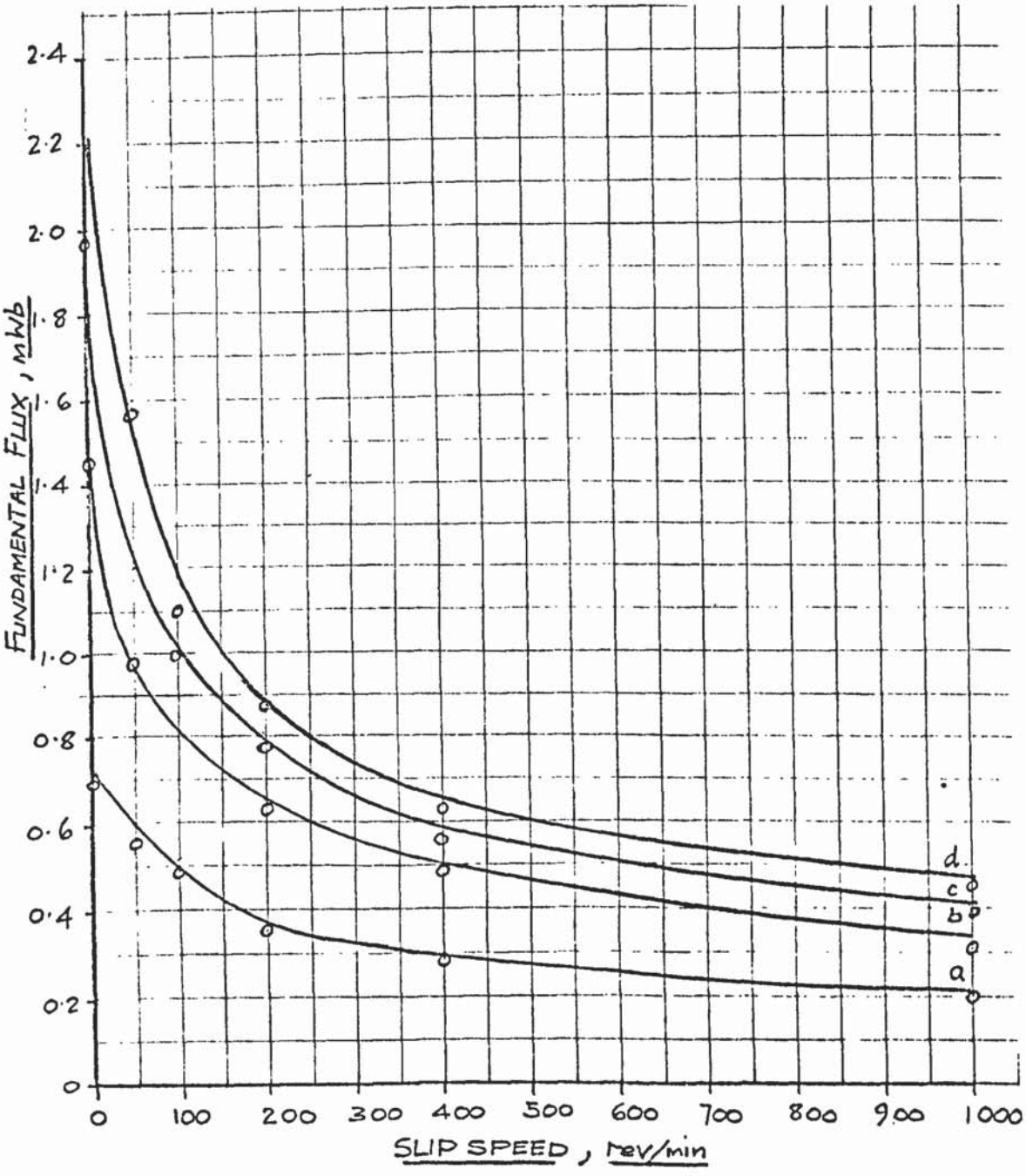

Excitation m.m.f.s:

a: 100 AT/pole b: 200 AT/pole

c: 300 AT/pole d: 400 AT/pole.

o: values of total flux/pole.

FIGURE 8.11

ARMATURE REACTION M.M.F / SLIP SPEED
AT VARIOUS EXCITATION M.M.FS

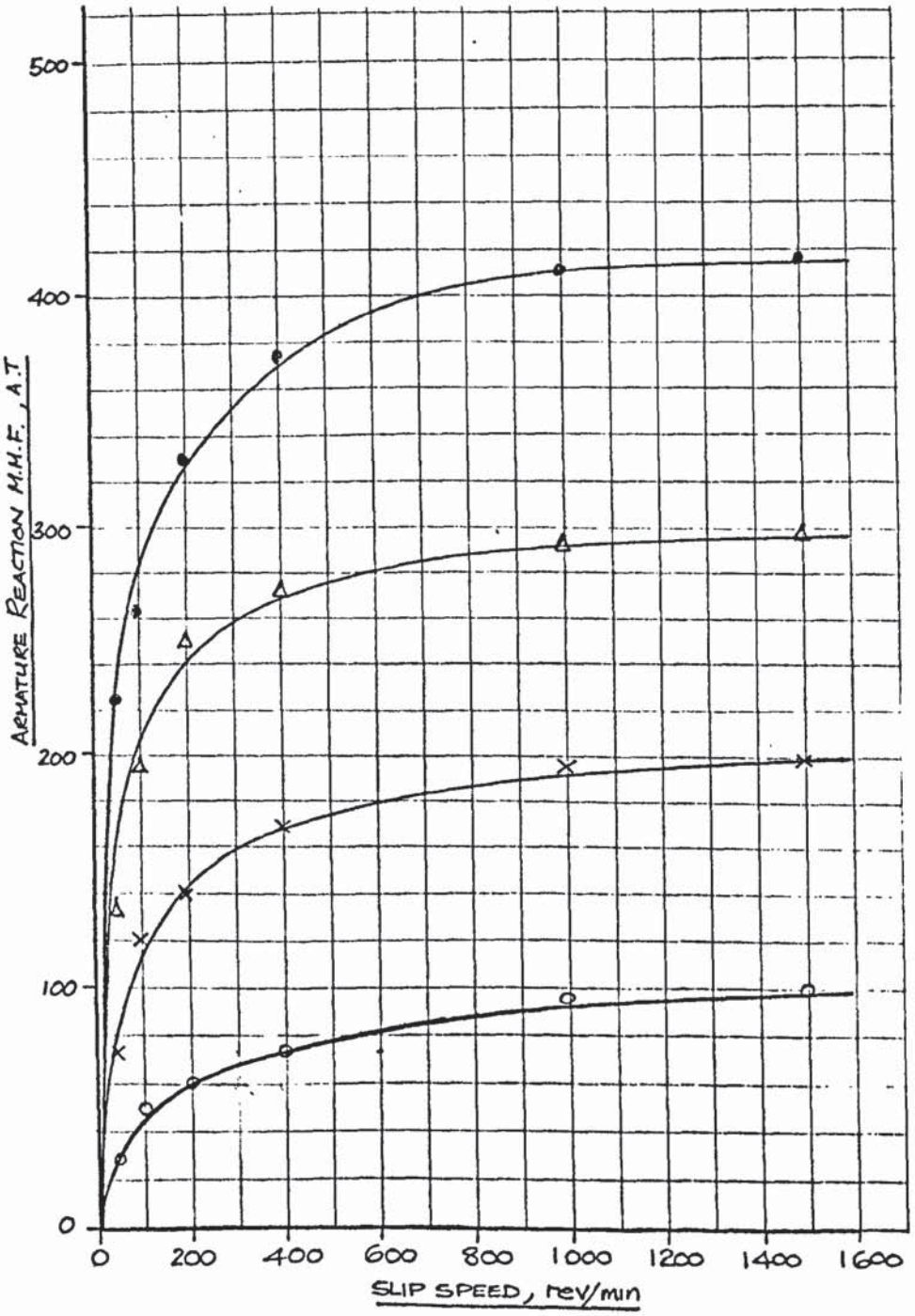

EXCITATIONS: ○: 100 AT/POLE , △: 300 AT/POLE
× : 200 AT/POLE , ● : 400 AT/POLE

FIGURE 8.12.

TORQUE AGAINST FUNDAMENTAL FLUX

AT CONSTANT SLIP.

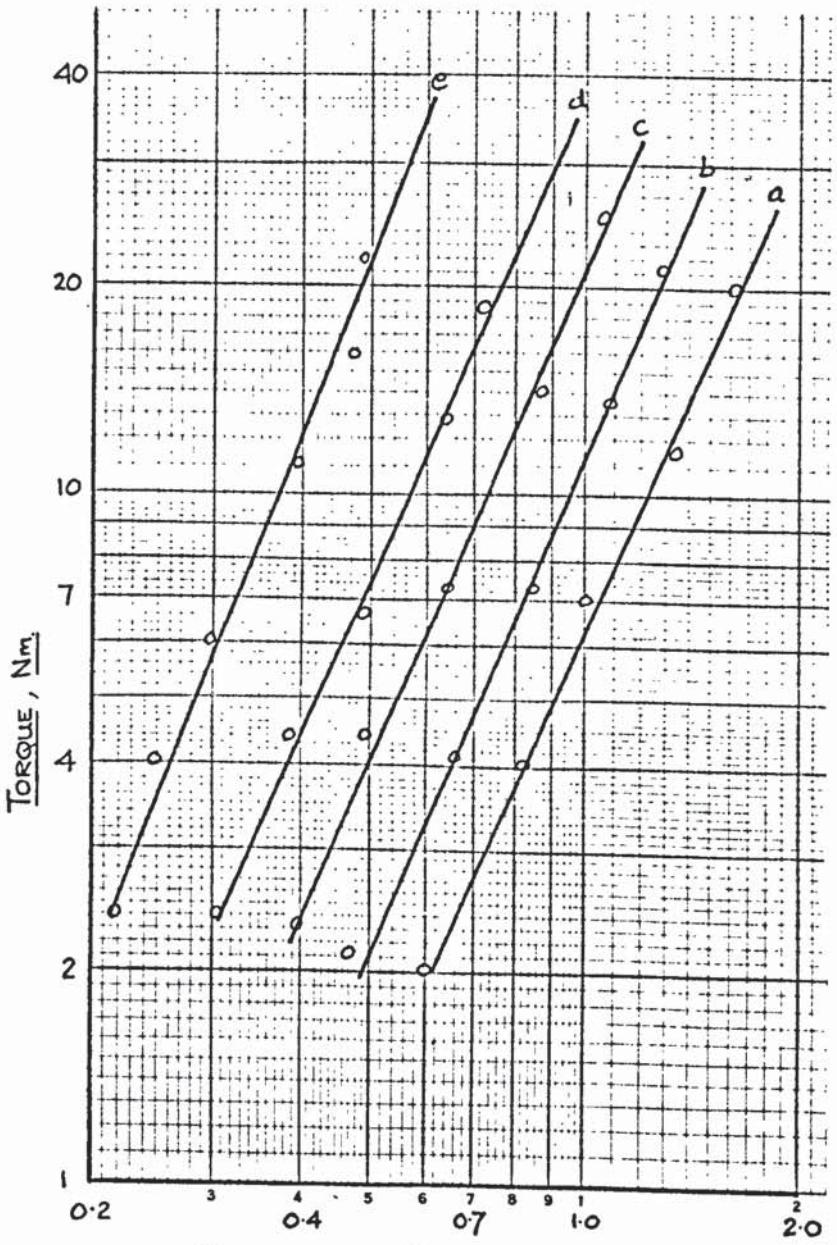

a: 50 rev/min, SLOPE = 2·35. d: 400 rev/min, SLOPE = 2·65

b: 100 rev/min, SLOPE = 2·6. e: 1000 rev/min, SLOPE = 2·7.

c: 200 rev/min, SLOPE = 2·6.

FIGURE 8.13

TORQUE AGAINST SLIP SPEED

AT CONSTANT FLUX.

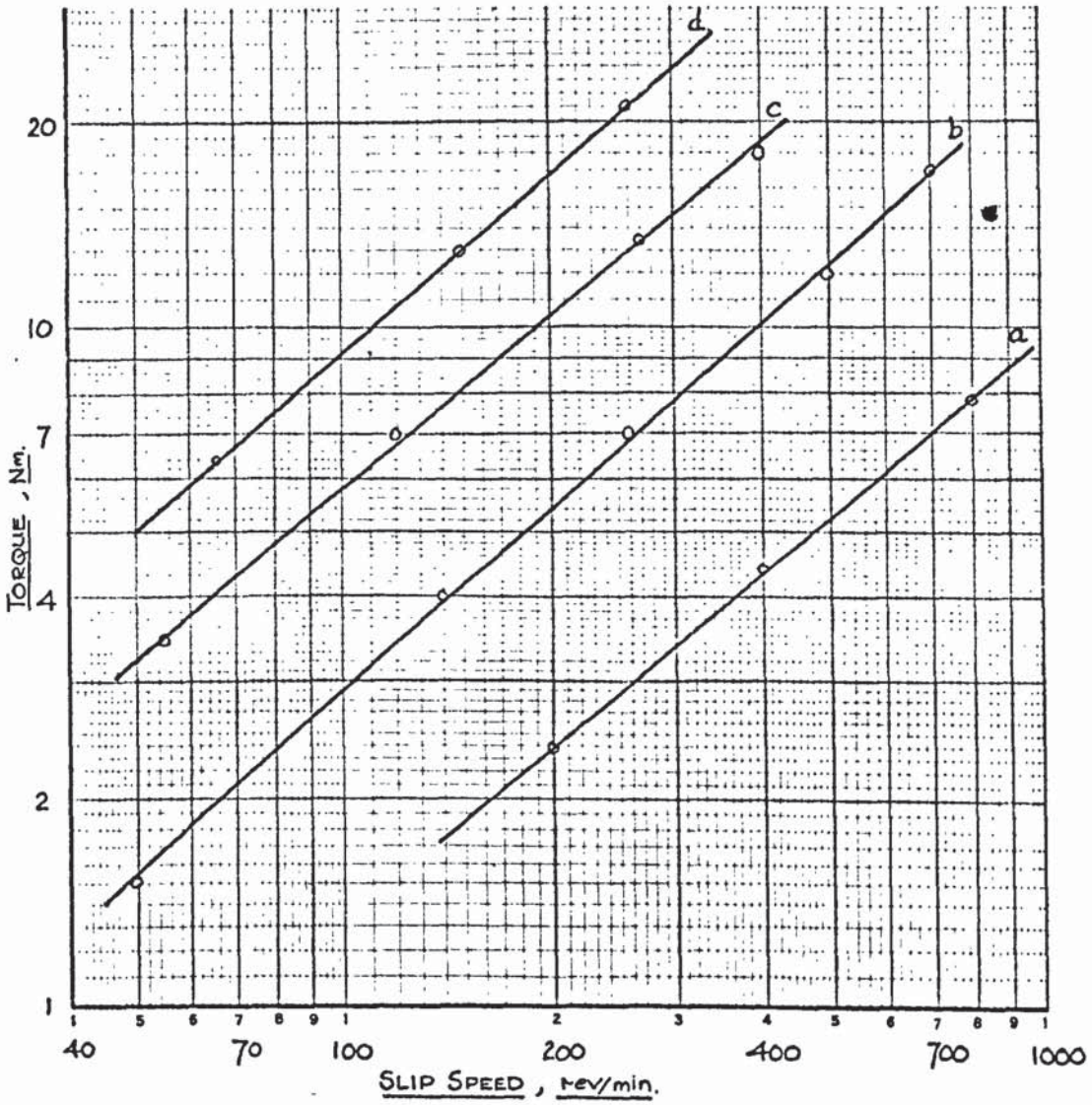

a: 0·4 mWb., SLOPE = 0·85. c: 0·8 mWb., SLOPE = 0·9.

b: 0·6 mWb., SLOPE = 0·9. d: 1·0 mWb., SLOPE = 0·93.

Figure 8.14

NORMALISED CURVES

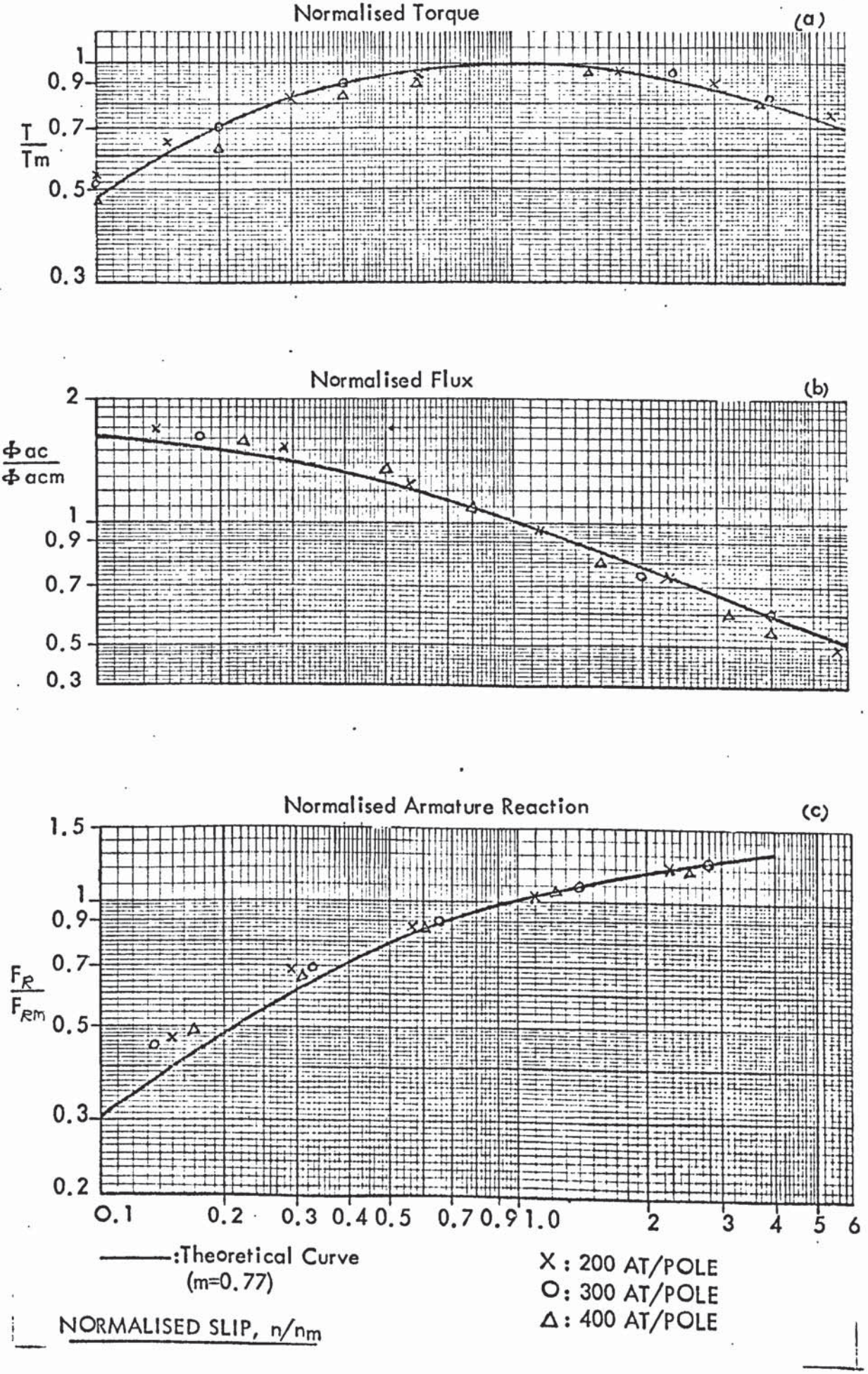

Figure 8.16

Transient pole face flux-density distribution at different instants in time, following a voltage step on the field winding
Slip speed = 100 rev/min

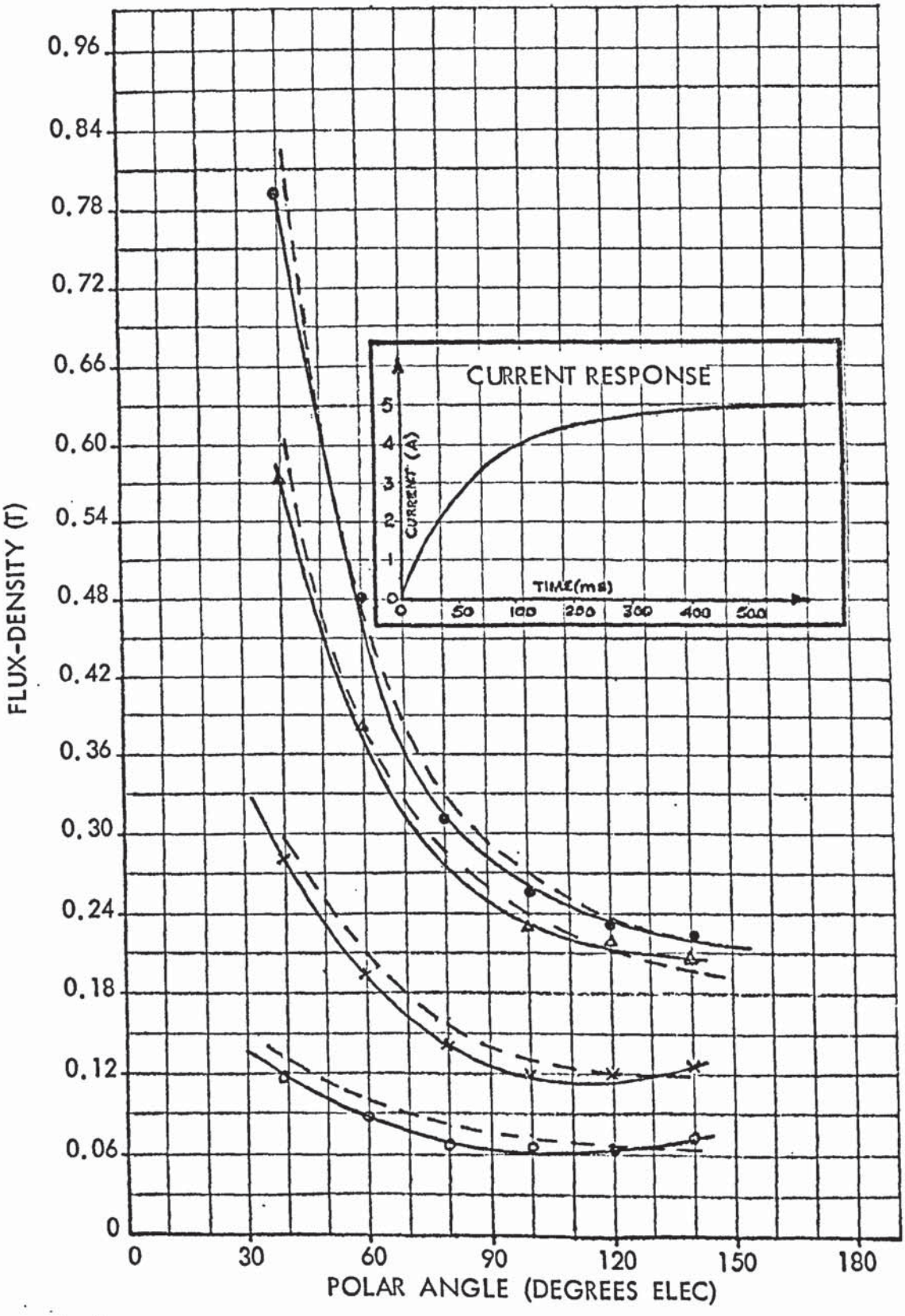

——: Transient curve - - -: Steady-state curve for same field current
o : 0.5A (5.6 ms) x : 1.0A (11.2 ms) △ : 2.0A (34 ms) ● : 3.0A (61 ms)

Figure 8.17

Transient pole face flux-density.
Distribution at various slip speeds.
(Each distribution curve corresponds to a field current of 3.0A).

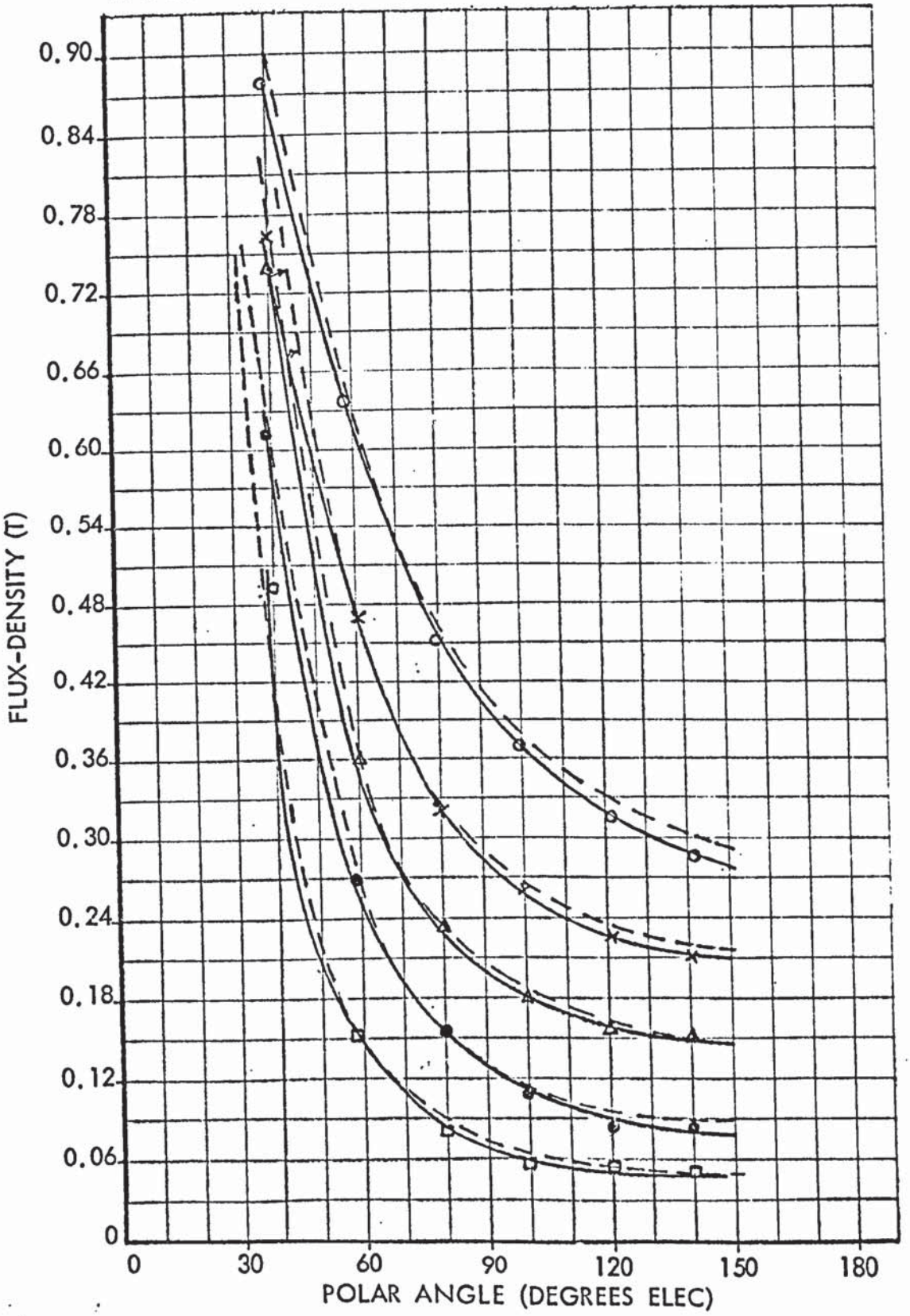

——: Transient curve. — — —: Steady-state for same slip speed
○ : 50 rev/min × : 100 rev/min △ : 200 rev/min ● : 400 rev/min
□ : 1000 rev/min

Fig. 8.18. Response of pole flux and excitation current at various slip speeds.
(time base = 20 ms/cm)
(lower trace is flux response)

(a)

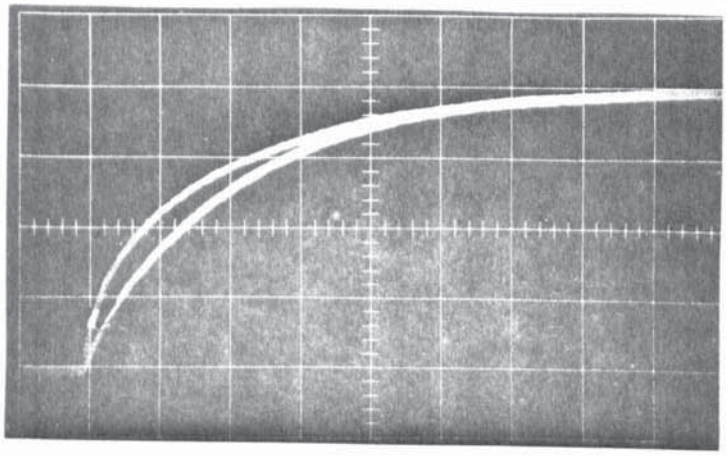

standstill

(b)

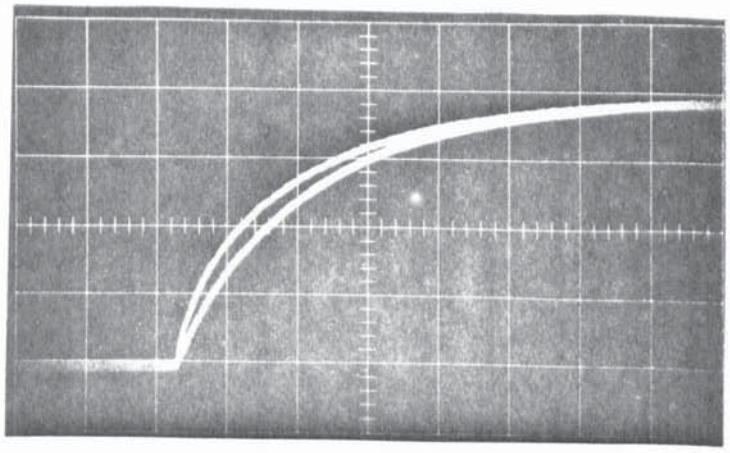

10 rev/min(1 Hz)

(c)

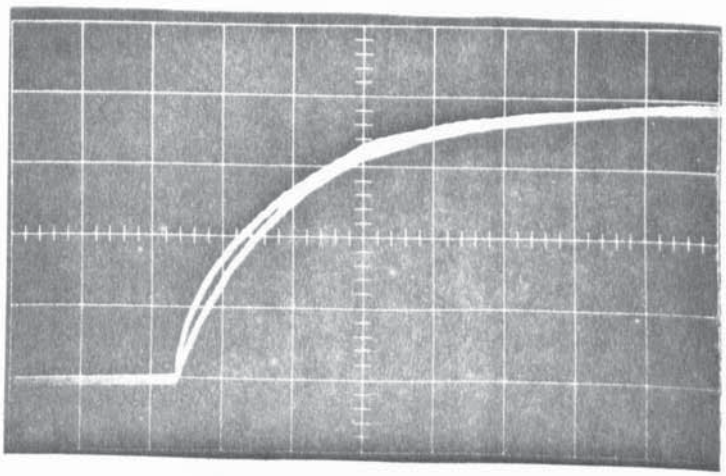

20 rev/min(2 Hz)

Fig. 8.18. Response of pole flux and excitation current at various slip speeds. (contd.)
(time base = 20 ms/cm)
(lower trace is flux response)

(d)

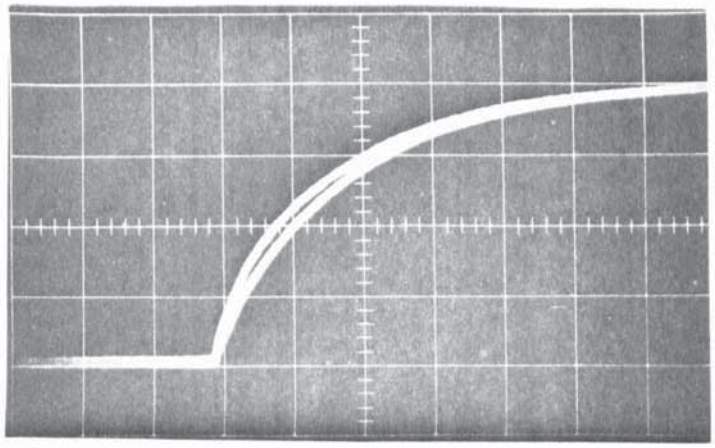

50 rev/min(5 Hz)

(e)

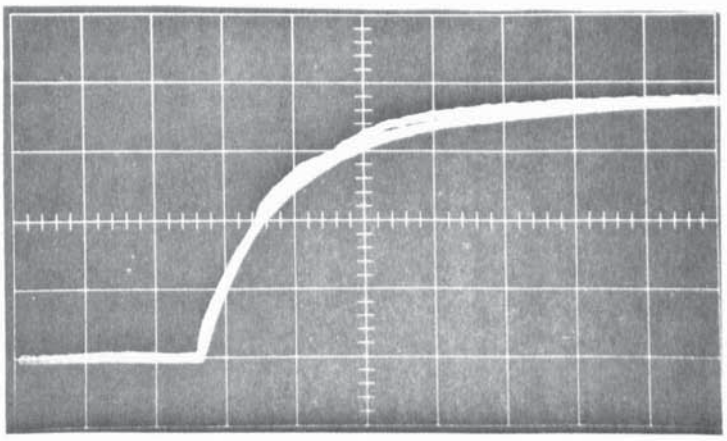

100 rev/min(10 Hz)

(f)

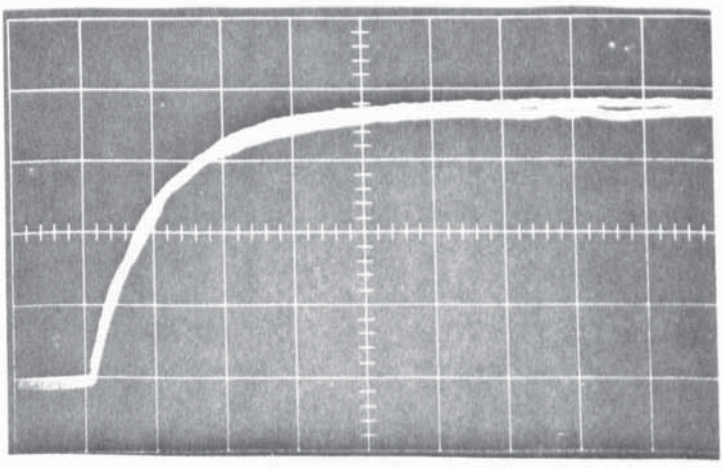

200 rev/min(20 Hz)

Fig. 8.18. Response of pole flux and excitation current at various slip speeds. (contd.)
(time base = 20 ms/cm)
(lower trace is flux response)

(g) 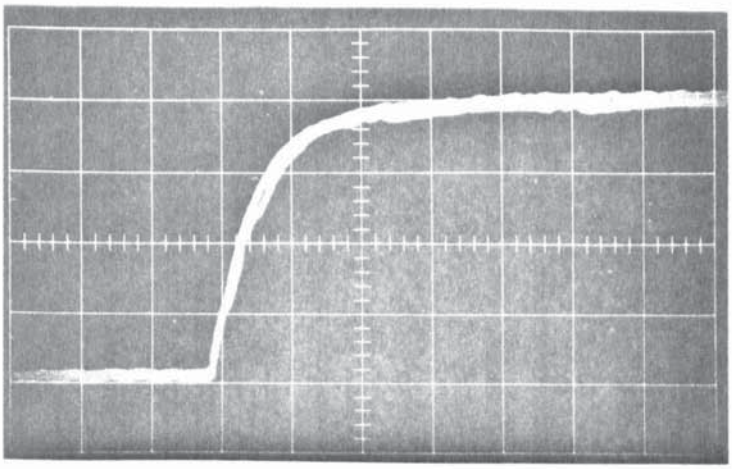 400 rev/min (40 Hz)

(h) 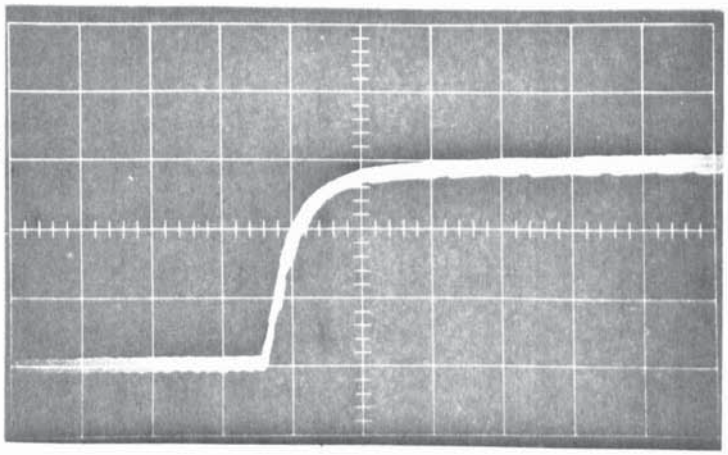 1000 rev/min (100 Hz)

Figure 8.19

VARIATION OF THE LINEAR COUPLED TIME CONSTANT, τ_g, WITH SLIP SPEED.

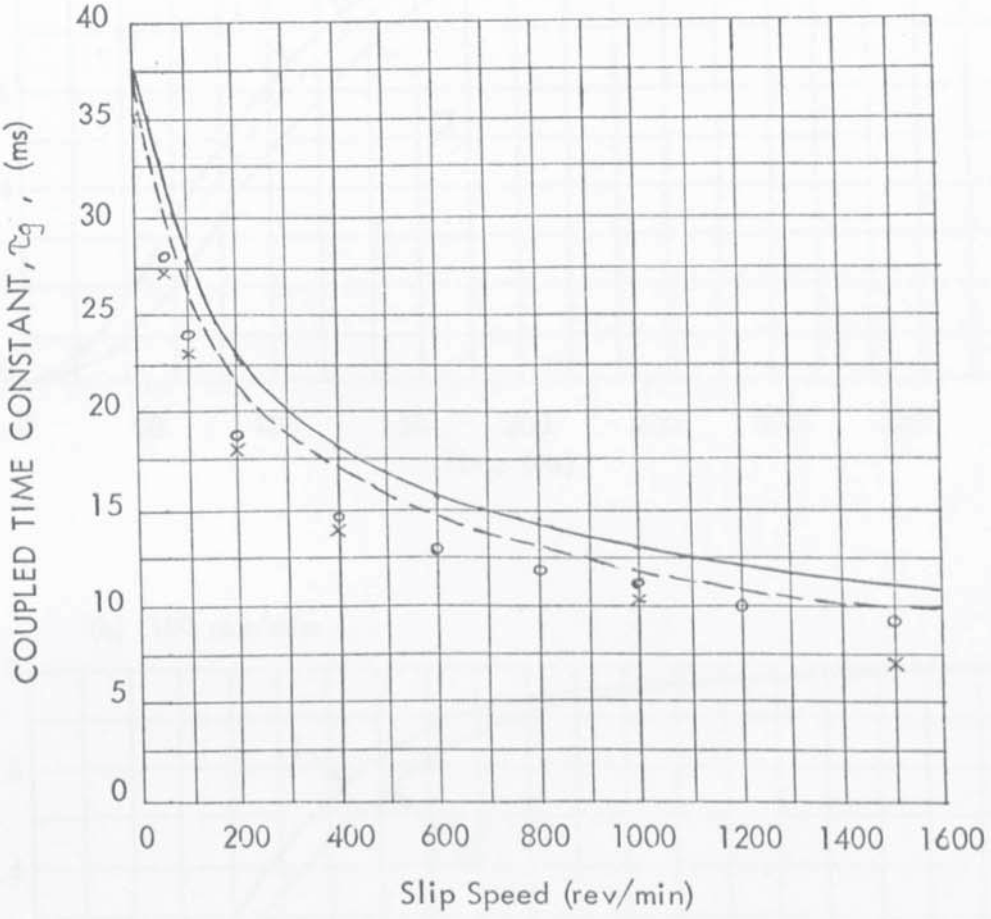

——— : Theoretical

– – – – : Calculated using Equation (8.2)

× : Calculated values from load magnetisation curves

o : Measured values from oscillograms

Figure 8.19

VARIATION OF THE LINEAR COUPLED TIME CONSTANT, τ_g, WITH SLIP SPEED.

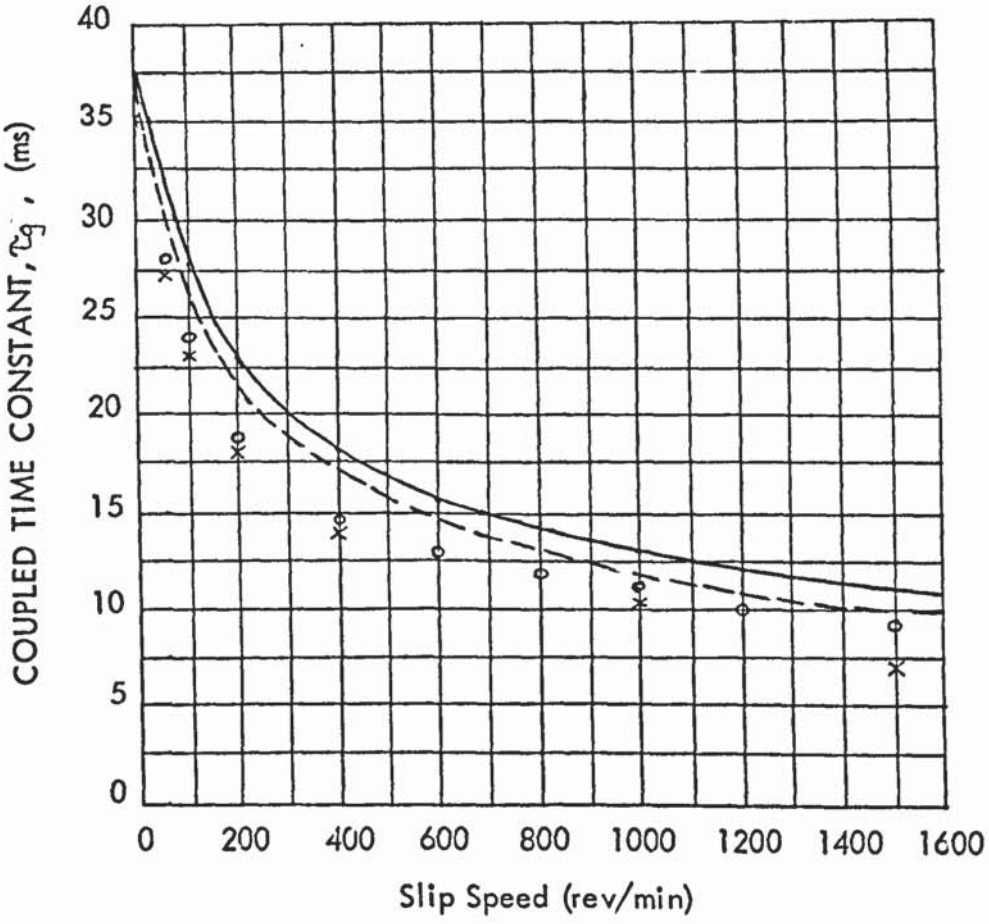

——— : Theoretical

– – – – : Calculated using Equation (8.2)

× : Calculated values from load magnetisation curves

o : Measured values from oscillograms

Figure 8, 20

TORQUE RESPONSE TO A STEP OF
FIELD VOLTAGE AT VARIOUS SLIP SPEEDS

(a) 50 rev/min

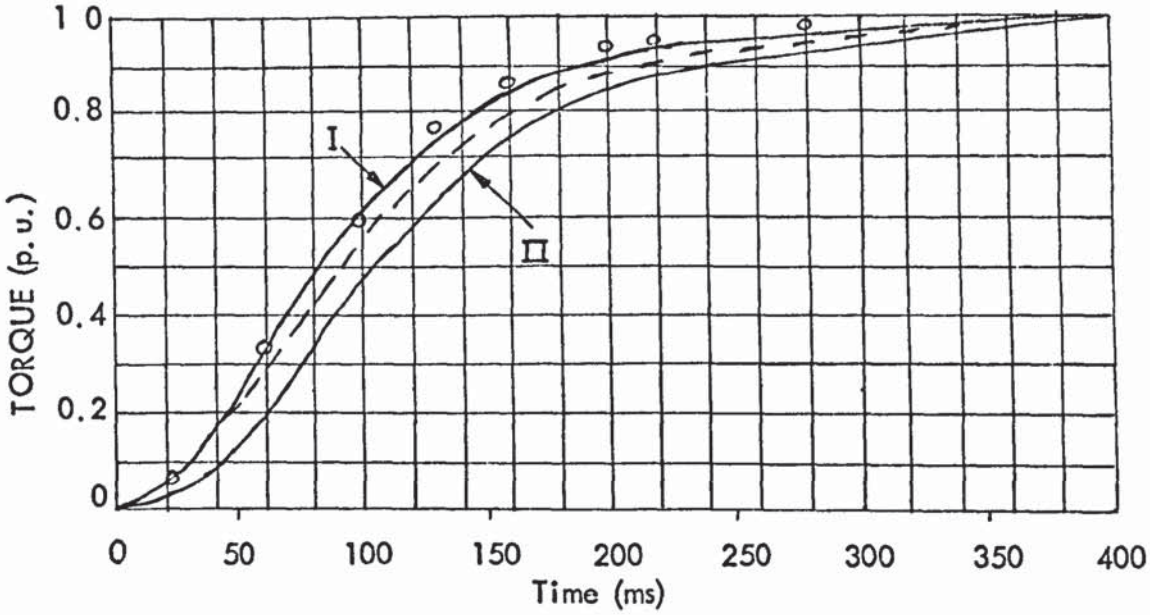

(b) 100 rev/min

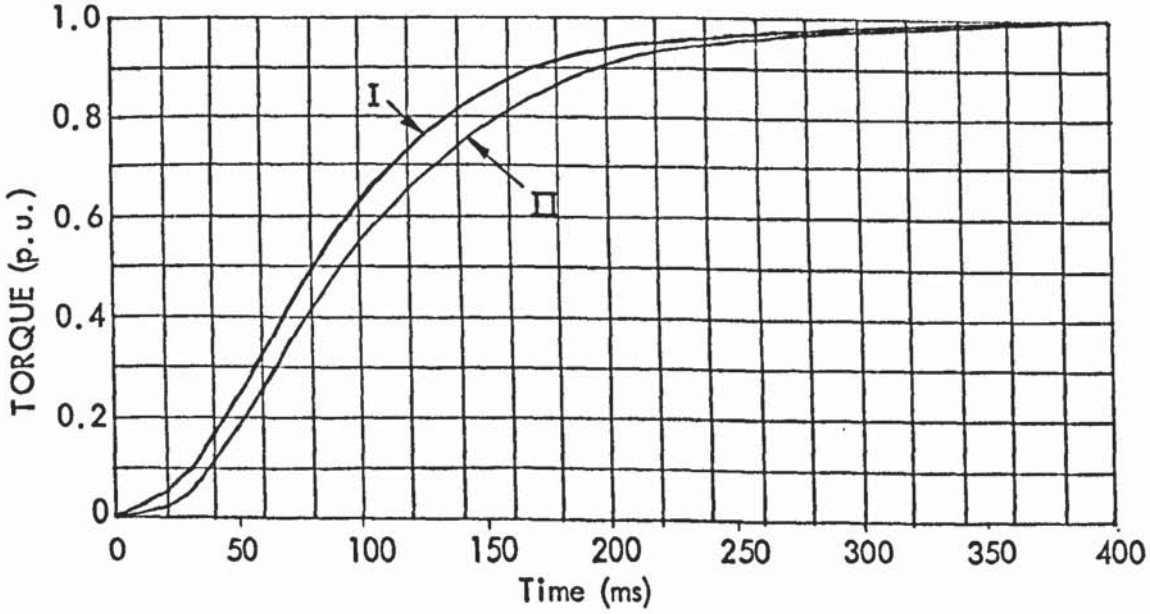

I: Measured Response
II: Theoretical Response

----: Curve calculated with measured index and theoretical time constant.

0: Points calculated with measured index and measured time constant.

Figure 8.20 (continued)

(c) 200 rev/min

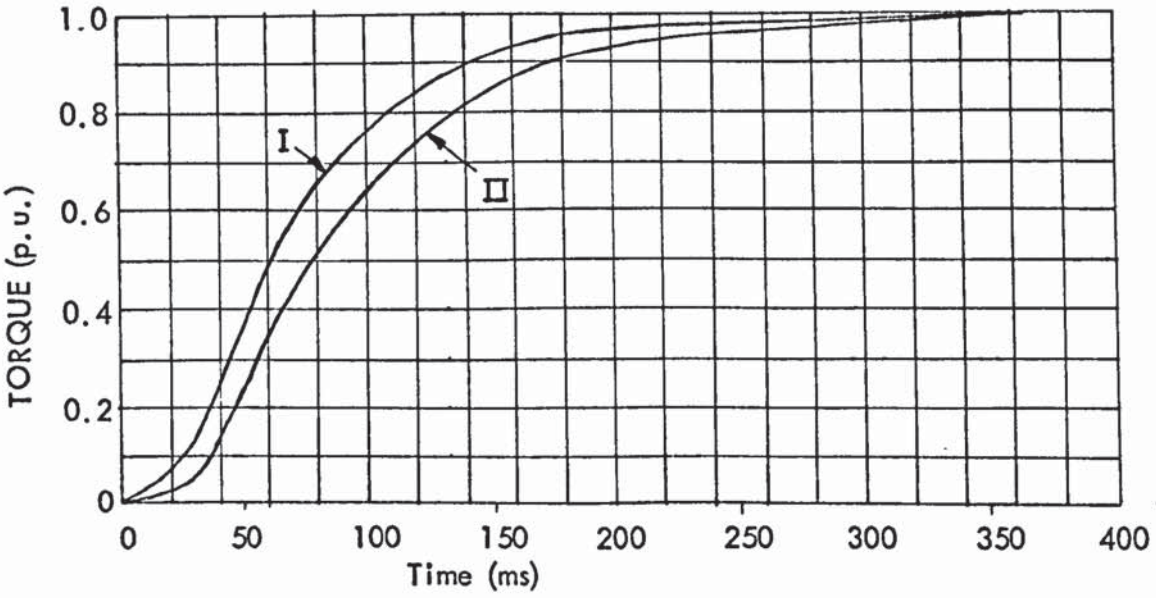

(d) 400 rev/min

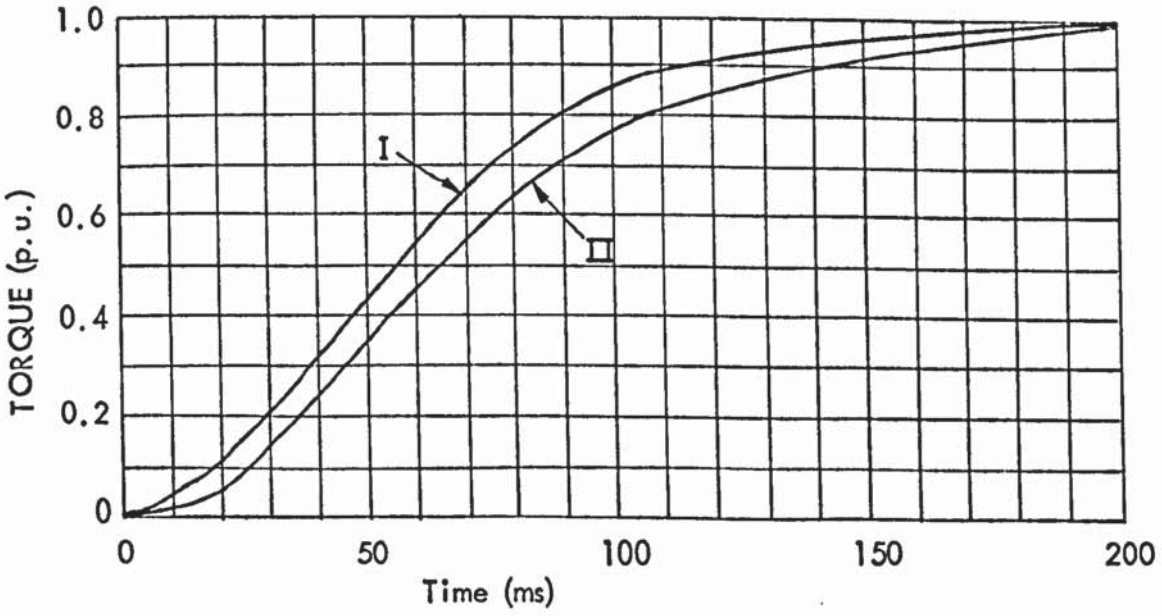

I: Measured Response
II: Theoretical Response

Figure 8.20 (continued)

(e) 800 rev/min

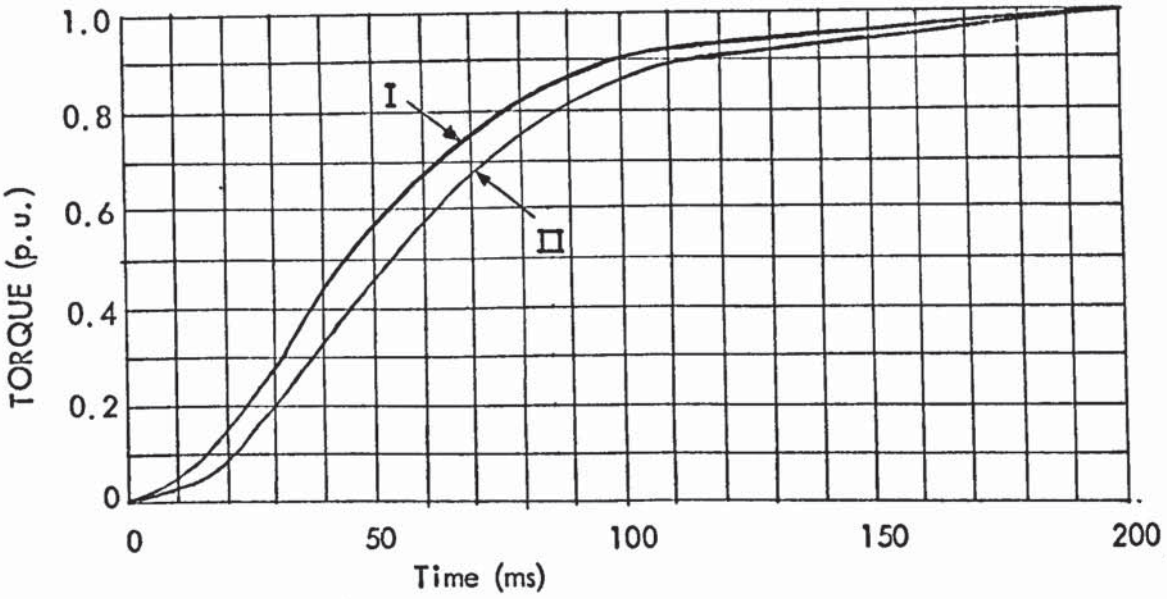

(f) 1000 rev/min

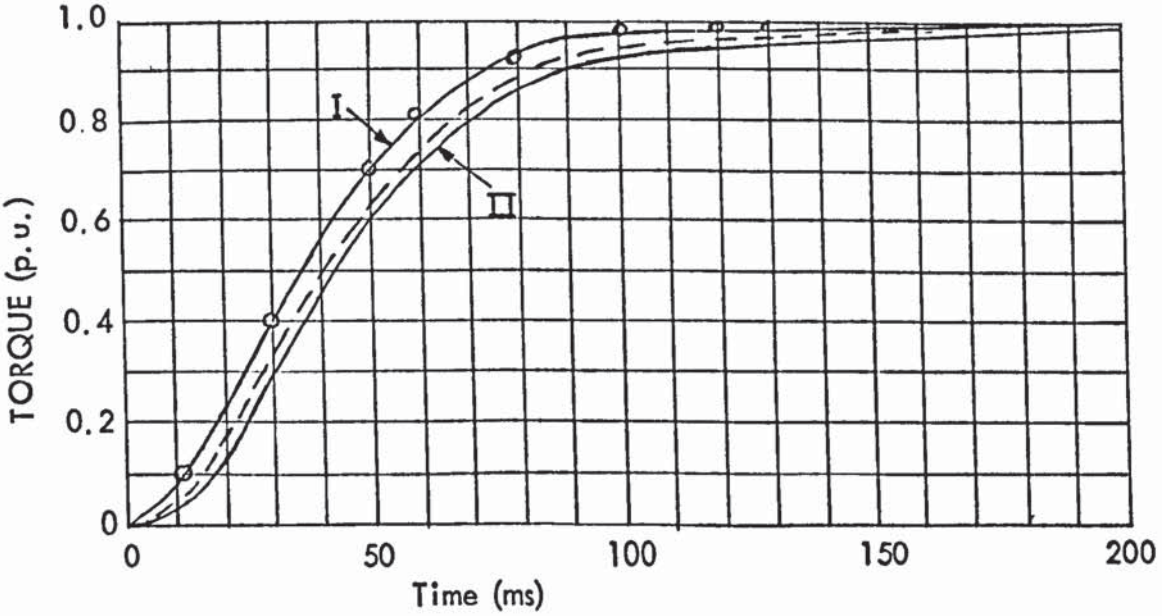

I: Measured Response
II: Theoretical Response

----: Curve calculated with measured index and theoretical time constant

0: Points calculated with measured index and measured time constant.

Figure 8.21

TORQUE RESPONSE TO A LARGE STEP
OF FIELD VOLTAGE AT LOW SLIP

(a) Slip Speed = 50 rev/min, Steady-State Field Current = 2.5A

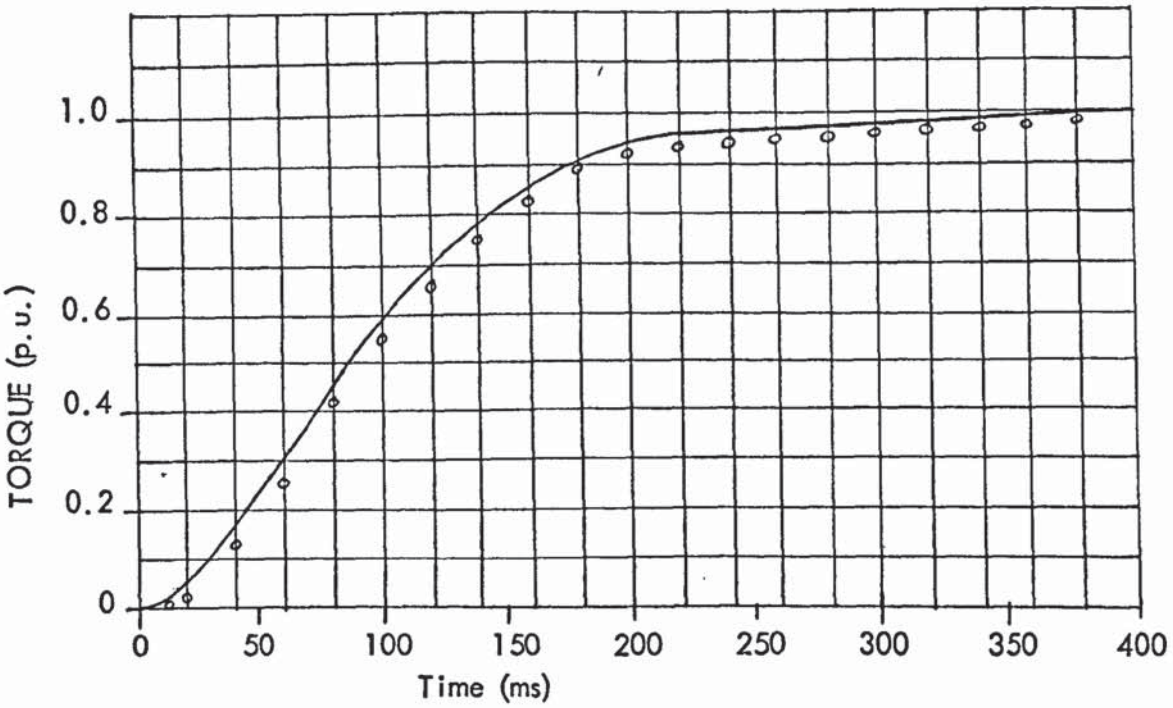

(b) Slip Speed = 100 rev/min, Steady-State Field Current = 2.0A

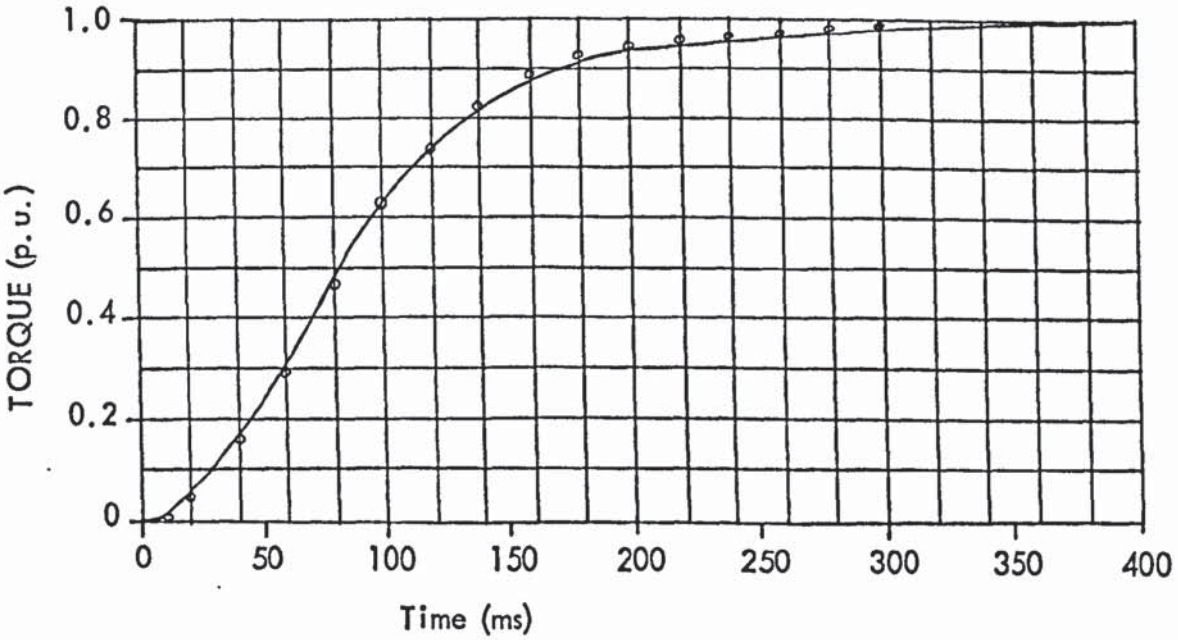

——— : Measured Response

o : Calculated Points

Figure 8.22

TORQUE RESPONSE TO AN INCREMENTAL VOLTAGE STEP FROM 29.1–40.8V

(a) 50 rev/min

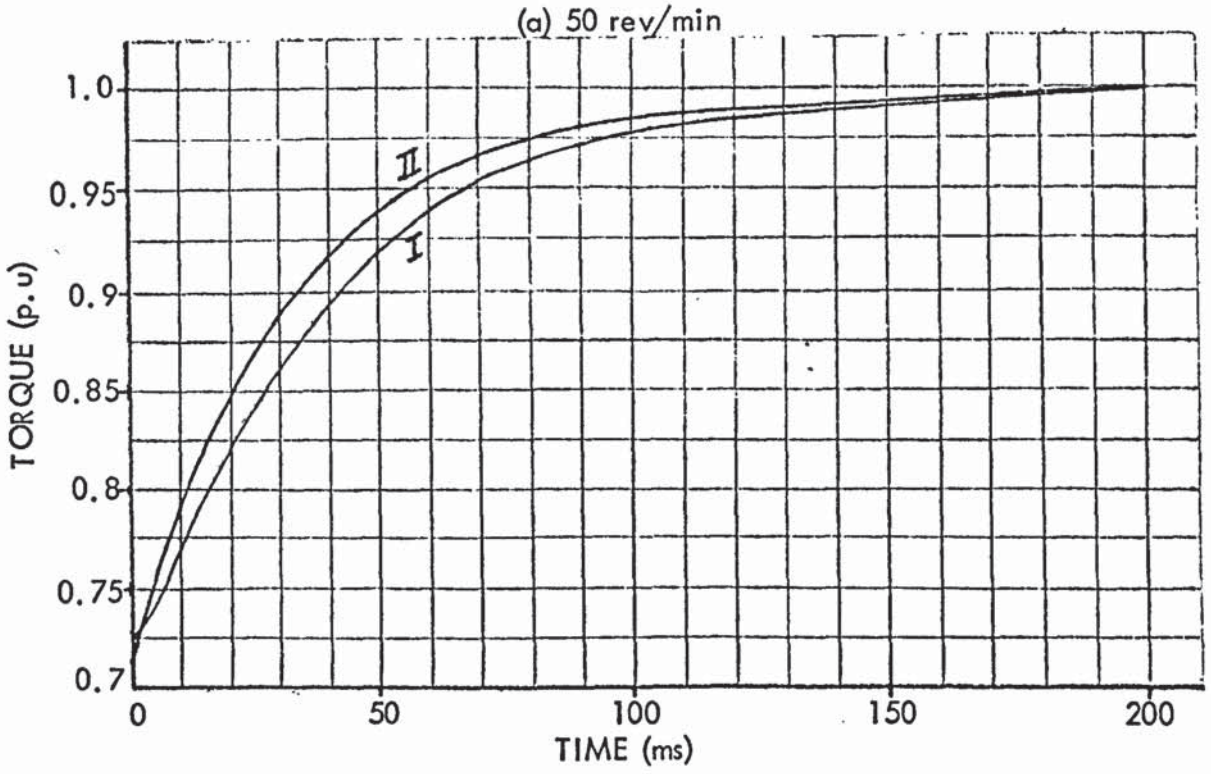

(b) 100 rev/min

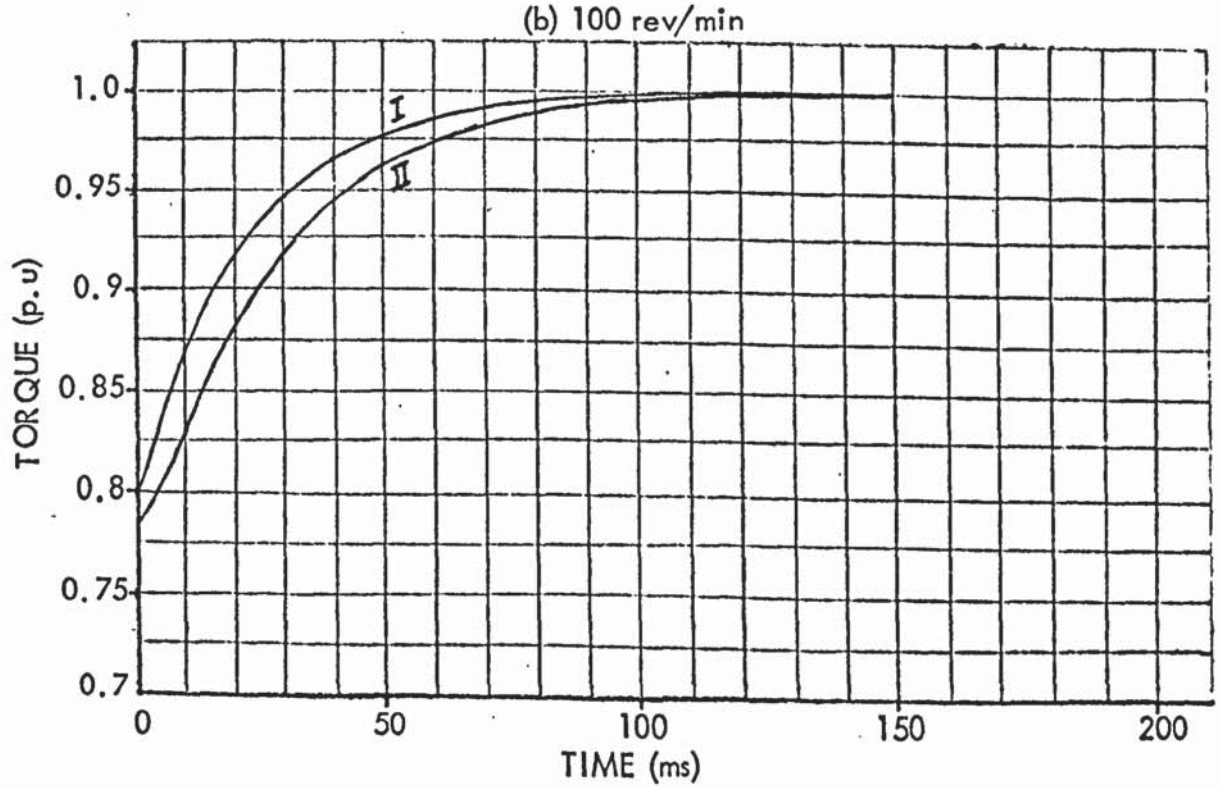

I : MEASURED RESPONSE
II : THEORETICAL RESPONSE

Figure 8.22 (cont.)

(c) 400 rev/min

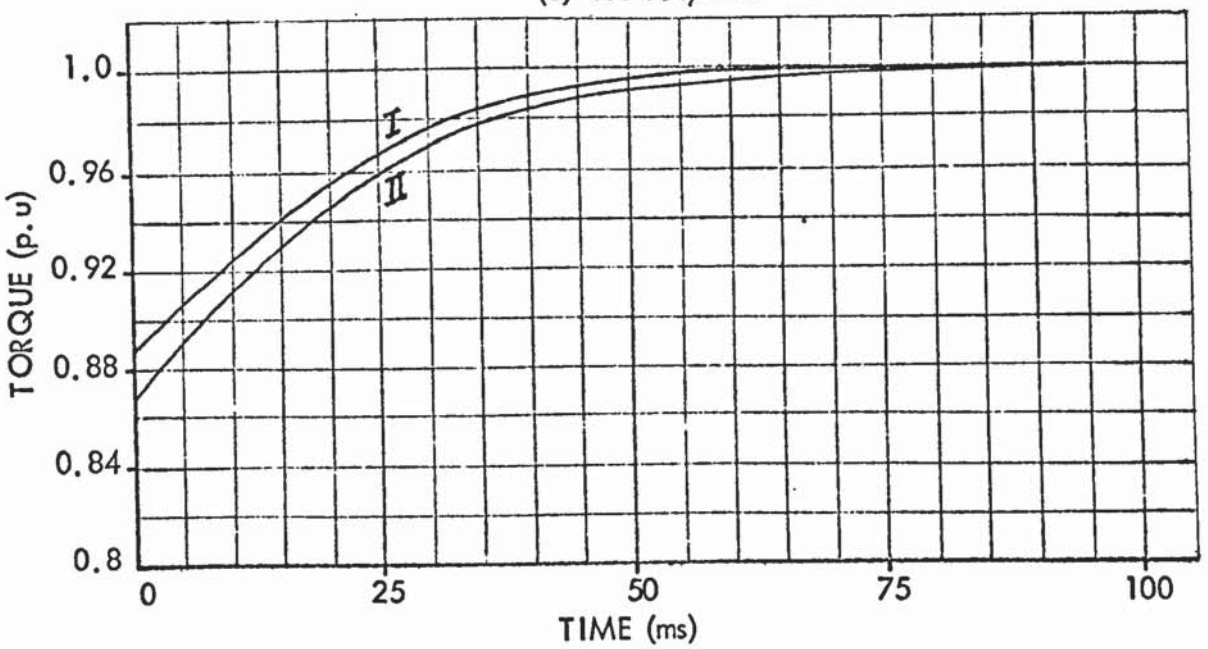

(d) 1000 rev/min

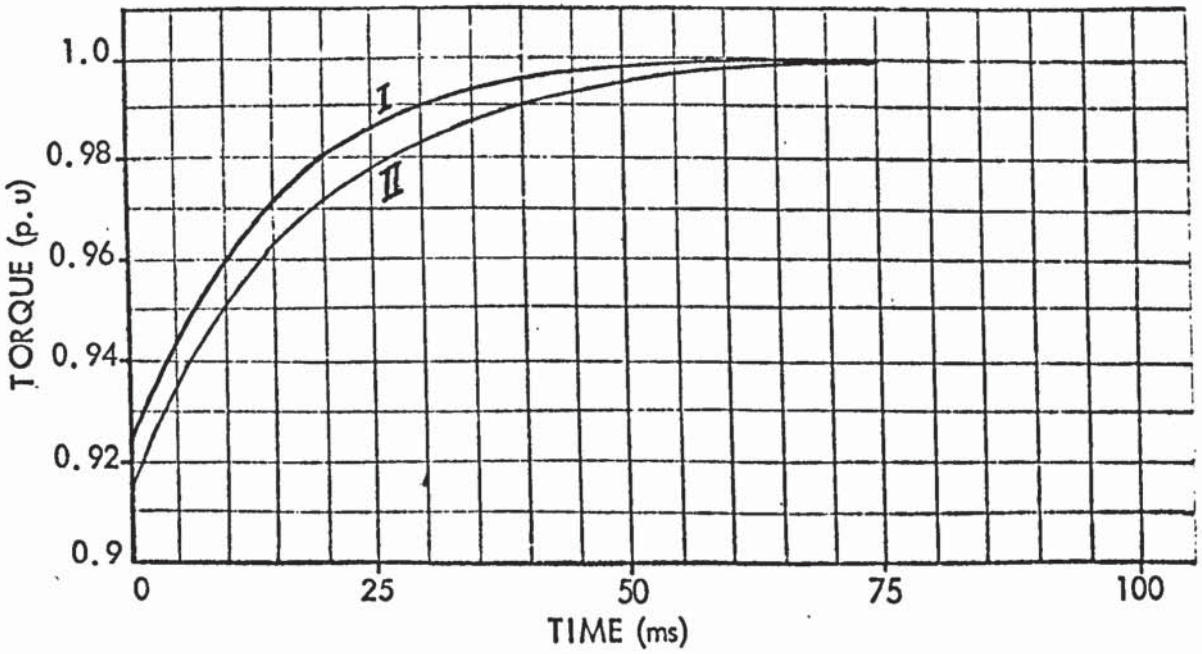

I : MEASURED RESPONSE
II : THEORETICAL RESPONSE

FIGURES FOR CHAPTER 9.

EXPERIMENTAL TORQUE-SLIP CURVES OF P.I. COUPLING

Figure 9.1

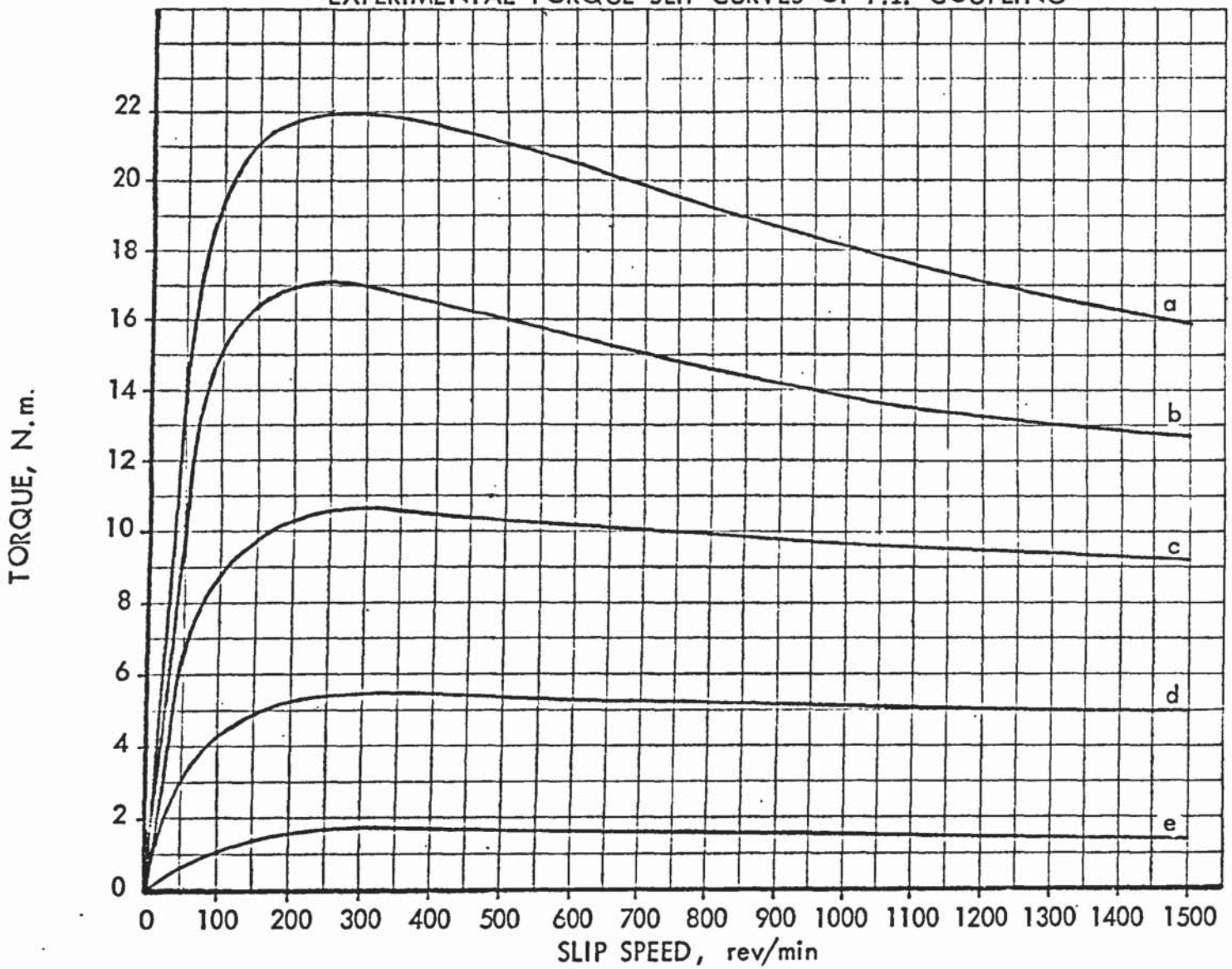

a : 500 AT/POLE
b : 400 AT/POLE
c : 300 AT/POLE
d : 200 AT/POLE
e : 100 AT/POLE

Figure 9.2

CORE FLUX AND LEAKAGE FLUX AS A FUNCTION OF EXCITATION M.M.F. AT VARIOUS SLIP SPEEDS

(Fluxes are reduced to a per pole basis)

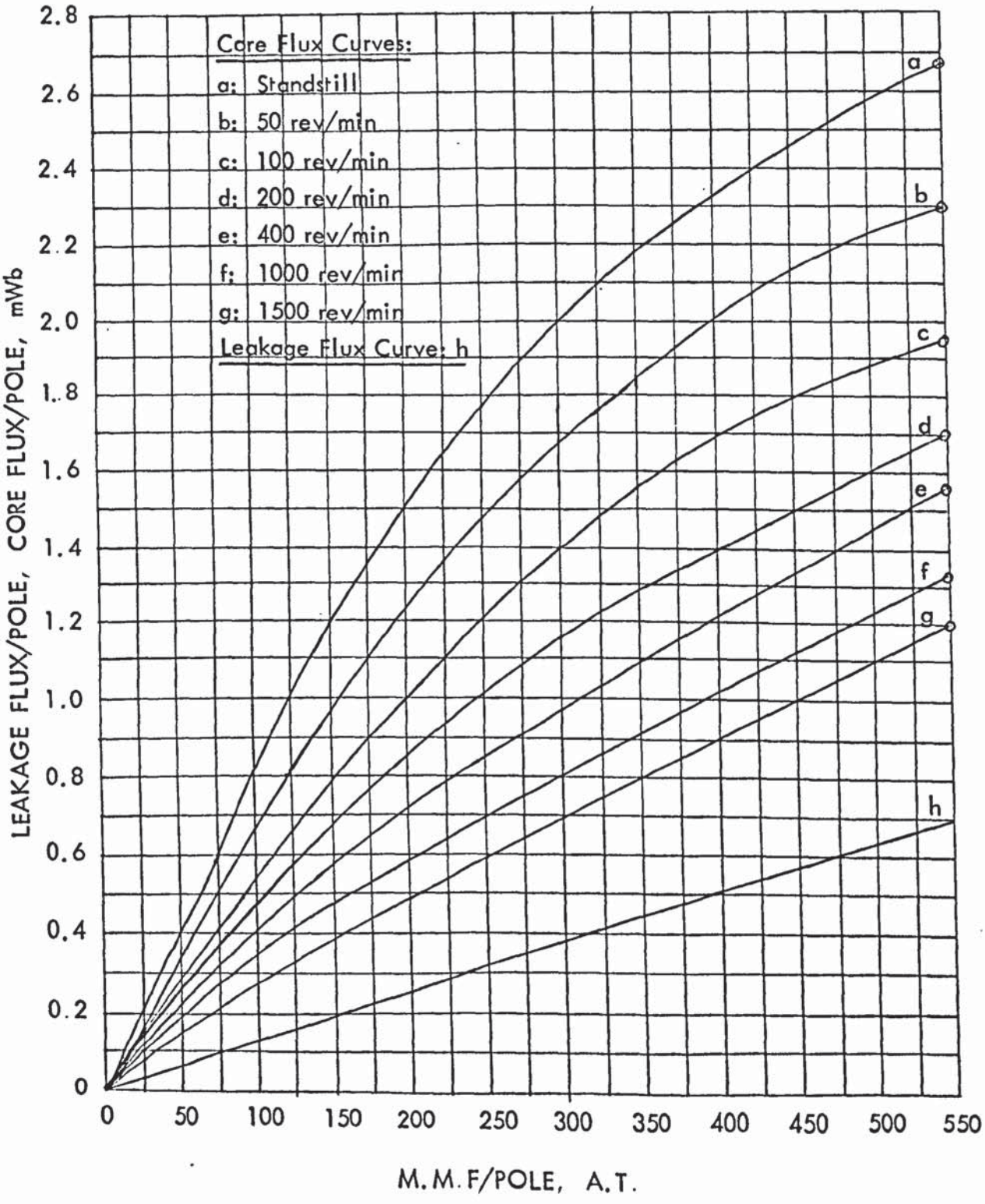

Figure 9.3

LUNDELL REGION FLUX/POLE AS A FUNCTION OF EXCITATION M.M.F. AT VARIOUS SLIP SPEEDS

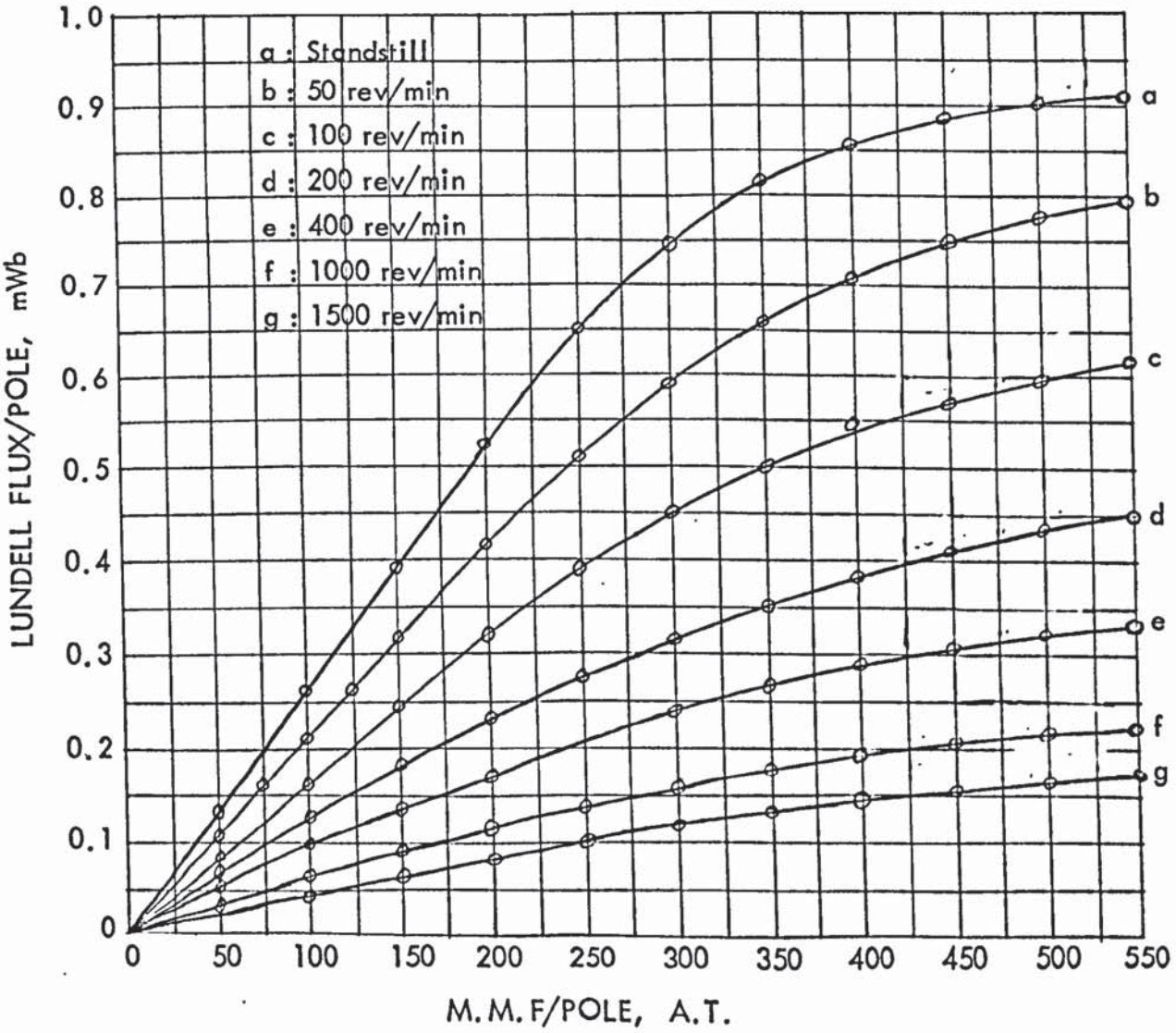

Figure 9.4

INDUCTOR REGION FLUX/POLE AS A FUNCTION OF EXCITATION M.M.F. AT VARIOUS SLIP SPEEDS

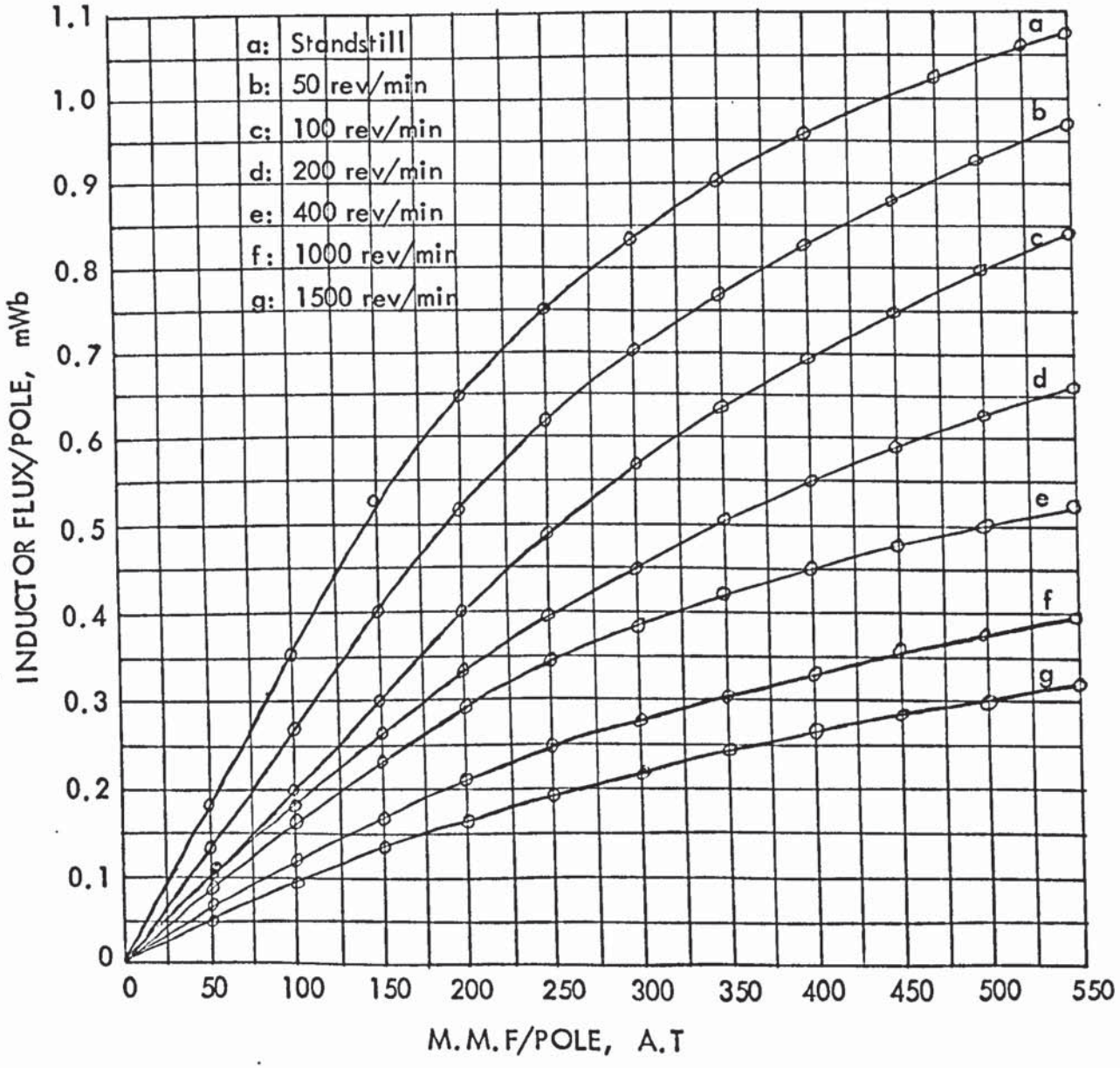

Figure 9.5

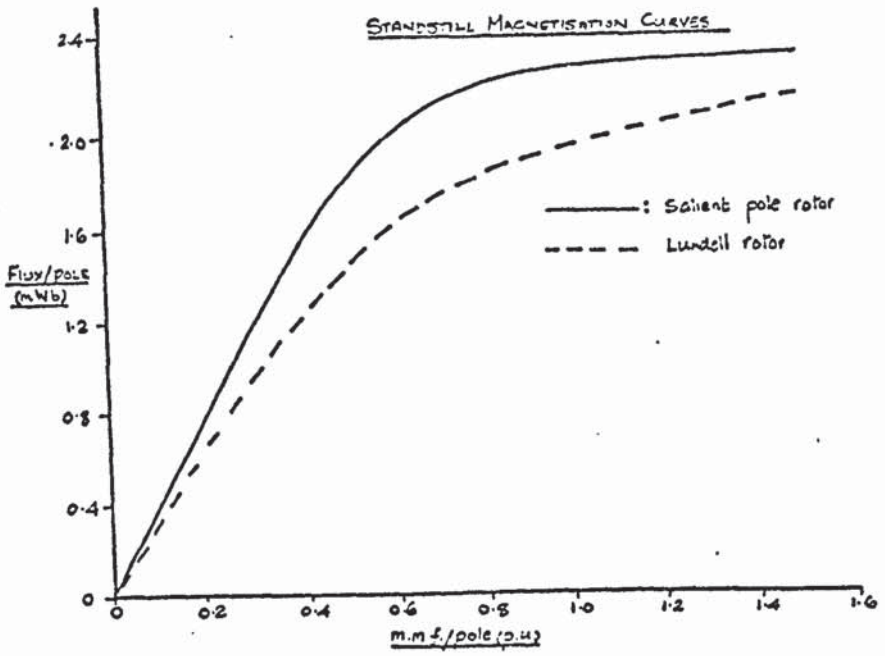

Figure 9.6

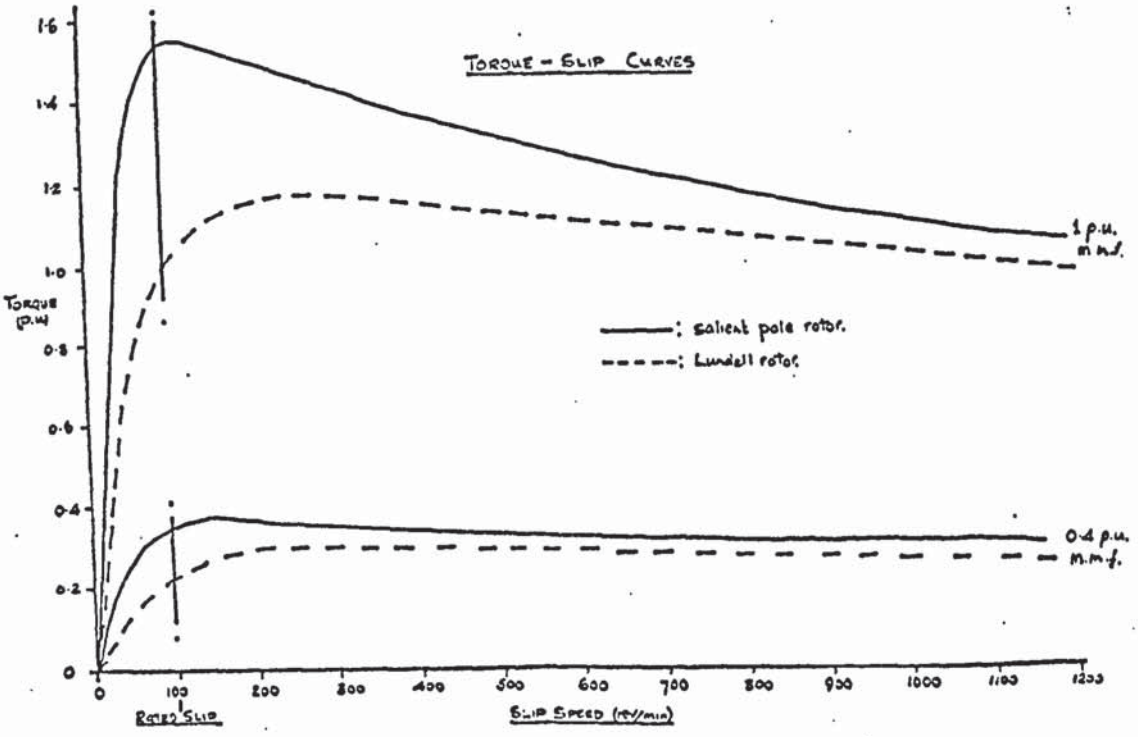

FIG. 9.7

MEASURED STEP RESPONSE OF FIELD CURRENT IN P.I. ROTOR
(Time base = 0.5 s/cm)

a) 50 rev/min slip

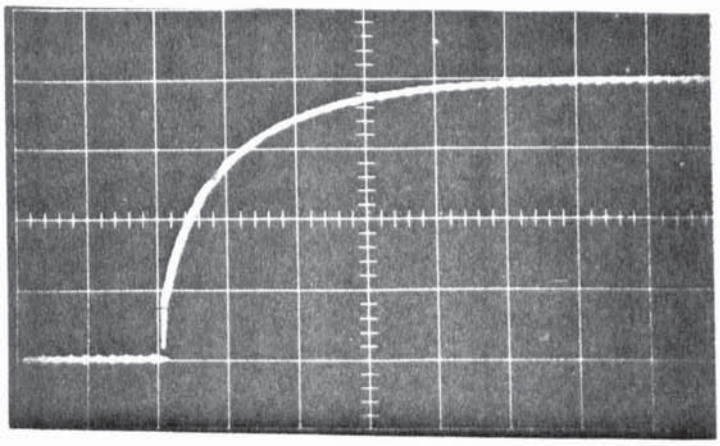

b) 400 rev/min slip

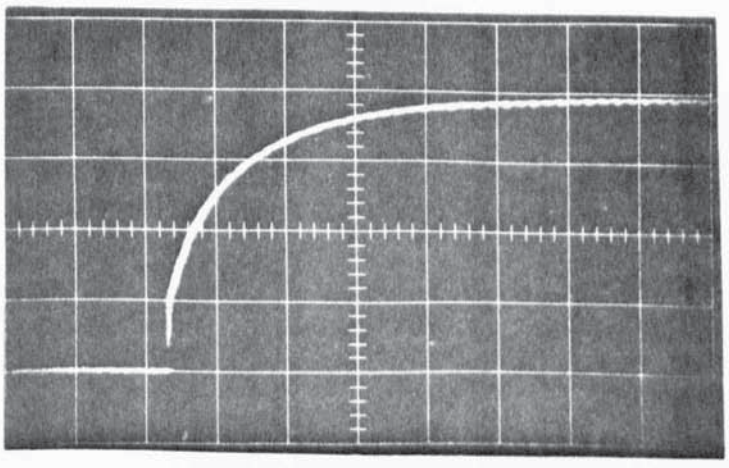

FIGURE 9.8

COMPARATIVE TORQUE RESPONSE CURVES

a) 50 rev/min

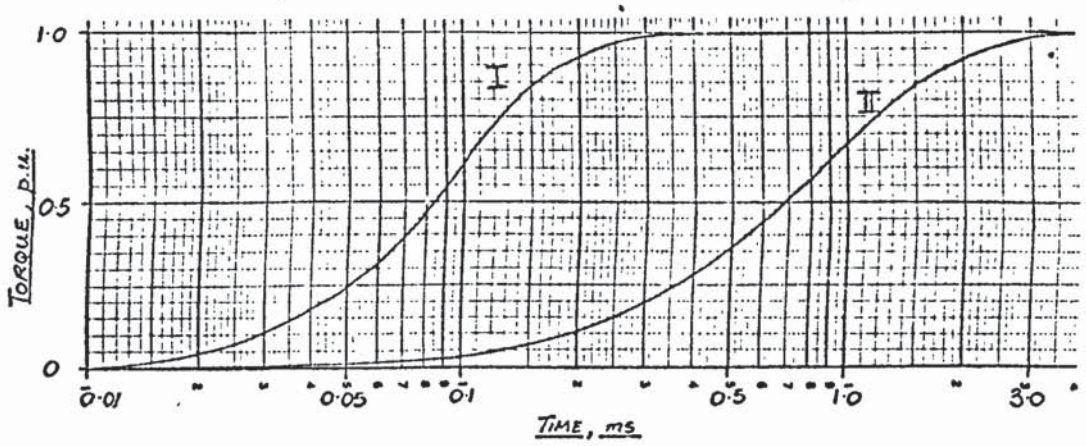

b) 100 rev/min

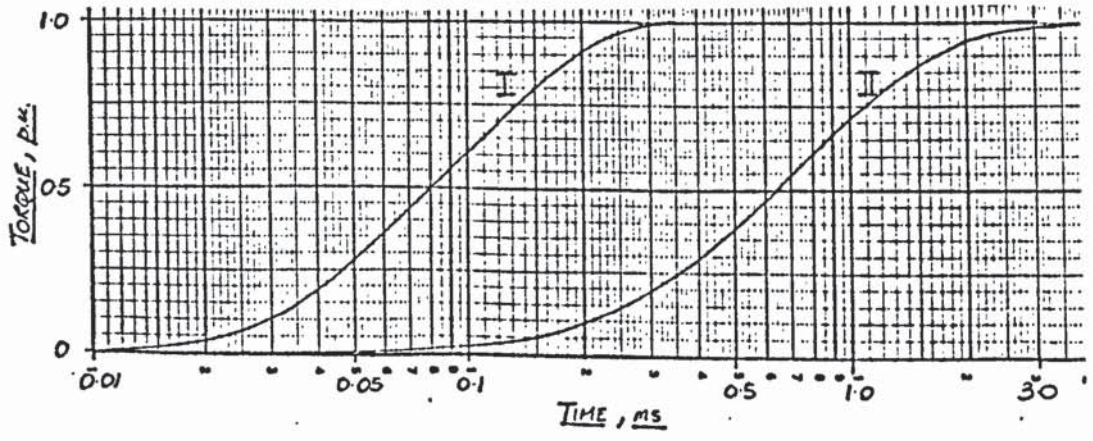

I: SALIENT-POLE ROTOR

II: PARTIALLY-INTERDIGITATED ROTOR

FIGURE 9.8(cont)

COMPARATIVE TORQUE RESPONSE CURVES

c) 400 rev/min

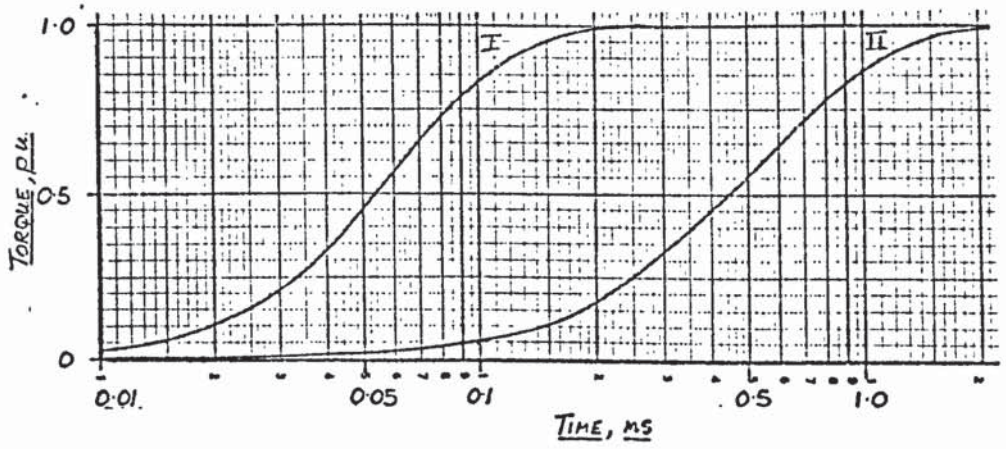

d) 1000 rev/min

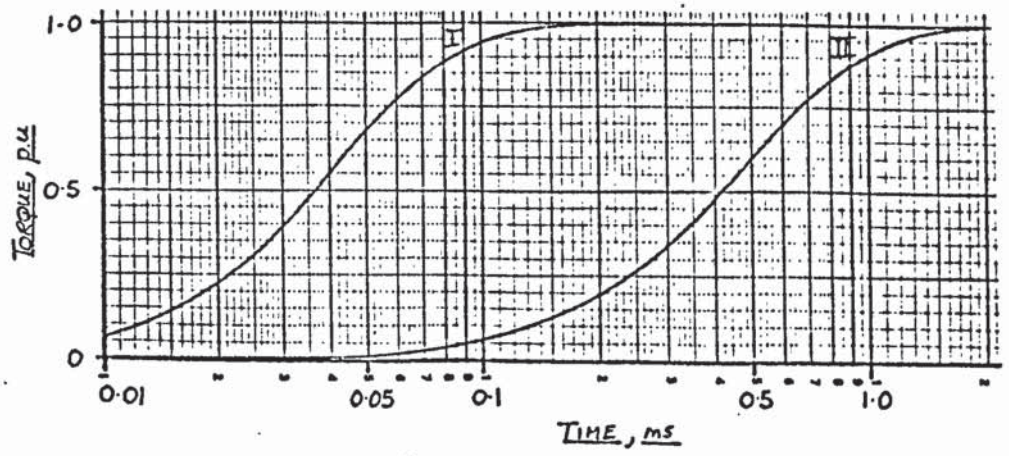

I: SALIENT-POLE ROTOR

II: PARTIALLY-INTERDIGITATED ROTOR